PROPELLER WAKE IMPINGEMENT ON A STRUT

MOQIN HE

Propeller Wake Impingement on a Strut

by

© Moqin He, B. Eng., M. Eng.

A thesis submitted to the
School of Graduate Studies
in partial fulfillment of the
requirements for the degree of
Doctor of Philosophy

Faculty of Engineering and Applied Science
Memorial University of Newfoundland

May, 2006

St. John's Newfoundland

Your file Votre référence
ISBN: 978-0-494-31318-3
Our file Notre référence
ISBN: 978-0-494-31318-3

Abstract

An unsteady and strong vortical propeller wake can have significant interaction with a body in its race. Since the pod and strut is located downstream an operation propeller for a tractor-type podded propeller, it faces risks of earlier cavitation on the strut, severe vibration of the pod unit, and noise of the propulsor. The aim of this work is to develop a prediction method for the pressure fluctuation on the surface of the pod and strut.

The study consists of two parts, experimental and numerical. In the experimental study, a podded propeller was tested in a cavitation tunnel. The tip-vortex interacting with the strut was visually investigated, and the strut surface pressure and the propeller shaft loads were measured. By using a data processing procedure, the load and pressure measurements were broken down into time-averaged and phase-averaged components. These components were then linked to the steady and dynamic performance of the propulsor. Pressure measurements showed that the low time-averaged pressure was concentrated in the area around the leading edge of the strut. The lowest pressure was located on the strut suction side near the junction of the strut and pod. However, the largest amplitude of the phase-averaged pressure occurred on the strut leading edge where the tip-vortex impacts the strut. Based on measurement of the propeller shaft loads, the wake impingement effect on the propeller performance was evaluated. The evaluation

was made by comparing the shaft loads measured in two tests with and without the installation of the pod and the strut. These showed that wake impingement had no significant effect on the propeller shaft loads, neither on the steady component nor the dynamic components.

In the numerical study, a Wake Impingement Model (WIM) was developed and inserted into a panel code, PROPELLA. Simulations of the pressure variation on the strut surface were then conducted using the software. The WIM starts from the relaxed and aligned propeller wake. The motion of the wake sheet was traced step by step. For each time step, every wake panel moved from its previous location to a new position. The new position was determined by the product of the time interval and the local induced velocity. When the wake approached the strut, a scheme was applied to keep the wake from penetrating the body surface. To avoid the large numerical disturbance resulting when two dipole panels get too close, the two dipole panels were merged before the calculation of influence coefficients. Numerical simulations on the same tractor-type podded propeller as that in the experimental study were conducted. Although the amplitude of the pressure fluctuation in the tip-vortex/strut interaction zone was under-predicted, comparisons of the numerical results with the experimental data indicated that the simulated pressure was in good agreement over most of the impingement area. Both experimental and numerical studies with the WIM show that WI has insignificant (around 2%) effects on the propeller thrust and torque.

Acknowledgements

This doctoral work would not have been possible without the support of my supervisors, Dr. Pengfei Liu and Professor Brian Veitch, and co-supervisors, Professor Neil Bose and Dr. Bruce Colbourne. Dr. Liu has been thanked by his students for his insightful comments and great guidance. My indebtedness extends in addition to his having arranged the nice office where I stayed for years in the National Research Council Canada, the Institute for Ocean Technology and his offer of open access to his source panel codes *DF-OSFBEM* and *PROPELLA*. It is certain that I could not have finished the PhD study without Professor Veitch's patient assistance, continued confidence, trust, and acceptance. I want to express my sincere gratitude to Professor Neil Bose, the Canadian Research Chair for Offshore and Underwater Vehicles Design, who was always generous to me and gave me valuable suggestions during the research, and he continues to show his interest in my success and has accepted me as a team member of his underwater vehicle group. Dr. Bruce Colbourne inspired thought toward the application of this research to practical problems.

I would like to express deep thanks to my previous supervisor, Professor Hongcui Shen, and the former director of China Ship Scientific Research Center, Professor Shitong Dong for their support. Without their encouragement, I would not even have come to MUN and started my PhD study.

I also appreciate the support and advice from Dr. Christopher Williams, time of discussions from Dr. Wayne Raman-Nair and Dr. Shin N. Chin, and

experimental data shared from Dr. Ayhan Akinturk and Mr. Jungyong Wang. There are still many others at MUN and IOT that I have to express my thanks to them for their help from the computer set up, the model design, manufacture, to the pressure measurement and the data acquisition. They include: Messrs Gilbert Wong, Trent Slade, Tony Randell, Darrell Sparks, Craig Kirby, James Williams, Peter Hackett, and Andy Wallace.

Last but not least I want to express my special thanks to my wife Jie and my son Roger for their support and patience during the entire study.

This work was performed under the Systematic Investigation of Azimuthing Podded Propeller Performance program supported by Natural Sciences and Engineering Research Council of Canada, Oceanic Consulting Corp., Thordon Bearings Inc., the National Research Council Canada and Memorial University of Newfoundland.

Contents

List of Tables

List of Figures

Nomenclature

BPF	*blade passing frequency = propeller shaft rps × propeller blade number*
C_p	*pressure coefficient*
$C_{\overline{p}}$	*pressure coefficient of the time-averaged component*
$C_{\widetilde{p}}$	*pressure coefficient of the phase-averaged component*
D	*horizontal distance between the two foils, see Figure 2.4*
D_p	*propeller diameter*
f	*oscillation frequency*
$F_{\_cut}$	*marker for where and which panel side intersects with a leading edge segment*
I_{bp}	*body panel index*
I_{es}	*foil leading edge segment index*
I_{pc}	*wake panel corner index*
I_{wp}	*wake panel index*
J	*advance coefficient* $J = V / n / D_p$
$\overrightarrow{l_{a\backslash}}$	*leading edge segment position vector, subscript a/b indicates two ends*
$t / t + \Delta t$	*indicates time*
M_{bp}	*total number of body panels*
M_{es}	*total number of the strut leading edge segments*
n	*propeller shaft revolution speed in revolution/s*

p	*pressure measured*
$\bar{p}$	*pressure of the time-averaged component*
$\tilde{p}$	*pressure of the phase-averaged component*
p'	*pressure of the high frequency component*
$\overrightarrow{r_{a1}}$	*vortex filament position vector, subscript a/b indicates two ends, and 1/2 indicates* $t/t+\Delta t$
$\vec{r}_t$	*position vector at time* t
$\overrightarrow{r_{t+\Delta t}}$	*position vector at time* $t+\Delta t$
$\overrightarrow{r_w B_1}$	*vector point from a wake panel corner,* $\vec{r}_w$*, to a body panel corner,* $\overrightarrow{B_1}$
r_σ	*radius of vortex filament*
R_p	*radius of propeller*
rps	*revolution per second*
U	*the ambient normal velocity passing a body*
V_l	*induced velocity component tangent to the body panel*
$\vec{V}_t$	*induced velocity at time* t
Y_r	*vertical position of the rear foil, see Figure 2.4*
Z	*vertical distance from the propeller shaft centre*
Z/R_p	*dimensionless vertical distance by the propeller radius*
Δt	*time increment*

Γ *vortex filament strength, vortex ring strength*

Γ_{ij} *vortex ring strength, subscripts i and j are panel index*

μ_{ij} *dipole strength, subscripts i and j are panel index*

λ *aspect ratio*

Chapter 1 Introduction

The world's earliest pod propeller may have been constructed by Hiram S. Maxim over a century ago. In fact, it was built as an apparatus to test the efficiency of various kinds and forms of screws, and the lifting power of airplanes of various sizes and shapes set at various angles (Maxim, 1891). As shown in Figure 1.1, the pod propeller consists of a four-bladed propeller, a pod that houses the propeller shaft, and a frame that connects the pod to the airplane. In 1990, just one century after this aerial pod propeller was made, the world's first application of a podded propeller to marine propulsion, *Azipod*, was installed on the vessel "Seili" by Asea Brown Boveri Ltd (ABB, 2003).

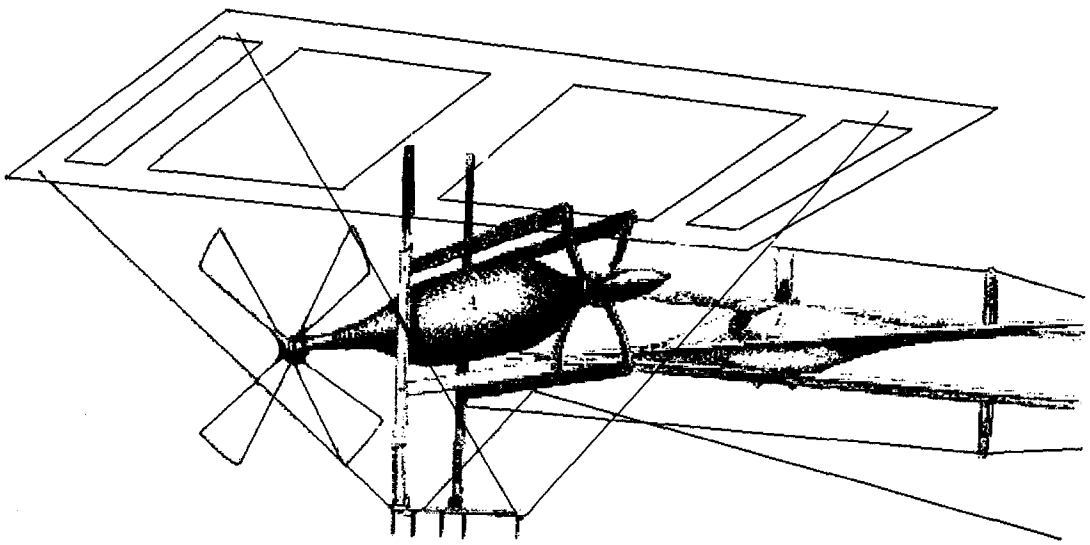

Figure 1.1 A Podded Propeller in the 19th Century

Seili is a buoy tender and is propelled by a single *Azipod* of 1.3 MW. Comparing it with her sister ship, which is propelled by a conventional nozzle propeller, *Seili* performed with higher efficiency and better maneuverability in heavy ice conditions both forward

and astern (Juurmaa et al., 2002). Since the world's first commercial and successful introduction of an electric drive podded propeller to a marine vessel, the range of podded propeller applications, capacity and type have increased tremendously (Atlar, 2004).

Applications are growing while the technology is still under development. In recognition of the need to increase the understanding of pod propeller hydrodynamics, structure, and safety and thereby improve designs and reliability of future products, a number of projects have been carried out by national and multi-national collaborations. There is a summary of these collaborations in the report by The Specialist Committee on Azimuthing Podded Propulsion of the 23rd International Towing Tank Conference (Atlar et al., 2005): Between 1999 and 2005, three large scale projects have been conducted under the EU Framework Programme (FP5). First, OPTIPOD brought together 14 EU partners to establish design guidelines for pod-driven ships. Next, PODS-in-Service brought together 18 partners to investigate the reliability of pods through in-service monitoring and measurement. Finally, FASTPOD brought together 17 partners aiming to identify the maximum feasible limits when using podded propulsors on large fast commercial ships in an efficient, safe and environmentally friendly manner. In Canada, a 5-year research programme was started in 2002. The research programme has several objectives: quantify the effect of podded propulsor configuration on performance; develop instrumentation for model tests and numerical methods for performance prediction; and quantify the blade loading effects in open water and in ice at off-design conditions (Veitch, 2001). In Japan, a national programme entitled "Super-Ecoship" was initialized. In order to promote cargo transportation from land to sea, this project aims to

develop novel coastal ships driven by a CRP-Podded propulsor (a pair of Contra-Rotating Propellers at the same end of a podded propeller) with a higher cargo capacity, propulsive efficiency, maneuverability and less vibration and noise (Ukon et al., 2004). In Finland, a Hybird CRP-Podded propulsor (a conventional propeller followed by a contra-rotating tractor type podded propeller) was being researched. One of the hybrid systems was installed on a *Ropax* ferry (Bushkovsky et al., 2004).

Podded propellers can be categorized by their configurations. As shown in Figure 1.2, there are six types of podded propellers. A similar summary has also been made in a report of Studio di Ingegneria Navale e Meccanica (SINM, 2004). Beside the CRP-Podded propulsor and the Hybird CRP-Podded propulsor referred to in the previous paragraph, tandem-type and single propeller type podded propellers are also included. Both contra-rotating and single-propeller types of podded propeller are subdivided into tractor-type and pusher-type respectively. The two simplest configurations are the tractor-type and the pusher-type single propeller podded propulsors. The pulling propeller (the propeller is located upstream from the pod where an electrical motor is housed) provides various advantages concerning efficiency, controllability, comfort and vessel layout (PODs-in-Service, 1999). The investigations include numerical simulations and scale model tests on the hydromechanical and structural performance. In some cases speed and power, as well as pressure fluctuations, have been measured during ship trials and in-service. Juergen (2004) showed the wake field for at least a twin screw podded vessel to be very smooth and nearly uniform by doing a large series of model tests (cavitation observations, pressure fluctuation and noise measurements) with different types of pod

propulsors in the Hydroacoustic and Cavitation Facility (HYKAT), Hamburg Ship Model Basin (HSVA). The very smooth wake field results in low excitations induced by the propellers, both in terms of hull pressure fluctuations and shaft forces. This is one of the main advantages for podded propulsion concerning the vibration and noise behavior.

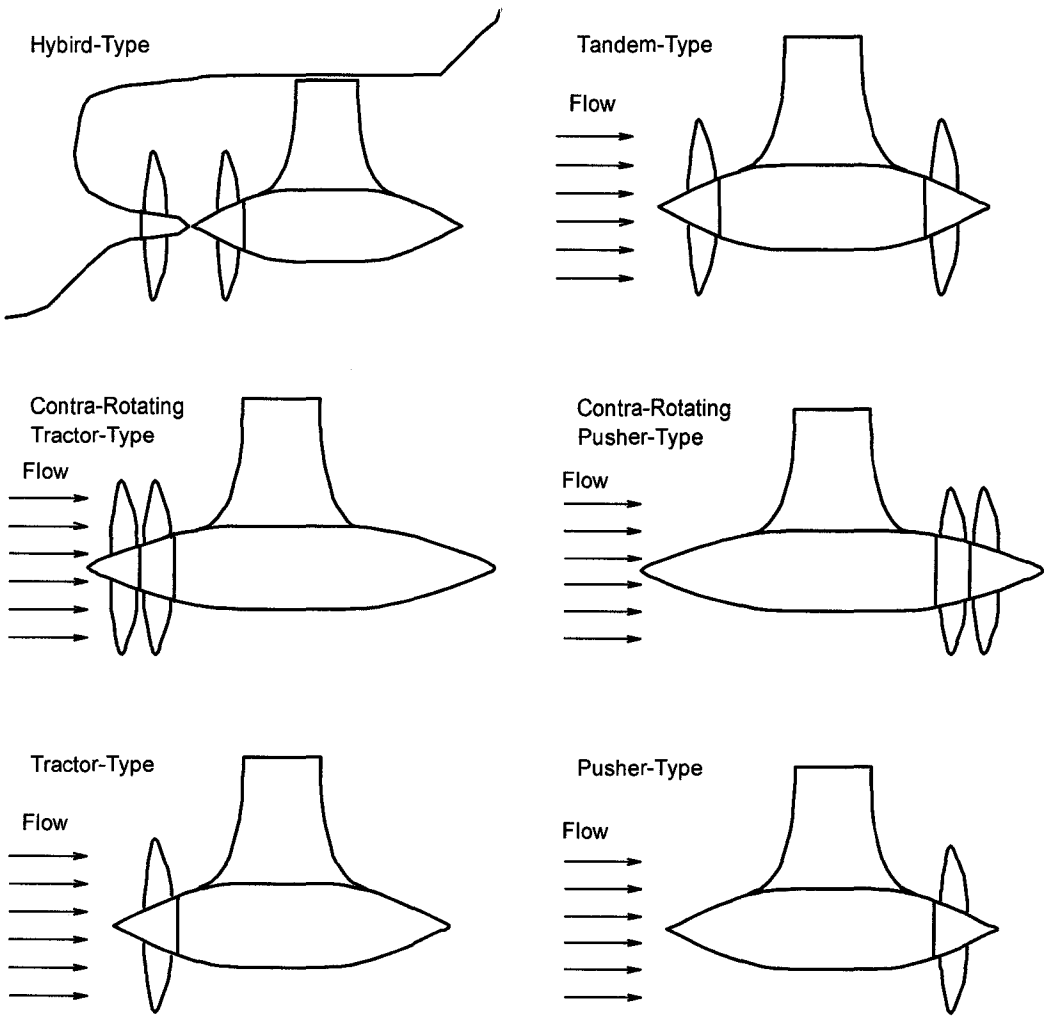

Figure 1.2 Types of Podded Propellers

On the other hand, studies have shown that problems still exist with podded propulsor applications. A study by Carlton (2002) of sources of failure on podded propulsors of 27

podded propeller propelled ships showed that bearing problems accounted for 34% of failures of the propulsion systems. The distribution of failures was given as follows:

Table 1.1 Relative Sources of Pod Propulsor's Failure (-source: Carlton 2002)

Bearings	Seals	Electrical	Cavitation	Grounding	Shafting	Miscellaneous
34%	21%	20%	11%	5%	2%	7%

This suggests that the estimated bearing forces arising from hydrodynamic loads were under-predicted, or considerations given to bearing forces were insufficient. Bearing forces transferred from propellers can be split into averaged forces and fluctuating (cyclic and non-cyclic) forces similar to the study on the effect of an oscillatory free-stream-flow on a NACA profile by Krause and Schweitzer (1990) in which the velocity and pressure measurements were broken down into three components. Precise evaluation of average components is sufficient for power and speed predictions. However, the fluctuating components of these forces are very important in the design of bearings, because bearing failures are more related to the maximum values of forces, which are equal to average components plus fluctuating components. This finding suggests that more accurate bearing force prediction methods are needed in additional to mechanical solutions in the prevention of bearing failures.

Following bearings failures, cavitations ranks as the second within these sources of failures related to hydrodynamics. In the case of the tractor-type podded propellers, the propeller is located upstream from the pod and strut, and the blade wake impacts on the

strut and pod. The pressure fluctuations on the strut and pod will be increased by the wake impingement compared with that of pusher-type podded propellers. The increased pressure fluctuation may lead cavitation inception to occur earlier on the strut of the tractor-type than the pusher-type podded propellers.

Some studies have found that a vessel installed with a single-podded-propeller (either tractor-type or pusher-type) may face problems on the course keeping performance. The rotating propeller swirls the flow around the vessel stern and downstream of the propeller. The swirling flow generates asymmetrical hydrodynamic forces on the vessel as well as on the pod and strut. Grygorowicz and Szantyr (2004) found that in their single-pod-unit without fin, during self-propelled manned model tests, the tested vessel had to apply an approximate 5° drift angle to balance the lateral force generated by the propeller operation. Another example is the modification design of the Double Acting Tanker (DAT). The DAT is propelled by a single tractor-type podded propeller and is efficient for forward propulsion in open water conditions. The original design was found to not comply with the International Maritime Organization (IMO) Maneuvering Standards based on model tests (Tragardh et al., 2004). The main reason was that the lateral force generated by the propeller operation on the propulsor was too large. After a fin was attached to the bottom of the pod (Figure 1.3), the lateral force on the strut was then mostly balanced by another lateral force on the fin which was also induced by the rotating propeller. Although the modified design complied with the IMO Maneuvering Standards, it may leave room to improve the design by applying the knowledge of the interaction of propeller wake and strut as well as the wake impingement.

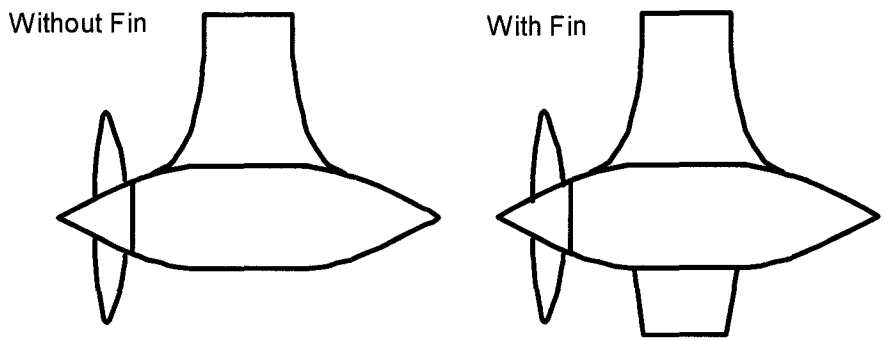

Figure 1.3 Pod Unit With/Without a Bottom Fin

In recognition of the wide application potential of the podded propulsor and knowing that some problems still exist, a group of researchers are working collaboratively to carry out a systematic investigation of azimuthing podded propeller performance (Veitch, 2001). The investigation includes the following goals: quantify the effects of podded propulsor configuration variations on propulsion performance; develop computational methods for podded propeller performance prediction; develop an extrapolation method for powering prediction of ships fitted with podded drives; quantify the blade load effects of propeller operation in steady oblique flow; quantify the blade load effects of propeller operation in ice; develop model propeller manufacture capability and instrumentation for performance evaluation of podded propellers in model scale.

Commercial applications of podded propulsors are growing quickly while improvements to podded propeller hydrodynamics, structure and safety are still necessary (Carlton, 2002). Many investigations and studies show the tractor-type podded propeller, comparing it to the pusher-type, providing various advantages concerning efficiency, controllability, comfort, and vessel layout (POD in SERVICE, 1999). However, some

studies (Tragardh et al., 2004) show that the tractor-type podded propulsor has some problems raised by its configuration. Since the pod and strut are located in the race of the wake generated by the operating propeller, pressure and pressure fluctuation on the pod and strut surface are changed by the propeller wake impacting on the surfaces. This might cause cavitation to occur earlier on the strut surface and raise a larger lateral force on the strut than those of a pusher-type podded propeller. An experimental study on the mechanism of the interaction between a propeller wake and a strut has been carried out and is reported here. Based on the improved understanding of the wake impingement, a more accurate numerical prediction method on the strut pressure fluctuation is developed. This can be applied in designs to help avoid the types of failures noted above and improve podded propeller reliability.

Chapter 2 Review of Literature

To provide a background for the study on strut surface pressure variation induced by the propeller wake impacting on the strut, the literature review will concentrate on the following three fields: studies on podded propellers, modeling of wake impingement, and improvements of panel methods.

2.1 Podded Propeller

The world's first azimuthing electric propulsion drive was made in ABB in 1990 after several years of research and development (www.abb.com/marine). It was installed on a buoy tender, MV *Seili*, and was of 1.3 MW in power. Comparing *Seili* with her sister vessel driven by a conventional nozzle propeller, *Seili* has higher propulsion efficiency, better maneuverability, and higher ice breaking capability (Juurmaa et al., 2002). After this successful application, many high profile projects, OPTIPOD, PODS-in Service, etc, have been carried out and many types of podded propeller have been studied. The concept of an azimuthing submerged electrically driven puller propeller provides various economic, safety and comfort advantages. Increases up to 10% in the propulsion efficiency have been claimed, along with decreases of 30 to 60% in the noise and vibration levels (Pods in Service, 1999). Based on the model tests for a double acting tanker, Tragardh et al. (2004) found a bottom fin (Figure 2.1) was needed to improve the original design and to comply with IMO Maneuvering Standards. The reason was the lateral force on the strut induced by the propeller wake was mostly cancelled by that on the bottom fin. The first attempt to numerically predict the strut hydrodynamic forces are

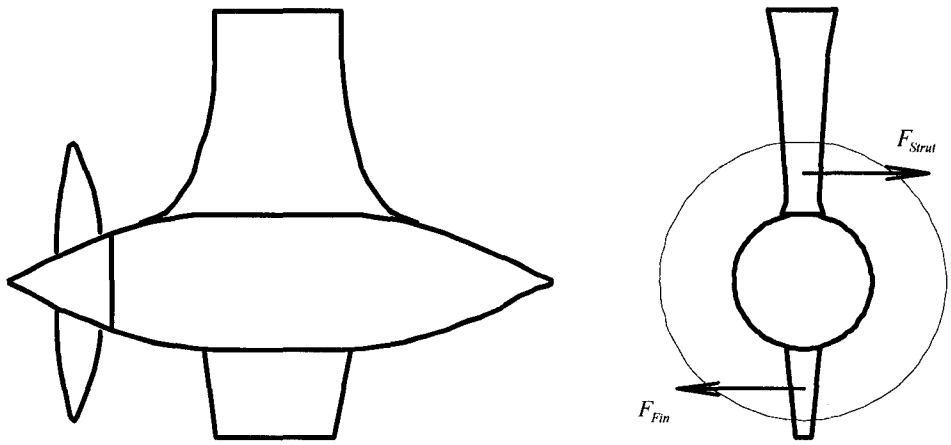

Figure 2.1 Reduce the Lateral Force by Adding a Bottom Fin

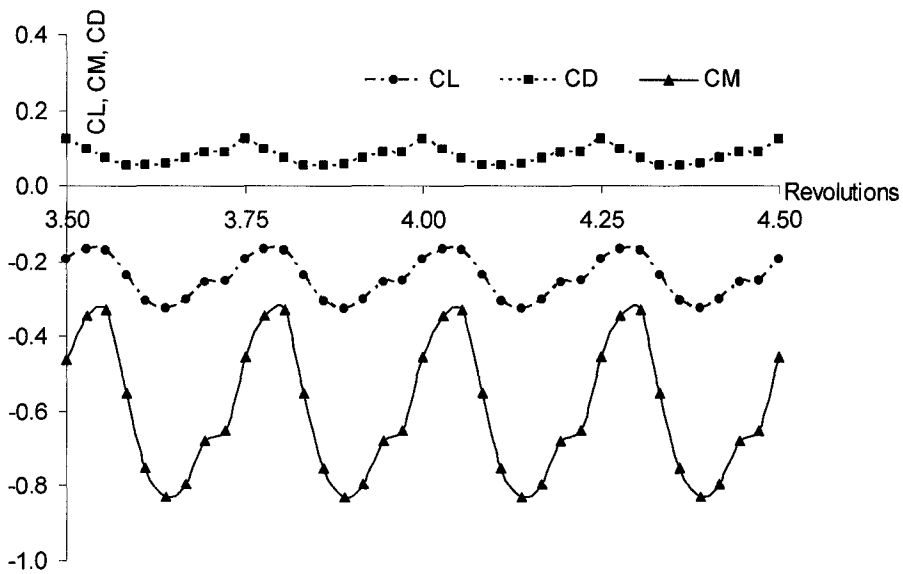

Figure 2.2 Unsteady Strut Lift, Drag and Moment Coefficients ($J=0.5$)

(from Deaniset et al., 2003)

thought to have been made by Deniset et al. (2003). In their study, a potential flow based method coupled with a RANS (Reynolds Averaged Navier Stokes) solver was used in the

predictions of the strut drag, lift, and moment. As shown in Figure 2.2, the unsteady strut hydrodynamic lift, drag and moment were dominated by the component of the blade passing frequency, four periods corresponding to four propeller blades. The amplitudes of the fluctuating components of the lift (lateral force), the drag and the moment were predicted to be around 1/3, 1/3 and 1/2 of their steady components respectively. Ohashi and Hino (2004) simulated the flow field around a vessel installed with either a tractor-type or a pusher-type contra-rotating podded propeller. By using a RANS solver, FINFLO, Sanchez-Caja and Pylkkanen (2004) designed a non-symmetric strut, shown in Figure 2.3, in order to avoid cavitation inception keeping at the same time low drag and low lateral forces for a tailor-made design as compared to a conventional symmetric strut.

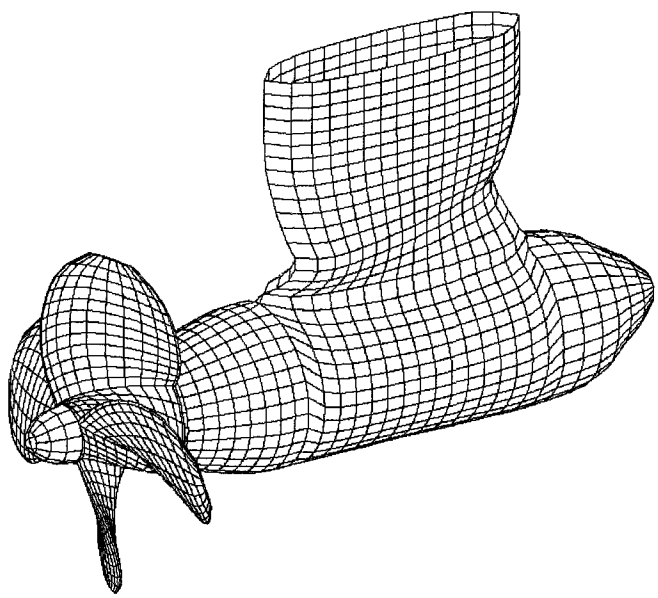

Figure 2.3 Illustration of an Asymmetric Strut and Pod (-source: Sanchez-Caja et al. 2004)

2.2 Panel Method

Since Hess and Smith (1964) led the study of panel methods for subsonic flows around complex three dimensional non-lifting bodies, and arbitrary lifting bodies (Hess, 1972), a lot of work has been done to improve the methods and/or extend the application of the method.

Morino (1973), Morino and Kou (1974), and Morino et al. (1975) developed a general formulation and code of a hyperboloidal panel method for steady and oscillatory, subsonic and supersonic, potential linearized aerodynamic flows around complex configurations. Constant strengths of sources and dipoles or dipoles alone were distributed on each element of the hyperboloidal surface. A hyperboloidal panel can be used to increase the accuracy of highly roll-up wake simulation (Pyo and Kinnas, 1997). The expression for a hyperboloidal surface panel is given by equation (A-9) in appendix A and a comparison of a flat and a hyperboloidal surface panel is made in Figure 2.4. Maskew (1987) developed a computer program (VSAERO) for calculating the subsonic aerodynamic characteristics of arbitrary configurations having vortex separation and

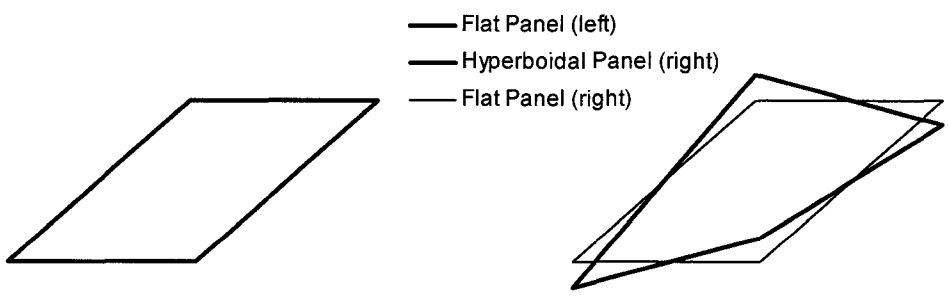

Figure 2.4 Comparison of a Flat and a Hyperboidal Panel

strong vortex/surface interaction. In this method, the planar panel was used to represent arbitrary body surfaces and wake sheet surfaces. Constant sources/sinks and doublets were distributed on body surfaces. On wake sheet surfaces, only doublets were distributed constantly on each panel. Hess and Valarezo (1985) apparently made the first attempt using panel methods to obtain pressure distribution on ship propellers as well as aircraft propellers. Kerwin et al. (1987) extended a panel method to hydrodynamic analysis of ducted propellers. Hoshino (1989a) applied panel methods to hydrodynamic analysis as well as wake modeling of propellers in steady flow. Comparisons of simulated results with LDV measurements were also made (Hoshino, 1989b).

Hsin (1990), and Kinnas and Hsin (1992) improved a low order panel code developed at the Massachusetts Institute of Technology (MIT) by using hyperboloidal panels, introduced a time-marching technique to the panel code, and applied the method to the analysis of the unsteady flow around highly skewed propellers. In the method, linear dipole distributions were used at the first wake panels adjacent to the blade trailing edge in order to render the method insensitive to the time step size and also avoid instability in the numerical method. Hoshino (1993) also conducted hydrodynamic analysis of propellers in unsteady flow by using a panel method. The surface of the propeller blade and hub was approximated by hyperboloidal quadrilateral panels with constant source and doublet distributions whose strengths varied with time. The surface of the trailing vortex sheet was also represented by hyperboloidal quadrilateral panels with constant doublet distributions. Strengths of the sources and doublets were determined by solving the boundary value problem at each time step. Hoshino's study has

shown that an iterative Kutta condition is indispensable to solve the unsteady propeller problem. The unsteady panel method could predict the unsteady pressure distribution on the blade of not only a conventional propeller but also of a highly skewed propeller.

Richason and Katz (1993) formulated an unsteady panel method in an initial frame-of-reference, attached to the undisturbed stationary fluid, for multiple bodies moving along various paths. This choice of the frame made the numerical interpretation of the multiple-body, solid-surface boundary condition and the viscous wake rollup considerably simplified. Liu (1996) and Liu et al. (1997) developed a PM (Panel Method) code, OSFBEM (Oscillating Foil Boundary Element Method), and used a time domain panel method to predict hydrodynamic performance from an oscillating foil with both spanwise and chordwise flexibility. The program was designed, and is able, to predict hydrodynamic properties for an unsteady, 3-D flexible wing. A number of features were implemented including the geometry of both 2-D and arbitrary 3-D planforms; large amplitude pitch and heave motions; non-zero trailing edge thickness; flexible motion and geometry parameters such as steady flow, unsteady motion, chordwise and spanwise flexibility; and approximate prediction of skin friction and qualitative examination of sectional flow patterns in terms of boundary layer growth. Simulations of whale flukes showed that passive spanwise flexibility reduces propulsive efficiency, but that propulsive efficiency of these planforms can be increased over the value for an equivalent rigid foil by careful control of the phase of the spanwise flexibility relative to other motion parameters. A time domain panel method code DF_OSFBEM (Liu, 2006) based

on OSFBEM was recently used to evaluate and optimize the performance and motion parameters of a wing-in-ground effect (WIG) dual-foil oscillating propulsor.

Panel methods have also been used in calculations of hydrodynamic forces acting on marine propellers with ice blockage effects, and the first application was carried out by Bose (1996). The inflow of the propeller was restricted by two conditions: a simplified inflow field estimated to account for approximately the wake behind an ice block; and the same inflow field in combination with a patch of panels placed upstream of the propeller to represent the ice blockage face. With an ice-contact-load model developed by Veitch (1995) and a panel method, PROPELLA, developed by Liu (1996a), Veitch et al. (1997) predicted the hydrodynamic load as well as the ice-contact-load on an ice-class propeller. A time-domain propeller-ice interaction model was used in the simulations. Liu et al. (1998, 2000, 2001) extended the panel code, PROPELLA, to predict ice-induced hydrodynamic loads on propellers due to blockage at a fixed proximity as well as variable proximity.

To obtain a unique solution to a lifting flow problem in potential flow, the Kutta condition needs to be enforced at the trailing edge. The development and improvement of procedures for the numerical Kutta condition started at almost the same time as that of panel methods. Hess (1972) found that use of a pressure-equality Kutta condition is more accurate and less sensitive than the flow-tangency Kutta condition. A procedure was given by Morino (1974) to fulfill the Kutta condition in steady flow problems to provide panel methods for lifting flow with a unique solution. Before the explicit Iterative Pressure Kutta (IPK) condition was proposed by Kerwin et al. (1987), Katz and Weihs

(1981) and Poling and Telionis (1986) studied oscillating airfoil wake rollup and airfoil responses to periodic disturbances with a steady and an unsteady Kutta condition respectively. IPK is an iterative numerical procedure that solves the pressure-equality equation during calculations of lifting bodies in unsteady flows. Bose (1994) implemented an explicit Kutta condition to a 2D unsteady potential flow panel code for thrust and propulsive efficiency calculations of oscillating hydrofoils with chordwise flexibility. Liu et al. (2002) increased unsteady IPK reliability by using the Broyden iteration instead of the Newton-Raphson iteration procedure; the later has been found to have convergence difficulties in some cases.

A large number of calculations have been made to simulate the wake sheet by replacing the continuous vortex sheet with a finite number of discrete vortices or alternatively, by replacing the dipole sheet with segments carrying a piecewise constant dipole distribution (Pyo, 1995). Suciu and Morino (1976) obtained wake alignment by an iteration to satisfy the condition that the velocity be tangential to the surface of the wake and the difference of potential to be a constant along the streamlines. Based on the measured velocity distributions of the propeller slipstream, a two-section wake model was proposed by Hoshino (1989, 1990). In the wake model, the contraction and the pitch of the wake are considered to vary in the transition wake region, while radial positions and pitch of the trailing vortex sheets are kept constant in the ultimate wake region. Pyo (1995) and Pyo and Kinnas (1997) applied a potential based boundary element method for the analysis of high skewed propeller flows. A FLow Adapted Grid (FLAG) was developed in order to solve the convergence problem which occurred when typical grid

arrangements were applied to such propellers. The geometry of the trailing wake was decided directly from the panel method and the vortex sheet roll-up was included in the FLAG. In order to model the wake sheet roll-up in three dimensions, bi-quadratic strength dipole distributions and hyperboloidal panel geometry were used. Throughout the numerical calculation, rediscretization was applied as a smoothing scheme.

2.3 Wake Impingement Model

Wake impingement refers to a kind of vortex/body interaction. It is described as vortices impacting a body. Wake impingement modeling is the simulation of the vortex response to the interaction and the load on the body induced by the interaction. To improve the understanding of this interaction, extensive studies on the flow physics and vortex structures have been conducted on simplified configurations. These studies include a normal vortex filament interacting with a blade or a cylinder (Marshall, 1994, Marshall and Yalamanchili, 1994, Krishnamoorthy et al., 1999), a streamwise vortex that splits or passes by a perpendicular blade (Mayori and Rockwell,1994, Wittmer et al., 1995, Gordnier and Visbal, 1997), a vortex that interacts with a parallel blade (Wilder and Telionis, 1998), interaction of vortex rings (Grant and Marshall, 1999), and a vortex ring encountering a wall (Orlandi and Verzicco, 1993, Fabris et al., 1996, Mammetti et al., 1999). The study of a blade cutting a vortex filament by Marshall and Krishnamoorthy (1997) indicated that a vortex impact factor, $2\pi r_\sigma U/\Gamma$, played an important role in the vortex response. Here r_σ is the radius of the vortex filament, U is the ambient normal velocity passing the cylinder, and Γ is the vortex filament strength. The radius of a vortex filament is defined as the distance from the filament centre to the location where the vortex induced tangential velocity reaches the maximum. When the impact factor was less than 0.08, the vortex/blade interaction was characterized by ejections of boundary layer vorticity from the blade prior to impact with the vortex and subsequent wrapping of this secondary vorticity around the primary vortex core. When the impact factor was greater than 0.24, there was no separation of the boundary layer prior to the impingement

of the body onto the vortex core. Gordnier and Visbal (1997) and Mamou and Khalid (2002) used Reynolds Averaged Navier Stokes Solver (RANS) solvers in simulations of the flow fields around the wake impingement zone. O'Brien and Smith (2005) studied rotor-fuselage interactions by using various rotor models. They found simulating a rotor by a constant actuator disk was inadequate for most applications, but it could be easily improved upon by allowing for pressure variations about the blade radius and azimuth.

On the side of engineering applications, the model of vortex/body interactions is greatly simplified while the complex body geometry is retained. For example, Chen and Williams (1987) used a panel method in the simulation of the flow around a counter-rotating-propfan. When a wake panel shed from the upstream propfan impacted on the downstream propfan, the wake panel was deformed and diverted to penetrate the downstream body at the nearest 'gap' located between the panels representing the propfan. One main reason for making this kind of treatment is to avoid the numerical disturbance raised when a vortex filament or an edge of a dipole panel passes through the collocation point of a body element (Chen and Williams, 1987). In a simulation of propeller/duct/rudder interaction, Liu and Bose (2001) disabled the effect of the propeller wake when it was in the domain between the leading edge and the trailing edge of the rudder. Other similar methods that have been applied in practical hydrodynamical problems including the Vortex Lattice Method (VLM) and the method of a VLM coupled with an Euler solver. Li (1992, 1993) studied propeller-rudder interaction by a VLM and non-linear potential method. In the method, influence coefficients of lattices which intersected the rudder or which were located inside the

rudder were set to zero to avoid large numerical disturbances. An iterative technique, including an Euler solver and a vortex-lattice method, was introduced by Kinnas et al. (2001) to predict the performance of two-component propulsors. Pressure distributions on propulsors were first calculated respectively by the VLM, then body force distributions obtained by the results were input to the Euler solver for calculation of the overall flow field. In the next iteration, the pressure distributions on the propellers were calculated by the VLM and the inflow predetermined by the previous iterative result from the Euler solver.

There are several studies that may be relevant to the study of wake impingement. Richason and Katz (1993) employed an unsteady panel method in flow simulations involving multiple bodies moving along various paths; this study did not consider the wake impingement either. However, the authors did mention that the modeling of the impingement would be included in their future studies. Liu and Bose (2001) used a panel code, PROPELLA, in the performance simulation of a propeller/duct/rudder assembly. In the simulation, the effect of the propeller wake between the leading edge and the trailing edge of the rudder was disabled. Since the source code is accessible and the blade wake panels are represented and stored independently, PROPELLA was used as the platform for the development of a numerical wake impingement model. A two-dimensional wake impingement condition was introduced by Yao and Liu (1998) in a numerical study of two oscillating foils in tandem (Figure 2.4). The approach used to divert the wake shed from the oscillating foil passing by the stationary foil was extended and applied to divert the blade wake passing by the pod and strut. The condition for the tandem foils is based

on the principle that the vortices usually slide along the foil surface in an inviscid-flow environment. It regulates and corrects the predicted trajectory of a vortex as it approaches the proximity of the airfoil surface. If the surface of the airfoil is defined as $S(x, y) = 0$, and the current and predicted vortex positions are $\vec{r}(t_k) = \{x_k, y_k\}$ and $\vec{r}(t_{k+1}) = \{x_{k+1}, y_{k+1}\}$, respectively, then the condition provides the following procedures:

1) If $S(x_{k+1}, y_{k+1}) > 0$, the predicted position is outside the airfoil surface; then the position predicted by $\vec{r}(t_{k+1}) = \vec{r}(t_k) + \vec{V}(t_k)\Delta t$ is the new position for the vortex.

2) If $S(x_{k+1}, y_{k+1}) < 0$, the predicted position is inside the airfoil surface; then the new position must be corrected by the following equation:

$$\vec{r}(t_{k+1}) = \vec{r}(t_k) + \left|\vec{V}(t_k)\right|\Delta t \cdot \hat{l}$$

where $\hat{l}$ is the unit vector tangent to the airfoil surface measured from position (x_k, y_k).

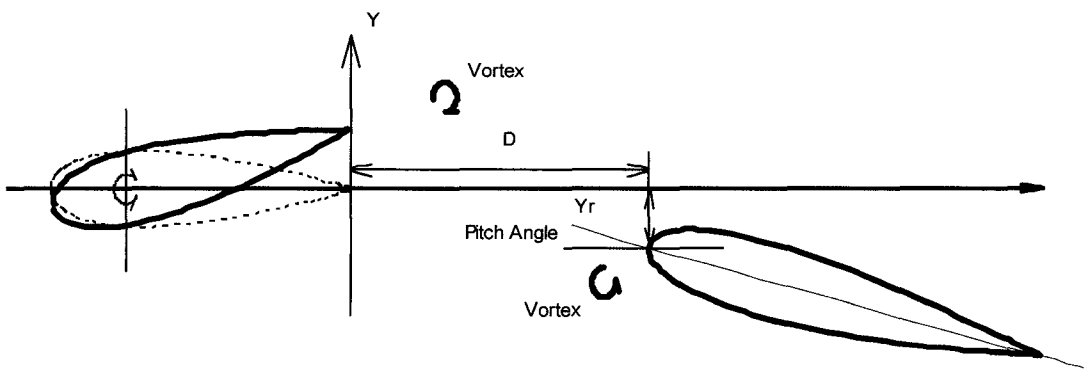

Figure 2.5 Oscillating Foils in Tandem

Greco et al. (2006) developed a potential flow based, time-accurate approach to describe the unsteady interactions among podded propulsors components. A wake alignment technique and a vortex/body impingement model were developed and used to deal with the propeller trailing wake and its interactions with the regions of the strut surface that were characterized by wake impacted in a tractor-type pod configuration. The wake alignment was performed by allowing that the propeller wake surface can cross the strut first, and then removed the wake aligned inside the strut and redistributed these wake outside the strut by a prescribed wake function.

Based on a review of collected literature, it has been found that most studies with considerations of viscous effects in wake impingement modeling are limited to problems having simple configurations. Although both RANS and potential flow-based method have been used in the simulations with considerations of wake impingement effects, for problems with geometric complexities the potential flow-based method is still a primary choice when a super computer is not accessible. The availability of the PROPELLA source code makes the potential flow-based method more favorable as a platform to develop a numerical wake impingement model in this work.

Chapter 3 Strategy of the Study

This study develops a wake impingement model (WIM) using experimentally derived understanding of the mechanism of the propeller wake impacting on a strut. The wake impingement model includes implementation of the kinematical and dynamical conditions for vortex/body interactions. The kinematical condition is a procedure that diverts the incoming vortical wake to pass by the body, and the dynamical condition is a procedure to deal with the strength change of the individual vortex elements. The wake impingement model was inserted into a panel code, and the panel code was used to predict wake impingement effects on the propulsor performance and the pressure fluctuation on the strut and the pod. The predicted pressure fluctuations ($\tilde{p}$) on the strut surface was validated by comparing them with the results of an experiment in a cavitation tunnel. The experimental data includes the time dependent (cyclic) thrust coefficient ($\tilde{K}_t$), the cyclic torque coefficient ($\tilde{K}_q$), and the lateral force on the strut $\tilde{F}_{st}$. Parameters of the wake impingement model were adjusted by analyzing the experimental result from a visual investigation on the tip vortex/strut interaction.

The study is divided into three steps: develop a three-dimensional wake impingement model for panel method; validate the wake impingement model with experimental data; and study podded propeller wake impingement on a strut by using the validated numerical model. The wake impingement model was developed first, and then assembled into two low-order panel codes, DF_OSFBEM and PROPELLA, for debugging, validations, and simulations. A podded propeller model test in a cavitation

tunnel was conducted and the time variation of the pressure distribution over the strut surface was measured. The validation of the wake impingement model was then made by comparing the numerical results with these data obtained from the tests.

3.1 Development of Wake Impingement Model

The development of the wake impingement model includes implementations of the kinematical and dynamical conditions for vortex/body interactions. The kinematical condition is a procedure that diverts the incoming vortical wake to pass by the body, and the dynamical condition is a procedure to deal with the strength change of the individual vortex element.

3.1.1 Kinematic Condition

The kinematic condition is a procedure that diverts the incoming vortical wake to pass by a body. This procedure prevents the vortical wake from penetrating the body surface. Since the wake is a flow structure carried by fluid particles, preventing the wake from penetrating the body is essential to satisfy the non-penetration boundary condition.

It took two steps to develop the non-penetration boundary condition for the three-dimensional wake impingement. The first step was to mathematically extend a wake impingement condition introduced by Yao and Liu (1998) from two-dimensional to three-dimensional. The second step was to implement the three-dimensional condition in a style of case-by-case assessment. Details of the development are described in Chapter 4.

3.1.2 Dynamic Condition

The dynamical condition is a procedure to simulate the strength variation of vortices attached to the body and in wake panels when they interact with each other and when wake panels are re-meshed. The procedure includes the merger of the vortex strengths of two or more vortex elements, and the vortex transfer between an impacting wake panel and the corresponding impacted body panel. The main principle to follow is conserving the total vortex strength.

When two wake panels get too close to avoid a numerical difficulty (singularity) in the induced velocity calculation, the two wake panels merge. The vortex strength of the older wake panel is assigned zero after its strength is transferred to the younger panel.

When a wake panel carrying vortex $\left(\vec{\omega}_t\right)_{incident}$ impacts on a body panel carrying vortex $\left(\vec{\omega}_t\right)_{imp}$ between the time of t and $t+\Delta t$, the vortex strengths for the impacting panel $\left(\vec{\omega}_{t+\Delta t}\right)_{incident}$ and the impacted panel $\left(\vec{\omega}_{t+\Delta t}\right)_{imp}$ after the impact are corrected by following equations:

$$\begin{aligned}\left(\vec{\omega}_{t+\Delta t}\right)_{incident} &= \left(\vec{\omega}_t\right)_{incident} + \left(\vec{\omega}_t\right)_{imp} k_2 \\ \left(\vec{\omega}_{t+\Delta t}\right)_{imp} &= (1-k_2)\times\left(\vec{\omega}_t\right)_{imp}\end{aligned} \tag{3.1.1}$$

where k_2 is a factor to be determined by numerical tests. These two equations do not keep two vortex strengths conserved independently, however they do maintain the sum of the two vortex strengths conserved.

3.2 Experimental Study

To increase understanding of the mechanism of the propeller wake impingement on the strut and to provide validation data for the numerical wake impingement model, the outcome of the model test included:

- the movement response of the blade wake due to the wake impingement,
- the time varied pressure distribution on the strut surface,
- the wake impingement effect on the propeller performance, and
- the wake impingement effect on the strut surface pressure.

With considerations of these objectives, accessibility of experimental facilities and instrumentation the model test included:

- a visual investigation of tip vortex/strut interaction on a tractor type podded propeller model in a cavitation tunnel,
- measurements of the time varied pressure distribution over the strut surface at a high sampling rate up to 5000 Hz, and
- measurements of the propeller shaft loads at the same sampling rate.

To evaluate the wake impingement effects on the propeller performance and the strut surface pressure variation, a data processing technique was used to break down each measurement to three components: the time-averaged, the phase-averaged, and the fluctuation component. The phase-averaged component was then linked to the contribution of wake impingement, and finally the wake impingement effect was evaluated.

Chapter 4 Numerical Method

A wake impingement model was developed for simulations including wake impingement effects. The model development was conducted and debugged with a panel code, PROPELLA. A tractor-type podded propeller that was geometrically similar to the model in the experiment was chosen for simulations. As the panel code was developed and described by Liu (1998), the description of the numerical method in this chapter focuses on the wake impingement model.

The wake impingement model includes two parts, a kinematic condition and a dynamic condition. The kinematic condition guarantees that wake panels shed by propeller blades will not penetrate a body surface. It was implemented by two treatments. The first treatment was re-meshing the wake panels after they had been cut by the leading edge of a strut, behind a propeller in a tractor type podded propulsion unit, and the second treatment was diverting the wake panel when it was going to pierce the body. Maintaining a minimum distance between wake panels and wake/body panel is necessary to avoid large numerical disturbances in the calculations of both the induced velocity and the induced velocity potential (IVP). The dynamic condition models the variation of the wake panel's doublet strengths, the body panel's doublet strengths and their equivalent vortex filament strengths. The implementation of the dynamic condition also consists of two treatments, i.e., merging of two overlapped dipole panels (either two wake panels or a wake and a body panel) and vortex diffusion. In the merger of two overlapped wake panels, the vorticity carried by the older panel is transferred to the younger panel. The

age of a wake panel is defined by the time starting from the moment when the wake panel sheds from a blade. In the merger of a wake and a body dipole panel, the dipole strength of the wake panel is transferred to the body panel. Vortex diffusion is considered by an empirical formulation introduced by Greene (1986) and Modi (2002).

4.1 Overview of the Wake Impingement Model

In the inertial coordinate system, *OXYZ*, the wake sheet is represented by wake panels which are positioned and oriented by their corners. On each of these panels, dipoles, μ_{ij}, are constantly distributed. They can also be represented as an equivalent rectangular vortex ring (Katz and Plotkin, 2001) with circulation Γ_{ij}, aligned on the boundaries as shown in Figure 4.1.

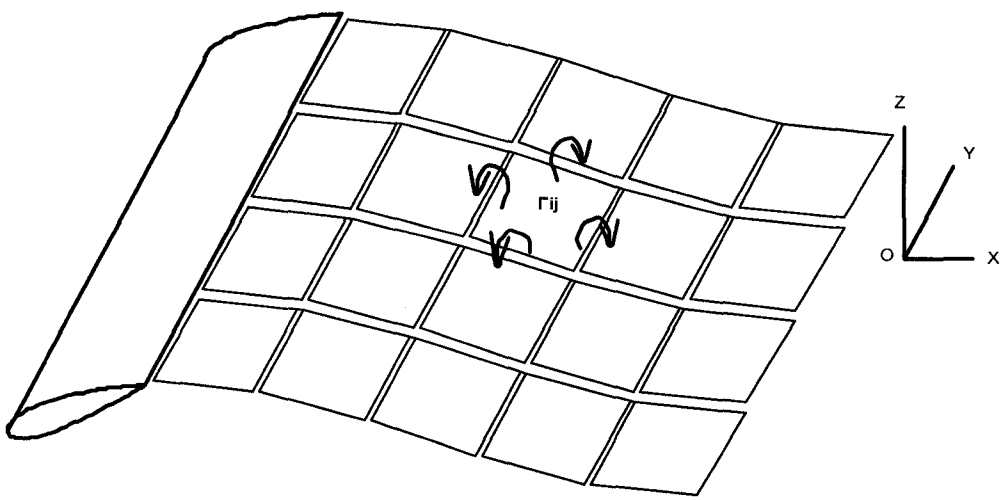

Figure 4.1 Vortex Wake Presentation by Dipole Panels

The implementation of the kinematical condition for wake impingement starts from tracing the wake panels once they are shed from the blade trailing edge. Each wake panel is geometrically represented by four corners, and the movement of the four corners is traced step by step. For each time step, the locations of the wake shed at the present time step are defined by the trajectory of the blade trailing edge, while other wake panels shed in previous time steps are marched from the position of the previous time step $\vec{r}_t$ to their new locations $\overrightarrow{r_{t+\Delta t}}$. The marching distance is the product of the time interval and the local induced velocity $\vec{V}_t$.

$$\overrightarrow{r_{t+\Delta t}} = \vec{r}_t + \vec{V}_t \Delta t \tag{4.1.1}$$

where $\vec{V}_t$ is the induced velocity at the corner of the wake panel at time t, and Δt is the time interval. Induced velocities from constant distributions of sources and dipoles on a hyperboliodal panel are derived from the formulae given by Morino et al. (1974). Formulations for these induced velocities are given in Appendix A.

A three-dimensional non-penetration condition was used to assess and treat every wake panel at every time step. For each time step, all wake panels are classified into three scenarios as shown in Figure 4.2.

Scenario 1: When the trajectory of a wake panel (panel 1 in Figure 4.2) keeps a "friendly distance" (a minimum allowable distance is required to keep the calculation from numerical disturbances, (Chen and Williams, 1987) from the body surface at any time during the time interval), the panel passes by the body along a track predicted by equation (4.1.1). "Friendly distance" is a notion that helps to define how close two vortex elements

can be placed while their inter-influence coefficients can still be reasonable calculated. If an element gets into another element diameter, the influence coefficient can not be correctly estimated b the formula of inviscid flow method since in the vortex core zone, within the vortex diameter, the viscous effect is significant. The "friendly distance" should be set to the sum of radii of the two vortex filaments.

Scenario 2: If a wake panel (panel 2 in Figure 4.1.2) is predicted to go through the body, the panel is diverted to slip over the body surface (non-penetration condition) by eliminating the velocity component in the direction normal to the body surface at the impacting point.

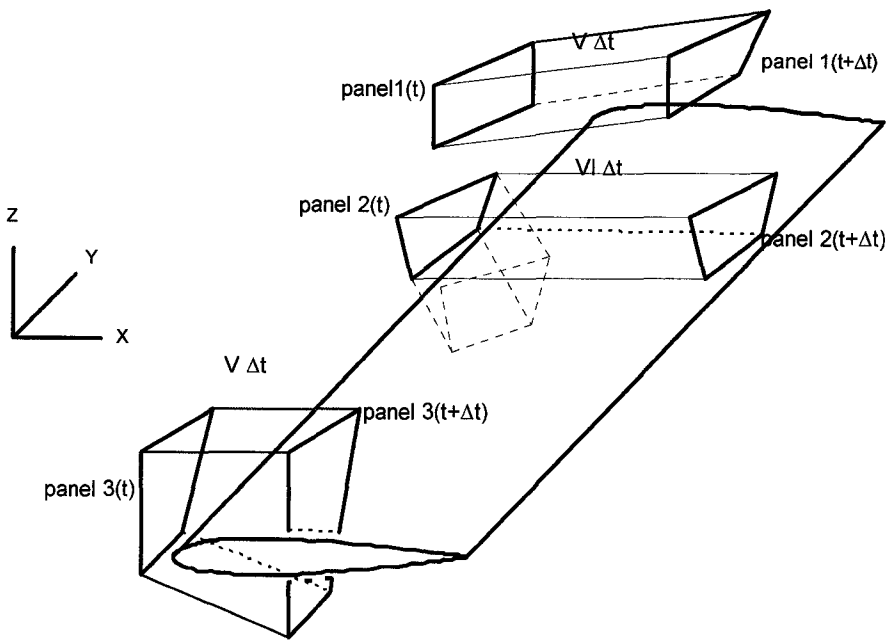

Figure 4.2 Classifications of Wake Impingement Cases

(Passing by, slipping over, and being cut)

Scenario 3: If the panel is cut into two parts by the leading edge, known as a stagnation line in general, as shown in Figure 4.2, the bigger part of the panel is kept as the "inheritor" of the panel while the smaller part is merged into its nearest neighbor (details are given in the following section).

The flowchart in Figure 4.3 shows the overview of the implementation of the non-penetration condition. I_{wp} is the index of the wake panel. I_{bp} is the panel index of the body in the wake. M_{bp} is the total number of body panels. I_{pc} is the index of the panel corner. I_{es} is the index of a line segment of the rear foil leading edge. M_{es} is the total number of the line segments. Details of the assessment of wake panel cuts and their re-meshing are presented in section 4.2, and the description of the method of diverting the wake panel to slip over the body is given in section 4.3.

The dynamic condition for the wake impingement governs the modeling of the wake panel's doublet strength variation. Based on different scenarios of interactions between dipole panels, the modeling of the doublet strength variation on the wake panel is subdivided into two cases. One scenario is when a wake panel overlaps or wraps around the strut before it is cut into 2 pieces, another scenario is when a wake panel stands alone without close interaction with others. For the first scenario, the dipole strength of the wake panel is merged or transferred to the body panel and zero dipole strength is assigned to the wake panel after the transfer. Although either keeping a "friendly distance" or merging dipole strength could avoid numerical disturbances, merging dipole strength is necessary to keep the simulation close to the wake response investigated when a wake panel impacts vortically on a body panel. For example, when a

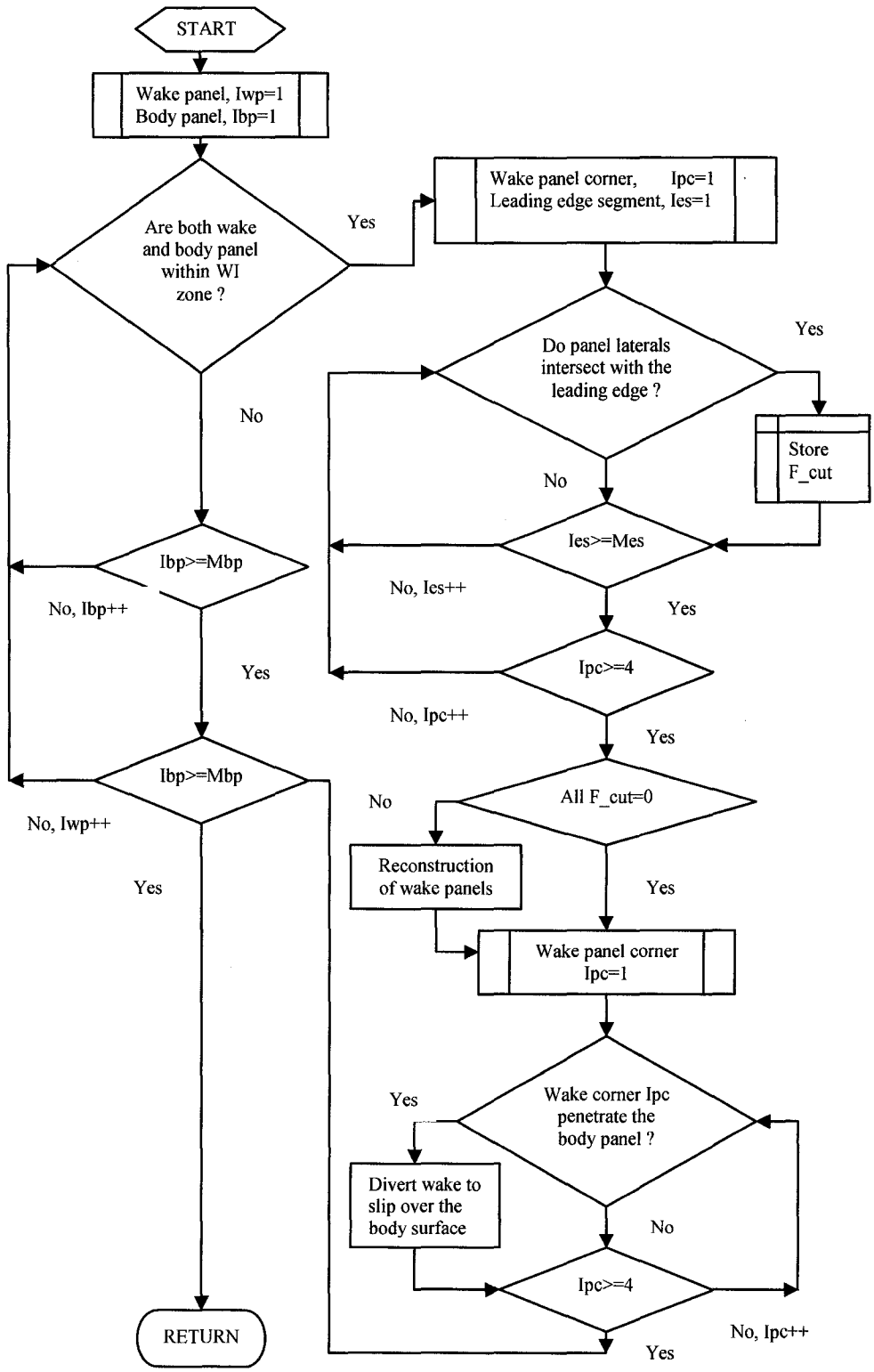

Figure 4.3 Diagram of Wake Impingement Flow Chart

wake panel of a blade is blocked and stretched by the leading edge of a strut, another wake panel shed from the following blade approaches and overlaps the stretched wake panel. In this case, the first wake panel is frozen around the leading edge while the second panel is approaching the first wake panel. Details are described in 4.5. For the second scenario, the dipole strength variation is dominated by vortex diffusion. It is modeled by an empirical formula. The method is discussed in section 4.6.

4.2 Wake Panels to be Cut and Re-meshed

When a wake panel from the propeller encounters the leading edge and is going to be cut in the next time step, the wake panel is re-meshed with one of its neighbors to prevent the wake panel from intersecting with body panels. In the panel re-meshing, one of the panel sides and the corresponding side of the neighbor panel are relocated to where it is going to encounter the leading edge. The relocation of the panel side guarantees that all re-meshed wake panels have their four corners located on the same side of the body. The description of a panel cut by a leading edge is decomposed into intersections of the leading edge with its four individual sides. The assessment of the intersection is based on a linear interpolation. As shown in Figure 4.4, during the time interval, a line segment of the leading edge moved from $\overrightarrow{l_{a1}l_{b1}}$ to $\overrightarrow{l_{a2}l_{b2}}$ while a side of a wake panel moves from $\overrightarrow{r_{a1}r_{b1}}$ to $\overrightarrow{r_{a2}r_{b2}}$, and they intersect each other (Spiegel and Liu, 1999). The trajectories of the leading edge segment and the panel side can be represented as:

$$\vec{l} = \overrightarrow{l_{a1}} + \left(\overrightarrow{l_{a2}} - \overrightarrow{l_{a1}}\right)\tau + \left(\overrightarrow{l_{b1}} - \overrightarrow{l_{a1}}\right)\eta + \left(\overrightarrow{l_{b2}} - \overrightarrow{l_{b1}} - \overrightarrow{l_{a2}} + \overrightarrow{l_{a1}}\right)\eta\tau \quad \text{where} \quad \eta \in [0,1] \ \tau \in [0,1] \qquad (4.2.1)$$

and

$$\vec{r} = \overrightarrow{r_{a1}} + \left(\overrightarrow{r_{a2}} - \overrightarrow{r_{a1}}\right)\tau + \left(\overrightarrow{r_{b1}} - \overrightarrow{r_{a1}}\right)\xi + \left(\overrightarrow{r_{b2}} - \overrightarrow{r_{b1}} - \overrightarrow{r_{a2}} + \overrightarrow{r_{a1}}\right)\xi\tau \quad \text{where} \quad \xi \in [0,1] \ \tau \in [0,1] \qquad (4.2.2)$$

After linearization of the two equations above, the impacting time τ, impacting locations on the leading edge η, and the wake panel side ξ can be solved by setting $\vec{l} = \vec{r}$. If, and only if, solutions for ξ, η and τ all fall within $[0,1]$ the intersection of the leading edge and the wake panel side is confirmed.

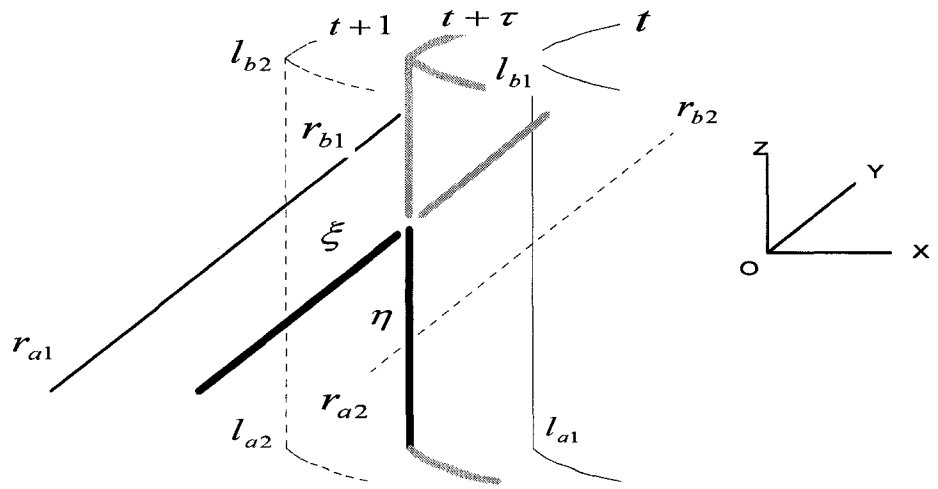

Figure 4.4 An Edge of a Wake Vortex Panel being Cut by a Leading Edge

After the assessment for all four sides of the panel has been finished the panel cutting is classified into three kinds, 10 cases in total as shown in Figure 4.5. The re-meshing of the panel is then performed case by case. The re-meshed panels corresponding to those in Figure 4.6.

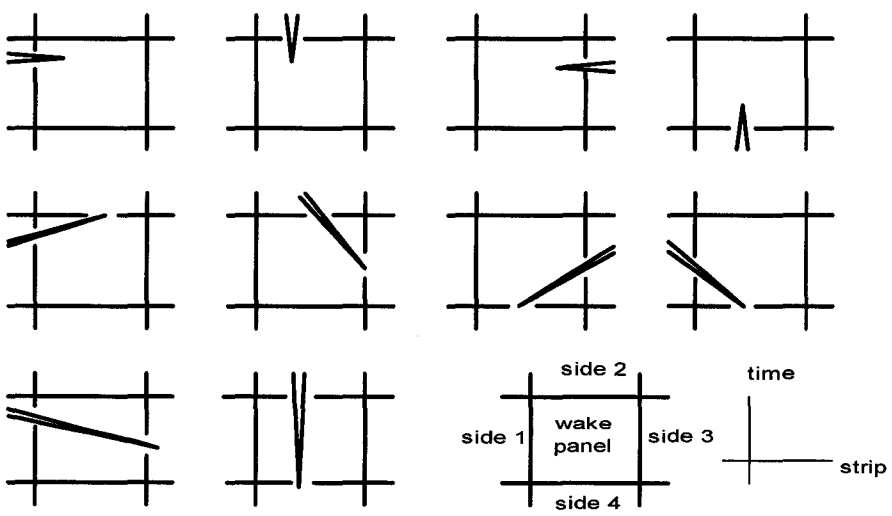

Figure 4.5 Classification of the Panel to be Cut

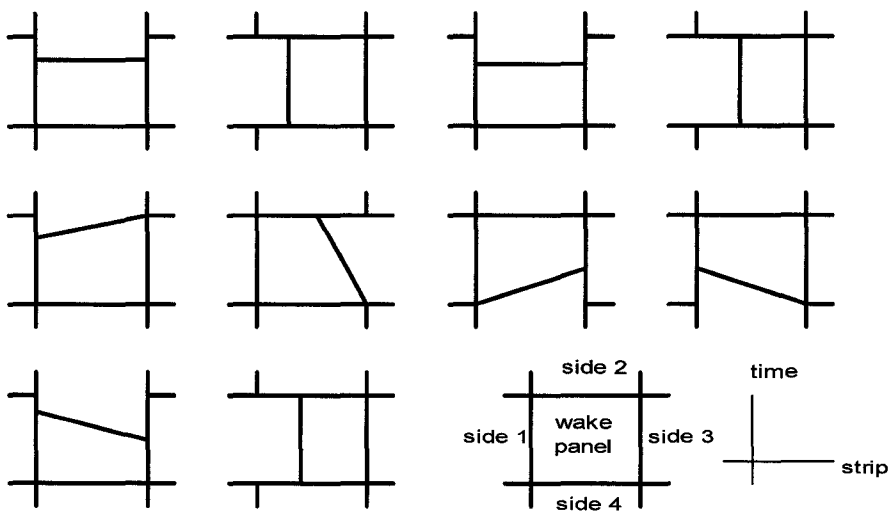

Figure 4.6 Re-meshed Panels Corresponding to Those in Figure 4.5

4.3 Wake Panels Slipping over the Body

All wake panels that have been predicted to impact on the body by equation (4.1.1) are diverted to pass by the body with a "friendly distance." A minimum allowable distance is required to keep the calculation from numerical disturbances. As shown in Figure 4.2, wake panel 2 is predicted to go through the body during the time interval and is diverted to slip over the body surface by eliminating the relative velocity component in the direction normal to the body surface at the impacting point. An impacting point, p_{imp} as shown in Figure 4.7, is a point on the body surface where a wake panel corner impinges, and an impacting panel is a body panel on which a wake panel corner interacts. To identify the impacting point and the impacting panel for each corner of each wake panel against each body panel within the impingement zone, an assessment was performed as follows:

$$\begin{aligned}
&\overrightarrow{r_w(t)B_1} \times \overrightarrow{r_w(t)B_2} \cdot \overrightarrow{r_w(t)r_w(t+\Delta t)} \geq 0 \qquad \overrightarrow{r_w(t)B_2} \times \overrightarrow{r_w(t)B_3} \cdot \overrightarrow{r_w(t)r_w(t+\Delta t)} \geq 0 \\
&\overrightarrow{r_w(t)B_3} \times \overrightarrow{r_w(t)B_4} \cdot \overrightarrow{r_w(t)r_w(t+\Delta t)} \geq 0 \qquad \overrightarrow{r_w(t)B_4} \times \overrightarrow{r_w(t)B_1} \cdot \overrightarrow{r_w(t)r_w(t+\Delta t)} \geq 0 \qquad (4.3.1) \\
&\overrightarrow{p_{imp}r_w(t)} \cdot \vec{n} \geq 0 \qquad\qquad\qquad \overrightarrow{r_w(t+\Delta t)p_{imp}} \cdot \vec{n} \geq 0
\end{aligned}$$

Here B_1, B_2, B_3, and B_4 are four corners of a body panel, $r_w(t)$ and $r_w(t+\Delta t)$ are positions of a wake corner at time t and time $t+\Delta t$ respectively, and p_c is the center point of the body panel. $\overrightarrow{r_w(i)B_j}$ is the vector from $r_w(i)$ points to B_j, $\vec{n}$ is the normal

vector of the body panel. These conditions are combined based on principles of solid geometry and vector analysis. The first four conditions in Figure (4.7) contain the $\overline{r_w(t)r_w(t+\Delta t)}$ in the corner formed by four triangles, $r_w(t)B_1B_2$, $r_w(t)B_2B_3$, $r_w(t)B_3B_4$ and $r_w(t)B_4B_1$. The last two conditions in (4.3.1) guarantee that the point $r_w(t)$ is outside the body and the point $r_w(t+\Delta t)$ is inside the body.

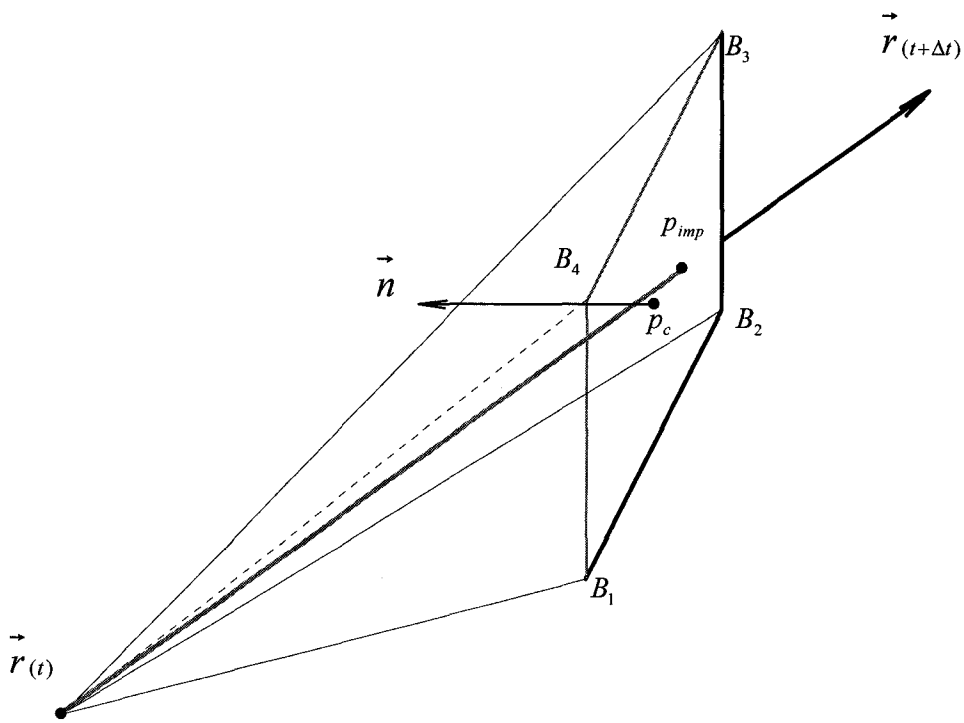

Figure 4.7 Identify Body Panel on Which a Wake Panel Impacts

4.4 Induced Velocity Potential of a Thick Dipole Panel

As reviewed in chapter 2, many studies have been conducted to improve the panel method by varying the distribution functions of the dipole and source strengths on the panel surface. All of these low and high order panel methods distribute sources and dipoles over the panel of zero-thickness. Concentrating the sources and dipoles within the zero-thickness panel does not make a difference on the induced velocity potential calculation when the field point is far from the panel. For cases of high Reynolds number and thin boundary layer, concentrating the sources and dipoles on the surface does not worsen the results unless the calculation of the field point is very close to the panel surface. In the case of a propeller wake panel (dipole panel) approaching a solid body (a strut), the distance between the wake panel and the approached body panel could be the same order as that of the boundary layer thickness or the same order of the diameter of the vortex in the wake. As the wake response is greatly dependent on the induced velocity contributed by the sources and dipoles on the impacted panel, the source and dipole strength distributions along the panel thickness direction will affect the wake body interaction significantly. To evaluate the difference on the induced velocity potential between a thin and a thick dipole panel, a formula for the induced velocity potential by a thick panel is derived, and comparisons of calculations are made in this section hereafter. The thin dipole is defined as a panel with dipoles evenly distributed over the area of the panel of zero-thickness. The thick dipole panel is defined as a panel with dipoles evenly distributed over the domain of the panel of a non-zero-thickness. The wake thickness is

defined as the diameter of the vortex in the wake panel. As shown in Figure 4.8, a wake panel S is placed on XOY plane. Dipole μ_s is evenly distributed over the panel, whose

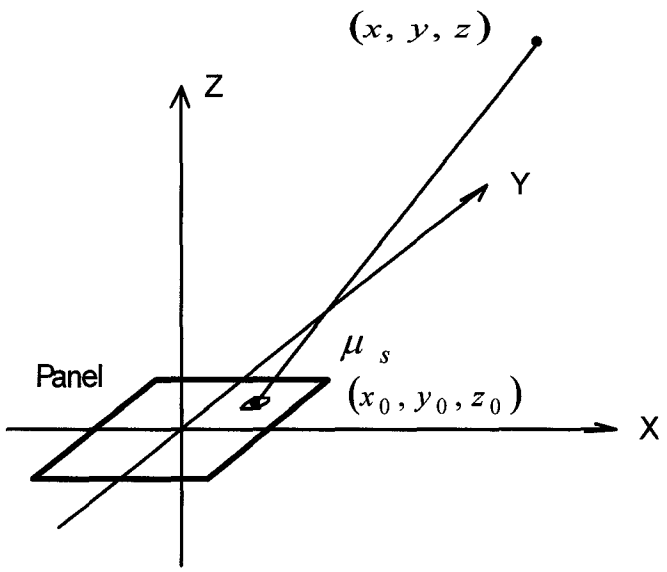

Figure 4.8 Zero Thickness Dipole Panel

thickness is assumed to be zero. The induced velocity potential at a field point (x,y,z) is given as (p.247 Katz & Plotkin, 2001):

$$\phi = \frac{-\mu_s}{4\pi} \iint_S \frac{zdS}{\left[(x-x_0)^2 + (y-y_0)^2 + z^2\right]^{3/2}} \tag{4.4.1}$$

Here, μ_s is the density of the dipole strength distributed over the panel surface.

(x_0, y_0, z_0) is the point of the integral over the wake panel.

(x, y, z) is the field point.

If the dipole distribution over the panel is considered to be vertically extended from $-r_\sigma$

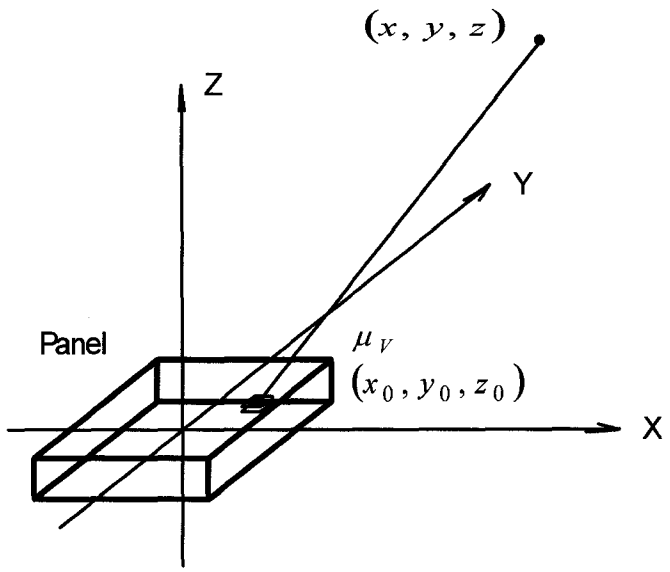

Figure 4.9 Thick Dipole Panel

to r_σ, as shown in Figure 4.9, the calculation of the induced velocity potential by this thick dipole panel turns out as,

$$\phi = \frac{-\mu_V}{4\pi} \iiint_V \frac{zdV}{\left[(x-x_0)^2+(y-y_0)^2+(z-z_0)^2\right]^{3/2}} \tag{4.4.2}$$

Here, μ_V is the dipole strength density distributed over a wake panel of $2h$ thickness, and

V is the domain of integration.

When the panel is considered to be a square with lengths $2a$, the above integrations for thin (zero thickness) and thick dipole panels are progressed to

$$\phi = \frac{\mu_s}{4\pi}\left[\begin{array}{l} -\tan^{-1}\left(\dfrac{(x+a)(y-a)}{z\sqrt{(x+a)^2+(y-a)^2+z^2}}\right) \\ +\tan^{-1}\left(\dfrac{(x-a)(y-a)}{z\sqrt{(x-a)^2+(y-a)^2+z^2}}\right) \\ -\tan^{-1}\left(\dfrac{(x-a)(y+a)}{z\sqrt{(x-a)^2+(y+a)^2+z^2}}\right) \\ +\tan^{-1}\left(\dfrac{(x+a)(y+a)}{z\sqrt{(x+a)^2+(y+a)^2+z^2}}\right) \end{array}\right] \quad \text{for zero thickness panel} \qquad (4.4.3)$$

$$\phi = \frac{\mu_V}{4\pi}\int_{r_\sigma}^{r_\sigma}\left[\begin{array}{l} -\tan^{-1}\left(\dfrac{(x+a)(y-a)}{(z-z_0)\sqrt{(x+a)^2+(y-a)^2+(z-z_0)^2}}\right) \\ +\tan^{-1}\left(\dfrac{(x-a)(y-a)}{(z-z_0)\sqrt{(x-a)^2+(y-a)^2+(z-z_0)^2}}\right) \\ -\tan^{-1}\left(\dfrac{(x-a)(y+a)}{(z-z_0)\sqrt{(x-a)^2+(y+a)^2+(z-z_0)^2}}\right) \\ +\tan^{-1}\left(\dfrac{(x+a)(y+a)}{(z-z_0)\sqrt{(x+a)^2+(y+a)^2+(z-z_0)^2}}\right) \end{array}\right] dz_0 \quad \text{for thick panel} \qquad (4.4.4)$$

Induced velocity potentials of a thin and a thick dipole panel along two identical routes are investigated and compared. Both thin and thick panels are the same size, 2×2 ($a=1$). However, the thin panel is distributed with dipole $\mu_S = 1$ over its surface 2×2, while the thick panel is evenly distributed with dipole $\mu_V = 1$ within the rectangular volume of $2\times 2\times(0.5+0.5)$. One investigated route was from $(0,\ 0,\ -6)$ to $(0,\ 0,\ 6)$, and another route was from $(1,\ 1,\ -6)$ to $(1,\ 1,\ 6)$.

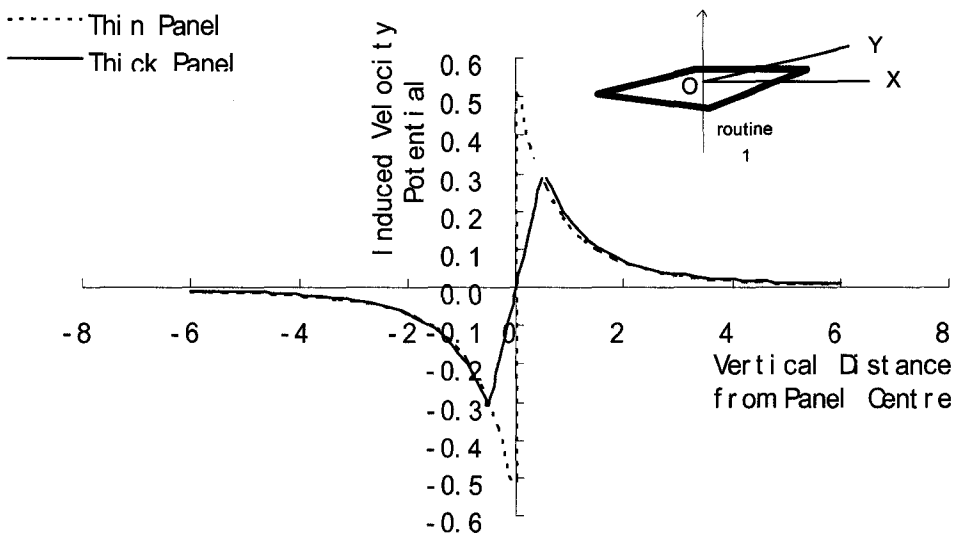

Figure 4.10 Induced Velocity Potential by Thin and Thick Dipole Panel (Route 1)

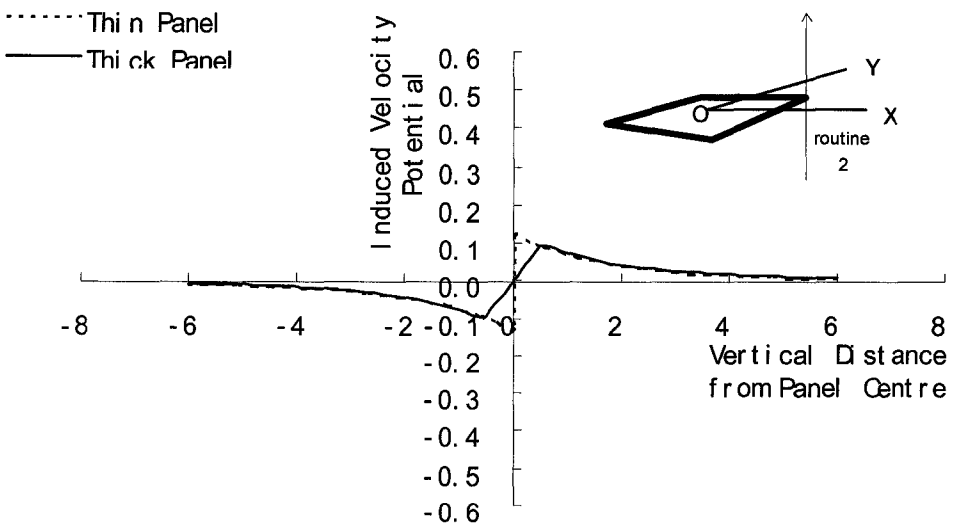

Figure 4.11 Induced Velocity Potential by Thin and Thick Dipole Panel (Route 2)

Since no analytical solution for the integral (4.4.4.) has been found, the thick dipole panel induced velocity potential calculation was carried out by Simpson's method (Spiegel and Liu, 1999). When comparing this with the induced potential by the thin panel along route 1 in Figure 4.10 and route 2 in Figure 4.11, it was found that the calculated induced velocity potentials for both thin and thick panels are almost the same outside of the thickness of the panel. Within the thickness of the panel, the induced potential by the thin panel continues to increase in magnitude until it reaches its maximum at the centre plane of the panel, while the induced potential by the thick panel drops in magnitude until it reaches zero at the centre plane of the panel. The patterns of the induced potential by a thick dipole panel in Figure 4.10 and 4.11 are very similar to the thin-dipole-panel induced-potential calculation with a linear cut-off treatment. The linear cut-off treatment linearly interpolated the tangential velocity profile inside the core of the vortex filament or inside the thick panel. The cut-off value is a half of the panel thickness. As the panel thickness is defined as the diameter of the vortex filament in the wake panel, the cut-off value is equivalent to the radius of the vortex filament. This indicates that the induced velocity potential of a thick dipole panel can be well estimated by the thin dipole formula with a properly chosen cut-off treatment.

To obtain a well estimated cut-off value that is equal to the radius of the vortex in the wake for numerical simulations, an estimation method for the tip vortex diameter by using the pressure measurement on the strut leading edge is made in section 5.7. The estimated tip-vortex diameter was used to set the cut-off value in the numerical simulations in chapter 6.

4.5 Merging of Overlapped Dipole Panels

A wake panel approaching a body panel of the pod and strut was dynamically modeled by a dipole panel approaching another dipole panel with a source in addition. This is because a wake panel can be simulated by a dipole panel while the simulation of a body panel needs both dipole and source distributed. Although keeping the wake panel a "friendly distance" away from the body panel can avoid numerical disturbances in calculations of induced velocities and induced velocity potentials, it is not applicable to all scenarios of the blade wake interacting with the strut around the leading edge. Similar to other studies reviewed in chapter 2, the visual investigation of tip vortex/strut interaction (chapter 5) found that parts of the tip vortex (broken ends) were immersed into the boundary layer around the strut leading edge after it was bent and cut. To retain the natural response of the blade wake during the interaction with the strut leading edge, the wake panel should be dynamically moved closer than a "friendly distance" to the body panel. In this case, the dipole strength of the wake panel was merged to the dipole strength of the body panel to avoid numerical disturbances in the velocity and the velocity potential calculations.

The procedure of merging the wake dipole panel to the body dipole panel was conducted when the distance between the two panels was found to be smaller than the "friendly distance" and the impacting angle β_{imp} was smaller than $45°$. The impacting angle is defined as the angle formed by the normal vector of the impacted body panel $B_1B_2B_3B_4$ and the trajectory of the wake panel center $r_{wc}(t)r_{wc}(t+\Delta t)$ in Figure 4.12. In this case, the dipole strength of the wake panel was transferred to the body panel. After the

transfer, the dipole strength of the wake panel was assigned zero and the dipole strength of the body panel was the summation of the dipole strengths of the wake panel and the body panel before the transfer.

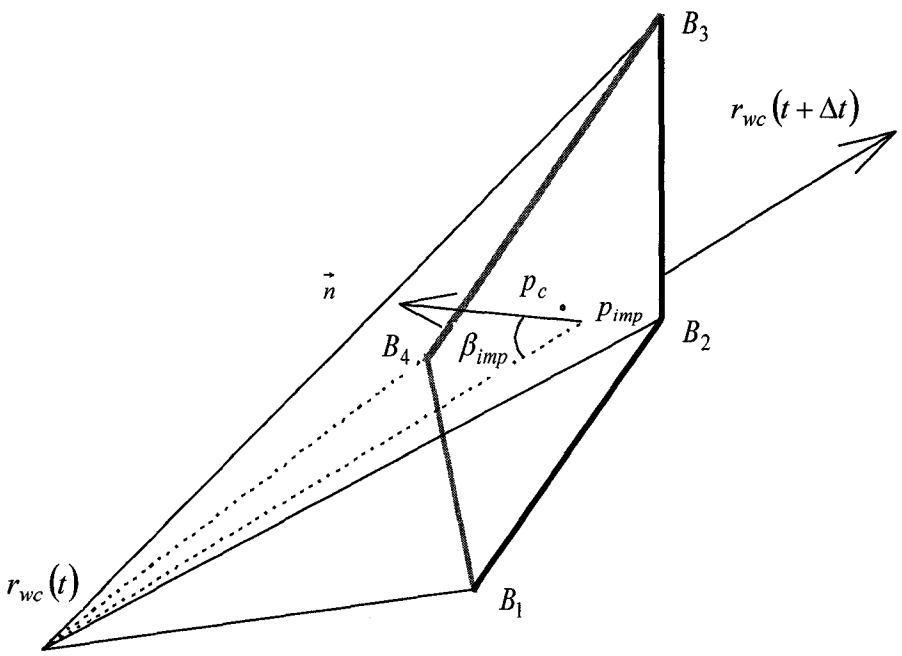

Figure 4.12 Definition of Impacting Angle

To assess the change on the induced velocity potential led by merging two overlapped dipole panels, comparisons of induced velocity potentials by two closely orientated dipole panels and the merged panel were made in Figure 4.13 and 4.14. For the sake of simplicity, the two dipole panels were assumed to be squares, and their side lengths were 2. The center of the body panel was placed in the origin of the local coordinate system. The wake panel was located above the body panel with a distance of

d_w. The induced velocity potential by the body panel, wake panel and the merged panel are described in equations (4.5.1), (4.5.2) and (4.5.3) respectively.

$$\phi_b = \frac{\mu_b}{4\pi}\left[\begin{array}{l} -\tan^{-1}\left(\dfrac{(x+a)(y-a)}{z\sqrt{(x+a)^2+(y-a)^2+z^2}}\right) \\ +\tan^{-1}\left(\dfrac{(x-a)(y-a)}{z\sqrt{(x-a)^2+(y-a)^2+z^2}}\right) \\ -\tan^{-1}\left(\dfrac{(x-a)(y+a)}{z\sqrt{(x-a)^2+(y+a)^2+z^2}}\right) \\ +\tan^{-1}\left(\dfrac{(x+a)(y+a)}{z\sqrt{(x+a)^2+(y+a)^2+z^2}}\right) \end{array}\right] \quad \text{body bounded dipole panel} \quad (4.5.1)$$

$$\phi_w = \frac{\mu_w}{4\pi}\left[\begin{array}{l} -\tan^{-1}\left(\dfrac{(x+a)(y-a)}{(z-d_w)\sqrt{(x+a)^2+(y-a)^2+(z-d_w)^2}}\right) \\ +\tan^{-1}\left(\dfrac{(x-a)(y-a)}{(z-d_w)\sqrt{(x-a)^2+(y-a)^2+(z-d_w)^2}}\right) \\ -\tan^{-1}\left(\dfrac{(x-a)(y+a)}{(z-d_w)\sqrt{(x-a)^2+(y+a)^2+(z-d_w)^2}}\right) \\ +\tan^{-1}\left(\dfrac{(x+a)(y+a)}{(z-d_w)\sqrt{(x+a)^2+(y+a)^2+(z-d_w)^2}}\right) \end{array}\right] \quad \text{wake dipole panel} \quad (4.5.2)$$

$$\phi_m = \frac{\mu_b + \mu_w}{4\pi}\left[\begin{array}{l} -\tan^{-1}\left(\dfrac{(x+a)(y-a)}{z\sqrt{(x+a)^2+(y-a)^2+z^2}}\right) \\ +\tan^{-1}\left(\dfrac{(x-a)(y-a)}{z\sqrt{(x-a)^2+(y-a)^2+z^2}}\right) \\ -\tan^{-1}\left(\dfrac{(x-a)(y+a)}{z\sqrt{(x-a)^2+(y+a)^2+z^2}}\right) \\ +\tan^{-1}\left(\dfrac{(x+a)(y+a)}{z\sqrt{(x+a)^2+(y+a)^2+z^2}}\right) \end{array}\right] \quad \text{dipole panel after merge} \quad (4.5.3)$$

Variations of the induced velocity potential before and after the merger were compared along a vertical line from the center of the impacted panel. Similar patterns were found for different distances between the body panel and the wake panel. As an example to discuss, the distance was set to be half of the length of the panel side. It is shown in Figure 4.13 that the induced velocity potential by the merged panel fit well with the induced velocity potential summation by the body and the wake panel when the distance is large. However, within the vertical distance of 3 times of the half length of the panel side, the difference between induced velocity potentials before and after the merge increased quickly when the distance decreased. In the range between the body panel and the wake panel, the trend of induced velocity potential by the merged panel was smooth

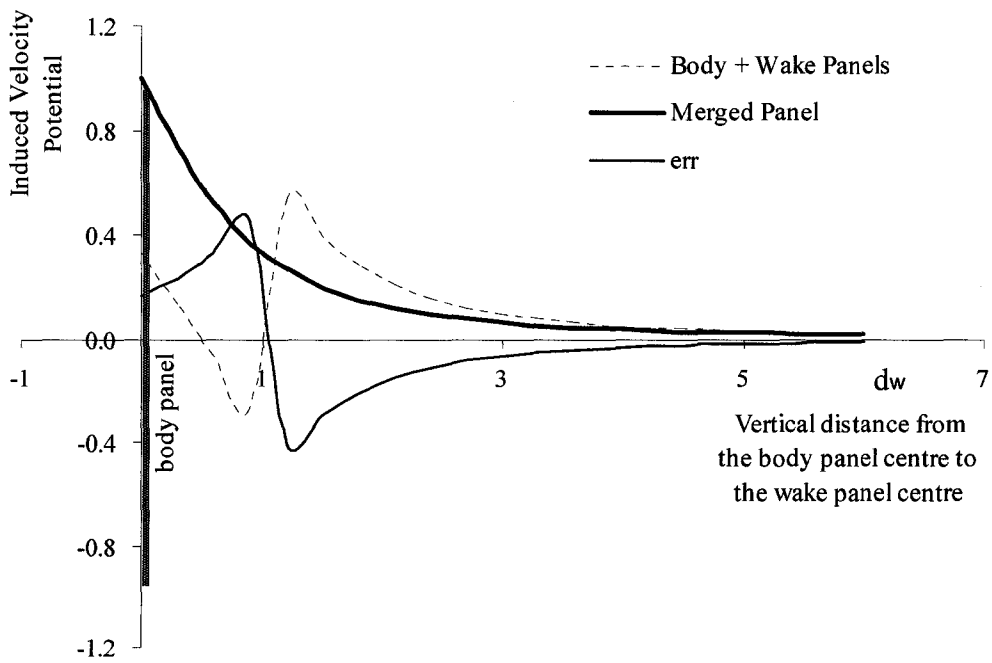

Figure 4.13 Comparison of Induced Velocity Potential

and completely different from the summation by the body panel and the wake panel. This indicated that substituting the induced velocity potential by a pair of interacting wake and body panels with the induced velocity potential by the merged panel successfully eliminated the numerical disturbance (sharp change) around the point p_{dist} in Figure 4.13, although there is a large error in the difference between calculated induced velocity potentials before and after the panel merged when it is near the panel. In fact, the big change on the induced velocity potential near the wake panel is necessary to reduce the numerical disturbance, and the calculation of the induced velocity potential around the wake panel and between the wake and the body panel should be avoided. There are two ways to avoid the numerical disturbance for this case, keep or divert the wake panels far away from each other or merge them together before they get too close.

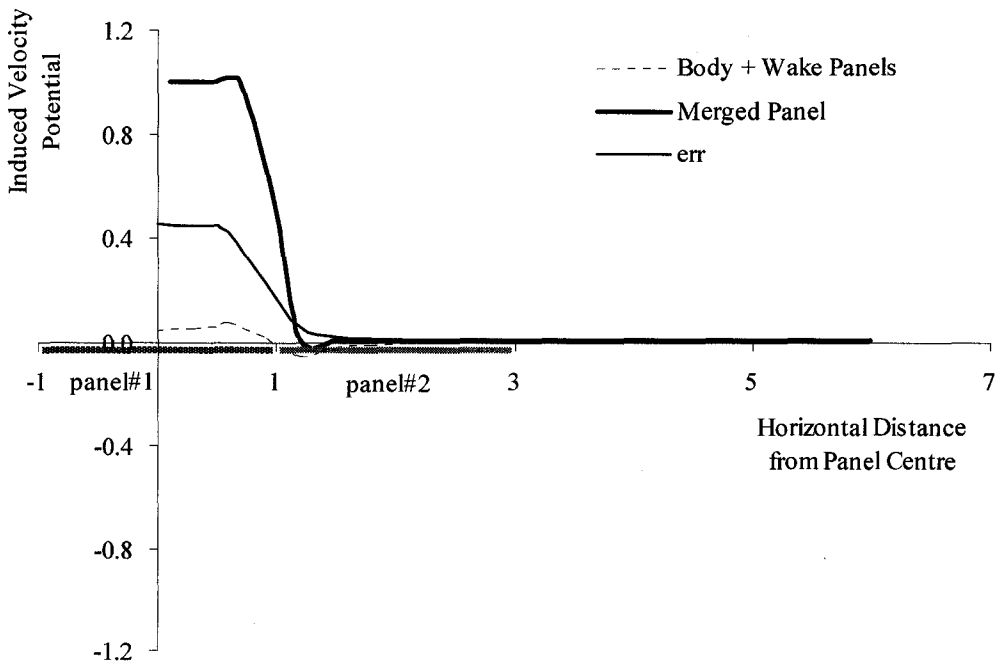

Figure 4.14 Comparison of Induced Velocity Potential

Calculated induced velocity potentials on the neighboring panels by the summation of body and wake dipole panels and the merged dipole panel are shown in Figure 4.14. There is almost no difference in calculated induced velocity potentials between the merged panel and the summation of the panels when the horizontal distance is larger than 1.6. For simplicity, body panels are assumed to be uniform in their sizes. The horizontal distance from the center of a neighboring panel to the impacted body panel center is 2. The merging of the two overlapped dipole panels has almost no effect on induced velocity potential calculations for its neighboring panels.

4.6 Vortex Diffusion

Vortex diffusion is considered by adjusting vortex strengths at every time step. For each time step, the strength of every vortex element was corrected by using a simplified model introduced by Greene (1986). The model used by Modi et al. (2002) in airplane vortex wake simulations is

$$\Gamma_{t+\Delta t} = \Gamma_t \left(1 - \frac{\Delta t V_t}{8S}\right) \tag{4.6.1}$$

Here, Γ_t and $\Gamma_{t+\Delta t}$ are vortex strengths at time t and time $t+\Delta t$ respectively, S is the span of the airplane, and V_t is the vortex velocity.

$$V_t = \frac{\Gamma_t}{2\pi S} \tag{4.6.2}$$

Substitute Eq. (4.6.2) for Eq. (4.6.1) and the panel side length, a, to the span, S, and the corrected equation for vortex strength decay in open field flow for the present model is shown as

$$\frac{\Gamma_{t+\Delta t}}{\Gamma_t} = 1 - k_1 \frac{\Delta t \Gamma_t}{a^2} \tag{4.6.3}$$

where k_1 is a factor to be determined by numerical tests.

4.7 Summary

A wake impingement model has been described. The model traces the propeller wake by using numbers of dipole panels. When a wake panel approaches a body, the wake panel is assessed to determine if it is going to pierce a panel of the body. All wake panels that are likely to pierce the body without being cut by the leading edge of the strut are diverted to pass by the body at a "friendly distance". Wake panels to be cut by the leading edge are re-meshed. These implementations satisfied the non-penetration condition for the wake/body interaction.

Variations of the wake strengths are modeled by two treatments: vortex diffusion and the merger of dipole panels. Strength variations by the vortex diffusion are considered by an empirical method for all vortex elements. For these wake panels several things of note occurred: they impact on body panels; dipole strengths of these wake panels are transferred to impacted body panels when the impacting angles are smaller than $45°$; otherwise, these wake panels sweep over the body surface with their dipole strengths. Transferring dipole strengths from impacting wake panels to these impacted body panels avoided numerical difficulty but have little effect on the solution.

The induced velocity potential by a thick dipole panel can be well modeled by the formulae for the dipole panel of zero thickness with a cut-off treatment.

Chapter 5 Experimental Study

This chapter describes an experimental study in a cavitation tunnel on the wake/strut interaction of a podded propeller model (D_p=0.27m). The primary objective of the experiment is to provide data for the strut surface pressure comparison with numerical results. The study includes surface pressure measurements on the strut around the leading edge, and visual investigations of cavitation tip vortices. The region of pressure measurements on the strut ranges from 0.6 to 1.2 of the propeller radius, R_p, and from the leading edge downstream to 0.4 of the chord length on both sides of the strut. Within this region, the pressure measurements at fifty six different locations were conducted by repeating the tests after changing the position of a seven-pressure-transducer assembly. All tests were performed with the propeller running at a constant rps, and each test consisted of five flow speeds which varied the advance coefficient, J, from 0.55 to 0.87. The pressure measured on the strut surface was broken down into three components and analyzed: time average, phase average, and fluctuation components. Definitions and calculations of these three components are given in section 5.2. In the visual investigation, the propeller tip vortex was observed by lowering the tunnel pressure so cavitating vapor formed in the vortex. The tip vortex was found to bend at the leading edge of the strut when the vortex approached the strut; the vortex then kept a minimum distance from the leading edge of the strut while it moved along the leading edge away from the shaft centerline. After the tip vortex was bent, stretched, and gradually faded out around the leading edge, it appeared to be separated around the two sides of the strut and propagated downstream. The vortex turned from a continuous

helical line into segments. The segmented vortex was compressed on one side of the strut and stretched on the other side. The vertical distance from the end of the segmented vortex to the shaft centerline on the stretched side remained a constant. However, this vertical distance increased on the compressed side with the increase of the axial distance from the propeller. The increment at a lower advance coefficient was larger than that at a higher advance coefficient.

The pressure measured at points located within 0.9 to 1.1 of the propeller radius showed that they were dominated by the Blade Passing Frequency (BPF). The measurements outside of this range rarely showed significant variation. The largest amplitude of pressure variation was found at the leading edge of the strut near $R_p = 1.0$ for all tested advance coefficients. The location of the lowest pressure was found on the stretched side near the leading edge of the strut near the intersection of the pod and the strut. In cases of low advance coefficient, the pressure at some measurement points on or close to the leading edge on the compressed side demonstrated a double-trough shape within a single period of filament impact (see Figure 5.15 for example).

The rest of this chapter is divided into sections. After a description of the model and instrumentation, procedures of pressure measurements and data reduction are introduced. Then results of the time averaged and phase averaged components are discussed and reasons for pressure variation patterns are explained. The pitch of the tip vortex and the tip vortex nominal diameter measurements are also briefly introduced in this chapter. Finally, a description of the tip vortex responses to the vortex/strut interaction is provided followed by a summary.

5.1 Model and Instrumentation

The goal of the test was acquisition of the time varied strut surface pressure distribution around the wake impingement zone, which provides validation data for numerical methods. The wake impingement zone is an area where the wake and body interact strongly. In the case of the blade wake interaction with the strut, the wake impingement zone is around the strut's leading edge. As the number of pressure transducers was limited to seven and the total number of measurement locations was set to be fifty-six, the test design required that the transducers be easily relocated between runs of the test. To meet the requirement, the model strut was designed and manufactured as several separable sections.

The set up of the model test in the cavitation tunnel at the Institute for Ocean Technology (IOT), National Research Council Canada (NRC) is shown in Figure 5.1. Principal dimensions of the test section of the cavitation tunnel are $0.5 \times 0.5 \times 2.2$ meters. The test set up consisted of a propeller dynamometer, a propeller (not shown in the figure), a pod model mounted on the shell of the dynamometer shaft, and a strut seated on the bottom window of the cavitation tunnel. The model strut shown in Figure 5.2 includes a base section at the bottom, three pairs of spacers in the middle, and a seven-transducer-assembly on the top. The assembly could be moved up and down along the strut spanwise by swapping its location with a pair of spacers. The tube connected to the assembly in Figure 5.2 provides transducers with a duct for wiring and ventilation. The seven-transducer-assembly with seven ENDEVCO 8010C pressure transducers installed is shown in Figure 5.3. The propeller model in Figure 5.4 used in this test was one model of a series of four propellers, whose geometry details can be found in a propeller design note

(Liu, 2006a). The geometry of the pod and propeller model and the profiles of the pod and strut are listed in Table 5.1 and Table 5.2 respectively. The distance from the propeller plane to the leading edge of the strut was 0.1 meter. The pod centerline was coincident with the centerline of the test section of the cavitation tunnel. The Reynolds number based on the blade chord length at $0.7R_p$ was higher than 1.4 million.

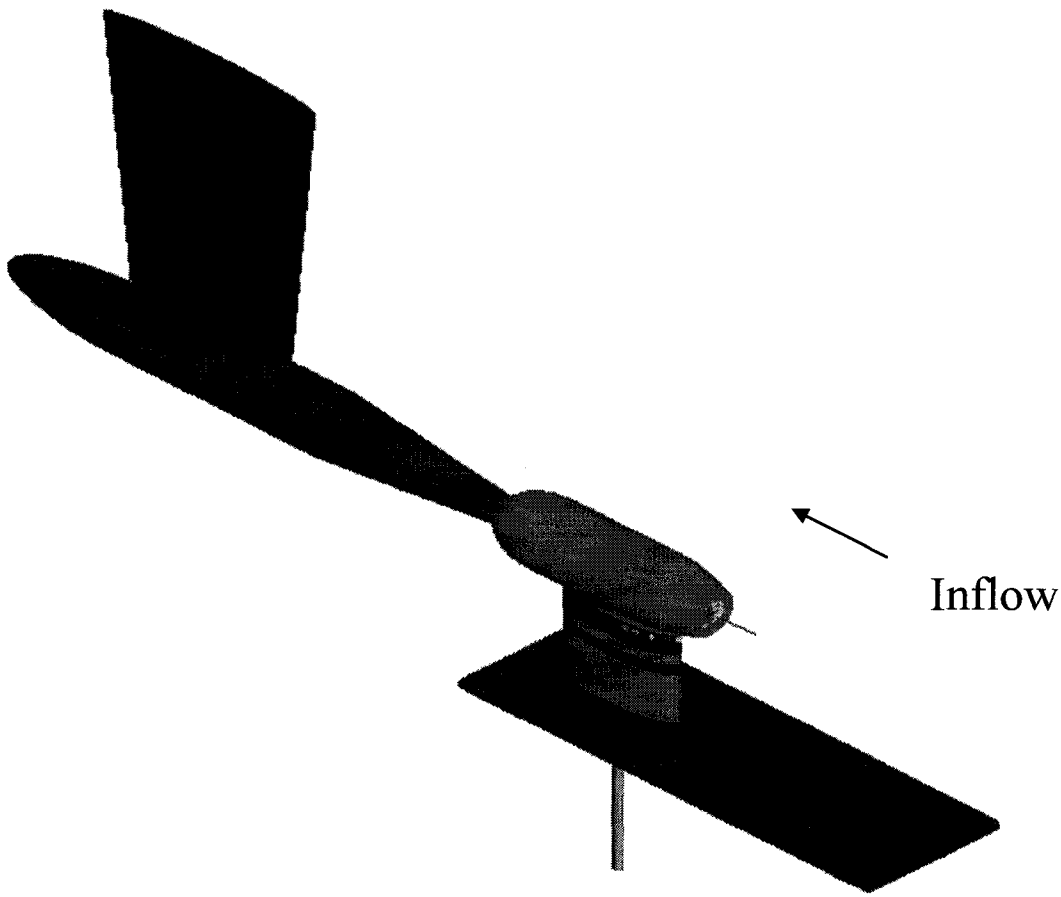

Figure 5.1 Test Set-up in the Cavitation Tunnel

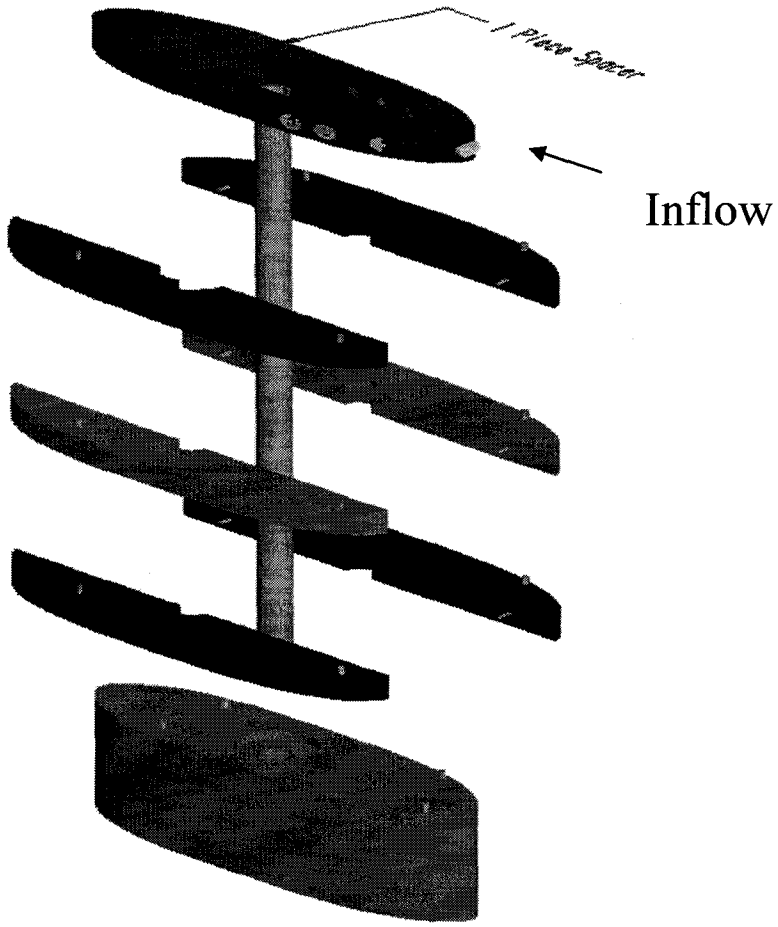

Figure 5.2 Strut Model

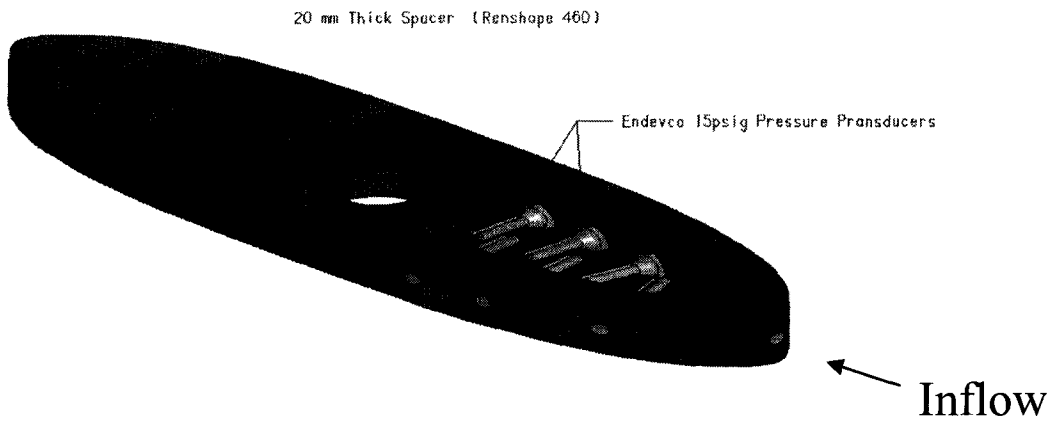

Figure 5.3 Seven Transducer Assembly

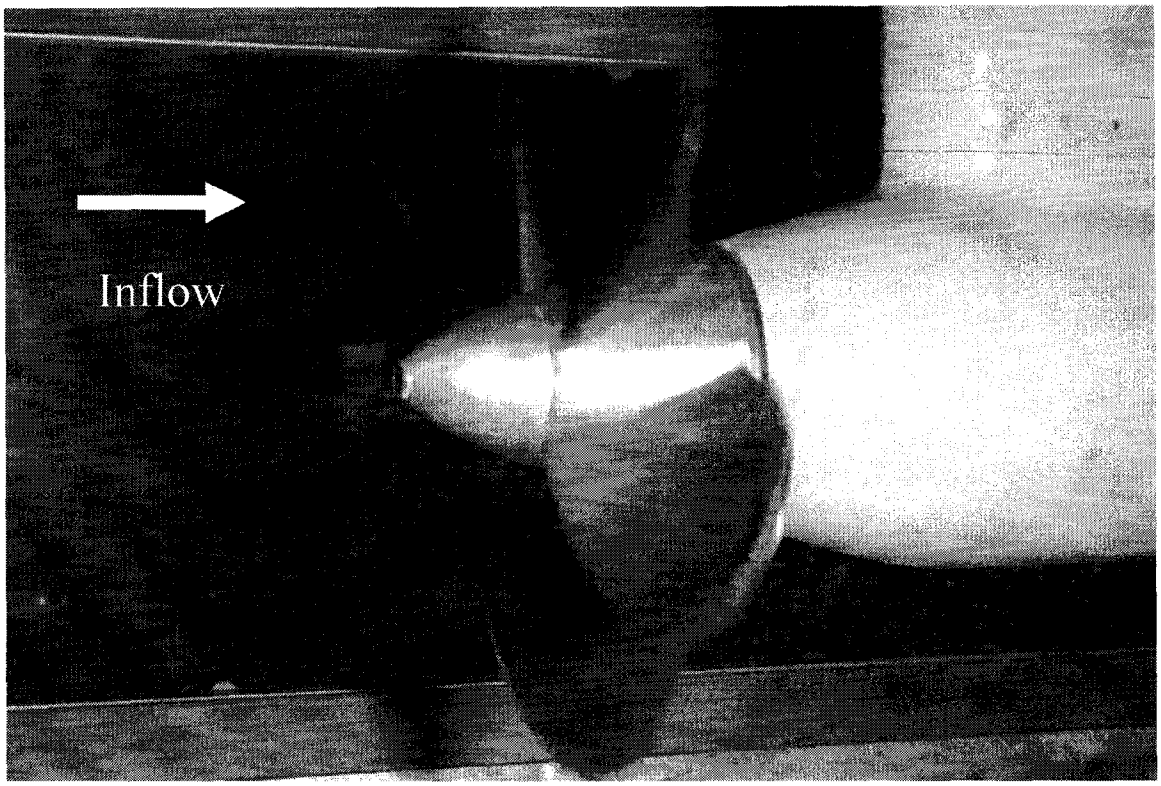

Figure 5.4 Propeller Model in the Test

Table 5.1 Parameters of the Tested Propeller

Diameter (m)	0.27
No. of blade	4
Design J	0.8
Hub-Diameter ratio, mean	0.26
Angular speed (*rps*)	23, left handed
Section thickness form	NACA 66, Modified
Section mean-line	NACA = 0.8
Expanded area ratio, EAR	0.60
Pitch distribution	Constant, P/D=1.0
Skew distribution	Zero
Rake distribution	Zero

Table 5.2 Geometry of the Tested Pod and Strut

Pod		Strut	
X (mm)	R (mm)	X (mm)	Y (mm)
0.00	0.00	0.00	0.00
4.09	13.72	0.29	1.89
12.32	23.83	1.12	3.61
27.67	34.71	17.48	17.60
43.02	45.59	37.79	24.71
70.50	59.29	113.43	29.85
100.84	64.00	189.06	24.71
224.79	64.00	209.38	17.61
348.74	64.00	225.73	3.61
361.79	63.15	226.56	1.89
374.62	60.60	226.85	0.00
432.48	44.46	Distance between origins of the Pod and the Strut=142.62	

5.2 Pressure Measurement

The measurement of the strut surface pressure was conducted in the cavitation tunnel while a constant tunnel pressure was maintained. In order to reduce the risk of the pressure transducer damage and maximize the measurement resolution to the surface pressure variation, the tunnel pressure was set to the pressure of the atmosphere. The measured time series of the pressure, $p_{(t)}$, was obtained by subtracting the measurement when the propeller was at rest (0.5 rps) from the measurement when the propeller was rotating (23 rps) under the same tunnel flow speed, V. The measured pressure was then broken down into three components shown as follows

$$p_{(t)} = \bar{p} + (\tilde{p}_{(t)} - \bar{p}) + p'_{(t)} \tag{5.2.1}$$

The time averaged pressure, $\bar{p}$, the phase averaged (blade phase angle) pressure, $\tilde{p}_{(t)}$, and the pressure of fluctuation, $p'_{(t)}$, are defined as followings

$$\bar{p} = \frac{1}{m}\Sigma_1^m (p_{(t)}) \qquad t \in [0,T] \tag{5.2.2}$$

$$\tilde{p}_{(t)} = \frac{1}{n}\Sigma_1^n \left[p_{(t+(i-1)T_p)}\right] \qquad t \in [0,T] \tag{5.2.3}$$

$$p'_{(t)} = p_{(t)} - \bar{p} - \tilde{p}_{(t)} \tag{5.2.4}$$

Here, m is the total number of sampling points, n is the total number of sampled propeller revolutions, i is the index of revolutions of the propeller shaft, T is the total sampling time, and T_p is the period of propeller rotation. For each measurement in this test, pressure and force signals were sampled at 5000 Hz for 15 seconds. Parameters for the measurements are listed in Table 5.3.

Table 5.3 Test Settings and Pressure Transducer Locations

Test Parameters				Transducer Location		
rps	*V*	*J*		No	*X/C*	Z/R_p
23	3.4	0.55		#7	0.381	1.14
23	4.2	0.68		#5	0.303	1.07
23	4.6	0.74		#3	0.207	0.99
23	5.0	0.81		#1	0.000	0.92
23	5.4	0.87		#2	-0.164	0.84
				#4	-0.267	0.77
				#6	-0.354	0.70
						0.62

Here, Z is the vertical distance from the centerline of the propeller shaft to the location of the pressure transducer, and R_p is the radius of the propeller. C is the chord length of the strut, and X is the chordwise distance starting from the leading edge. X is positive for the compressed side and negative for the stretched side. The stretched side is defined as the side of the strut where the propeller wake is stretched after it is split by the leading edge of the strut. For a left-handed tractor-type podded propeller, the port side of the strut is the stretched side and the starboard side is the compressed side. Left hand propeller rotates counterclockwise when viewed astern facing forward. All pressure components are transformed and represented in dimensionless coefficients of C_P.

$$C_p = p/(0.5\rho\omega^2 R_p^2) \tag{5.2.5}$$

where p is a component of pressure [Pa], ρ is the water density [kg/m^3], and ω is the propeller angular speed [rad/sec]. The whole set of processed data in terms of phase averaged pressure coefficient on the strut surface is plotted in Appendix B.

The propeller thrust and torque, T and Q, were also recorded simultaneously by the same data acquisition system as that of the strut surface pressure. As there was no transducer for the propeller blade phase angle, the propeller torque was used as a reference signal to determine the phase angle differential between pressure measurements at different locations, Z/R_p. The starting time for all pressure variations was set to points corresponding to peaks of propeller torque.

5.3 Time Averaged Component

The time averaged pressure coefficients for five different advance coefficients are shown in Figures 5.5 to 5.9. It can be seen that the pressure on the leading edge of the strut varies very little from the dimensionless vertical distance $Z/R_p = 0.6$ to $Z/R_p = 0.85$, then, it drops sharply close to zero around $Z/R_p = 1.1$. Here Z is the vertical distance from the propeller shaft centre, and R_p is the radius of the propeller. The value of the pressure coefficient on the leading edge within the range of Z/R_p from 0.6 to 0.85 decreases as the advance coefficient increases. It changes from 0.8 at $J = 0.55$ to 0.55 at $J = 0.87$. The pressure on the compressed side of the strut changes only slightly either chordwise or spanwise while the pressure on the stretched side changes significantly. For a left-handed tractor-type podded propeller, the port side of the strut is the stretched side, and the starboard is the compressed side. The change of the pressure on the stretched side along the chord is small outside of the propeller plane, but it increases almost linearly with the increase of the distance from the propeller shaft. The

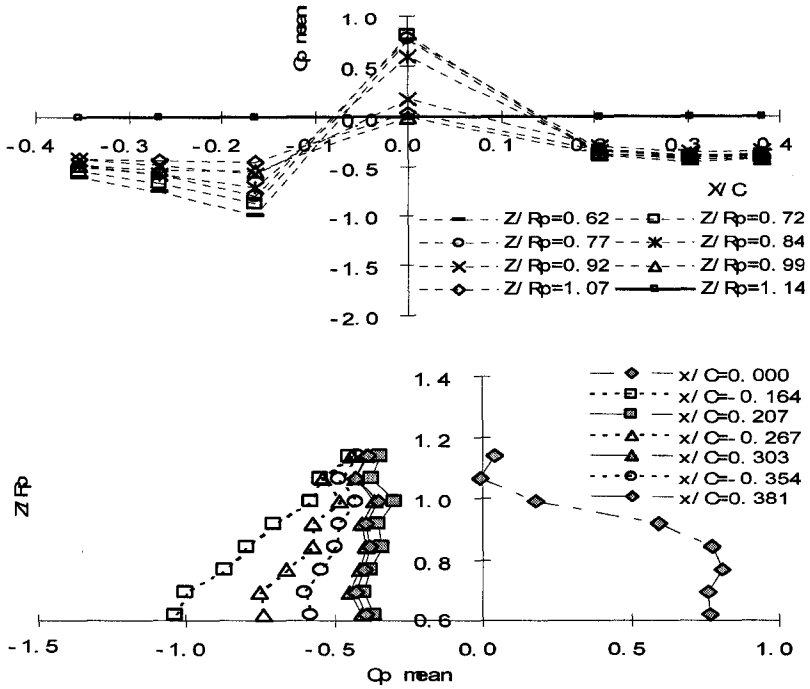

Figure 5.5 Mean Pressure Coefficient, *J=0.55*

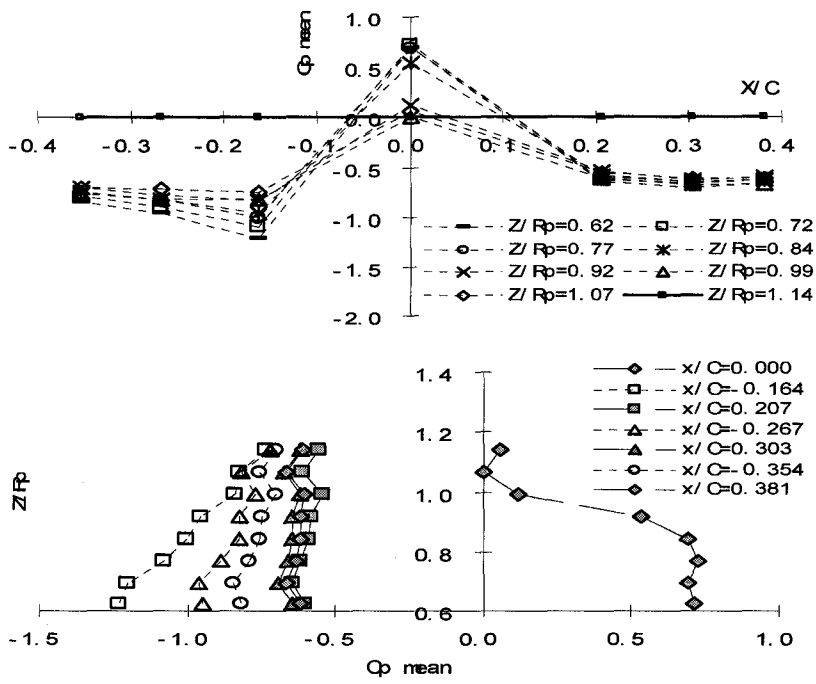

Figure 5.6 Mean Pressure Coefficient, *J=0.68*

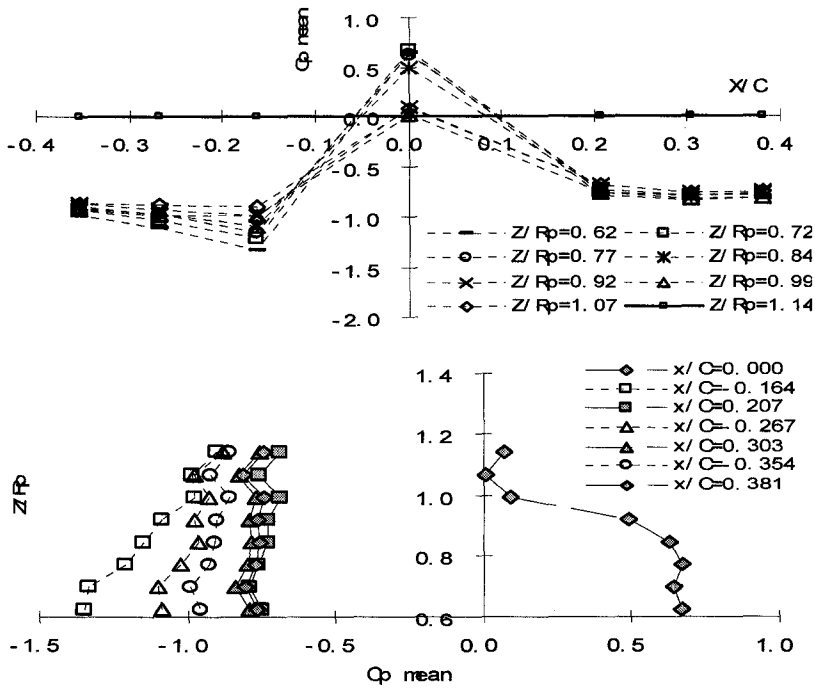

Figure 5.7 Mean Pressure Coefficient, *J=0.74*

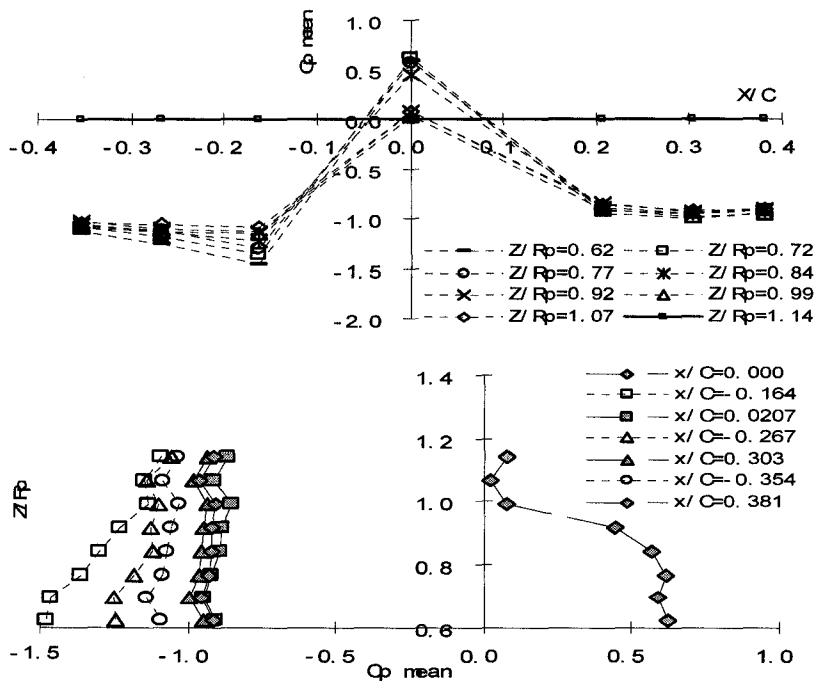

Figure 5.8 Mean Pressure Coefficient, *J=0.81*

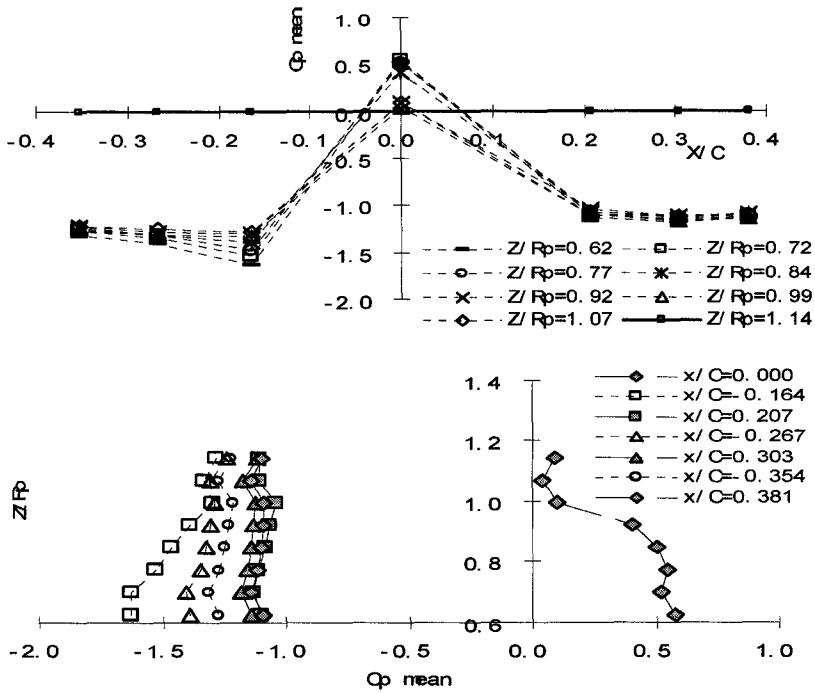

Figure 5.9 Mean Pressure Coefficient, *J=0.87*

pressure change becomes very rapid near the intersection of the pod and strut. In the case of $J = 0.87$ and $Z/R_p = 0.62$, the pressure coefficient drops from 0.58 at the leading edge to -1.63 at $X/C = 0.16$ and recovers to -1.27 at $X/C = 0.35$. The lowest point of the time-averaged pressure coefficient in the test was detected to be -1.63. It was located on the stretched side, near the leading edge, around the intersection of the strut and the pod at $J = 0.87$. The steepest drop on the time-averaged pressure coefficient was found around the leading edge of the strut near the pod/strut intersection. The change of the time-averaged pressure coefficient on the stretched side was sharper than that on the compressed side.

Comparing the pressure coefficients on the two sides of the strut, it was found that the pressure measured on the compressed side was always higher than that on the

stretched side. The differential of the pressure on the sides leads to an asymmetric force (the side force) on the strut. This difference on the pressure distributions on the two sides of the symmetrical strut is led by a non-zero effective angle of attack even if the strut is operated in a straight course. The non-zero effective angle of attack results from the wake swirl induced by the rotating propeller.

5.4 Phase Averaged Component

Representations and discussions of the phase averaged component are divided into two parts, the amplitude of the component and the time variation of the component. The amplitude of the phase averaged pressure coefficient is defined as

$$A_{C_p} = \left(\max\{C_{p(t)}\} - \min\{C_{p(t)}\}\right) \quad t \in [0, T_p] \tag{5.4.1}$$

The amplitudes of phase averaged pressure coefficients are shown in Figures 5.10 to 5.14. The largest amplitudes of the phase averaged pressure components for all cases appear around $Z/R_p = 1.0$. The vertical position (Z/R_p) of the amplitude peak increases when it

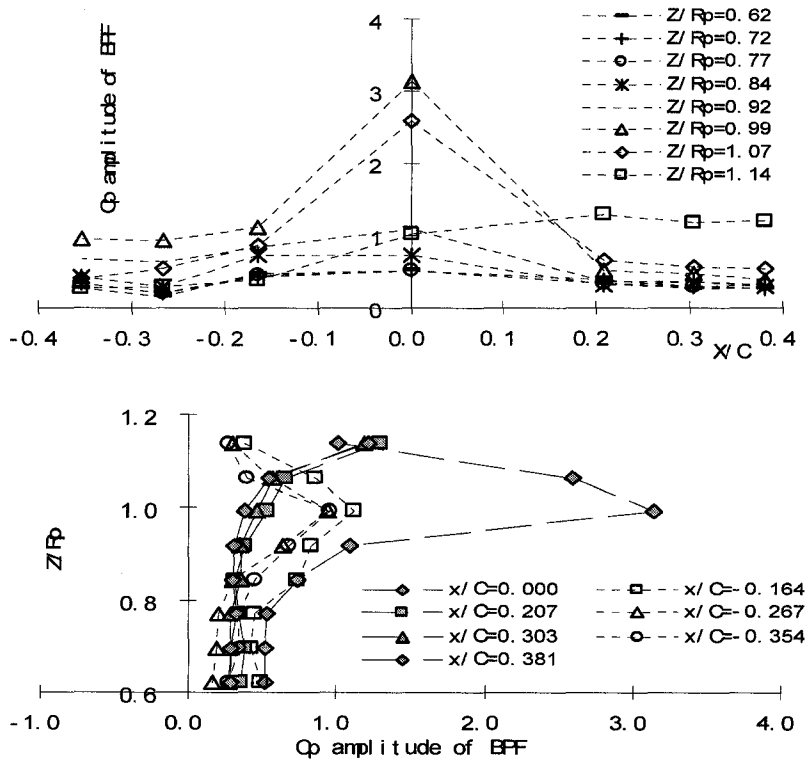

Figure 5.10 Amplitude of Pressure Coefficient, *J=0.55*

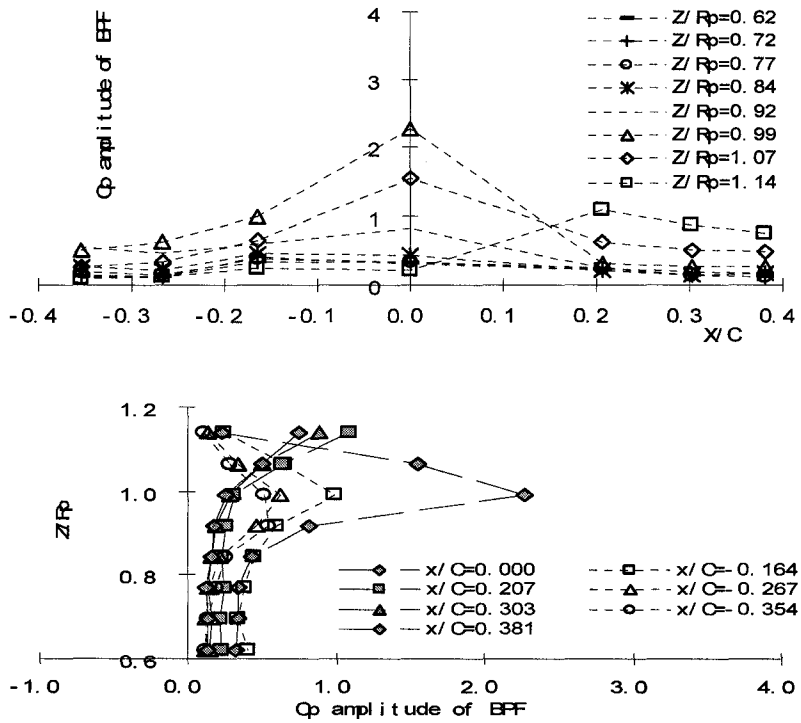

Figure5.11 Amplitude of Pressure Coefficient, *J=0.68*

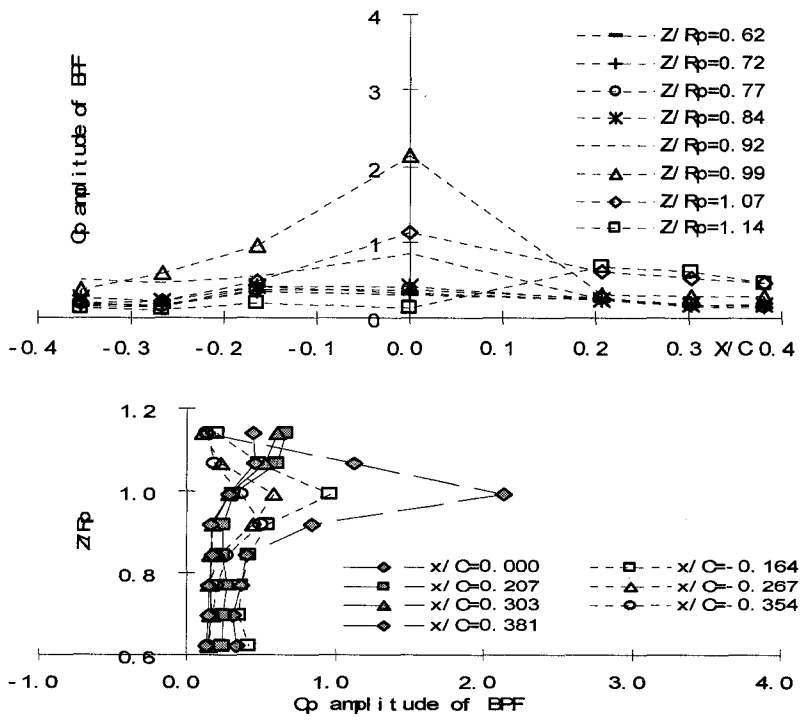

Figure 5.12 Amplitude of Pressure Coefficient, *J=0.74*

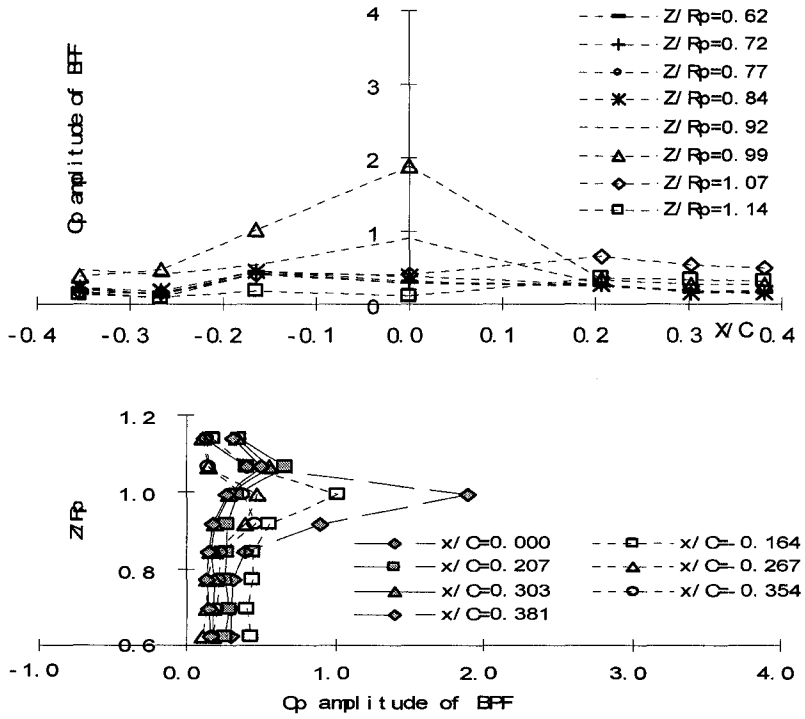

Figure 5.13 Amplitude of Pressure Coefficient, *J=0.81*

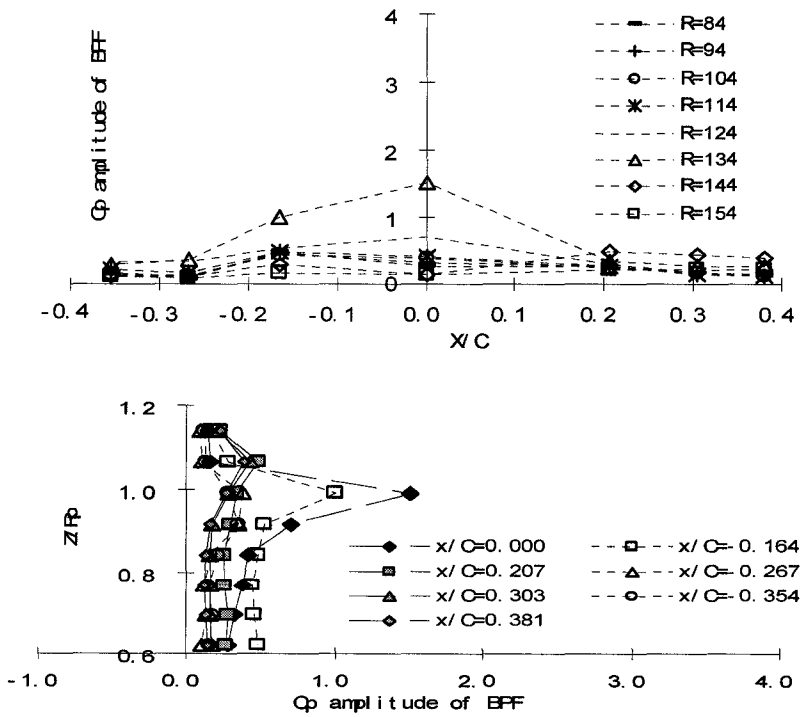

Figure 5.14 Amplitude of Pressure Coefficient, *J=0.87*

occurs downstream on the compressed side. However, the vertical position of the peak amplitude stays near $Z/R_p = 1.0$ on the stretched side.

Based on the investigation of the amplitude of the phase averaged component, it has been found that large pressure variations appear only around the position of $Z/R_p = 1.0$. In the visual investigation of the blade tip vortex/strut interaction, it was found that the blade tip vortices impacted on the strut right around the area where the highest pressure variation was measured. Scanning the whole set of time varied pressure coefficients of the phase averaged component in Appendix B, it was also found that the blade passing frequency *BPF* dominated the variation of the pressure on the leading edge in the region from the vertical distance $Z/R_p = 0.844$ to $Z/R_p = 1.141$. The location of the maximum pressure variation left the leading edge around $Z/R_p = 1.0$ and went downstream. It drifted up to $Z/R_p = 1.141$ on the compressed side and dropped down to $Z/R_p = 0.95$ on the stretched side when it reached $X/C = 0.4$. In this case, the discussion on the pressure time variation will focus on the area around $Z/R_p = 1.0$. Among these phase averaged variations dominated by the blade passing frequency, there were two patterns of variations. One has a single trough and a single peak pattern as shown in Figure 5.15, and another has double trough and double peak as shown in Figure 5.16. A comparison of these two Figures shows the amplitude of the double trough variation is only about 60% of that of the single trough variation. Checking the position of the measurement points where double troughs were measured, it was found that all of them were located very close to the trajectories of the two ends of the tip vortex which

was broken apart by the strut leading edge. This finding might be used to reduce the amplitude of pressure variation by changing the pressure variation from the single trough shape to the double-trough shape. This could be done by redesigning the strut's leading edge, or by breaking up the incoming vortex before it impacts on the strut.

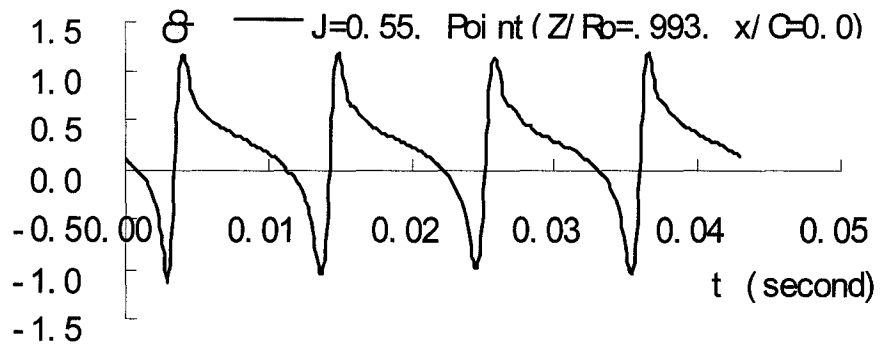

Figure 5.15 Variation of Phase Averaged Component

$(J = 0.55, Z/R_p = 0.993, x/C = 0.0)$

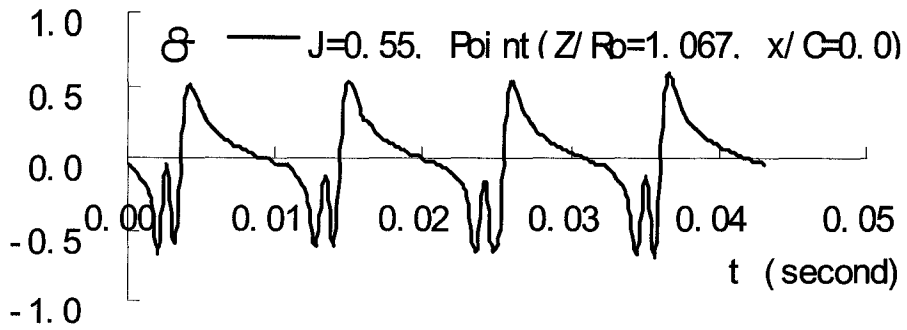

Figure 5.16 Variation of Phase Averaged Component

$(J = 0.55, Z/R_p = 1.067, x/C = 0.0)$

5.5 Double trough pressure variation

This section examines how a single trough or a double trough pressure variation occurs. A simple model of a single vortex filament placed in uniform flow was considered, and the pressure variations along different routes crossing the filament center were estimated by using the Bernoulli equation.

A vortex filament can be simply described by two parameters: its size, and its nominal circumferential velocity $V_{t\_\max}$. The size of the core of the vortex is defined as the nominal diameter d_σ, which is two times the radius r_σ. The azimuthal velocity of a vortex filament is a function of the distance from the vortex centre. When the distance from the vortex centre is larger than r_σ, the rotational velocity decreases and goes to zero at "infinity". Below this distance, the rotational velocity is approximated by different models. The vortex model introduced by Vatistas (1998) is a general vortex model which was discussed by Bhagwat and Leishman (2002). The generalized model is described as:

$$V_t(r) = V_{t\_\max}\left\{\frac{\bar{r}}{\left(1+\bar{r}^{-2n}\right)^{1/n}}\right\} \qquad \begin{array}{ll} n=1 & \text{Kaufmann vortex model} \\ n=2 & \text{similar to Lamb-Oseen model} \\ n\to\infty & \text{Rankine vortex model} \end{array} \qquad (5.5.1)$$

A vortex filament, whose strength was represented by $\Gamma = \pi d_\sigma V_{t\_\max}$, was placed in an uniform flow $(U,\ 0,\ 0)$ as shown in Figure 5.17. The symbol r is the route which goes through the vortex filament with an angle of β to the uniform flow direction, and offset

from the vortex centerline at a distance of e. The angle β can also be defined as the blade/vortex incision angle. The pressure variations

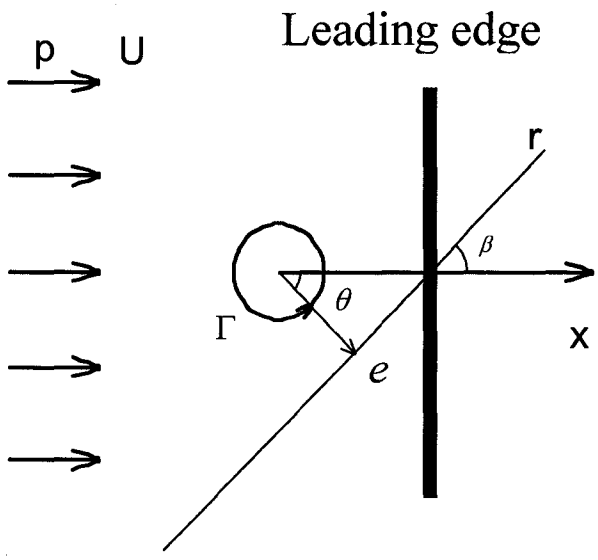

Figure 5.17 A vortex filament placed in Uniform Flow

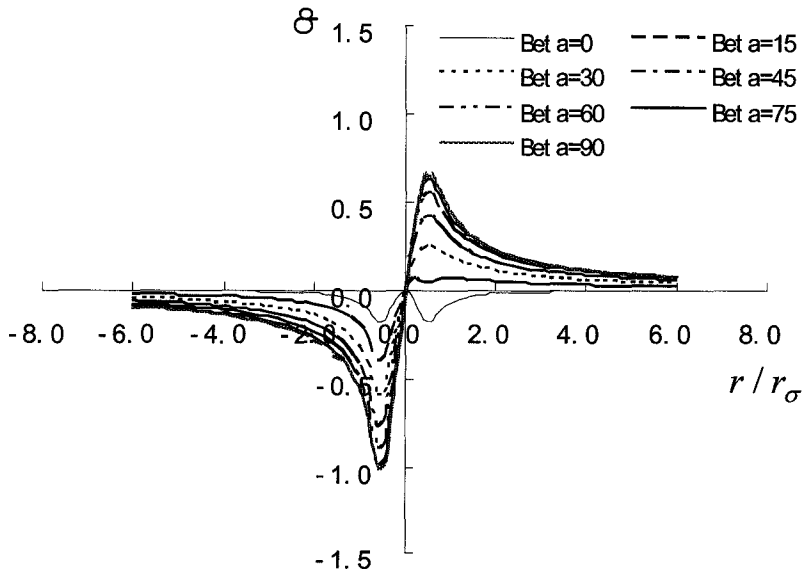

Figure 5.18 Pressure Variations of Different Routes ($e = 0$)

along the routes were estimated and analyzed against parameters of β and e. The combined velocity field of the vortex filament and the uniform flow can be expressed as:

$$\begin{Bmatrix} V_x \\ V_y \\ V_z \end{Bmatrix} = \begin{Bmatrix} U + V_t \cos\beta \\ V_t \sin\beta \\ 0 \end{Bmatrix} \tag{5.5.2}$$

This ensures the pressure far away from the vortex center was $p_1 = 0$, where velocity was undisturbed $V_1 = U$, and ignoring the gravity contribution $h_1 = h_2 = 0$. Application of the Bernoulli equation

$$p_1 + \frac{1}{2}\rho V_1^2 + \rho g h_1 = p_2 + \frac{1}{2}\rho V_2^2 + \rho g h_2 = C \tag{5.5.3}$$

to the combined velocity in equation (5.5.2) the pressure variation along different routes, $e = 0$ and changing β from 0° to 90° in an increment of 15°, was calculated and plotted in Figure 5.18. It was found that when β was 0° a double trough pressure variation pattern occurred. For those β higher than 15°, their pressure variations demonstrated a shape of a mirror image of "N". In other words, when a filament impacts on and is then cut by a leading edge, the pattern of the pressure on the strut induced by the cutting depends on the incision angle β. If the incision angle is smaller than 15°, the pressure variation on the leading edge will have a double trough shape with reduced amplitude of pressure variation. Otherwise, the pressure variation exhibits a single trough pattern.

5.6 Pitch of the Tip Vortex

The wake pitch distribution of an operating propeller is desired for both numerical method validation and propeller wake tracing. Although the wake pitch distribution can not be surveyed from the blade root to the blade tip in this model test, the pitch of the wake shed from the blade tip was visualized by the tip vortex cavitation. As the strut intruded into the wake race, the tip vortex pitch varied with the circumferential angle around as well as the axial position along the centre line of the propeller shaft. Photographs of cavitating tip vortices were taken at ten different advance coefficients varying from 0.52 to 0.81. Two of them are shown in Figure 5.19 and 5.20. Tip vortex positions down of the pod bottom, x, ranged from $x/D_p = 0$ to $x/D_p = 1.2$ were read from the photos, and the readings were formulated by regression. Here x/D_p is the axial dimensionless distance from the propeller plane. A predetermined second order, two polynomial parameters (J and x/D_p) and the least squares method were used in the regression. The tip vortex pitch, $H_{tipvortex}$, for this podded propeller model resulted as:

$$H_{tipvortex} = (0.0864 - 0.0168J)x/D_p + 0.828J + 0.4228 \qquad (5.6.1)$$

$$J \in [0.52,\ 0.81] \text{ and } x/D_p \in [0,\ 1.2]$$

The formula is only valid for advance coefficient from 0.52 to 0.81 and the distance from the propeller smaller than 1.2 times of the propeller diameter.

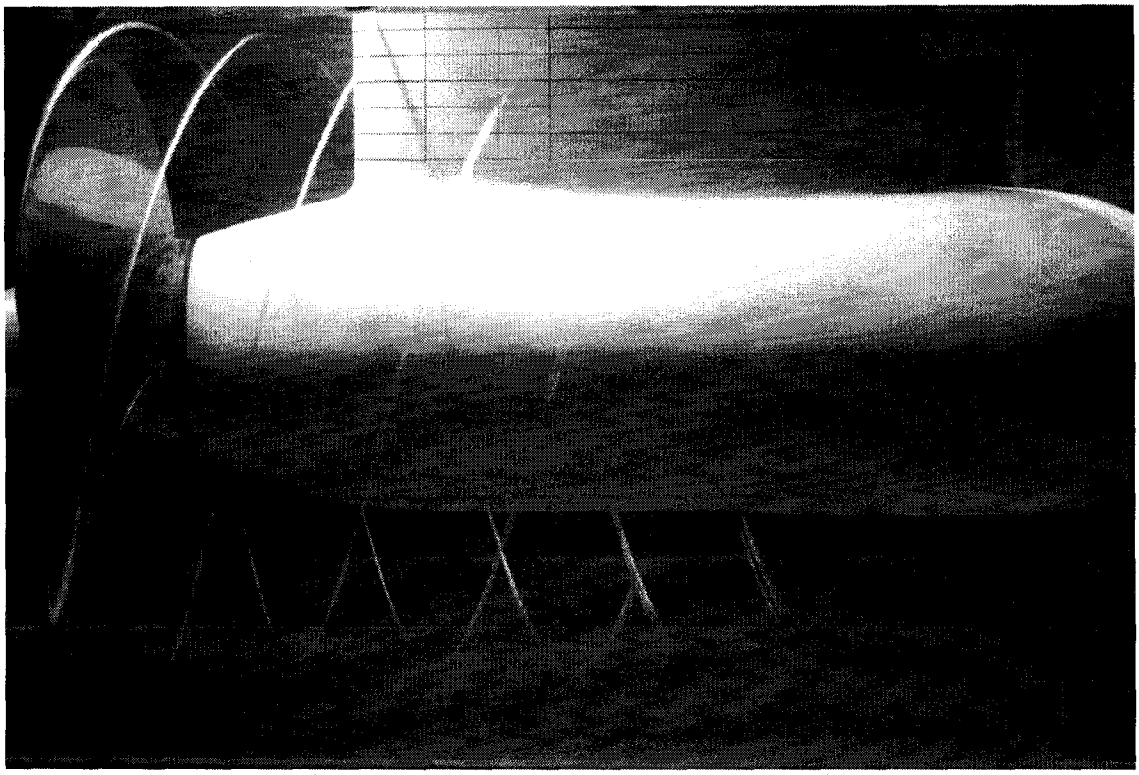

Figure 5.19 Tip Vortex (*23 rps, V=3.2 m/s*)

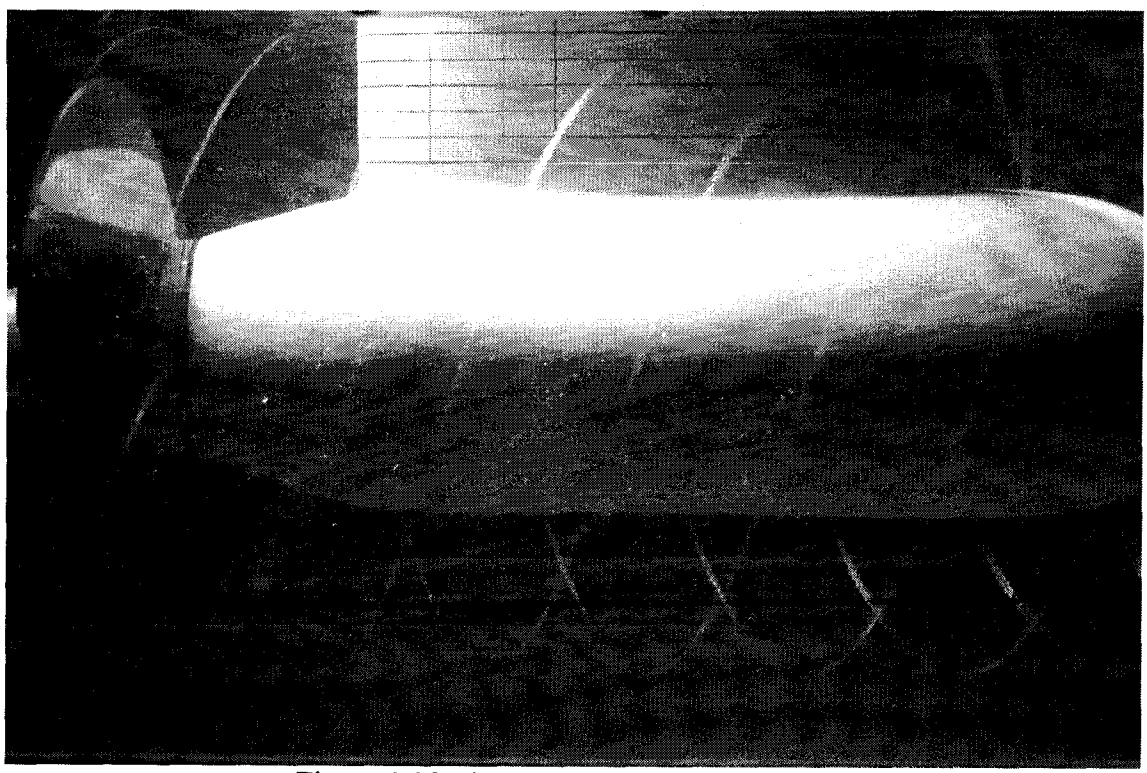

Figure 5.20 Tip Vortex (*23 rps, V=4.2 m/s*)

5.7 Tip Vortex Diameter

In this section, a method for estimating the tip vortex diameter around the strut leading edge based on the pressure measurement on the strut surface is introduced and estimations are performed. It has been discussed in previous sections that setting the cut-off value to be the vortex filament radius is important to carry out accurate simulations on the induced velocity. The estimated tip vortex diameter is helpful in setting parameters properly in numerical simulations.

The principle of the tip vortex nominal diameter estimation method is based on the distance that is the product of the tip vortex propagation speed V and the time interval between the trough and the peak or between the peaks. This can be formulated as:

$$d_\sigma = V \cdot t_\sigma \tag{5.7.1}$$

$$\text{Here } t_\sigma = \begin{cases} t_{peak} - t_{trough} & \textit{in case of Figure 5.21} \\ t_{peak2} - t_{peak1} & \textit{in case of Figure 5.22} \end{cases} \tag{5.7.2}$$

t_{peak} is the time where the pressure reaches its maximum,

t_{trough} is the time where the pressure reaches its minimum

$t_{trough1}$ is the time where the pressure reaches its first trough

$t_{trough2}$ is the time where the pressure reaches its second trough

The tip vortex propagation speed was calculated by

$$V = \frac{H_{tipvortex}}{T} \tag{5.7.3}$$

where T is the period of the propeller revolution and $H_{tipvortex}$ is calculated by Eq. (5.6.1).

The estimations of the tip vortex diameter are plotted against advance coefficients in Figure 5.23.

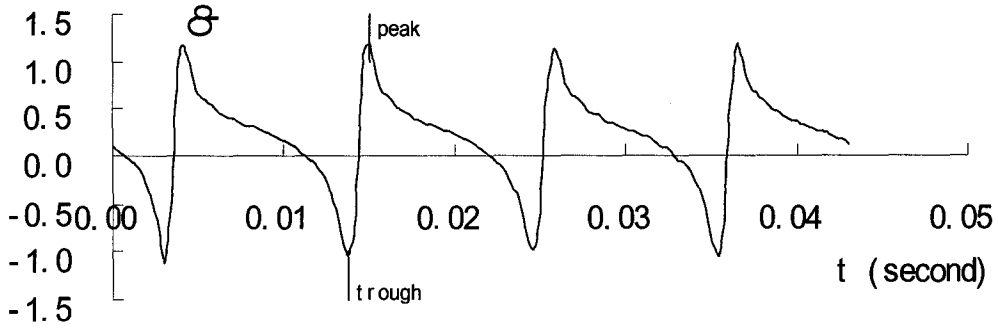

Figure 5.21 Trough and Peak Positions (1)

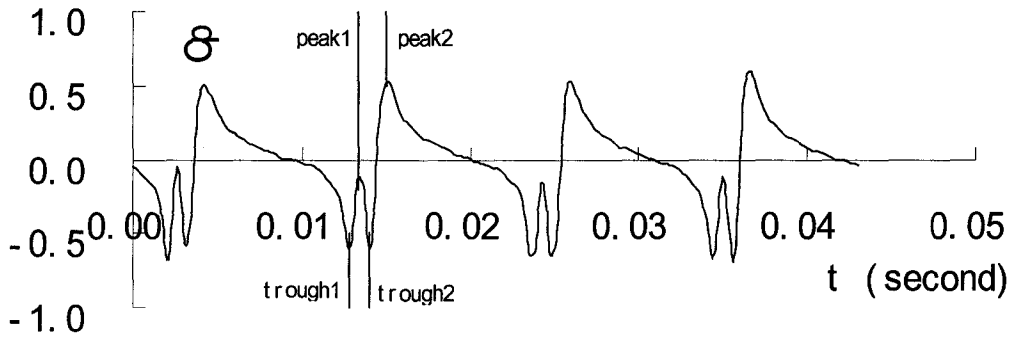

Figure 5.22 Trough and Peak Positions (2)

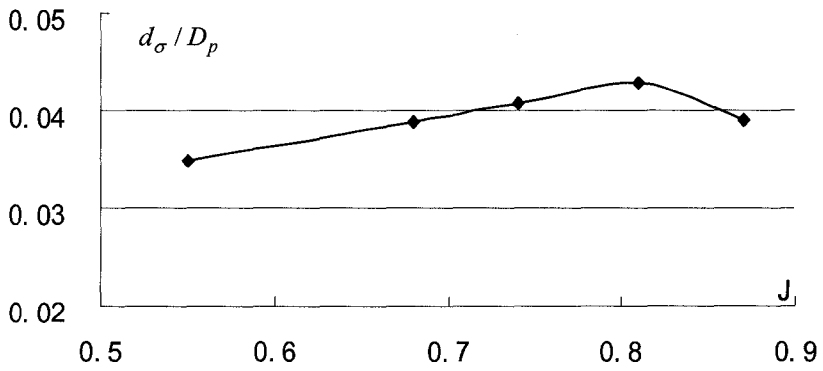

Figure 5.23 Tip Vortex Nominal Diameter against J

5.8 Tip Vortex / Strut interaction

In the visual investigation, the pressure transducer assembly was substituted by a dummy strut, and the tunnel was depressed to -41.36 kPa (-6 psi) relative to the atmospheric pressure. Running the test under this pressure maintained the tip-vortex cavitation steady and visible. The cavitation provided a clear view of the tip-vortex movement response to the vortex/strut interaction. The tunnel pressure in this test was different from that in the strut surface pressure measurement, since it was necessary to keep the tunnel pressure the same as the atmosphere pressure to protect the pressure transducers and maximize the measurement resolution to the pressure variation. The visible tip vortex response under the pressure of -41.36 kPa was similar to that invisible under the pressure of *0* kPa (relative to the atmosphere) during the pressure measurement.

A well known form of derivations from the Navier-Stokes equations is the vorticity-transport equation governing the flow of an incompressible Newtonian fluid. The equation shown as follows indicates that the transportation of vorticity is independent of the pressure, since there is no pressure term included in the equation.

$$\frac{D\boldsymbol{\omega}}{Dt} = \frac{\partial \boldsymbol{\omega}}{\partial t} + \mathbf{u} \cdot \nabla \boldsymbol{\omega} = \boldsymbol{\omega} \cdot \nabla \mathbf{u} + \upsilon \nabla^2 \boldsymbol{\omega} \qquad (5.8.1)$$

where D/Dt is the total derivative, $\mathbf{u} = (u, v, w)$ is the velocity vector, $\boldsymbol{\omega}$ is the vorticity which is defined as the curl of the velocity vector, υ is the kinematic viscosity and t is the time. The equation (5.8.1) implies the tunnel pressure variation does not change the vortex transportation directly.

The tip vortex was bent by the leading edge when it approached the strut (Figure 5.25, 5.30), and then kept a minimum distance from the leading edge while it moved

along the leading edge away from the shaft center (Figure 5.31, 5.32). After the tip vortex was bent, stretched, and gradually weakened around the leading edge (Figure 5.33), it appeared to be separated around the two sides of the strut and propagated downstream (Figure 5.34). A cycle of the tip vortex/strut interaction is demonstrated by two sets of pictures from Figure 5.24 to 5.35. One set was taken from the front and another was taken from the side. Test parameters during these two sets of pictures were the same. The tunnel flow speed was $V_{flow} = 3.4\ m/s$, the propeller revolution speed was 15 rps and the tunnel pressure was maintained at -41.36 kPa (-6 psi). For one revolution of the propeller, four tip vortex curves were found turning from continuous helical lines into segments around the strut's leading edge. While a segmental vortex propagated downstream, it was compressed on one side of the strut and stretched on the other side. The vertical distance from the end of the segmental vortex to the shaft centerline on the stretched side remained a constant. However, the distance increased on the compressed side: the lower the value of the advance coefficient, the faster this distance increased. There was no merger of broken ends of tip-vortex investigated downstream the trailing edge of the strut. The pressure measured at points located within 0.9 to 1.1 of the propeller radius showed that they were dominated by the blade passing frequency. The pressure measured outside of this range rarely showed significant fluctuation. The largest amplitude of fluctuation was found at the leading edge around 1.0 R_p for all tested advance speeds. For some low advance coefficient cases, the pressure at the measurement point close to the leading edge on the compressed side demonstrated a double-hollow shape within a single filament impacting period.

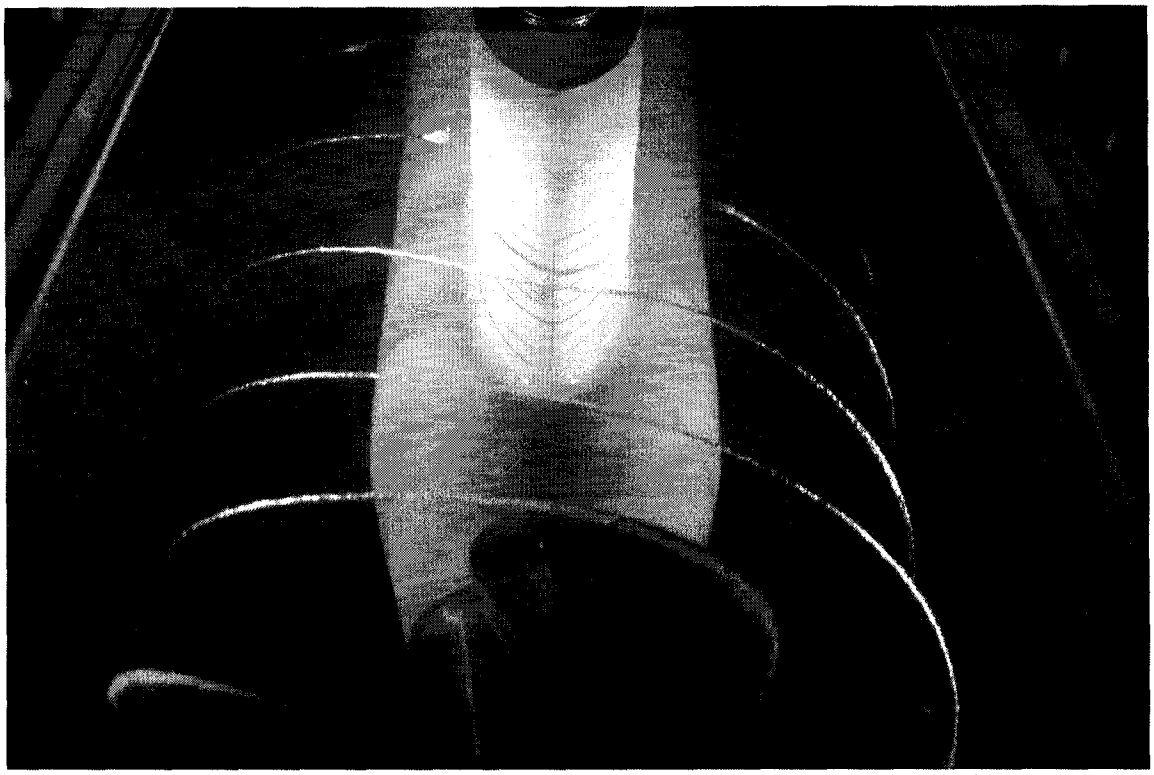

Figure 5.24 Top View of Tip Vortex/Strut Interaction; approach

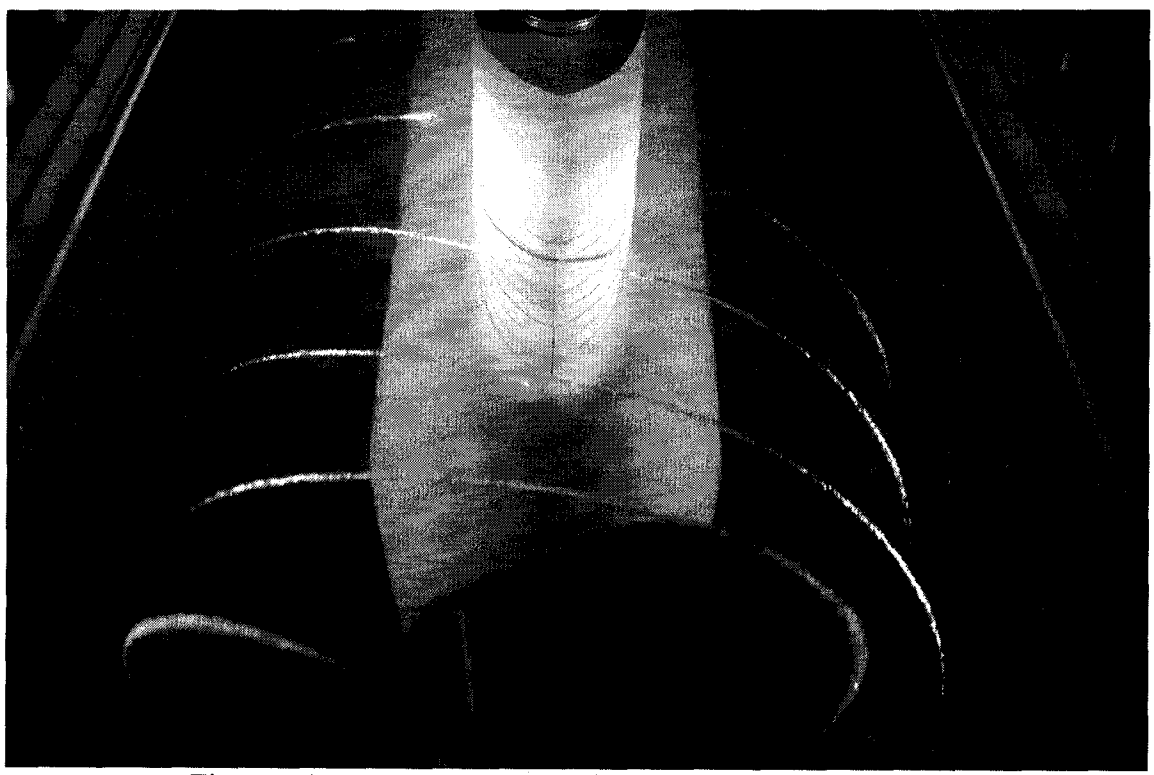

Figure 5.25 Top View of Tip Vortex/Strut Interaction; touch

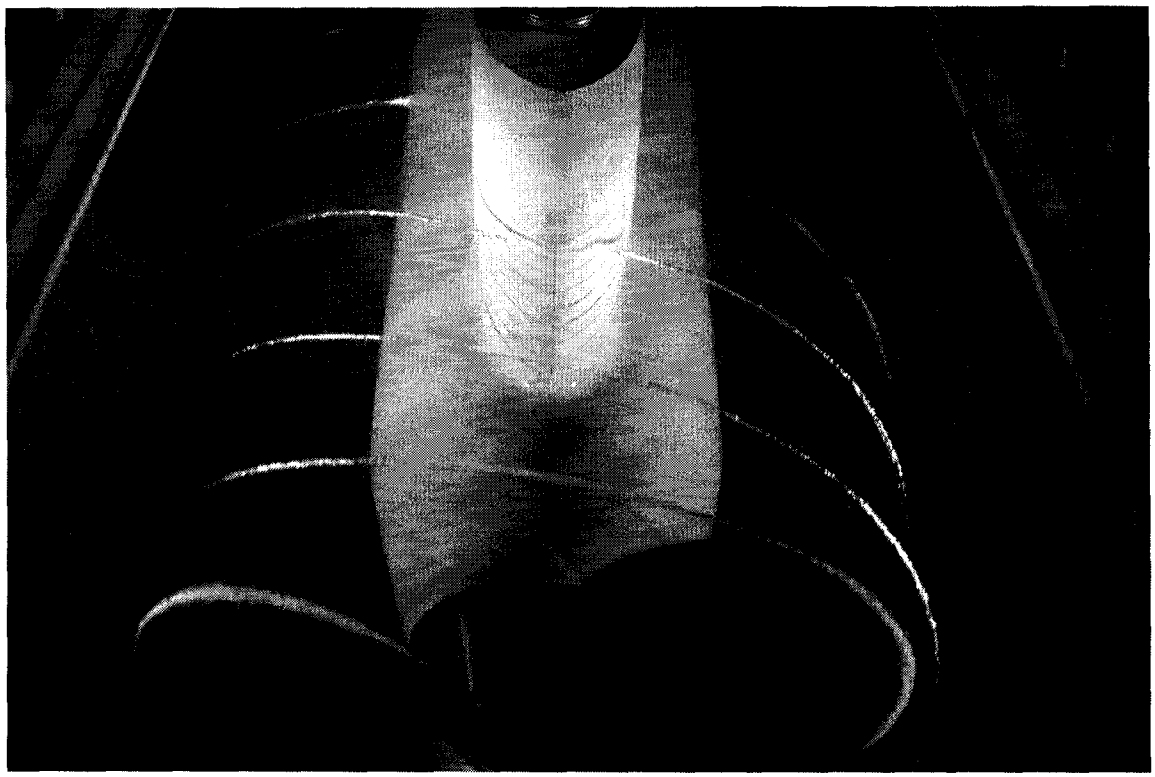

Figure 5.26 Top View of Tip Vortex/Strut Interaction; bend

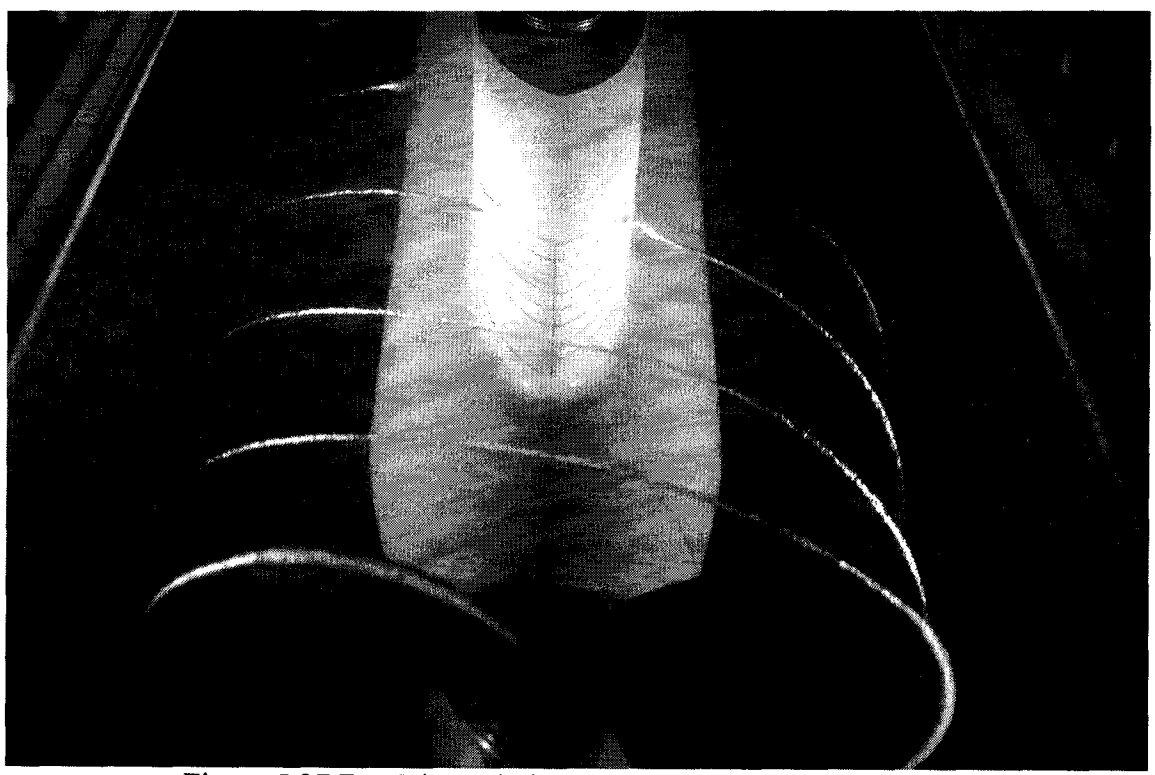

Figure 5.27 Top View of Tip Vortex/Strut Interaction; stretch

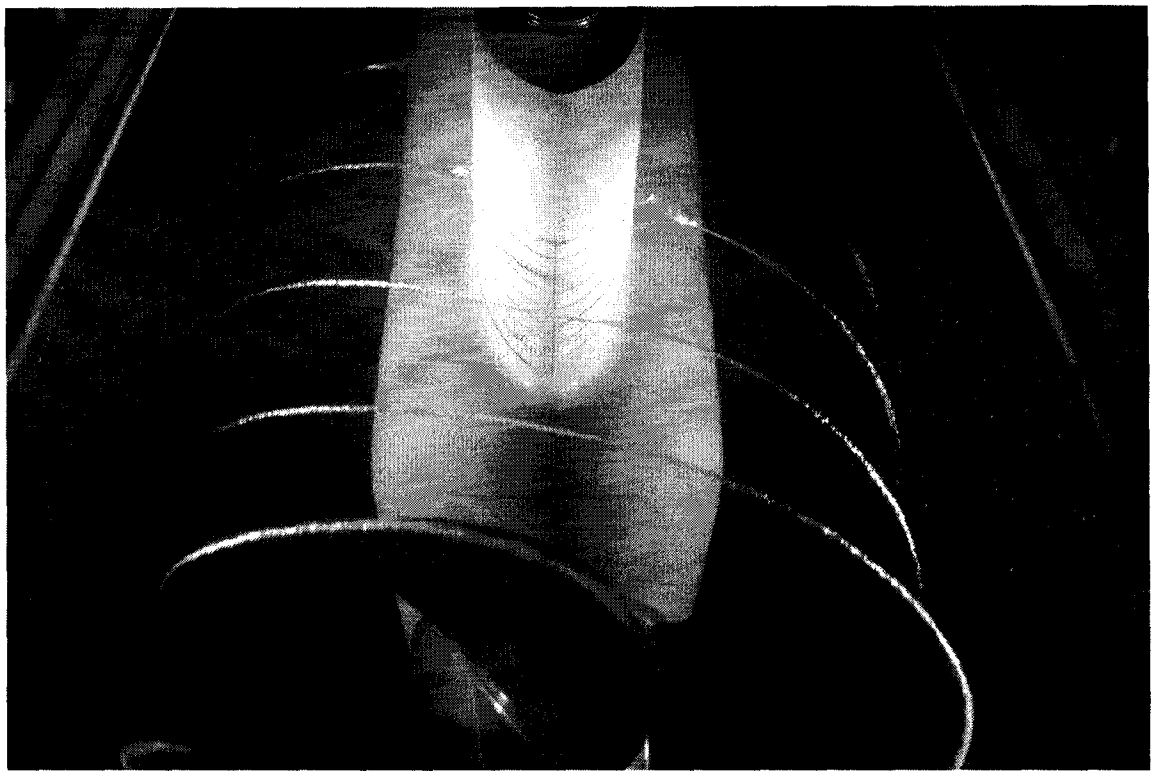

Figure 5.28 Top View of Tip Vortex/Strut Interaction; split

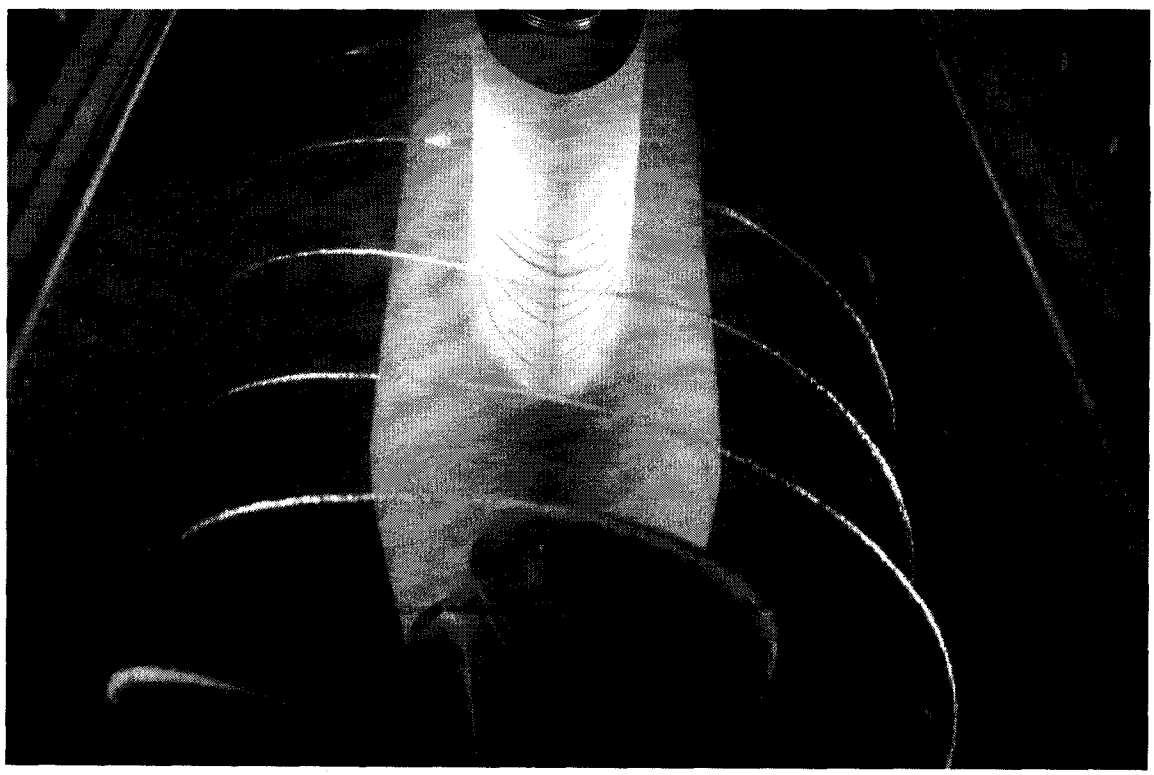

Figure 5.29 Top View of Tip Vortex/Strut Interaction; start the next cycle

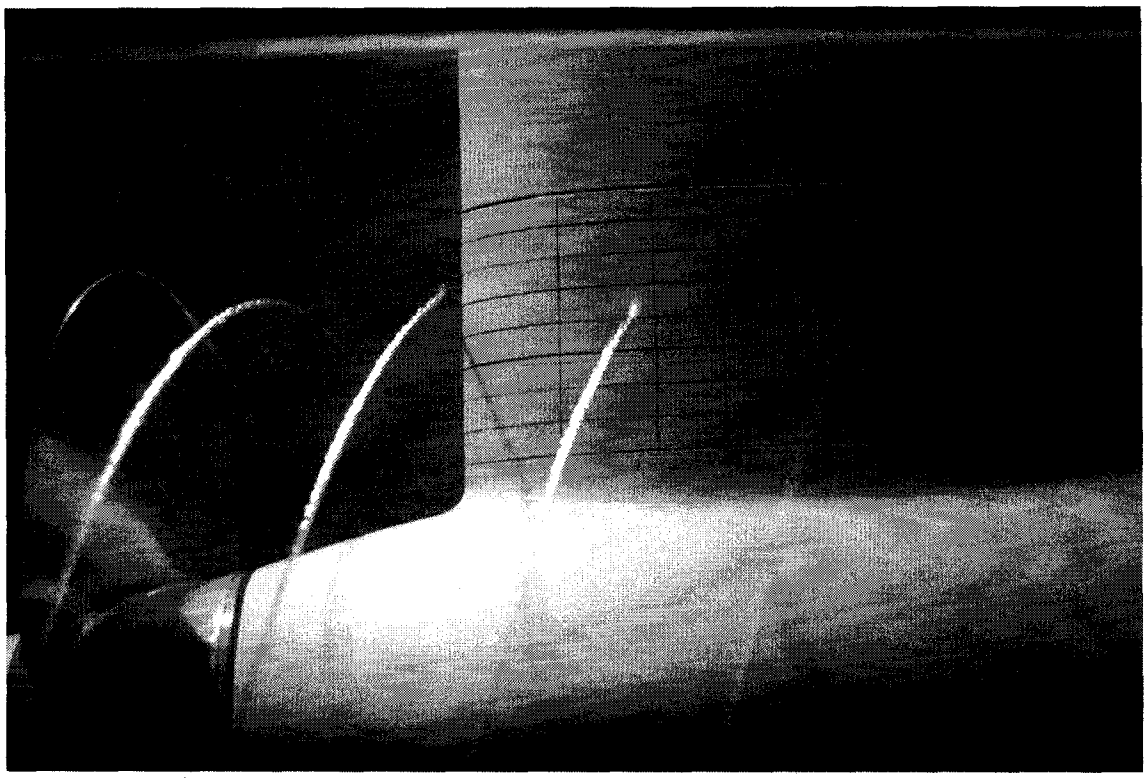

Figure 5.30 Side View of Tip Vortex/Strut Interaction; approach

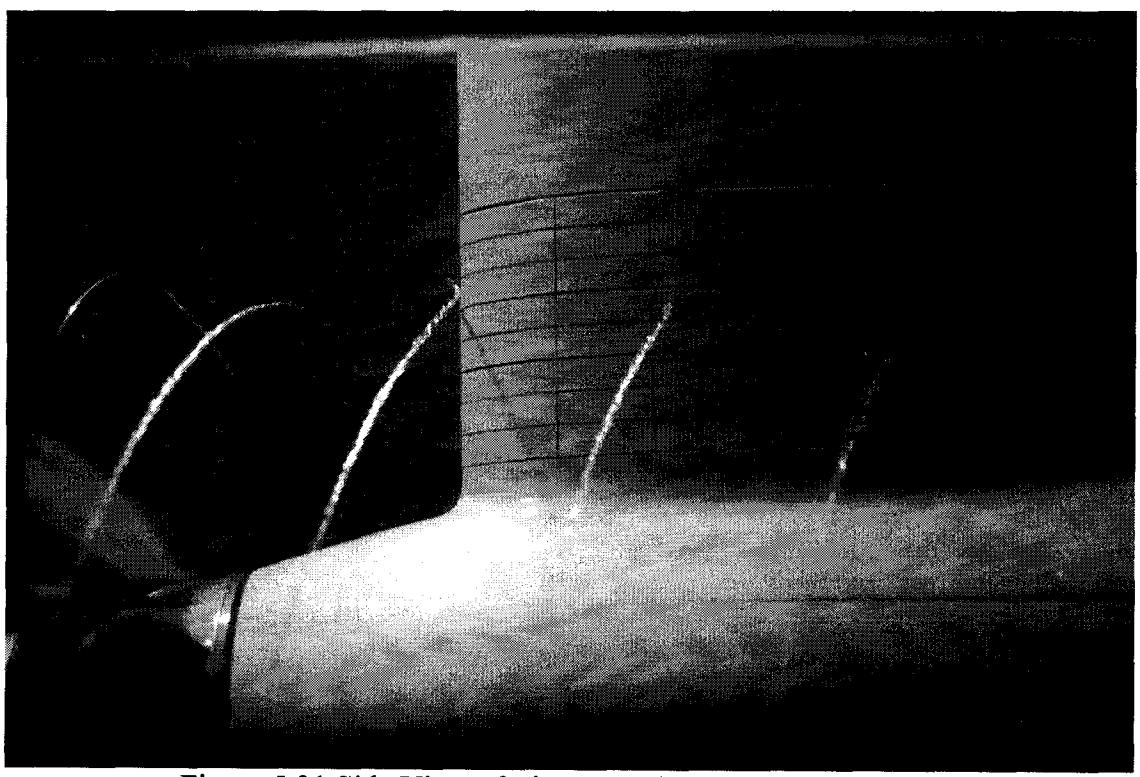

Figure 5.31 Side View of Tip Vortex/Strut Interaction; touch

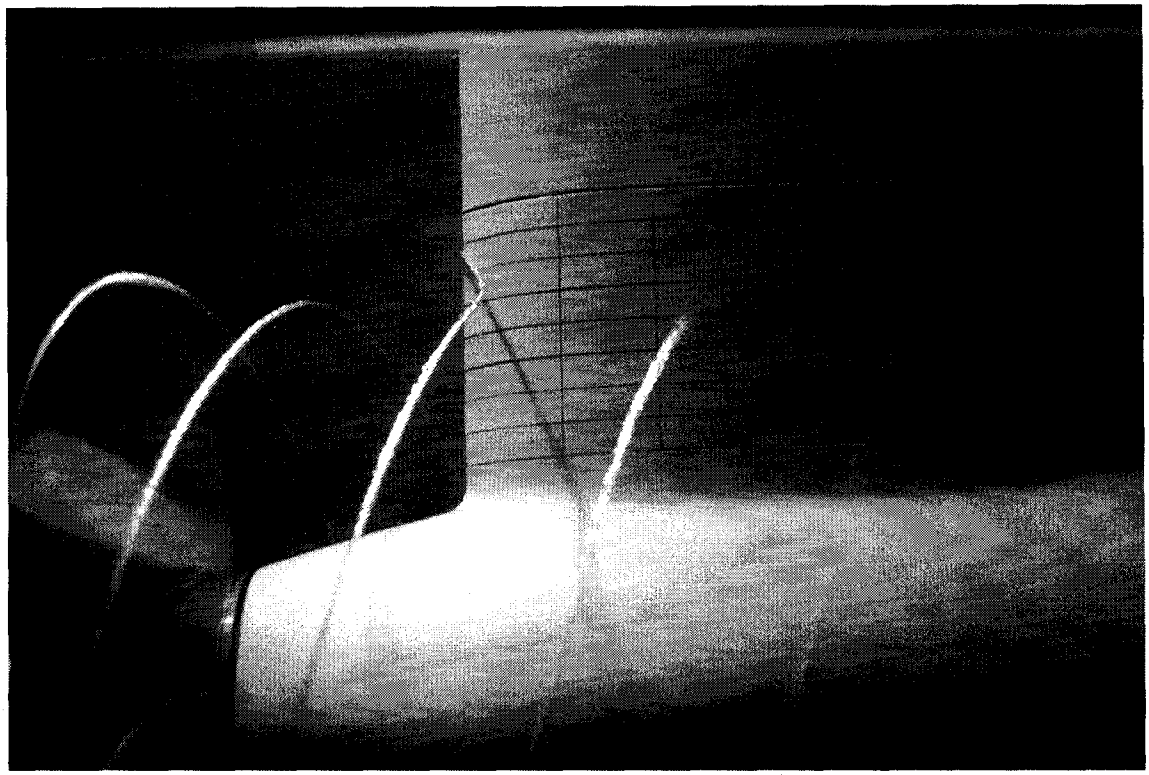

Figure 5.32 Side View of Tip Vortex/Strut Interaction; bend

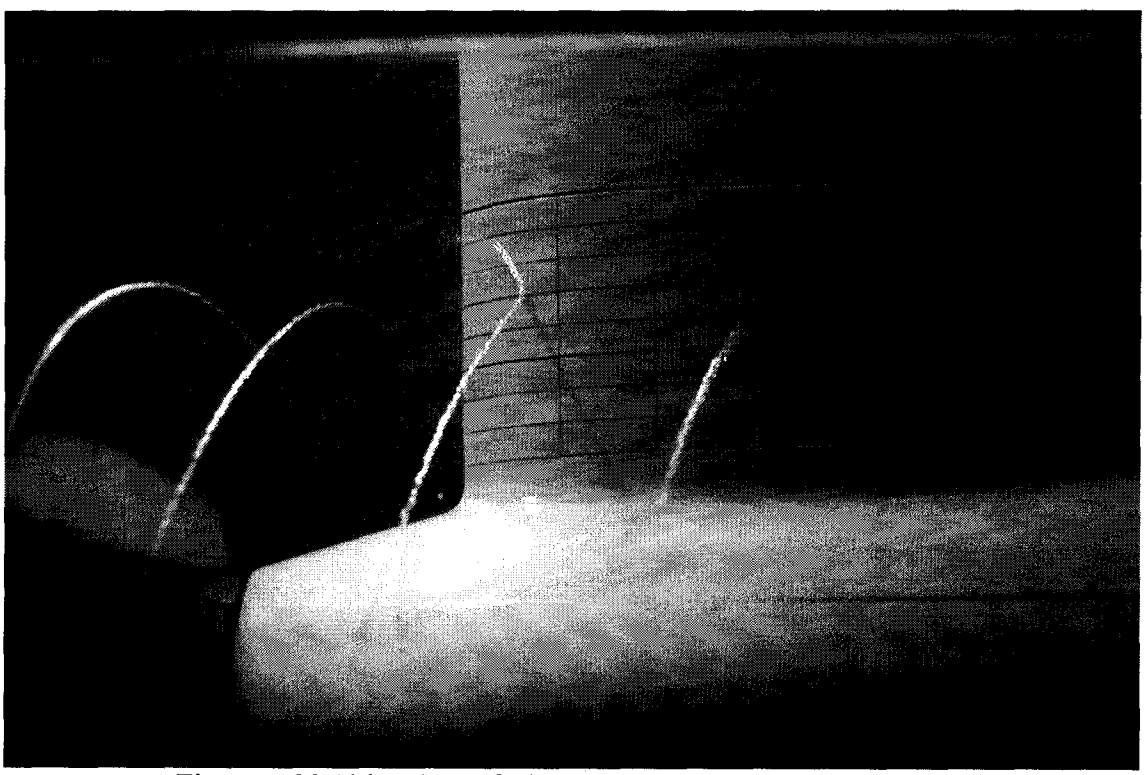

Figure 5.33 Side View of Tip Vortex/Strut Interaction; stretch

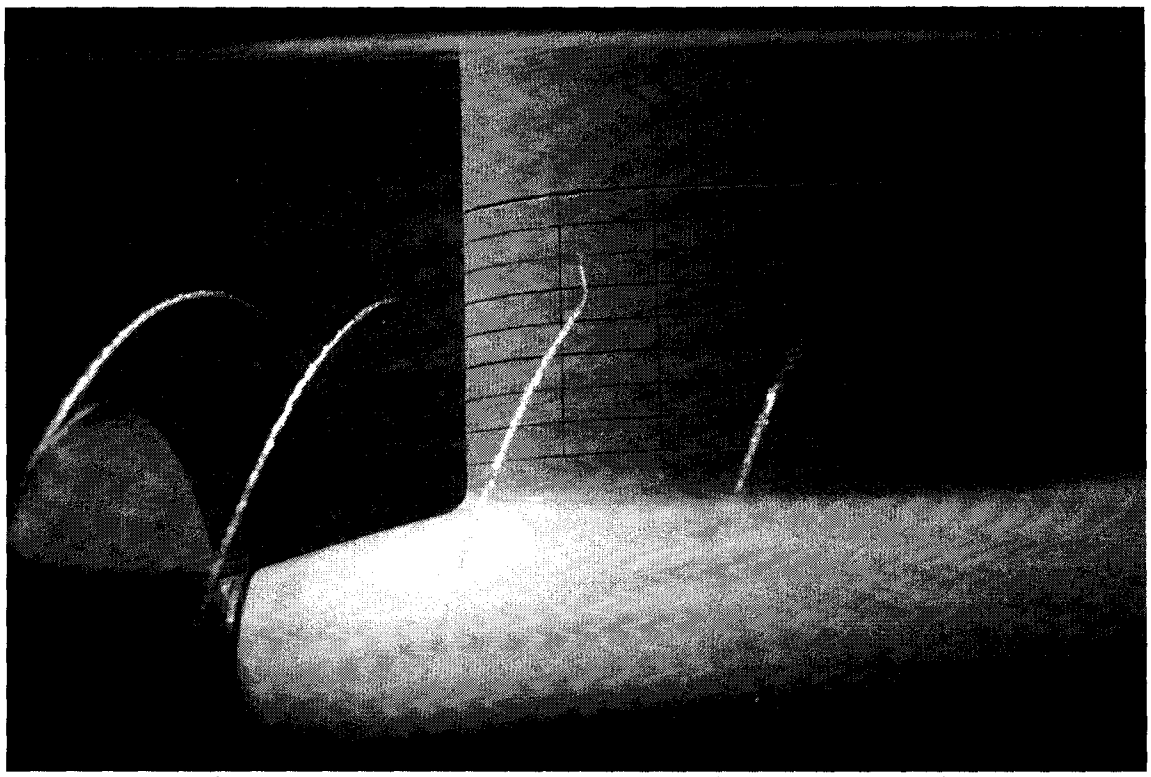

Figure 5.34 Side View of Tip Vortex/Strut Interaction; split

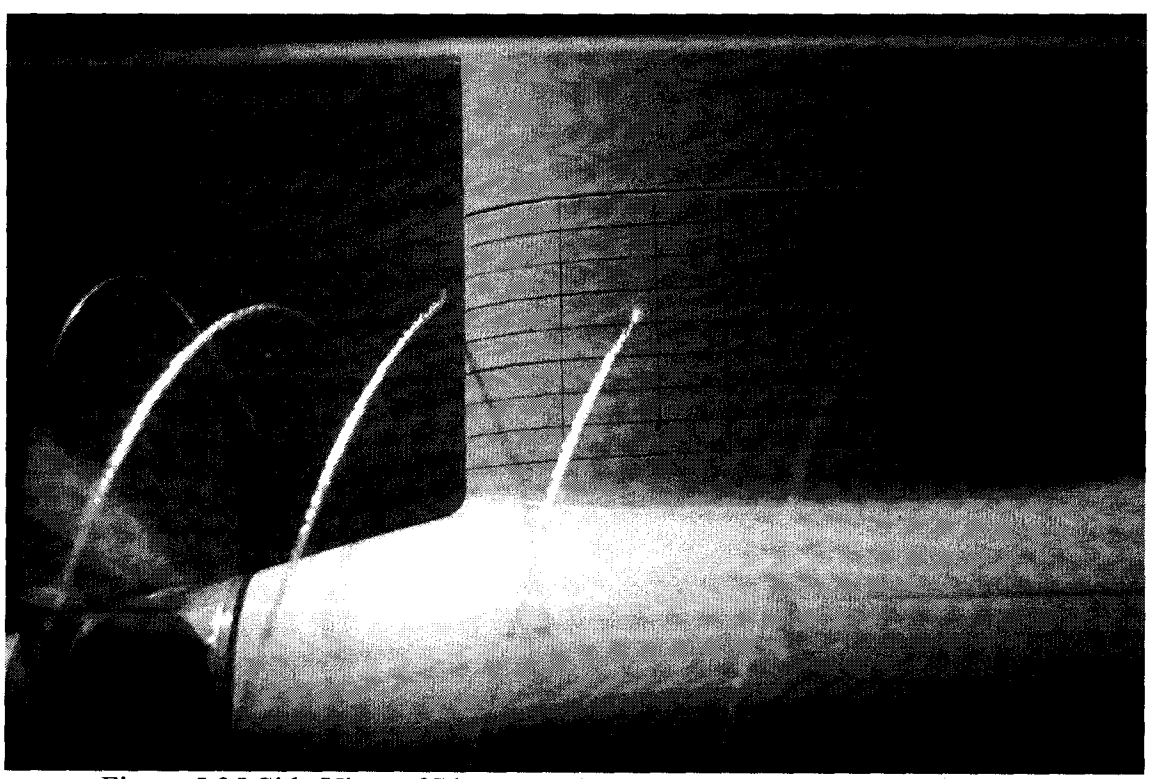

Figure 5.35 Side View of Tip Vortex/Strut Interaction; start the next cycle

5.9 The Pod and Strut Effects on the Propeller Performance

It was found from open water tests that the presence of the pod and strut in the race of the propeller wake affected the propeller performance significantly. Two open water tests of the same propeller were carried out in the cavitation tunnel at the Institute for Ocean Technology. One test was without the pod and another test was with the pod and the strut installed. The flow speed V, propeller rotation speed *rps*, propeller shaft torque Q, and propeller shaft thrust T were measured. These measurements were then presented in non-dimensional coefficients, torque coefficient $K_q = \frac{Q}{\rho n^2 D^5}$, thrust coefficient $K_t = \frac{T}{\rho n^2 D^4}$, and propeller efficiency $\eta = \frac{J}{2\pi}\frac{K_t}{K_q}$. Comparisons of the mean results (time-averaged component) are made in Figure 5.36. It was found that both K_t and K_q increased when the pod and strut were installed in the test. Increases of K_t and K_q grew with the advance coefficient. At the point of $J=0.9$, K_t increased 0.031 and K_q increased 0.0028. The propeller efficiency also increased after the pod and strut were installed. The peak efficiency increased from 71.4% to 81.6% while the advance coefficient for the peak efficiency moved from 0.86 to 0.94.

The increase in the efficiency of the propeller resulted from a larger increase of the propeller thrust coefficient than that of the propeller torque coefficient. The wake impingement contributed very little to the increase of the propeller efficiency since the amplitudes for K_t and K_q of the propeller varied only about 0.01 and 0.02 respectively

(Figure 5.39). The reason may be that the presence of the pod and strut build a higher pressure on the pressure side of the propeller plane.

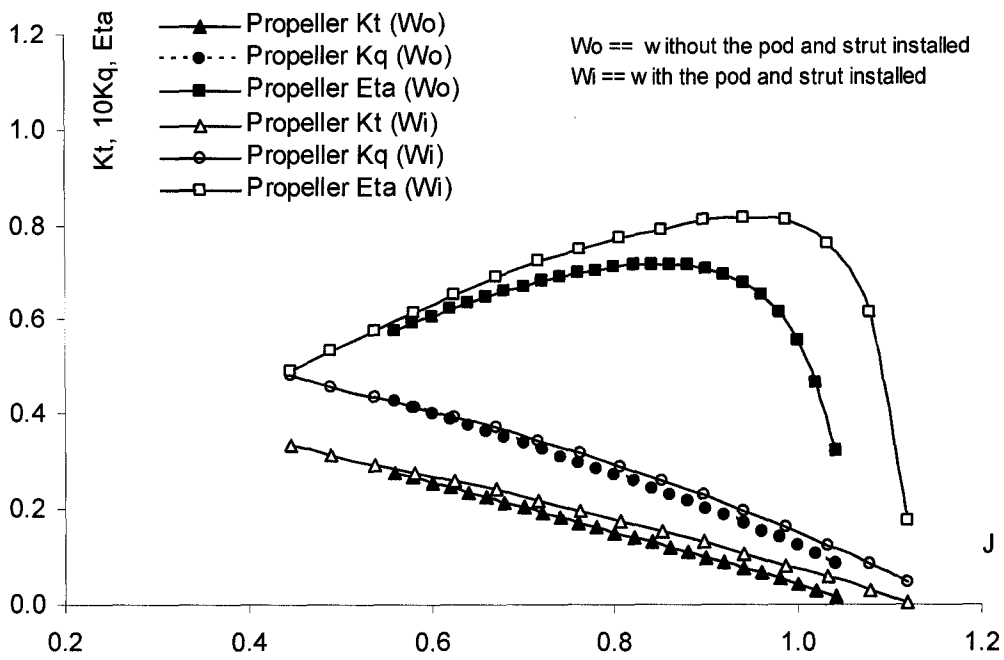

Figure 5.36 Comparisons of the Propeller Performance

The amplitudes of the fluctuations of the propeller shaft forces were not significant. Time varied thrust and torque coefficients for five different advance coefficients of one propeller revolution (processed by phase-average) were plotted in Figure 5.37 and 5.38 respectively. The plots demonstrated that both K_t and K_q change very little in their magnitudes for all advance coefficients. After the variation amplitudes of K_t and K_q were evaluated and plotted in Figure 5.39, ratios of the thrust and torque

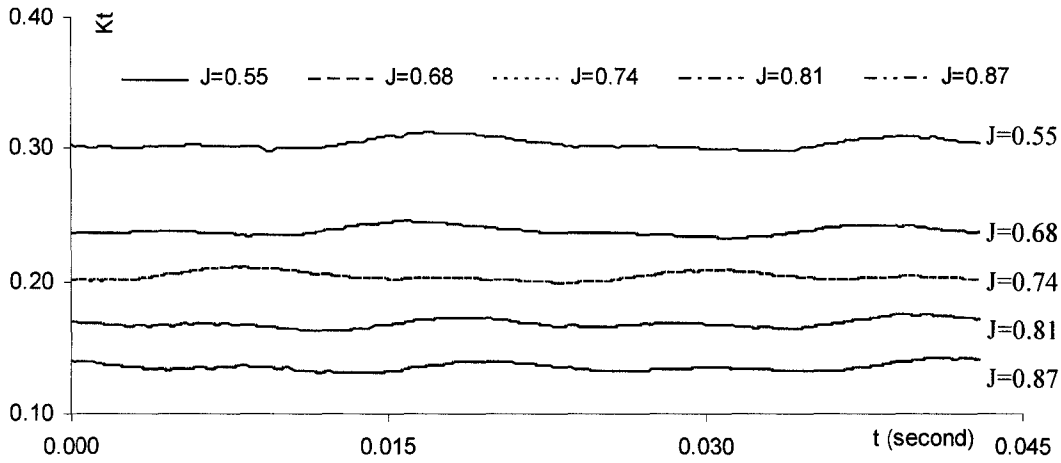

Figure 5.37 Variations of the Propeller Thrust Coefficient

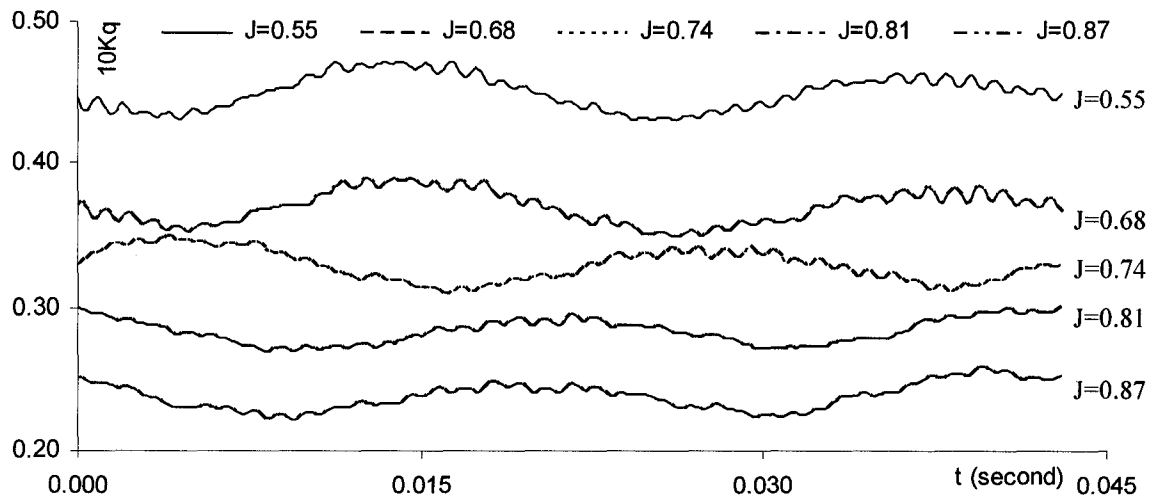

Figure 5.38 Variations of the Propeller Torque Coefficient

coefficients were also drawn in Figure 5.40. The variation amplitude of K_t and K_q in Figure 5.39 are defined as:

$$Amplitude\ (K_t) = \max(K_t) - \min(K_t)$$

$$Amplitude\ (K_q) = \max(K_q) - \min(K_q)$$

Definitions of variation amplitudes and fluctuation ratios of the thrust and torque coefficients in Figure 5.40 are given as following:

$$R_{Kt} = \frac{\max(K_t) - \min(K_t)}{2Average(K_t)} = \frac{Amplitude(K_t)}{Average(K_t)}$$

$$R_{Kq} = \frac{\max(K_q) - \min(K_q)}{2Average(K_q)} = \frac{Amplitude(K_q)}{Average(K_q)}$$

Although the variation amplitude of K_t and K_q decreased with increase of the advance coefficient as shown in Figure 5.39, the fluctuation ratios of thrust and torque coefficients,

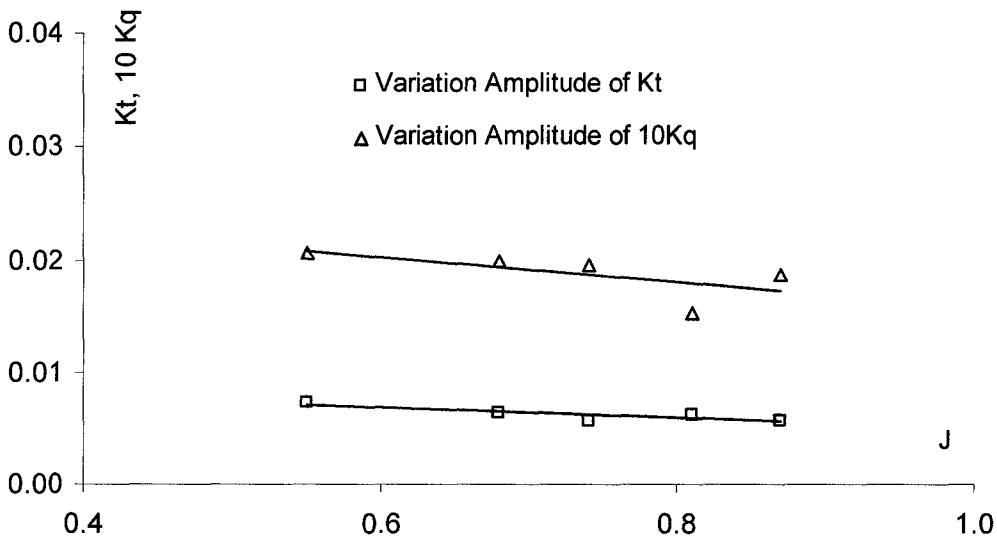

Figure 5.39 Variation Amplitudes of K_t and K_q

as it was shown in Figure 5.40, increased with the increase of the advance coefficient. This indicates that although the fluctuation amplitudes and the time averaged values of K_t and K_q decrease with the increase of the advance coefficient, the decreasing speed of the fluctuation amplitudes are slower than that of the time averaged values.

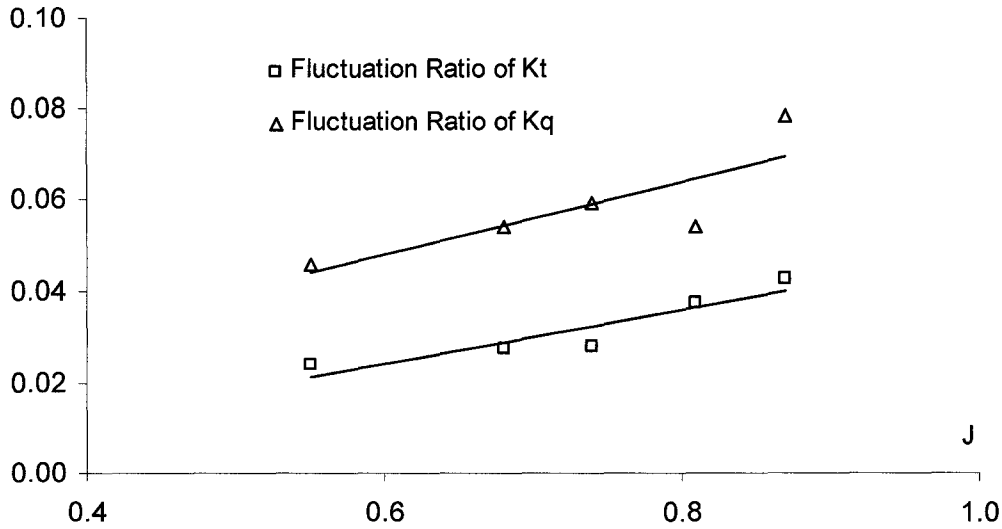

Figure 5.40 Fluctuation Ratios of K_t and K_q

5.10 Summary

A set of time series of pressure distributions on the surface of a strut impacted by tip vortices from an operating propeller has been measured by means of multiple pressure transducers. These measurements can be used in validations of numerical methods and in the assessment of the effects on the pressure and cavitation that are induced by the interaction of the propeller tip vortex and the strut. Based on the pressure measurements and the visual investigation of the tip vortex/strut interaction, the following conclusions can be made:

1. The lowest pressure measured was found to occur on the stretched side near the leading edge near the intersection of the pod and the strut. For a left-handed tractor-type podded propeller, the port side of the strut is the stretched side.

2. For all tested advance coefficients, the largest amplitude of pressure variation was found on the leading edge of the strut around $R_p = 1.0$.

3. In cases of low advance coefficients, the pressure at some of the measurement points on the compressed side demonstrated a double-trough shape within a single period of the vortex filament impacting process.

4. An empirical formula for the tip vortex pitch (Eq. 5.6.1) was obtained which gives input reference information for parameter settings in numerical simulations. Specifically for the wake alignment or initialization of wake locations.

5. Tip vortex nominal diameters estimated by using the pressure measurement results were formulated against the advance coefficient. This result is helpful in the determination of the cut-off value in numerical simulations. Since the inviscid flow

simulation provides only the vortex filament strength, a method to determine the vortex filament radius (cut-off value) is necessary in order to calculate the induced velocity contribution near the filament. Before the method is available the cut-off value in most cases was based on numerical tests.

6. The presence of the pod and strut had almost no effect on the variation amplitudes of the propeller shaft forces.

7. The presence of the pod and strut increased the propeller thrust coefficient by 10% and increased the torque coefficient by 5%. These increases led to a 5% increase in the propeller efficiency.

Chapter 6 Numerical Simulations

Before calculations on podded propellers, numerical simulations with applications of the developed wake impingement model on a simple configuration are conducted. In the simple configuration, a pitching foil, acting as a vortex generator, is located upstream of a stationary foil. The pitching foil is operated by a prescribed function. Lifts on the two foils in tandem are calculated by using a panel method, OSFBEM (Liu, 1996), with and without the wake impingement model. Comparisons on the lift are made among calculations with and without using the wake impingement model as well as the data from surface pressure measurements published by Booth (1986). The comparison on the rear foil lift shows that the panel methods with the wake impingement model give results closer to the experimental data than that without applications of the wake impingement model. Details of the preliminary simulations can be found in a paper by He et al. (2007).

In the rest of this chapter, calculations of a podded propeller using three different wake panel sizes are first described. Results are compared and discussed before a panel size is chosen for further simulations. The comparison and discussion include the thrust and the torque coefficient of the propeller, and the surface pressure coefficient on the pod and strut in terms of distributions of the time-averaged and at an instant. Simulations of the same podded propeller with and without using the wake impingement model are then conducted. Results are compared and discussed to assess how much difference results by introducing the wake impingement model into the simulation. The comparison consists of the blade wake trajectories, the thrust and torque coefficients, and the surface pressure distributions on the pod and strut. To evaluate the effectiveness of the numerical method

with the wake impingement model on the simulation of the pressure on the strut surface, comparisons with experimental data are performed and discussions are made in this chapter as well. As it was found in the experimental study introduced in chapter 5 that the strongest pressure variation was around the leading edge of the strut, comparisons and discussions on the time-varied pressure concentrate along the leading edge. The pressure distribution over the whole measured area on the strut is also compared in terms of the time-averaged components of five different advance coefficients from 0.55 to 0.87. Discussions of possible reasons for the differences between the simulations and the measurements are discussed and followed by suggestions for the further improvement in the simulation method.

6.1 Simulations Using Different Panel Sizes

Three panel sizes, coarse, medium and fine, were used in simulations of a podded propeller. Results of the propeller performance and the pressure patterns on the pod and strut using the three different panel sizes at $J=0.55$ were selected and compared. After a brief discussion of the results, a panel size was chosen for further simulations.

Since the interest was to investigate the panel size effects on the propeller performance and the strut surface pressure induced by the propeller wake, the size changes were made only to the blade wake panels. Combining the changing of the blade panel and the time interval, both radial and circumferential sides of the blade wake panels were changed. The panelized propulsor by three panel sizes are plotted in Figure 6.1 to 6.3 and the panel number distributions are summarized in Table 6.1.

Table 6.1 Summary of Panel Arrangements

	Blade	Hub+Cone	Pod	Strut	No. of	Degrees	Time	Comp
Panel size	Blade no. × radial × chordwise × sides	Blade no. × axial × circular + axial × circular	Axial × circular	Spanwise × Chordwise × sides	Total body panels	of the blade sweep per step	steps per prop. rev.	Time by a PC 1.7GHz 1G RAM
Coarse	4×8×8×2	4×5×8+3×8	30×32	18×16×2	2232	15	24	4.8 hrs
Medium	4×12×12×2	4×5×12+3×12	30×32	18×16×(2)	2964	10	36	21.3 hrs
Fine	4×16×12×2	4×5×12+3×12	30×32	18×16×(2)	3348	7.5	48	33.2 hrs

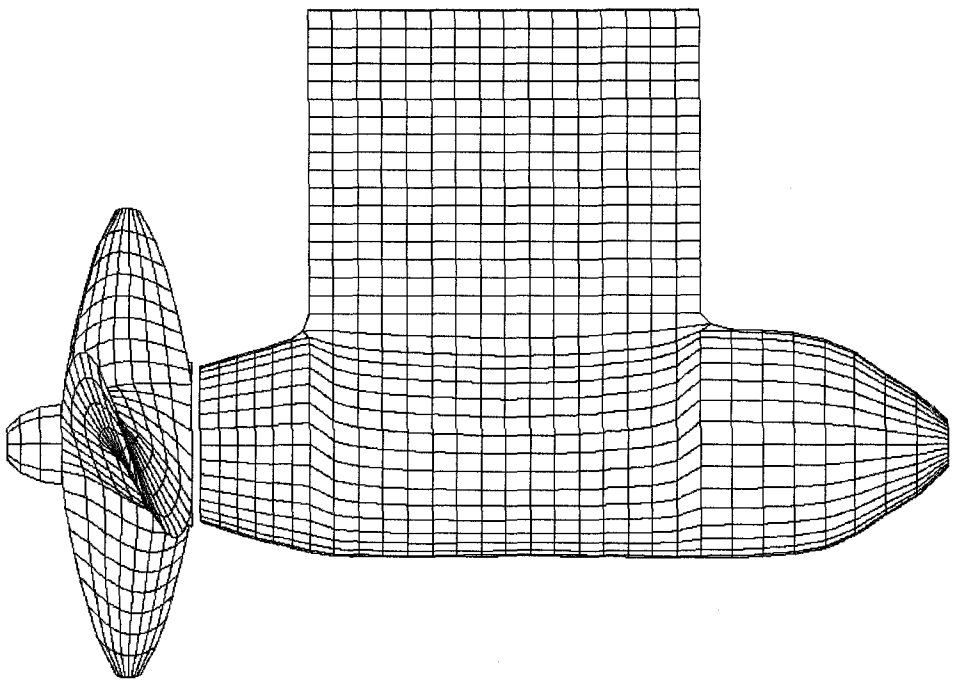

Figure 6.1 Panelized Podded Propeller (coarse)

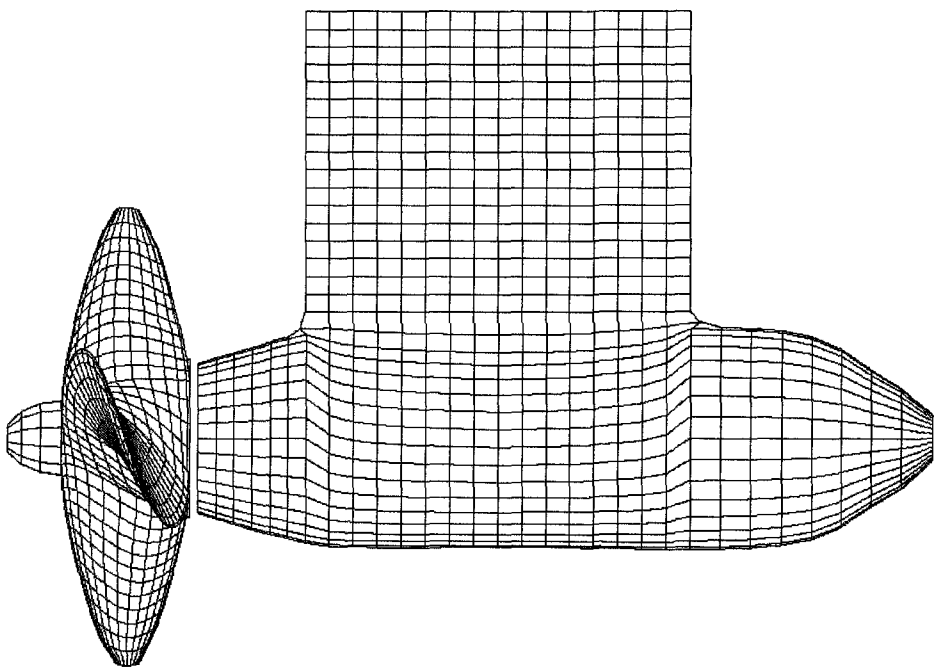

Figure 6.2 Panelized Podded Propeller (medium)

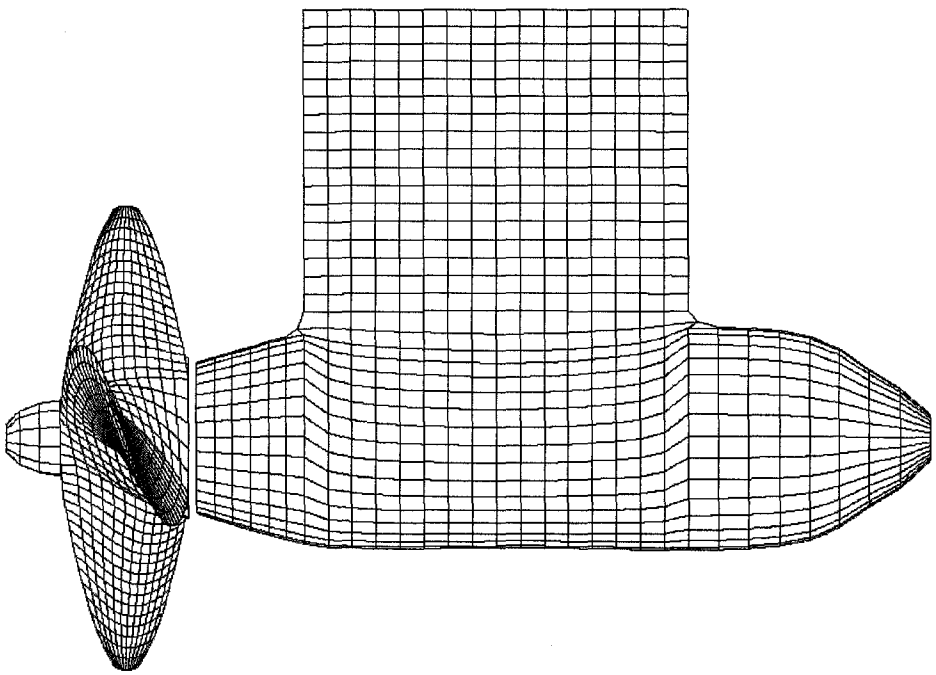

Figure 6.3 Panelized Podded Propeller (fine)

Simulated propeller thrust and torque coefficients of the propulsor by using three different panel sizes are plotted in Figure 6.4. It was found that the two coefficients, propeller K_t and propeller K_q, obtained by using fine panels were the highest, and the coefficients obtained by using coarse panels were the lowest. Coefficients of K_t and K_q increased with the increase of the total number of panels. However, the increases resulting from the change of the panel size from medium to fine were much smaller than those resulting from the panel size change from coarse to medium. Both thrust and torque coefficients obtained using the medium size panel, were almost the same as those obtained using the fine panel size. Their relative differences are all less than 3%. A trend is shown in Figure 6.5 that the calculated K_t and K_q are approaching constants when the

total panel number is larger than 3000. This suggested the medium panel size was fine enough to eliminate significant effects on the propeller thrust and torque coefficients from the panel size used in the simulations.

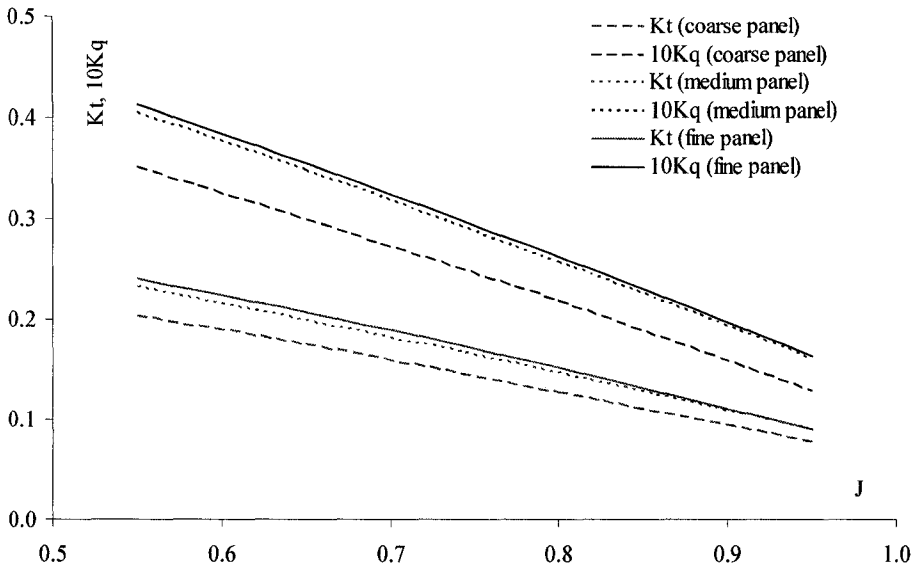

Figure 6.4 Open Water Characteristics Obtained by Using Different Size Panels

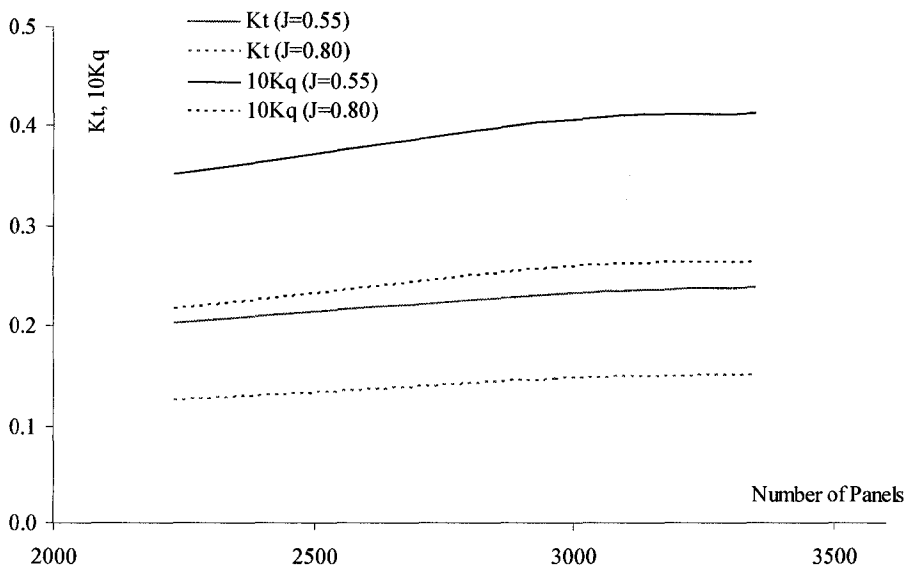

Figure 6.5 Panel Size Effect on Simulated Propeller Performance

Simulated pressure distributions on the pod and strut using three different panel sizes are shown in Figure 6.6, 6.7 and 6.8. The advance coefficient for these three simulated cases was 0.55. These pressure distributions were time-averaged over the last

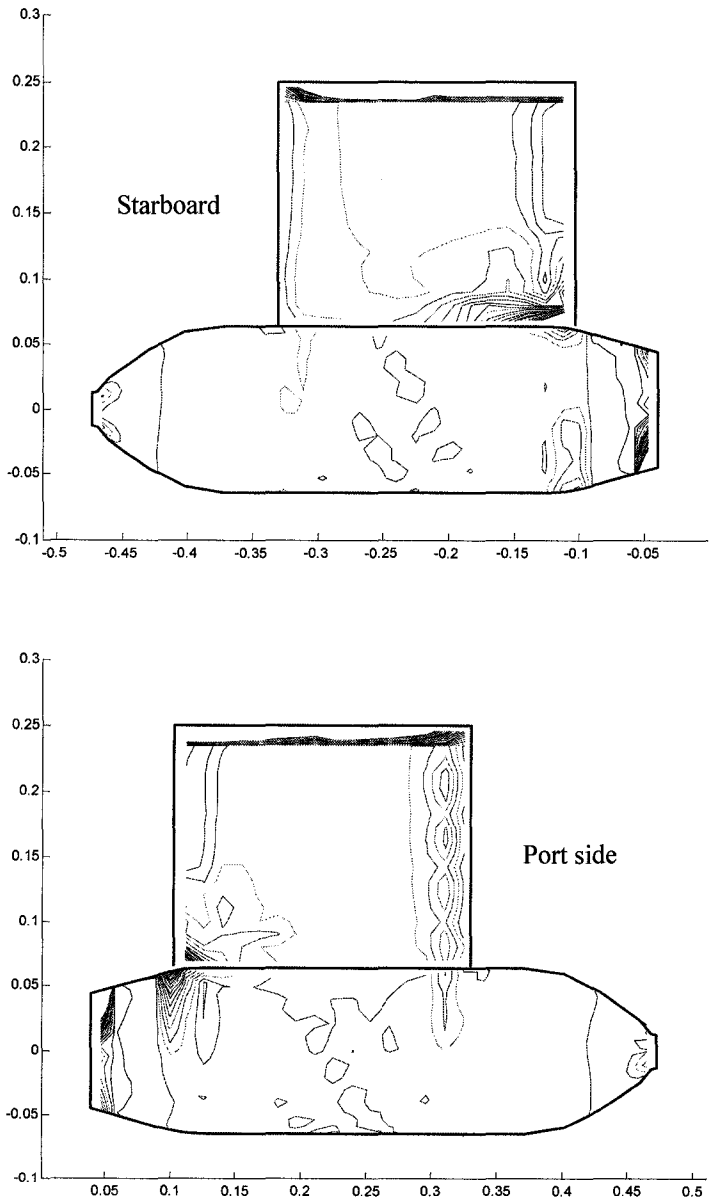

Figure 6.6 Time-Averaged Pressure Distribution *J=0.55* (coarse panel)

revolution of the simulations. Most simulations needed four revolutions and some others (low J) needed five or more revolutions to carry out results without significant difference from the blade wake truncation. In the case of using a coarse panel, the pressure

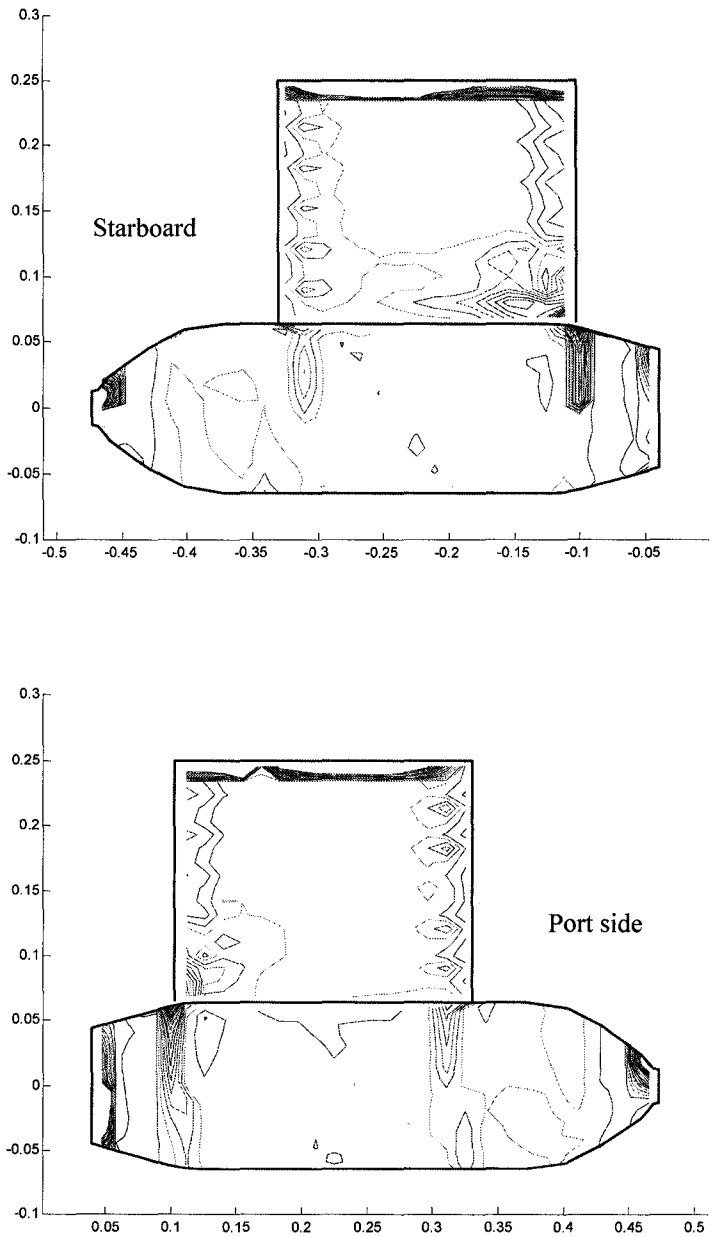

Figure 6.7 Time-Averaged Pressure Distribution $J=0.55$ (medium panel)

distribution was obtained by averaging the pressure distributions of the last 24 time steps. For cases using medium and fine panels, the time steps were increased to 36 and 48 respectively. All of these pressure patterns captured the main characteristic that was

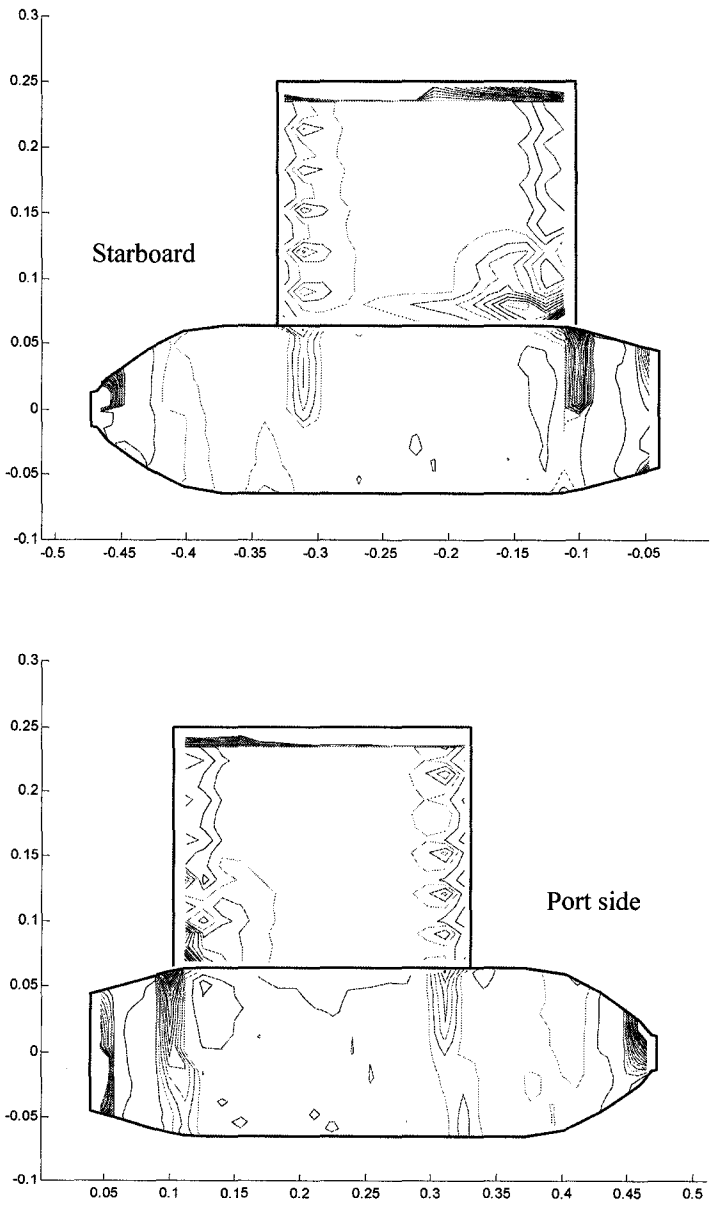

Figure 6.8 Time-Averaged Pressure Distribution *J=0.55* (fine panel)

found in the pressure measurement, two low pressure pockets were located on the two sides of the strut near the junction of the leading edge and pod. However, the pattern from the fine panels demonstrated more similarities with the pattern using the medium panels than that using the coarse panels. For example, the pocket size of the large pressure gradient on the pod near the strut leading edge simulated by using fine panels and by using medium panels was similar, while those simulated by using coarse panels were much smaller. There were not many pockets in the middle of the pod for both simulations using fine and medium panels while the simulation using coarse panels showed several big pockets there. On the surface of the strut, all pressure patterns obtained by using fine panels and medium panels were almost the same. Comparing the result using the coarse panels with the others it was found that the size and the shape of the low pressure pockets near the junction of the pod on the strut starboard side were different. This indicated that the medium and fine panels were fine enough while the coarse panel was not enough to eliminate significant effects on the time-averaged pressure pattern.

The pressure distributions calculated by using the three different panel sizes at an instant are demonstrated in Figure 6.9 to 6.11. All three patterns were taken at the same propeller blade angle, four revolutions after the propeller started to rotate from the initial position. There were lots of details of the pressure distribution in the simulated results. The most significant characteristics were the helical strips of the pressure distribution on the pod surface and two low pressure pockets on the strut's sides near the leading edge and around the junction with the pod. In general, the pressure distribution on both the pod and the strut showed more in common between results using medium and fine panels than

those using coarse panels. To quantify the difference of the pressure distribution led by using different size panels, three parametrical pressures were selected for comparison. They were the area-averaged, the maximum of 95% coverage, and the minimum

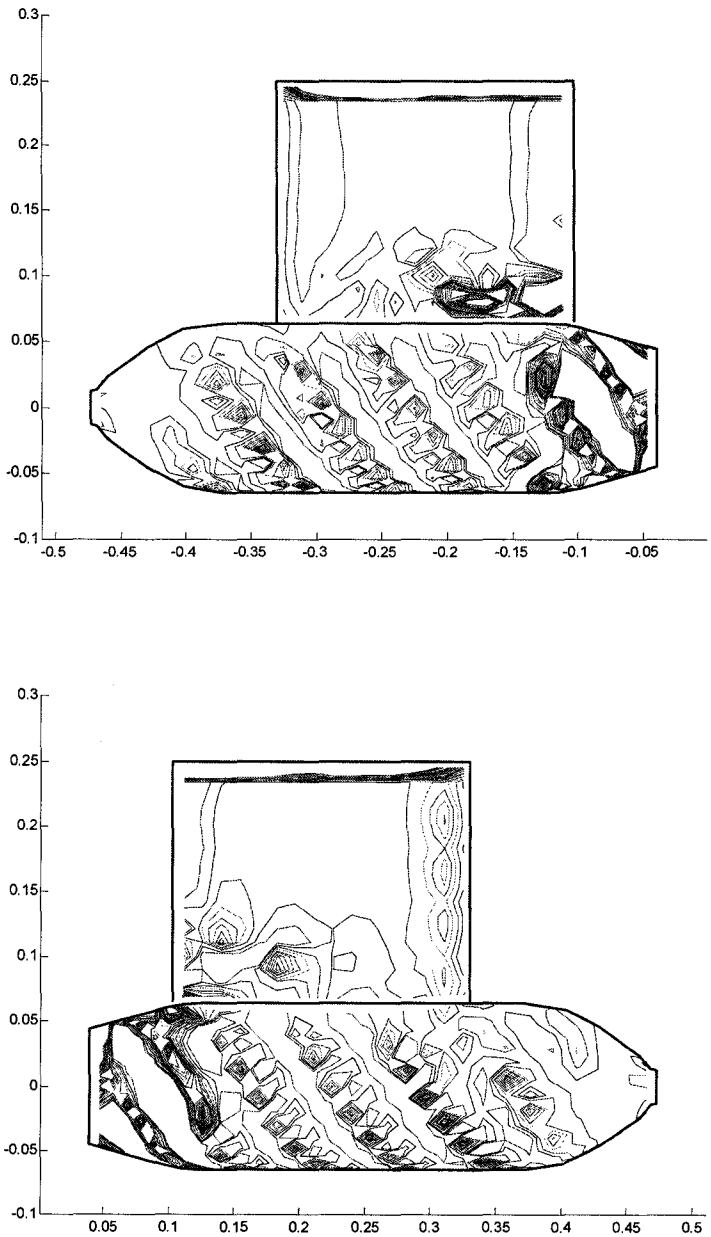

Figure 6.9 The Pressure Distribution at One Instant $J=0.55$ (coarse panel)

of 95% coverage of the pressure over the surface of the pod and strut. The reason of using 95% coverage maximum and minimum to represent the maximum and the minimum pressure over the surface is to eliminate the effect from unavoidable numerical

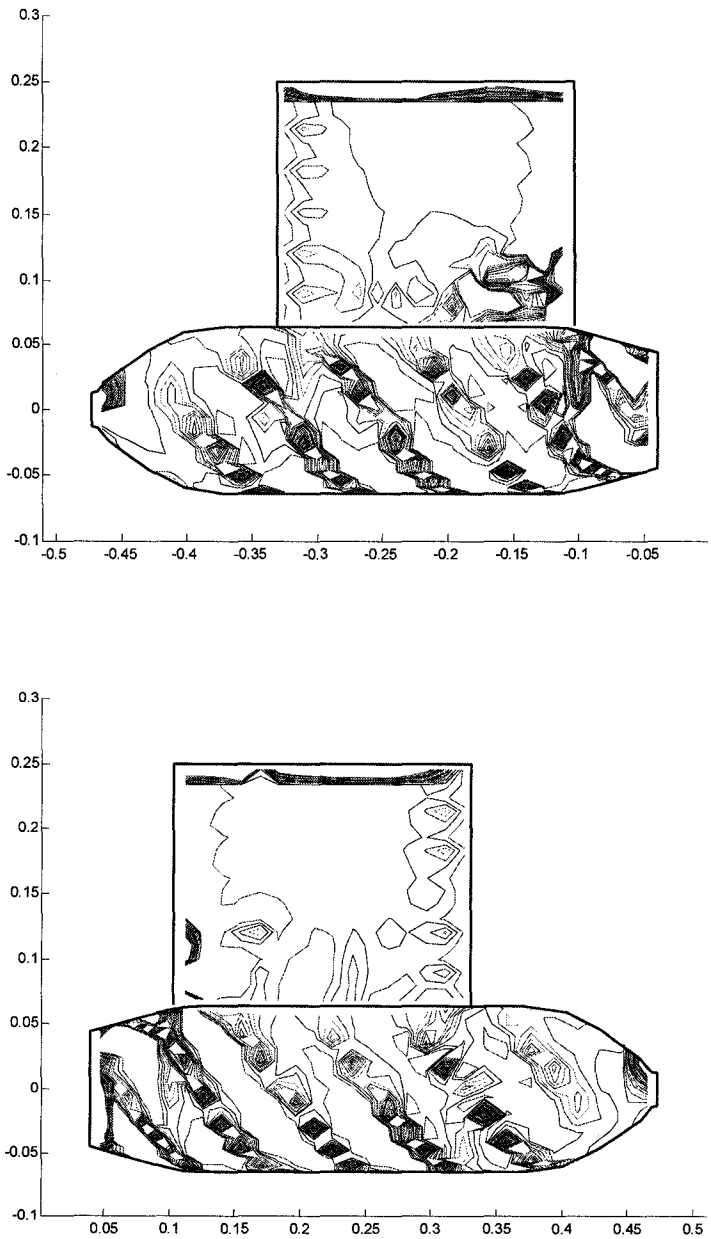

Figure 6.10 The Pressure Distribution at One Instant $J=0.55$ (medium panel)

disturbance to the pressure on some panels. The maximum pressure of 95% coverage is defined as the lowest pressure in the top 5% highest pressure over the pod and strut surface, and the minimum pressure of 95% coverage is defined as the highest pressure

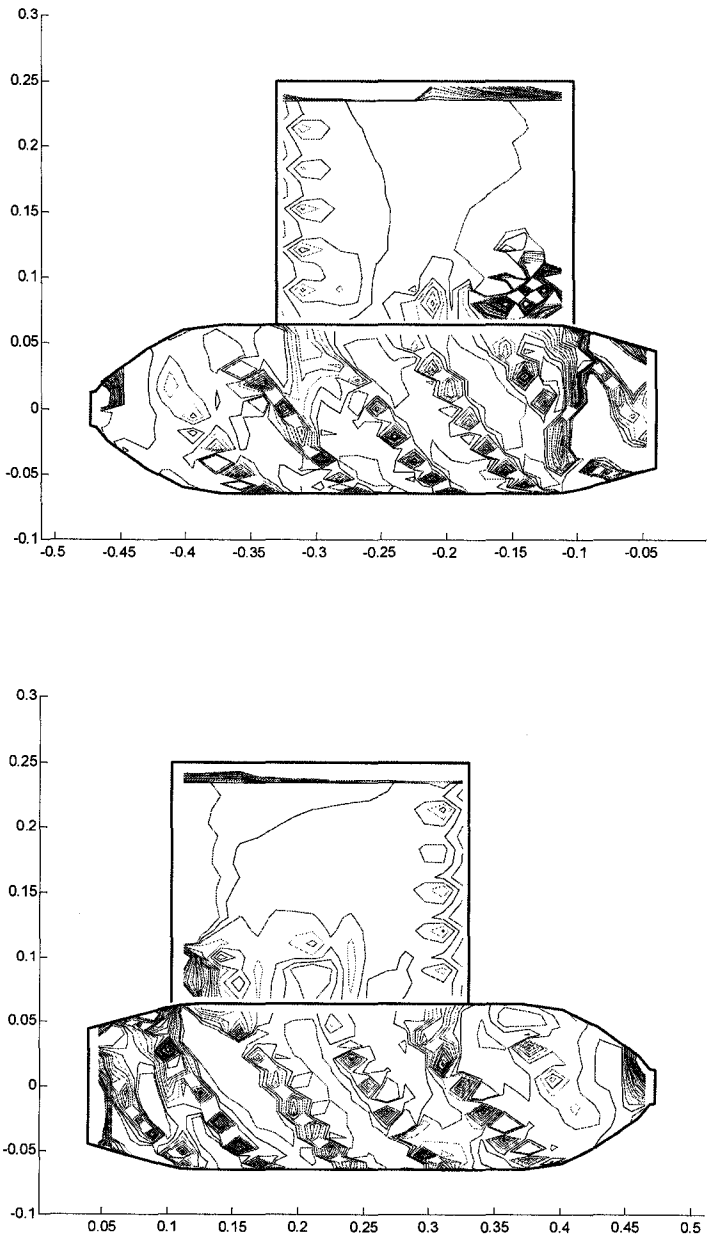

Figure 6.11 The Pressure Distribution at One Instant *J=0.55* (fine panel)

in the 5% lowest pressure over the pod and strut surface. It is indicated in Figure 6.12 that the simulated area-average, the maximum and the minimum of 95% coverage pressure over the pod and strut surface change very little when the total panel number increases from 2964 to 3348. All these changes are less than 5% relative to their simulated values by using 2964 panels. This implies that the panel size effect on the pressure distribution should not be significant when the medium or the fine panel is used.

From the comparisons of the simulations using the three different sizes of blade wake panels, coarse, medium, and fine, a conclusion was made that the medium panel was fine enough to eliminate significant effects. These effects included the propeller thrust and torque coefficients, static and dynamic pressure distributions on the pod and strut.

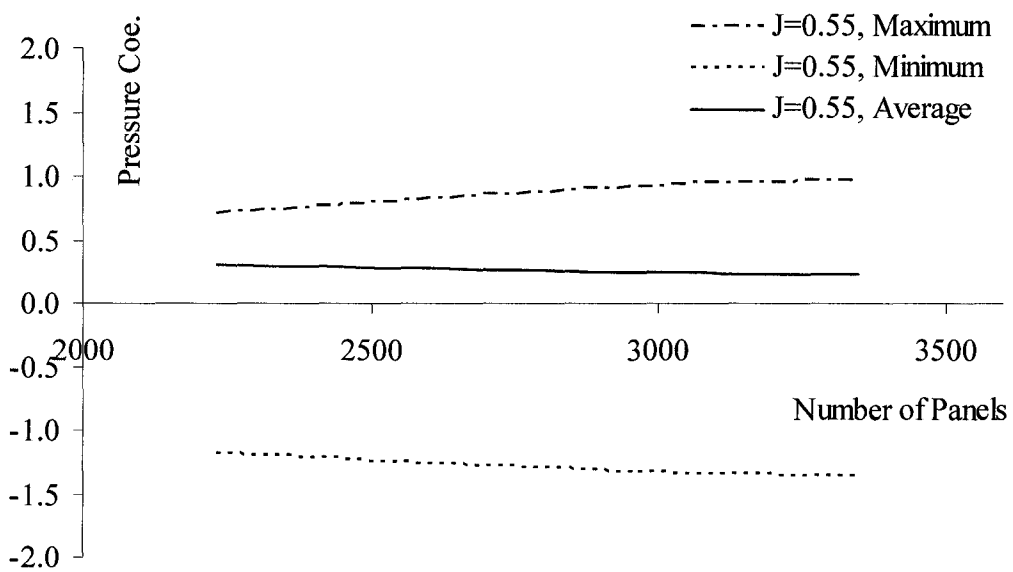

Figure 6.12 Panel Size Effect on Simulated Propeller Performance

6.2 Simulations with and without Wake Impingement Model

Simulations of the podded propeller with and without using the wake impingement model were conducted, and results were compared to evaluate the effects of the wake impingement model on the simulation of the blade wake, propeller performance, and the pressure variations on the pod and the strut surfaces.

For most potential flow based lifting surface methods, the deformation of the blade wake due to wake impingement is not properly considered. Therefore, the wake geometry after the collision with a body in the propeller race might not have been realistically presented and some hydrodynamic properties, such as the pressure and force fluctuations on the afterbody might not be accurately predicted. When they are applied to a tractor type podded propeller, the influence of the part of the blade wake that originally goes through the pod and strut as shown in Figure 6.13 (upper) has been cancelled in the work by Liu and Bose (2001) or artificially reduced in the work by Chen and Williams (1987). The blade wake simulated by the panel code with wake impingement model is shown in Figure 6.13 (lower). The wake panels that have a tendency to go through the body surface have been diverted to pass around the body. The continuous helical wake sheet has been cut into pieces, forming a set of spring washer shaped wake sheets (Figure 6.13) after it passes the strut. The blade wake simulated by using the wake impingement model appears to be more realistic.

The simulated propeller open water characteristics with and without using the WIM are plotted in Figure 6.14. The propeller thrust coefficient, $K_t = T/\left(\rho n^2 D^4\right)$,

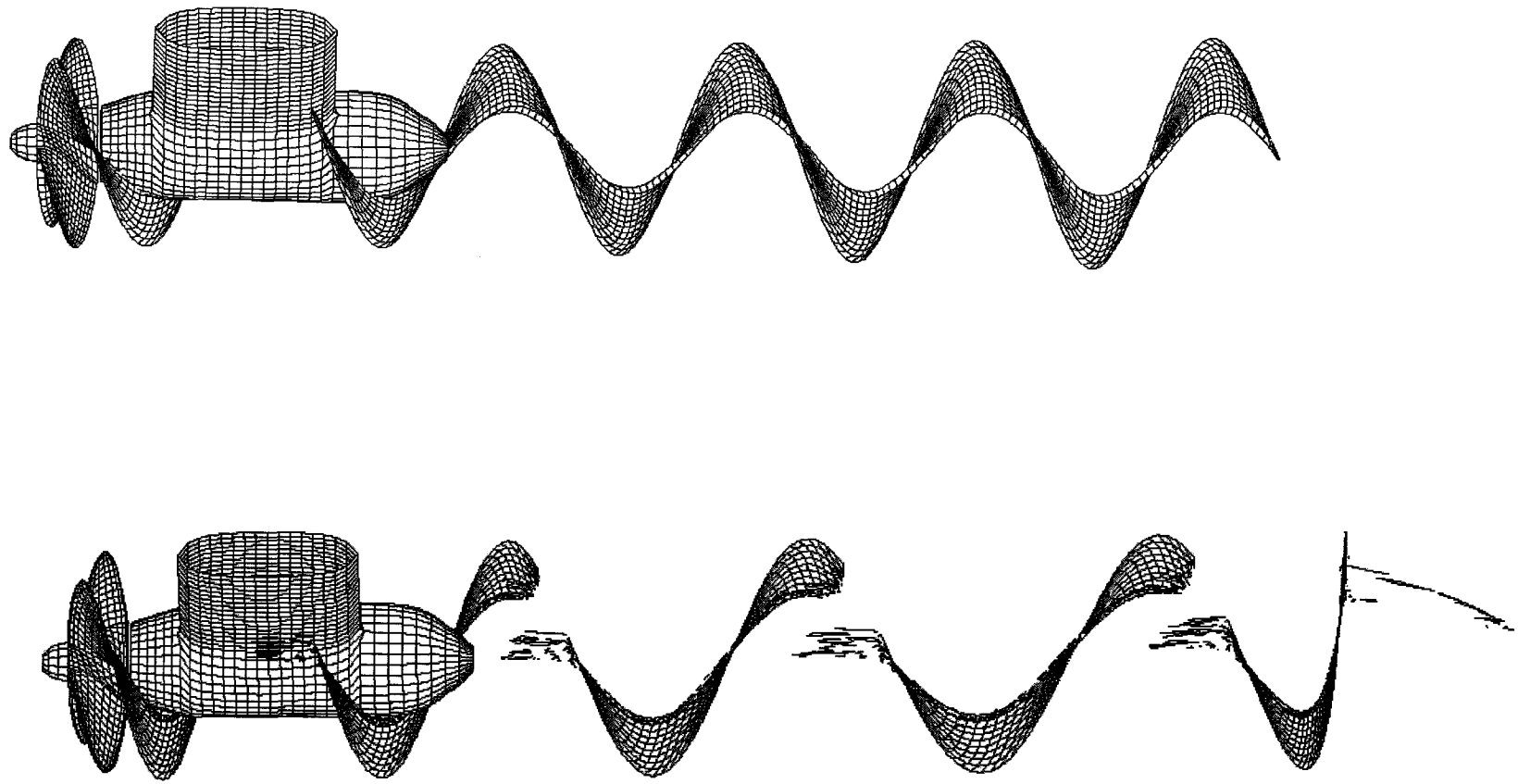

Figure 6.13 Simulated Blade Wake without WIM (upper) and with WIM (lower) for $J = 0.81$

simulated with the wake impingement model was around 1% lower than that simulated without using the wake impingement model. The difference decreased as the advance coefficient increased. Comparing the simulated torque coefficients, $K_q = Q/\left(\rho n^2 D^5\right)$, with and without the WIM shows that they intersected each other. The intersection point is around $J = 0.8$. The simulated K_q using the WIM was lower than that without using the WIM when $J < 0.8$. For $J >= 0.8$, the simulated K_q using the WIM was higher than that without using the WIM. The differences of both K_t and K_q all over the range of the advance coefficient from 0.55 to 0.95 were very small, not higher than 2%.

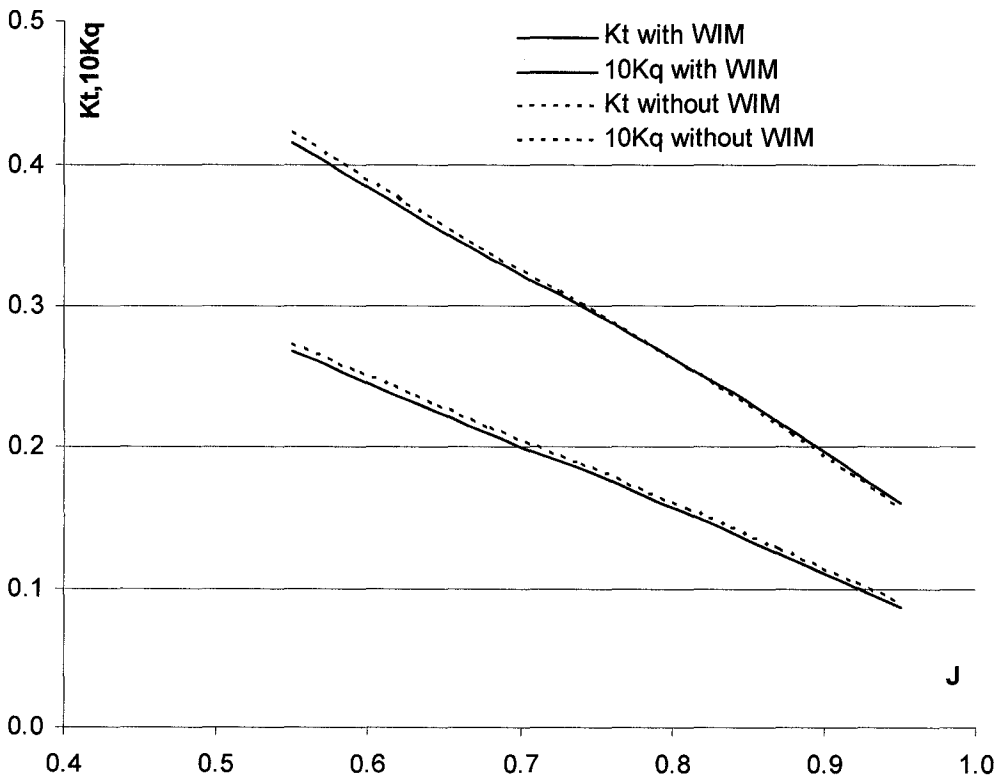

Figure 6.14 Open Water Characteristics with and without Using of the WIM

The above comparisons show that there was no significant difference found in the propeller thrust coefficient and the torque coefficient between simulations with and without using the WIM. This indicates that the use of the WIM had little influence on the propeller performance prediction.

Pressure distributions on the pod and strut surface at an instant by the panel code with and without using the WIM are compared in Figure 6.15. The simulated distribution by the panel code using the WIM shows more variations than that without using the

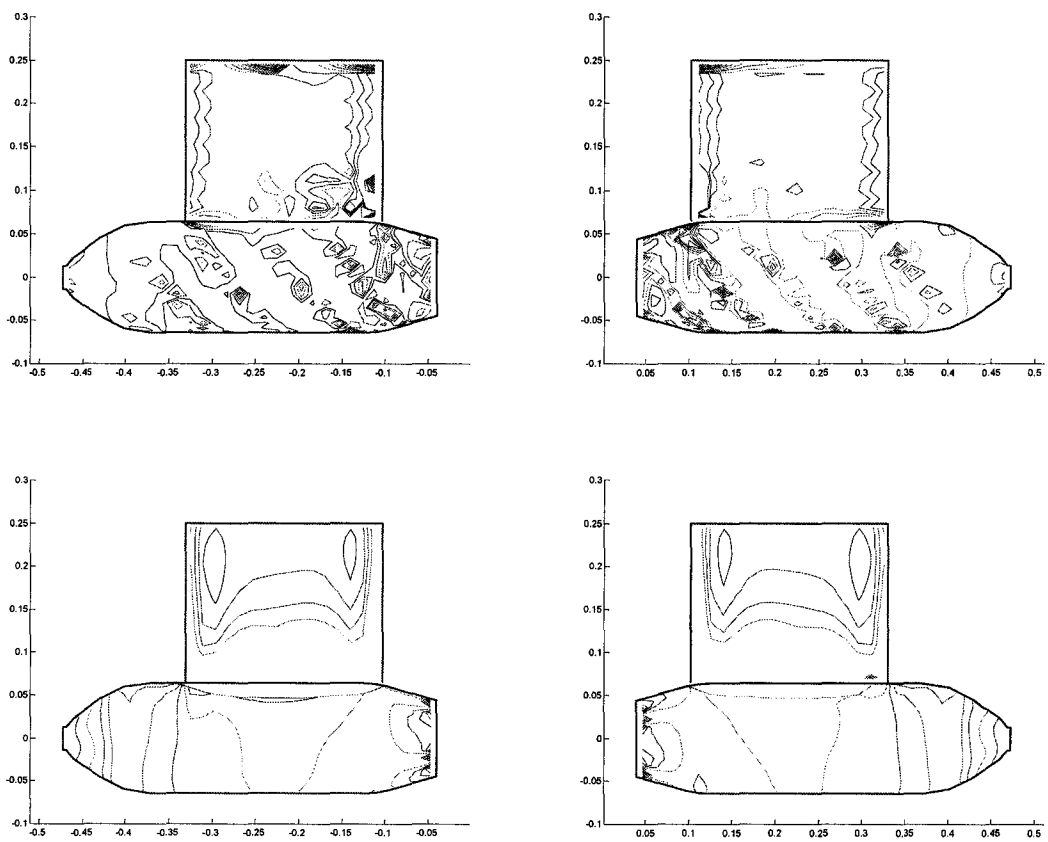

Figure 6.15 Simulated Pressure Distributions with/without WIM at an Instance
istep=144, 36 steps/revolution, blade phase angle = 0°
upper left – with WIM, star; upper right – with WIM, port;
lower left – without WIM, star; lower right – without WIM, port

WIM did. For example, the pressure variation of the helical strips on the pod induced by the blade root vortex and the large pressure gradient around the leading edge of the strut are not shown in the result without using the WIM while they do in the result with using the WIM. Although the pod surface has not been included in the surface pressure measurement, the pressure measurement on the strut surface in chapter 5 shows the large pressure gradient and high pressure variation around the leading edge. Comparisons of these details on the pressure distributions with experimental data are made in the following section.

6.3 Pressure Variation on the Leading Edge

As described in Chapter 5, there were eight positions along the strut leading edge where surface pressures were measured at five different advance speeds. Simulated pressure variations on the strut leading edge are compared with the measurements and are discussed in this section. Calculated pressures at the locations of the measurement were interpolated from the pressures at the panel centers. Comparisons for the five different advance coefficients are made in Figure 6.16 to 6.20 respectively.

It is shown in Figure 6.16 that amplitude of the pressure variations from both the measurement and the numerical simulation are large near $Z/R_p = 1.00$ when the propeller is heavy loaded, $J = 0.55$. The means of the simulated pressure for $Z/R_p = 0.99$, $Z/R_p = 1.07$, and $Z/R_p = 1.14$ were found to be close to the measurements. However, simulated pressure means for these $Z/R_p <= 0.92$ were under predicted around 0.23 referring to the measurements. Comparing with the experimental results the amplitude of the pressure fluctuation at $Z/R_p = 0.99$, the result was under-predicted by 0.60 or 57% while these for $Z/R_p = 0.84$, and $Z/R_p = 0.77$ were over-predicted by 55%. The troughs of the pressure variation at $Z/R_p = 0.99$ were well modeled while the peaks were not. The simulated pressure variation pattern at $Z/R_p = 1.07$ was close to that of the measurement. The simulated amplitude was only 4% higher than that by the experiment and the time-averaged pressure by the simulation was 0.15 or 12% higher than measurement. In spite of these differences, experimental

and numerical results show a similar sketch of a peak between two troughs that represent a cycle of a blade wake impingement. The calculated and the measured pressure variations at $Z/R_p = 1.14$ in Figure 6.16 are almost exactly the same. The reason is potential flow-based panel methods work better in the area with weak viscous effect ($Z/R_p >= 1.14$) than in the area with strong viscous effect. The flow in the race of the blade wake and the vicinity of the pod and strut is considered to be highly vortical. In addition to this, it was also found in Figure 6.16 that all simulated pressure coefficients within $Z/R_p \leq 0.92$ were under-predicted by about 0.3. In general, potential flow-based

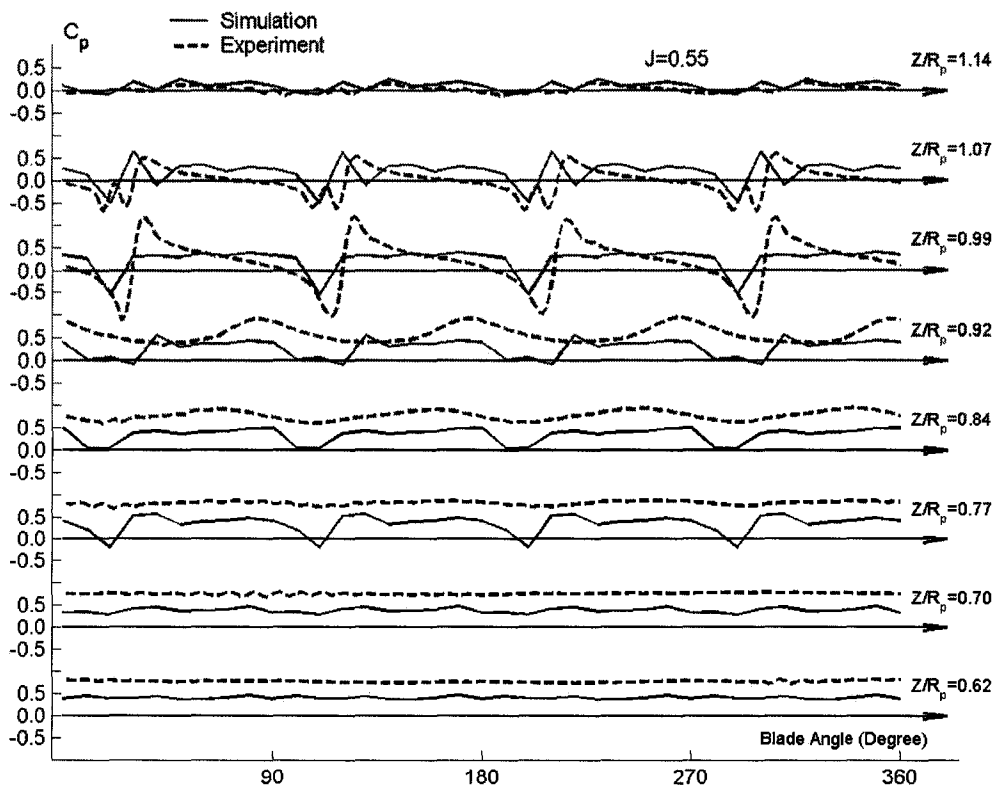

Figure 6.16 Comparison of the p on the L.E. (*J=0.55*)

methods over-predict the velocity, hence under-predict the pressure in the vicinity of a solid boundary. These imply that including the viscous effect may lead to improvements on the precision of the present method in the area near the pod and strut.

The calculated pressure means on the leading edge for $J = 0.68$ in Figure 6.17 were also found to be about 0.3 lower than the corresponding measurements for these positions of $Z/R_p <= 0.84$, but for other locations of $Z/R_p >= 0.92$ the calculated results were close to the measurements. Both the simulated and the measured pressures at $Z/R_p = 1.14$ were around zero. The means of calculated pressure for the vertical distance

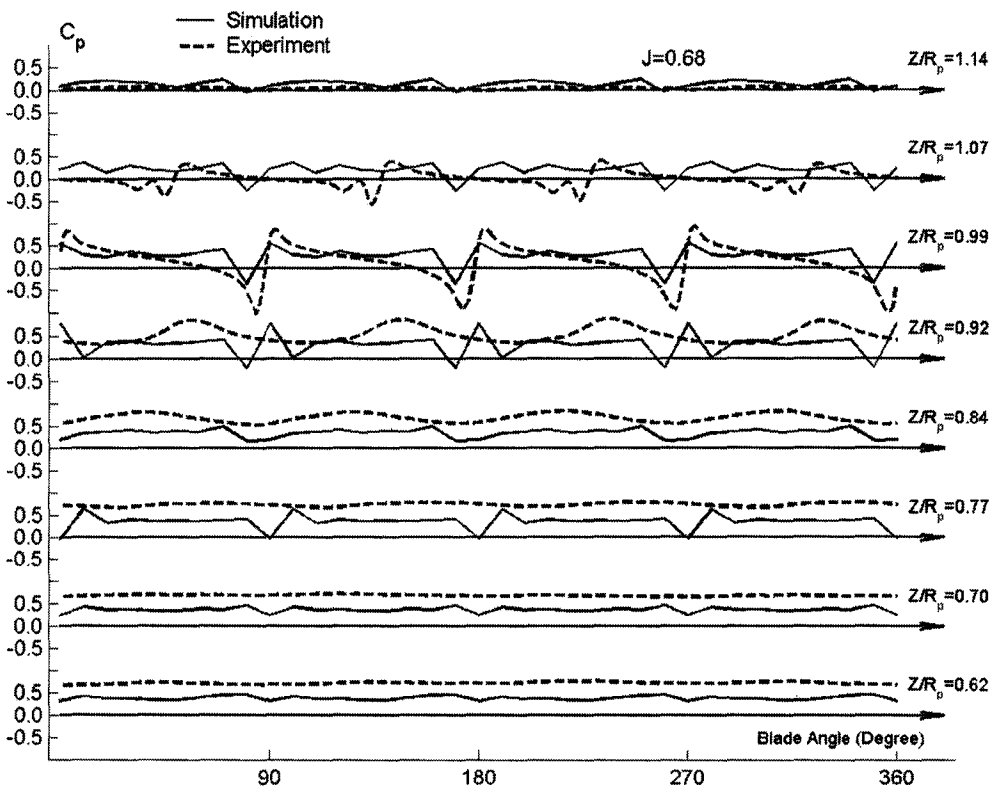

Figure 6.17 Comparison of the p on the L.E. (*J=0.68*)

Z/R_p of 1.07 and 0.99 were larger than the measurements by 0.2 and 0.1 respectively. At the location of $Z/R_p = 0.92$, the simulated mean was 0.3 lower than that of the experiment. The amplitudes of the pressure variation calculated at $Z/R_p = 0.77$ and 0.92 were about 0.25 higher than those of the measurements. However, the simulated amplitude at $Z/R_p = 0.99$ was lower than the measurement by 0.44. The predicted amplitudes at $Z/R_p = 1.07$, 0.92, and 0.84 were very close to the experimental results.

Similar to the two comparisons made above, both measured and simulated pressure variations along the strut leading edge were plotted in Figure 6.18. The

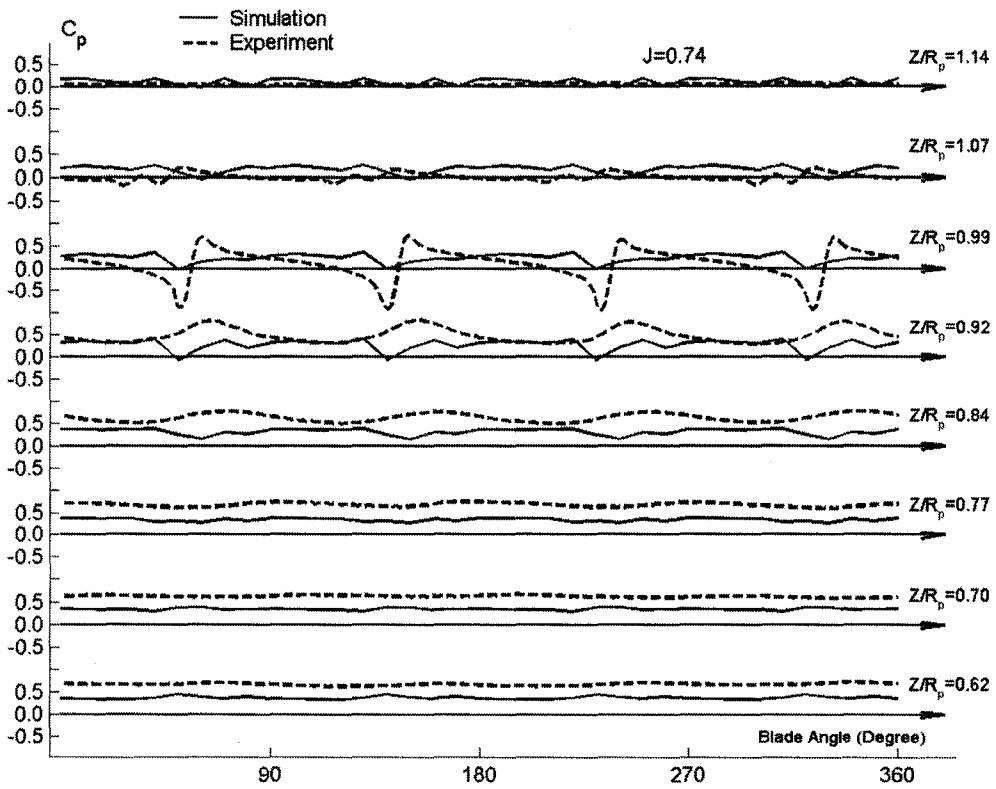

Figure 6.18 Comparison of the p on the L.E. (*J=0.74*)

differences between calculations and measurements at $Z/R_p = 0.77$, $Z/R_p = 0.84$ and $Z/R_p = 0.92$ were comparatively smaller than those in Figure 6.16 and Figure 6.17. It indicated that the simulation method gives better result for moderate advance coefficient than for low advance coefficient.

Comparisons of the pressure variations between the calculations and the measurements for $J = 0.81$ and 0.87 were made in Figure 6.19 and 6.20 respectively. It was noted that the differences between the experimental and the theoretical results at

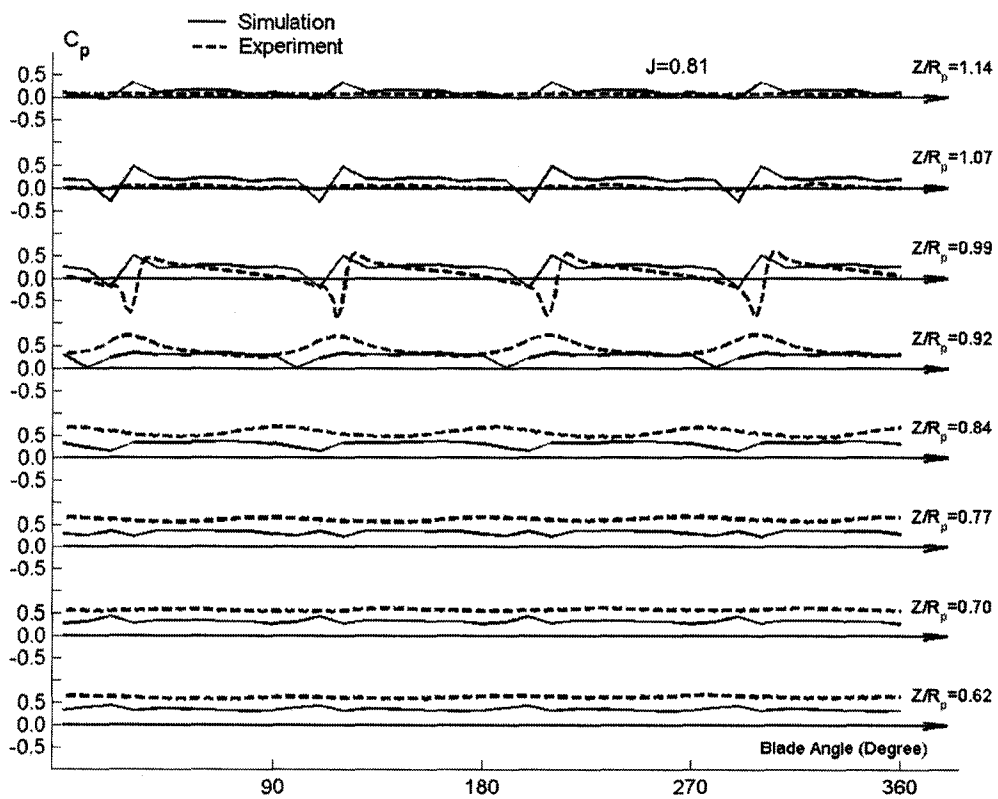

Figure 6.19 Comparison of the p on the L.E. (*J=0.81*)

these two high advance coefficient conditions were smaller than those at the low advance coefficient conditions. The difference between simulations and measurements dropped from around 0.3 at $J = 0.55$ to less than 0.2 at $J = 0.87$. Although the amplitude of the phase-averaged components was still under-predicted compared to the measurement, the differences had also been reduced significantly. For example, the amplitude difference at $Z/R_p = 0.99$ dropped from 0.60 at $J = 0.55$ to 0.24 at $J = 0.87$. In the case of $J = 0.87$ all simulated results were very close to the measurements except the amplitudes

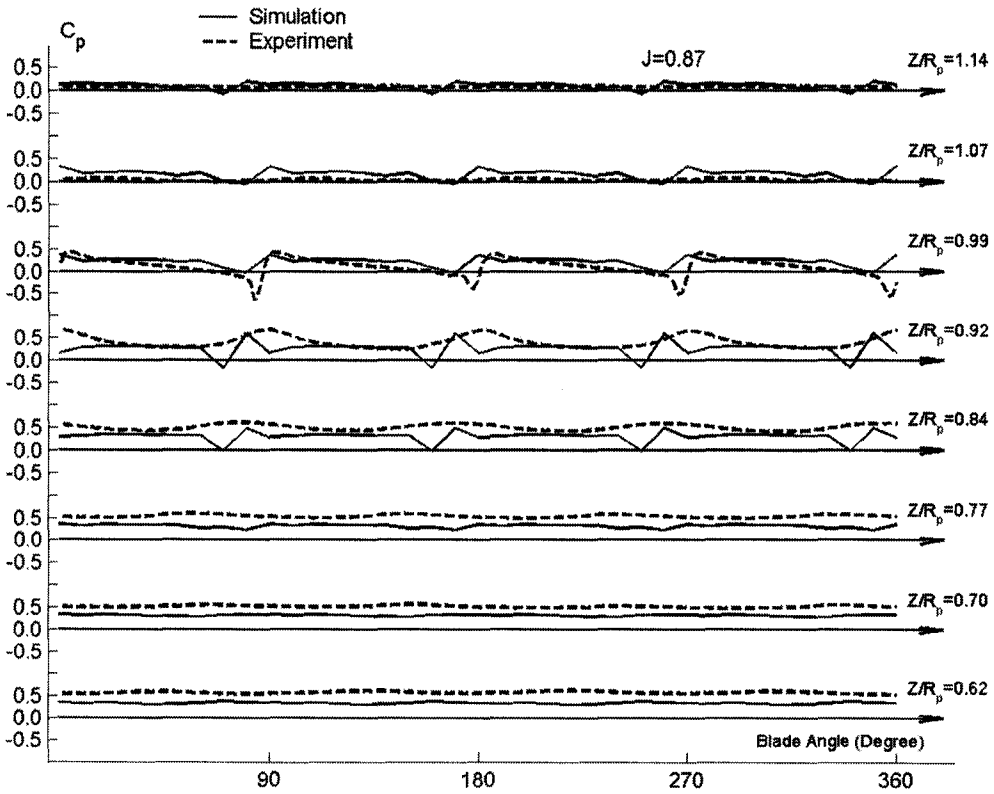

Figure 6.20 Comparison of the p on the L.E. (*J=0.87*)

of phase-averaged pressure were slightly over-predicted at $Z/R_p = 0.84$ and $Z/R_p = 0.92$.

The time-averaged pressure along the leading edge against the advance coefficient was plotted in Figure 6.21. It clearly shows that the differences between simulated results and measurements for all locations of Z/R_p decreases as the advance coefficient increases. The simulated pressures at these locations of $Z/R_p >= 0.99$ were higher than the measurements by 0.15. However, the simulated pressures at locations of $Z/R_p <= 0.92$ were lower than the measurements by 0.20. It was also found that the

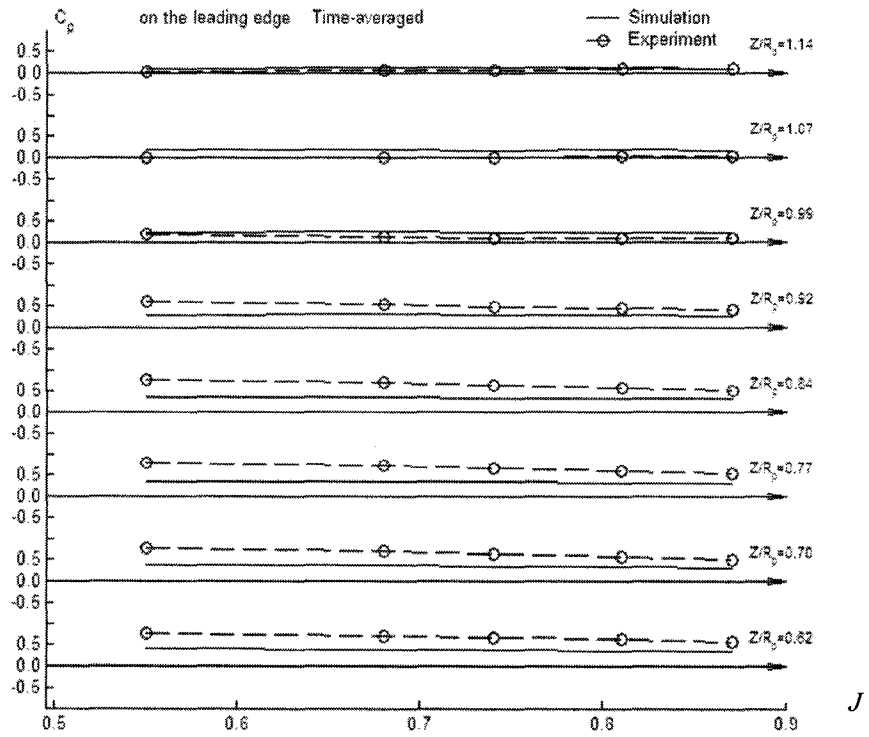

Figure 6.21 The Time-Averaged Pressure on the L.E.

differences between the measurement and the simulation out of the propeller wake race ($Z/R_p > 1.0$) were smaller than those within the propeller wake race. These differences might be explained partially due to viscous effects, which are not modeled in the calculation.

The amplitudes of the phase-averaged pressure against the advance coefficient were shown in Figure 6.22. It is obvious that the amplitude of the phase-averaged pressure decreased with the increase of the advance coefficient, especially for those at $Z/R_p > 1.07$ and $Z/R_p > 0.99$. The calculated results were in good agreement with the measurements except for the locations of $Z/R_p > 1.07$ and $Z/R_p > 0.99$. In general, the

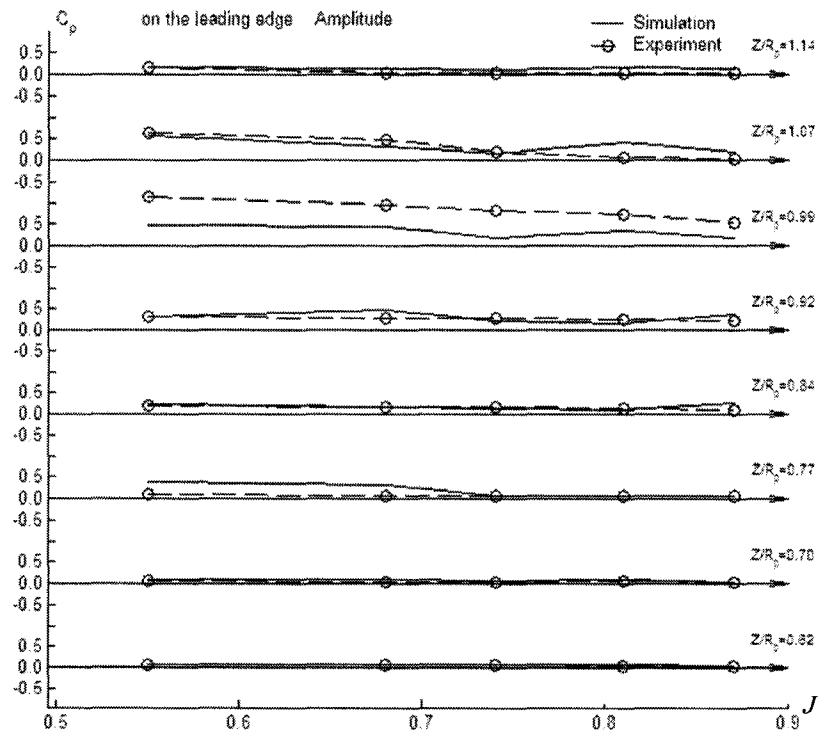

Figure 6.22 Amplitude of the Phase-Averaged Pressure on the L.E.

simulations matched with the experimental data in the high advance coefficient range ($J>0.7$) better than in the low advance coefficient range ($J<0.7$). The largest difference occurred at the position of $Z/R_p > 0.99$ where the tip-vortex impacted on the leading edge. The calculated phase-averaged amplitudes were about half of the corresponding measurements for the range of the advance coefficient from 0.55 to 0.87.

6.4 Comparisons of the Strut Pressure Distribution with Experimental Data

Simulated pressure distributions of the time-averaged component are compared with the measurements in Figure 6.23 to 6.27. Each figure demonstrates the pressure contours for one of the five advance coefficients, 0.55, 0.68, 0.74, 0.81, and 0.87. Since the measurement covered only a part of the strut surface around the leading edge, the comparison could only be made within the measurement zone. The zone was marked with a rectangle in the figures. Based on the comparison of the pressure contours for $J = 0.55$ in Figure 6.23, it was found that there were more variations in the simulated result than in the measurement. The simulated magnitude of the pressure away from the leading edge was closer than around the leading edge. Comparing the calculated with the measured on the left side of Figure 6.23, sizes and shapes of pressure contours of -0.5 and -0.75 are very similar. Both the simulation and the measurement showed a joint on the leading edge which separates the pressure contours into two, upper and lower groups. This joint is considered to be the intersection point of tip-vortex and the leading edge. The point located at Z/R_p of 0.95 for advance coefficient of 0.55 from the simulation and it laid around Z/R_p of 1.04 from the measurement. The reason may be that the wake simulated by a potential flow-based method is over-contracted since the flow is inviscid and it does not consider the displacement induced by the boundary layer of the pod and strut. Comparisons made for $J = 0.68$ in Figure 6.24 show the same similarities between simulation and measurement for $J = 0.55$ demonstrated in Figure 6.23. The pressure simulated on the right side of the figure is closer to the measurement than that on the right side.

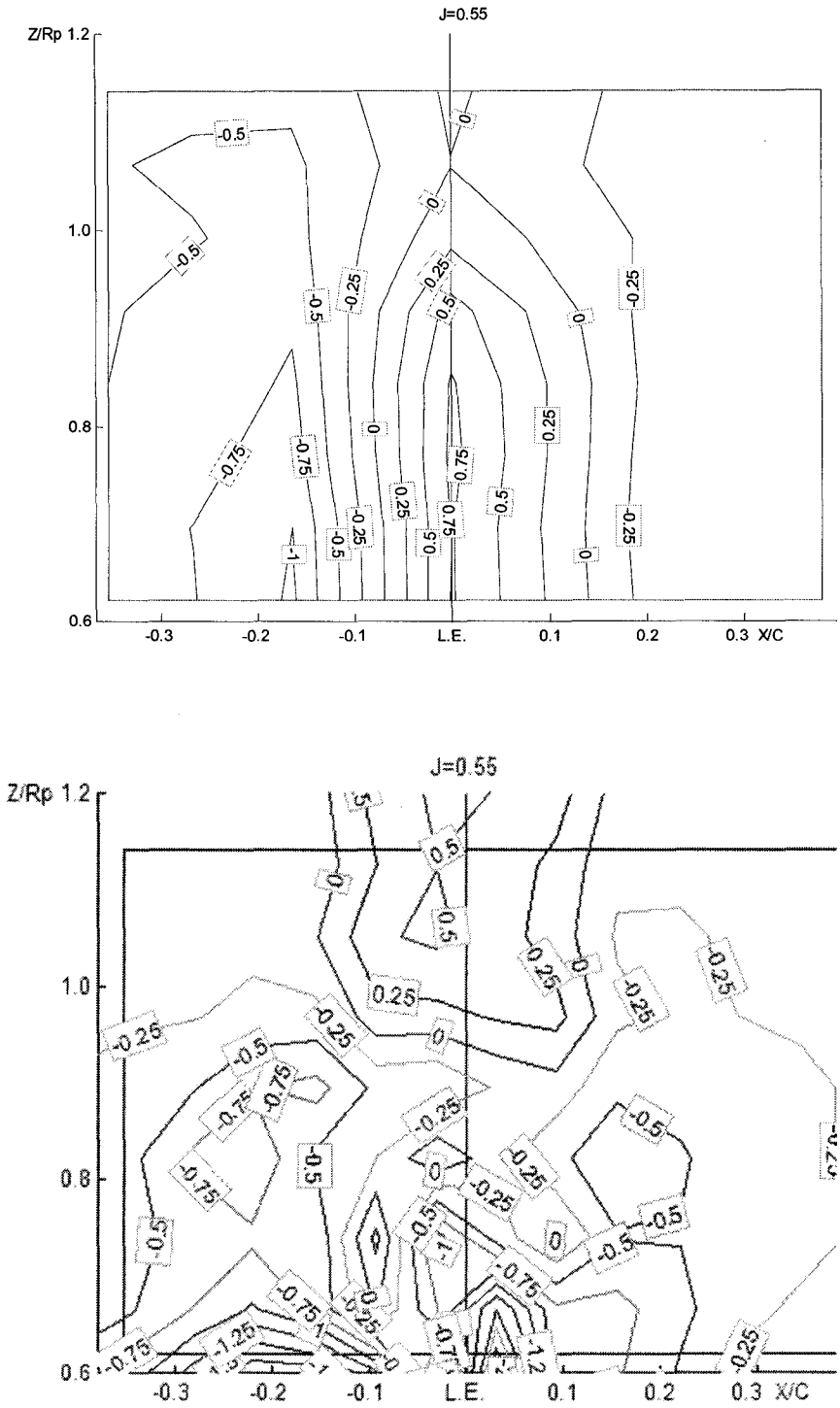

Figure 6.23 Comparison of the Time-Averaged Pressure on the Strut
J=0.55; upper: measured; lower: calculated

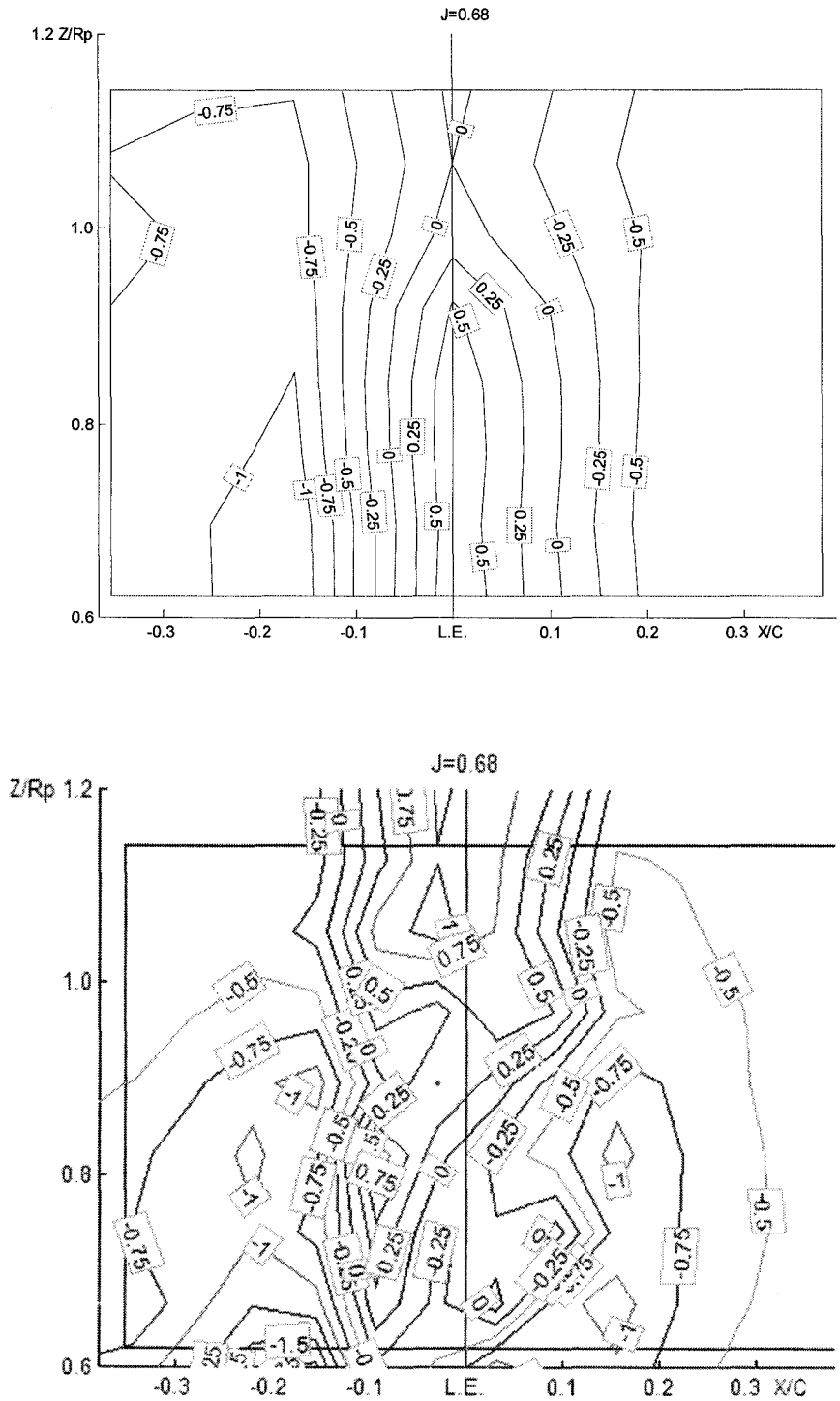

Figure 6.24 Comparison of the Time-Averaged Pressure on the Strut
J=0.68; upper: measured; lower: calculated

The simulated time-averaged pressure distributions with the wake impingement model for $J = 0.74$, $J = 0.81$ and $J = 0.87$ are shown in Figure 6.25, 6.26 and 6.27. Most of simulated lines of the pressure contours shown at the Figure lower parts lay vertical and that is the same trends as the measured lines shown in the upper parts. Except for some small pockets near the strut leading edge on the left side in the simulated results, their patterns were very similar to the patterns of corresponding measurements. Some pressure contours (-1.25, -1.0, and -0.75) were chosen as representatives for comparisons in detail. On the left side in Figure 6.25, the size, the shape, and the location of the contour of -1.0 are almost the same as those from the measurement. On the right side of the figure, the simulated pocket of -0.75 is smaller than and located closer to the leading edge than that obtained by the experiment. Comparisons made for $J = 0.81$ in Figure 6.26 shows the calculated contour of -1.25 on the left side of the figure consists of two parts, and the summation of the two parts is slightly larger than the correspondent from the experiment. On the right side, the contour of -0.75 from the simulation still shows most parts of a pocket containing contours of -1.0 and -1.25 while the experimental result demonstrates only a straight line. The reason was the measurement area was not big enough to cover all parts of the contour of -0.75. Comparisons made in Figure 6.27 for $J = 0.87$ show the simulated contours of -1.25 on the left and -1.0 on the right side match the experimental results though the contour position on the right side is closer to the leading edge than the experimental data. Through the comparison of the time-averaged pressure coefficient with the experimental data, it was found that the numerical method captured most of characteristics of the pressure distributions with acceptable accuracy.

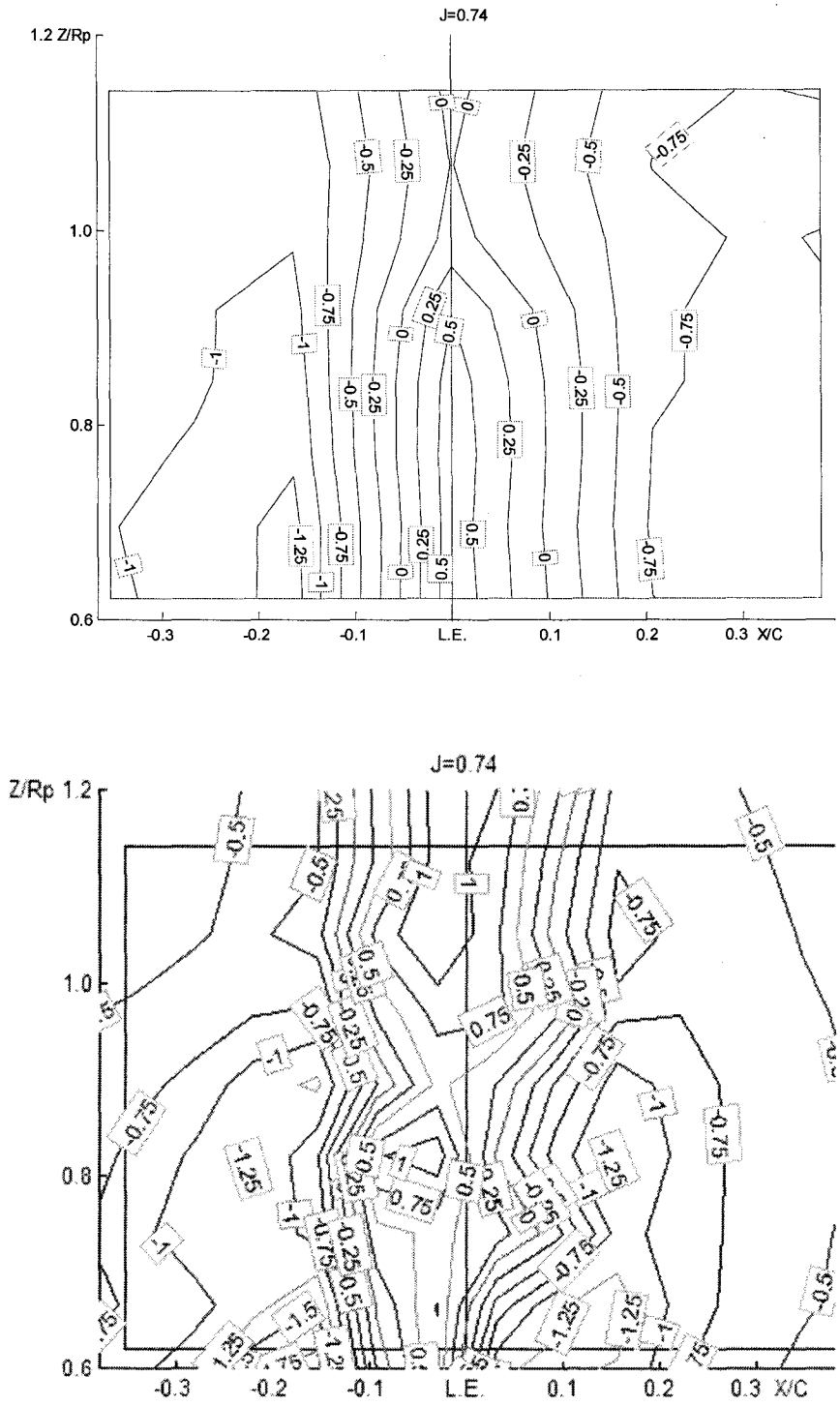

Figure 6.25 Comparison of the Time-Averaged Pressure on the Strut
J=0.74; upper: measured; lower: calculated

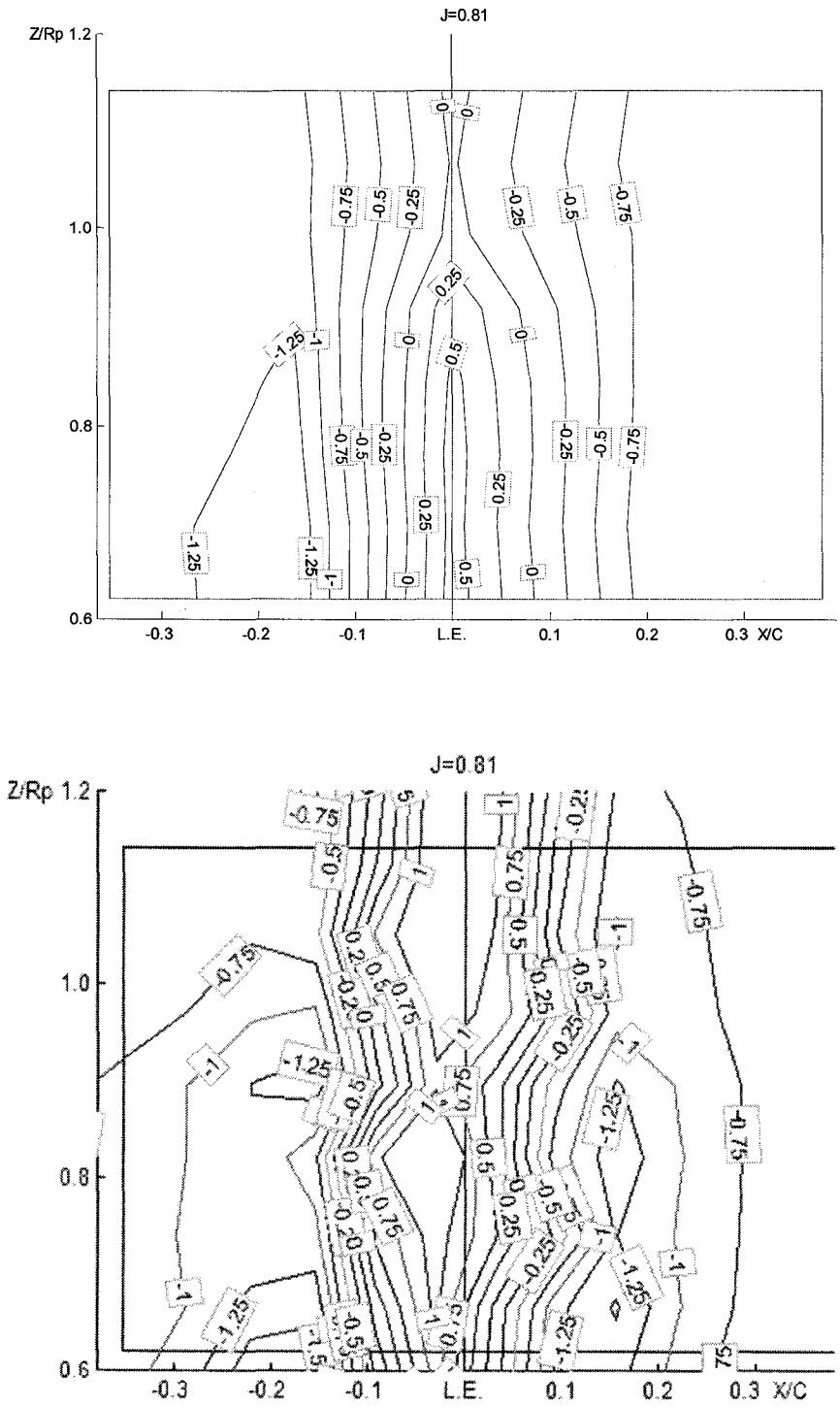

Figure 6.26 Comparison of the Time-Averaged Pressure on the Strut *J=0.81*; upper: measured; lower: calculated

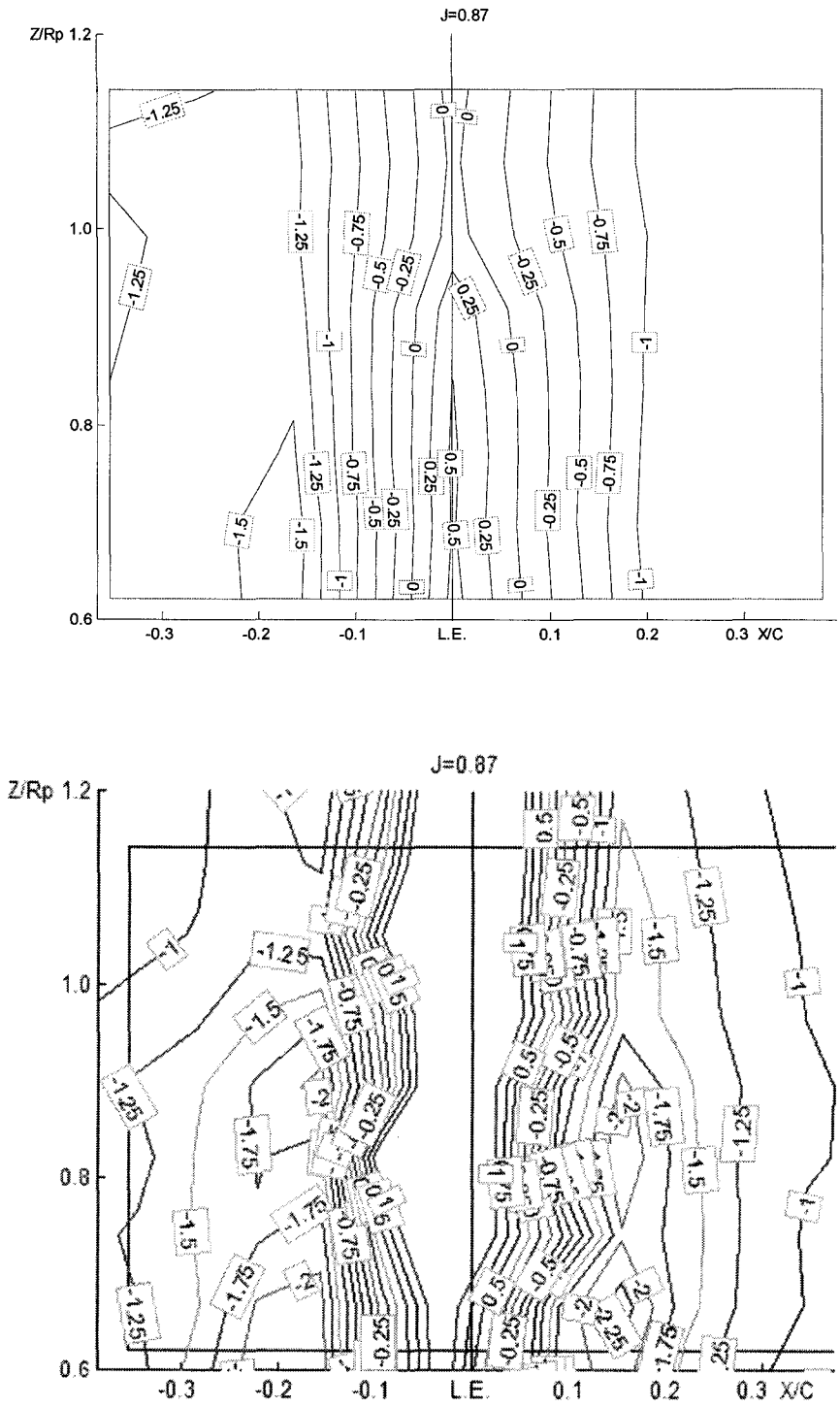

Figure 6.27 Comparison of the Time-Averaged Pressure on the Strut
J=0.87; upper: measured; lower: calculated

Chapter 7 Conclusion

The present study included the development of a wake impingement model and the implementation of a set of tractor-type podded propeller tests in a cavitation tunnel. The set of models tests consists of the strut surface pressure measurement, the propeller shaft thrust and torque measurements and the tip-vortex visual investigation. The developed wake impingement model was incorporated into a panel code and used to predict the time-varied pressure distribution on a pod and strut surface subject to the propeller wake. The simulated surface pressure and propeller shaft forces have been compared with the experimental data. The comparisons indicate that the developed panel method wake impingement model provides an excellent model to predict the time-varied pressure distribution on a body surface which is acted on by a strong vortical wake.

Based on the numerical simulations, the following points were concluded:

- Incorporation of the wake impingement model into a panel code provides a numerical tool for prediction of surface pressure fluctuations on a pod and strut due to interaction with the propeller wake.
- The wake impingement model affects the prediction of propeller performance very little in comparison with the original panel code. The differences in the thrust and torque coefficients, with and without using the wake impingement model were less than 2%. Using the wake impingement model improves the simulation by capturing the fluctuation pressure of the blade passing frequency on the surface of the pod and strut.

- Comparison of the numerical results with corresponding experimental data indicates that the numerically predicted pressure is in a good agreement. Hence, it is concluded that the wake impingement model incorporated in the panel code provides a tool for the prediction of surface pressure fluctuation on a strut due to interaction with a propeller wake. However, the amplitude of the pressure fluctuation in the tip-vortex/strut interaction zone is under-predicted; further refinement to the numerical theoretical method is necessary to improve this aspect of the model.
- A no-penetration boundary condition for vortex/body interaction has been developed for potential based vortex numerical methods. The model satisfies the no-penetration condition, and accounts for the strength change of the incident vortex from the impingement consideration.
- To increase the prediction precision of the amplitude of the pressure fluctuation around the tip-vortex/strut interaction zone it may be necessary to include introducing corrections of viscous effects to the wake impingement model.

In the strut surface pressure measurement, the measured time series of pressure was first broken down into three components, the time-averaged component, the phase-averaged component and the fluctuation component. After getting these components by a data processing procedure the time-averaged component was used in the discussion of the propulsive performance. The phase-averaged component was then used in the analysis of the wake impingement effects. Based on the pressure measurements, the following observations were made:

- The lowest time-averaged pressure within the measured area was found to occur on the suction side of the strut around the leading edge near the intersection of the pod and the strut. The lowest time-averaged pressure coefficient was about -1.7 at $J = 0.87$
- The largest amplitude of the phase-averaged pressure was found on the leading edge of the strut around $Z/R_p = 1.0$, for all tested advance coefficients. The amplitude of the phase-averaged pressure decreased with increases in the advance coefficient. The largest peak-trough amplitude was around C_p =3.2 and it occurred at the advance coefficient of 0.55 which was the lowest tested.
- The pressure time-variation on the strut was dominated by the blade passing frequency, and the large amplitude pressure variation was confined within a range of Z/R_p from 0.9 to 1.1 where the tip vortex impact on the strut. The pressure measured outside of this range rarely showed significant fluctuation.
- In cases of low advance coefficients, the pressure at some of the measurement points on the compressed side demonstrated a double-trough shape within a single period of the vortex filament impacting process. For a left-handed tractor-type podded propeller, the starboard side of the strut is the compressed side. The amplitude of the double-trough shape pressure was only about 60% of the amplitude of the single-trough shape pressure. Further study may lead to a new approach to reduce the pressure variation in the design of the strut.
- The presence of the pod and strut in the race of the propeller wake increased the propeller time-averaged components, thrust, torque and efficiency of the propeller. However, the amplitudes of the phase-averaged thrust and torque coefficients of

the propeller changed less than 1% and 2% respectively. This indicates the wake impingement had no significant effect on the propeller propulsive performance in this configuration.

The following findings come from the visual investigation of the tip vortex/strut interaction:

- The tip vortex was bent by the leading edge when it approached the strut, and then kept a minimum distance from the leading edge while it moved along the leading edge. The tip-vortex drifted away from the shaft center for a certain distance before being shrunk and separated into two parts around the leading edge.
- After the tip-vortex was bent, stretched, and visually weakened around the leading edge, it appeared to be separated into two parts. Each of the two parts propagated downstream on the two sides of the strut. The tip-vortex turned from a continuously helical line into segments. The segmental vortex was compressed on one side of the strut and stretched on the other side.
- The vertical distance from the end of the segmental vortex to the shaft center on the stretched side remained a constant (Figure 5.33). However, the distance increased on the compressed side: the lower the value of advance coefficient, the faster this distance increases. There was no merger of the broken ends of the tip-vortex found downstream of the trailing edge of the strut.

REFERENCES

Asea Brown Boveri, (2003), http://search.abb.com/library/ABBLibrary.asp? Document ID=3BFV000246R01&LanguageCode=en&DocumentPartID=&Action=Launch

Atlar M. et al., (2005), "Final Report and Recommendations to the 24th ITTC, The Specialist Committee on Azimuthing Podded Propulsion", Proceedings of the 24th ITTC Vol. II pp.543-587

Atlar M., (2004), "Preface", Proceedings of First International Conference on Technological Advances in Podded Propulsion, Newcastle, UK.

Bhagwat M. J. and Leishaman J. G., (2002), "Generalized Viscous Vortex Model for Application to Free-Vortex Wake and Aeroacoustic Calculations", The 58th Annual Forum and Technology Display of the American Helicopter Society International, Montreal, Canada, June 11-13.

Booth E.R., (1986), "Surface Pressure Measurement during Low Speed Two-Dimensional Blade-Vortex Interaction," *AIAA Paper 1986-1856.*

Bose N. (1994), "Explicit Kutta Condition for an Unsteady Two-Dimensional Constant Potential Panel Method", *AIAA Journal,* Vol. 32, No. 5, pp.1078-1080.

Bose N. (1996), "Ice Blocked Propeller Performance Prediction Using a Panel Method", *Transaction of the Royal Institution of Naval Architects*, pp. 213-226.

Bushkovsky V.A., Frolova I.G., Kaprantsev S.V., Pustoshny A.V., Vasiljev A.V., Jakovlev A.J., and Veikonheimo T., (2004), "On the Design a Shafted Propeller Plus Electric Thruster Contra-Rotating Propulsion Complex", Proceedings of First

International Conference on Technological Advances in Podded Propulsion, Newcastle, UK. pp. 247-261.

Carlton J. S. (2002), "Podded Propulsors: Some Design and Service Experience", The Motor Ship Marine Propulsion Conference, Copenhagen, Denmark

Chen, S. H. and Williams, M. H., (1987), "A Panel Method for Counter Rotating Propfans," AIAA Paper 1987-1890, SAE, ASME and ASEE, Joint Propulsion Conference, 23rd , San Diego, CA, June 29 – July 2. 12 pages.

David M. O'Brien, Jr and Marilyn J. Smith (2005), "Analysis of Rotor-Fuselage Interactions Using Various Rotor Models", *AIAA paper 2005-0468.*

Deniset F., Laurens J.M. and Jaouen R. (2003), "Numerical Simulations of Podded Propulsors", 6th Numerical Towing Tank Symposium, Rome, Italy. 29, Sept – 1, Oct.,

Fabris D., Liepmann D. and Daniel M., (1996), "Quantitative experimental and numerical investigation of a vortex ring impinging on a wall," *Phys. Fluids* Vol. 8, No. 10, pp. 2640-2649.

Gordnier, R. E., and Visbal, M. R., (1997), "Numerical Simulation of the Impingement of a Streamwise Vortex on a Plate," AIAA Paper 97-1781.

Grant, J. R., and Marshall, J. S., (1999), "Invisicid Interaction of Vortex Rings: Approach to Singularity?" Proceedings of Third International Workshop on Vortex Flows and Related Numerical Methods, Vol. 7, pp.183-194.

Greco L., Colombo C., Salvatore F., Felli M., (2006), "An Unsteady Inviscid-Flow Model to Study Podded Propulsors Hydrodynamics", Proceedings of T-POD 2006, 15 pages.

Greene G. C., (1986), "An Approximate Model of Vortex Decay in the Atmosphere," *Journal of Aircraft,* Vol. 23, No.7, pp. 566-573.

Grygorowicz M. and Szantyr J.A., (2004), "Open Water Experiments with Two Pod Propulsor Models", Proceedings of First International Conference on Technological Advances in Podded Propulsion, Newcastle, UK. pp. 357-370.

He, M., Veitch, B., Bose, N., Colbourne, B., Liu, P., (2007), "A Three-Dimensional Wake Impingement Model and Application on Tandem Oscillating Foils," to be published in Ocean Engineering.

Hess J. L. and Smith A. M. O. (1964), "Calculation of Nonlifting Potential Flow about Arbitrary Three-Dimensional Bodies", *Journal of Ship Research*, pp. 22-44.

Hess J. L. (1972), "Calculation of Potential Flow about Arbitrary Three-Dimensional Lifting Bodies", AD-755 480, 160 pages.

Hess J. L. and Valarezo W. O. (1985), "Calculation of Steady Flow about Propellers by Means of a Surface Panel Method", 23rd Aerospace Sciences Meeting, AIAA, Reno, NV, 8 pages.

Hoshino T. (1989a), "Hydrodynamics Analysis of Propeller in Steady Flow Using a Surface Panel Method", Read at the Spring Meeting of The Society of Naval Architectures of Japan.

Hoshino T. (1989b), "Hydrodynamics Analysis of Propeller in Steady Flow Using a Surface Panel Method 2nd report: Flow Field around Propeller", *Journal of the Society of Naval Architectures of Japan*, Vol.165, pp. 79-92.

Hoshino T. (1990), "Numerical and Experimental Analysis of Propeller Wake by Using a Surface Panel Method and a 3-Component LDV", Proceedings of The 18th Naval Hydrodynamics, Aun Arbor, Michigan.

Hoshino T. (1993), "Hydrodynamics Analysis of Propeller in Unsteady Flow Using a Surface Panel Method", *Journal of the Society of Naval Architectures of Japan*, Vol.174, pp. 71-87.

Hsin C-Y. (1990), "Development and Analysis of Panel Methods for Propellers in Unsteady Flow", PhD. Thesis, Massachusetts Institute of Technology.

http://www.sinm.it/downloads/ENG_POD.pdf, SINM, (2004), "Focus on Propulsion Pods", SINM report 060/2004

http://search.abb.com/library/ABBLibrary.asp?DocumentID=3BFV000246R01&LanguageCode=en&DocumentPartID=&Action=Launch, 2003

Juurmaa K., Mattsson T., Sasaki N., Wilkman G., (2002), "The Development of the Double Acting Tanker for Ice Operation", Okhotsk Sea and Sea Ice, Mombetsu, Japan, Feb. 24-28,

Juergen F., (2004), "Cavitation and Vibration Investigations for Podded Drives", Proceedings of First International Conference on Technological Advances in Podded Propulsion, Newcastle, UK. pp. 387-399.

Katz J. and Weihs D. (1981), "Wake Rollup and the Kutta Condition for Airfoils Oscillating at High Frequency", *AIAA Journal,* Vol. 19, No. 12, pp. 1604-1606.

Katz J. and Plotkin A. (2001), *Low-Speed Aerodynamics*, Second Edition, Cambridge University Press.

Kerwin J. E., Kinnas S. A. and Lee J. T. (1987), "A Surface Panel Method for the Hydrodynamic Analysis of Ducted Propellers", *SNAME Transactions,* Vol. 95, pp. 93-122

Kinnas, S. A. et al. (2001), "A General Computational Technique for the Prediction of Cavitation on Two-Stage Propulsors", the 26th ATTC, Webb Institute, Glen Cove, NY.

Kinnas S. A. and Hsin C-Y. (1992), "Boundary Element Method for the Analysis of the Unsteady Flow around Extreme Propeller Geometries", *AIAA Journal*, Vol.30, No. 3, pp. 688-696.

Krause E. and Schweitzer W.-B., (1990), "The effect of an oscillatory freestream-flow on a NACA-4412 profile at large relative amplitudes and low Reynolds-numbers", *Experiments in Fluids*, Vol. 9, pp. 159-166.

Krishnamoorthy S., Gossler A. A., and Marshall J. S., (1999), "Normal Vortex Interaction with a Circular Cylinder," *AIAA Journal*, Vol. 37, No. 1, pp. 50-57.

Li D. Q. (1992), "Interaction between propeller slipstream and rudder", Report NO. 21, Chalmers University of Technology, Gothenburg, Sweden.

Li D.-Q., (1993), "A simplified nonlinear method for the calculation of propeller-rudder interaction", Report NO. 32, Chalmers University of Technology, Gothenburg, Sweden.

Liu P. (1996), "A time-domain panel method for oscillating propulsors with both chordwise and spanwise flexibility", PhD thesis, Memorial University of Newfoundland, St. John's, Newfoundland, Canada, 226 pages.

Liu P. (1996a), "Software Development on Propeller Geometry Input Processing and Panel Method Predictions of Propulsive Perfromance of the R-Class Propeller", Report of TDC Contract# T8200-6-6507-001/XSD, MMC Engineering & Research, Burin Bay Arm, NL, Canada, 53 pages.

Liu P. and Bose N. (1997). Propulsive performance from oscillating propulsors with spanwise flexibility. *Proc. R. Soc. Lond.*

Liu P. and Bose N. (1998), "An Unsteady Panel Method for Highly Skewed Propellers in Non-Uniform Inflow", 22nd ITTC Propulsion Committee Propeller RANS/Panel Method Workshop, Grenoble, France

Liu P., Doucet J. M., Veitch B., Robbins I. and Bose N. (2000), "Numerical Prediction of Ice Induced Hydrodynamic Loads on Propellers Due to Blockage", *Ocean Engineering International*, Vol. 4, No.1, pp. 31-38.

Liu P., Colbourne B. and Shin C. (2001), "Prediction of Transient Loading on a propeller from an Approaching Ice Block", PRADS – International Symposium on Practical Design in Shipbuilding, Shanghai, China, pp. 741-747.

Liu P. and Bose N., (2001), "Hydrodynamic Characteristics of a Screw-Nozzle-Rudder Assembly," *Computational Fluid Dynamics Journal of Japan (CFDJJ), Special number 2001*, pp. 477-484.

Liu P., Colbourne B. and Bose N. (2002), "A Broyden Numerical Kutta Condition for an Unsteady Panel Method", *Int. Shipbuild. Progr.,* Vol. 49, No. 4, pp. 263-273.

Liu P. (2006), "Propulsive Performance of a Twin-Rectangular-Foil Propulsor in a Counterphase Oscillation", *Journal of Ship Research,* Vol. 49, No. 3, pp. 207-215.

Liu, P., (2006a), "The Design of a Podded Propeller Base Model Geometry and Prediction of Its Hydrodynamics", IOT Report No. : TR-2006-16, 16 pages.

Mammetti, M., Verzicco, R., and Orlandi, P., (1999), "The study of vortex ring/wall interaction for artificial nose improvement," Proceedings of Third International Workshop on Vortex Flows and Related Numerical Methods, Vol.7, pp. 258-269.

Marshall, J. S., (1994), "Vortex Cutting by a Blade, Part 1: General Theory and a Simple Solution," *AIAA Journal,* Vol. 32, No. 6, pp. 1145-1150.

Marshall, J. S., and Yalamanchili, R., (1994), "Vortex Cutting by a Blade, Part II: Computations of Vortex Response," *AIAA Journal,* Vol. 32, No. 7, pp. 1145-1150.

Marshall, J. S., and Krishnamoorthy, S., (1997), "On the instantaneous cutting of a columnar vortex with non-zero axial flow," *Journal of Fluid Mechanics,* Vol. 351, pp. 41-74.

Maskew B. and Rao B. M. (1987), "Calculation of Vortex Flows on Complex Configurations", ICAS paper 82-6.2.3

Maxim H. S. (1891), "Locomotion through the air: Aerial Navigation", *The Century; A popular Quarterly,* Vol. 42 No. 6, pp.829-837.

Mayori, Alejandro, and Rockwell, Donald, (1994), "Interaction of a Streamwise Vortex with a Thin Plate: A Source of Turbulent Buffeting," *AIAA Journal,* Vol. 32, No. 10, pp. 2022-2029.

Modi A., (2002), "Real-Time Visualization of Wake-Vortex Simulations using Computational Steering and Beowulf Clusters", PhD thesis in Computer science and engineering, Pennsylvania State University, 166 pages.

Morino L. (1973), "Unsteady compressible potential flow around lifting bodies: General Theory", AIAA Paper, No. 73-196, 6 pages.

Morino L. and Kuo C. C. (1974), "Subsonic potential aerodynamics for complex configuration: A general theory", *AIAA Journal,* Vol.12, NO. 2, pp. 191-197.

Morino L., Chen L. T. and Suciu E. O. (1975), "Steady and Oscillatory Subsonic and Supersonic Aerodynamics around Complex Configurations", *AIAA Journal* Vol.13 No.3, pp. 368-374.

Ohashi K. and Hino T., (2004), "Numerical Simulations on Flows around a Ship with Podded Propulsor", Proceedings of First International Conference on Technological Advances in Podded Propulsion, Newcastle, UK. pp. 211-221.

Orlandi, P., and Verzicco, R., (1993), "Vortex rings interacting with walls, analogies with wall turbulence structures," *Near-Wall Turbulent Flows*, R.M.C. So, Elsevier Science Publishers B.V., pp. 497-506.

PODS in SERVICE, (1999), "PODS in SERVICE", Annex 1, Description of Work, GROWTH Project GRD1-1999-10395, rev1.0/30 Sep.

Poling D. R. and Telionis D. P. (1986), "The Response of Airfoils to Periodic Disturbances – The Unsteady Kutta Condition", *AIAA Journal,* Vol.24, No.2, pp.193-199.

Pyo S. (1995), "Numerical Modeling of Propeller Tip Flows with Wake Sheet Roll-Up in Three Dimensions", PhD thesis, MIT.

Pyo S. and Kinnas S. A. (1997), "Propeller Wake Sheet Roll-up Modeling in Three Dimensions", *Journal of Ship Research,* Vol. 41, No. 2, pp. 81-92.

Richason T. F. and Katz J. (1993), "Unsteady Panel Method for Flows with Multiple Bodies Moving along Various Paths", AIAA Paper 93-0640, 31st Aerospace Sciences Meeting and Exhibit, Reno, NV. 9 pages.

Sanchez-Caja A. and Pylkkanen J. V., (2004), "On the Hydrodynamic Design of Podded Propulsors for Fast Commercial Vessels", Proceedings of First International Conference on Technological Advances in Podded Propulsion, Newcastle, UK. pp. 201-210.

SINM , (2004), "Focus on Propulsion Pods", SINM Report 060/2004

Spiegel, Murray R., and Liu, (1999), John, *Mathematical Handbook of Formulas and Tables*, 2nd edition, McGraw-Hill Companies, Section II.

Suciu E. O. and Morino L. (1976), "A Nonlinear Finite-Element Analysis of Wings in Steady Incompressible Flows with Wake Roll-Up", AIAA 14th Aerospace Sciences Meeting, Washington D.C. 10 pages.

Tragardh P., Lindell P., and Sasaki N., (2004), "Double Acting Tanker – Experiences from Model Tests and Sea Trials", Proceedings of First International Conference on Technological Advances in Podded Propulsion, Newcastle, UK. pp. 173-186.

Ukon Y., Ohashi K., Fujisawa J., Hasegawa J., (2004), "Propulsive Performance of a Contra-Rotating Podded Propulsor", Proceedings of First International Conference on Technological Advances in Podded Propulsion, Newcastle, UK. pp. 289-302

Vatistas G.H., (1998) "New Model for Intense Self-Similar Vortices", *Journal of Propulsion and Power*, Vol. 14, No. 4, pp. 462-469

Veitch B., Bose N., Meade C. and Liu P. (1997), "Predictions of Hydrodynamic and Ice Contact Loads on Ice-Class Screw Propellers", Proceedings, Offshore Mechanics and Arctic Engineering, American Society of Mechanical Engineers, Vol. 4, pp. 119-125.

Veitch B., (1995), "Predictions of ice contact forces on a marine screw propeller during the propeller ice cutting process", Thesis for the degree of Doctor in Technology. Helsinki, Acta Polytechnica Scandinavica, *140 pages.*

Veitch B. (2001) "Systematic Investigation of Azimuthing Podded Propeller Performance" Form 101, a proposal for a grant from NSERC.

Wilder, M. C., and Telionis, D. P., (1998), "Parallel Blade-Vortex Interaction," *Journal of Fluids and Structures,* Vol. 12, pp. 801-838.

Wittmer, K. S., Devenport, W. J., and Rife, M. C., (1995), "Perpendicular Blade Vortex Interaction," *AIAA Journal,* Vol.33, No.9, pp. 1667-1674.

Yao, Z. X., and Liu, D. D., (1998), "Vortex Dynamics of Blade-Blade Interaction," *AIAA Journal,* Vol. 36, No. 4, pp. 497-504.

APPENDIX A

The formulation of induced velocities for the hyperboloid panel method

Velocity potentials induced by uniform source and dipole distribution on a quadrilateral element which is represented by a hyperboloid surface panel are given by Morino etc (1975) as following:

$$c_{hk} = [\frac{1}{2\pi}\iint \frac{\partial}{\partial N}\left(\frac{1}{R}\right)d\sigma_k]_{P_*=P_h}$$
$$= I_D(1,1) - I_D(1,-1) - I_D(-1,1) + I_D(-1,-1) \tag{A-1}$$

$$b_{hk} = [-\frac{1}{2\pi}\iint \frac{1}{R}d\sigma_k]_{P_*=P_h}$$
$$= I_S(1,1) - I_S(1,-1) - I_S(-1,1) + I_S(-1,-1) \tag{A-2}$$

where

$$I_D(\xi,\eta) = \frac{1}{2\pi}\tan_p^{-1}\left(\frac{\vec{R}\times\vec{a}_1\cdot\vec{R}\times\vec{a}_2}{|\vec{R}|\vec{R}\cdot\vec{a}_1\times\vec{a}_2}\right) \tag{A-3}$$

$$I_S(\xi,\eta) = -\frac{1}{2\pi}\left\{-\frac{\vec{R}\times\vec{a}_1\cdot\vec{n}}{|\vec{a}_1|}\sinh^{-1}\left(\frac{\vec{R}\cdot\vec{a}_1}{|\vec{R}\times\vec{a}_1|}\right)\right.$$
$$\left.+\frac{\vec{R}\times\vec{a}_2\cdot\vec{n}}{|\vec{a}_2|}\sinh^{-1}\left(\frac{\vec{R}\cdot\vec{a}_2}{|\vec{R}\times\vec{a}_2|}\right)+\vec{R}\cdot\vec{n}\tan_p^{-1}\left(\frac{\vec{R}\times\vec{a}_1\cdot\vec{R}\times\vec{a}_2}{|\vec{R}|\vec{R}\cdot\vec{a}_1\times\vec{a}_2}\right)\right\} \tag{A-4}$$

and

$$\vec{R}(\xi,\eta) \equiv \begin{pmatrix} R_x \\ R_y \\ R_z \end{pmatrix} = \vec{P} - \vec{P}_h = \vec{p}_0 + \xi\vec{p}_1 + \eta\vec{p}_2 + \xi\eta\vec{p}_3 - \begin{pmatrix} x \\ y \\ z \end{pmatrix} \tag{A-5}$$

$$\vec{a}_1(\xi,\eta) = \frac{\partial\vec{R}}{\partial\xi} \Rightarrow \vec{a}_1(\eta) = \vec{p}_1 + \eta\vec{p}_3 \tag{A-6}$$

$$\vec{a}_2(\xi,\eta) = \frac{\partial\vec{R}}{\partial\xi} \Rightarrow \vec{a}_2(\xi) = \vec{p}_2 + \xi\vec{p}_3 \tag{A-7}$$

$$\vec{n}(\xi,\eta) \equiv \begin{pmatrix} n_x \\ n_y \\ n_z \end{pmatrix} = \frac{\vec{a}_1 \times \vec{a}_2}{\left|\vec{a}_1 \times \vec{a}_2\right|} \tag{A-8}$$

The panel surface is expressed as:

$$\vec{p} = \vec{p}_0 + \vec{p}_1\xi + \vec{p}_2\eta + \vec{p}_3\xi\eta \tag{A-9}$$

and

$$\begin{Bmatrix} \vec{p}_0 \\ \vec{p}_1 \\ \vec{p}_2 \\ \vec{p}_3 \end{Bmatrix} = \frac{1}{4}\begin{bmatrix} 1 & 1 & 1 & 1 \\ 1 & 1 & -1 & -1 \\ 1 & -1 & 1 & -1 \\ 1 & -1 & -1 & 1 \end{bmatrix}\begin{Bmatrix} \vec{p}_{++} \\ \vec{p}_{+-} \\ \vec{p}_{-+} \\ \vec{p}_{--} \end{Bmatrix} \tag{A-10}$$

where

$\vec{p}_{--} = (x_1, y_1, z_1)$

$\vec{p}_{-+} = (x_2, y_2, z_2)$

$\vec{p}_{++} = (x_3, y_3, z_3)$

$\vec{p}_{+-} = (x_4, y_4, z_4)$

are the four corner coordinates of the panel 'I'.

Rewrite (A-3) and (A-4) as following:

$$2\pi I_D(x,y,z) = \tan_p^{-1}\left(\frac{\vec{R}\times\vec{a}_1 \cdot \vec{R}\times\vec{a}_2}{\left|\vec{R}\right|\vec{R}\cdot\vec{a}_1\times\vec{a}_2}\right) \equiv g(x,y,z) \tag{A-3'}$$

$$\begin{aligned} 2\pi I_S(x,y,z) &= \frac{\vec{R}\times\vec{a}_1\cdot\vec{n}}{\left|\vec{a}_1\right|}\sinh^{-1}\left(\frac{\vec{R}\cdot\vec{a}_1}{\left|\vec{R}\times\vec{a}_1\right|}\right) \\ &\quad -\frac{\vec{R}\times\vec{a}_2\cdot\vec{n}}{\left|\vec{a}_2\right|}\sinh^{-1}\left(\frac{\vec{R}\cdot\vec{a}_2}{\left|\vec{R}\times\vec{a}_2\right|}\right) - \vec{R}\cdot\vec{n}\tan_p^{-1}\left(\frac{\vec{R}\times\vec{a}_1\cdot\vec{R}\times\vec{a}_2}{\left|\vec{R}\right|\vec{R}\cdot\vec{a}_1\times\vec{a}_2}\right) \\ &\equiv f_1(x,y,z) - f_2(x,y,z) - \vec{R}\cdot\vec{n}g(x,y,z) \end{aligned} \tag{A-4'}$$

---

* $(\vec{A})_x$ represents the derivative of $\vec{A}$ to x, or $\partial\vec{A}/\partial x$; and $\vec{A}_x$ is the x component of $\vec{A}$.

Components of induced velocity by sources and dipoles distributed on the panel are derivatives of equation (A-1) and equation (A-2) to x, y, and z. As x, y, and z only appear in $\vec{P}_h = \vec{P}_h(x,y,z)$, or $\vec{R}$, with equations (A-3') and (A-4'), we have the formula for dipole induced velocity

$$\nabla(g) \equiv \begin{pmatrix} \partial g/\partial x \\ \partial g/\partial y \\ \partial g/\partial z \end{pmatrix} = \frac{1}{1+\left(\frac{\vec{R}\times\vec{a}_1\cdot\vec{R}\times\vec{a}_2}{|\vec{R}|\vec{R}\cdot\vec{a}_1\times\vec{a}_2}\right)^2}\nabla\left(\frac{\vec{R}\times\vec{a}_1\cdot\vec{R}\times\vec{a}_2}{|\vec{R}|\vec{R}\cdot\vec{a}_1\times\vec{a}_2}\right)$$

$$= \frac{(|\vec{R}|\vec{R}\cdot\vec{a}_1\times\vec{a}_2)^2}{(|\vec{R}|\vec{R}\cdot\vec{a}_1\times\vec{a}_2)^2+(\vec{R}\times\vec{a}_1\cdot\vec{R}\times\vec{a}_2)^2} * \frac{\nabla(\vec{R}\times\vec{a}_1\cdot\vec{R}\times\vec{a}_2)(|\vec{R}|\vec{R}\cdot\vec{a}_1\times\vec{a}_2)-(\vec{R}\times\vec{a}_1\cdot\vec{R}\times\vec{a}_2)\nabla(|\vec{R}|\vec{R}\cdot\vec{a}_1\times\vec{a}_2)}{(|\vec{R}|\vec{R}\cdot\vec{a}_1\times\vec{a}_2)^2}$$

$$= \frac{[\nabla(\vec{R}\times\vec{a}_1)\cdot\vec{R}\times\vec{a}_2+\vec{R}\times\vec{a}_1\cdot\nabla(\vec{R}\times\vec{a}_2)](|\vec{R}|\vec{R}\cdot\vec{a}_1\times\vec{a}_2)}{(|\vec{R}|\vec{R}\cdot\vec{a}_1\times\vec{a}_2)^2+(\vec{R}\times\vec{a}_1\cdot\vec{R}\times\vec{a}_2)^2} - \frac{(\vec{R}\times\vec{a}_1\cdot\vec{R}\times\vec{a}_2)[\nabla(|\vec{R}|\vec{R})\cdot\vec{a}_1\times\vec{a}_2+(|\vec{R}|\vec{R})\cdot\nabla(\vec{a}_1\times\vec{a}_2)]}{(|\vec{R}|\vec{R}\cdot\vec{a}_1\times\vec{a}_2)^2+(\vec{R}\times\vec{a}_1\cdot\vec{R}\times\vec{a}_2)^2}$$

$$= \frac{[\nabla(\vec{R}\times\vec{a}_1)\cdot\vec{R}\times\vec{a}_2+\vec{R}\times\vec{a}_1\cdot\nabla(\vec{R}\times\vec{a}_2)](|\vec{R}|\vec{R}\cdot\vec{a}_1\times\vec{a}_2)-(\vec{R}\times\vec{a}_1\cdot\vec{R}\times\vec{a}_2)[\nabla(|\vec{R}|\vec{R})\cdot\vec{a}_1\times\vec{a}_2]}{(|\vec{R}|\vec{R}\cdot\vec{a}_1\times\vec{a}_2)^2+(\vec{R}\times\vec{a}_1\cdot\vec{R}\times\vec{a}_2)^2}$$

$$= \frac{|\vec{R}|\vec{R}\cdot\vec{a}_1\times\vec{a}_2}{(|\vec{R}|\vec{R}\cdot\vec{a}_1\times\vec{a}_2)^2+(\vec{R}\times\vec{a}_1\cdot\vec{R}\times\vec{a}_2)^2}\left[\begin{pmatrix}(-1,0,0)\times\vec{a}_1\\(0,-1,0)\times\vec{a}_1\\(0,0,-1)\times\vec{a}_1\end{pmatrix}\cdot(\vec{R}\times\vec{a}_2)+(\vec{R}\times\vec{a}_1)\cdot\begin{pmatrix}(-1,0,0)\times\vec{a}_2\\(0,-1,0)\times\vec{a}_2\\(0,0,-1)\times\vec{a}_2\end{pmatrix}\right]$$

$$- \frac{\vec{R}\times\vec{a}_1\cdot\vec{R}\times\vec{a}_2}{(|\vec{R}|\vec{R}\cdot\vec{a}_1\times\vec{a}_2)^2+(\vec{R}\times\vec{a}_1\cdot\vec{R}\times\vec{a}_2)^2}\left[\nabla(|\vec{R}|)\vec{R}\cdot\vec{a}_1\times\vec{a}_2+|\vec{R}|\begin{pmatrix}(-1,0,0)\\(0,-1,0)\\(0,0,-1)\end{pmatrix}\cdot(\vec{a}_1\times\vec{a}_2)\right]$$

$$= \frac{\left|\vec{R}\right|\vec{R}\cdot\vec{a}_1\times\vec{a}_2}{\left(\left|\vec{R}\right|\vec{R}\cdot\vec{a}_1\times\vec{a}_2\right)^2+(\vec{R}\times\vec{a}_1\cdot\vec{R}\times\vec{a}_2)^2}\left[\begin{pmatrix}(0,a_{1z},-a_{1y})\\(-a_{1z},0,a_{1x})\\(a_{1y},-a_{1x},0)\end{pmatrix}\cdot(\vec{R}\times\vec{a}_2)+\begin{pmatrix}(0,a_{2z},-a_{2y})\\(-a_{2z},0,a_{2x})\\(a_{2y},-a_{2x},0)\end{pmatrix}\cdot(\vec{R}\times\vec{a}_1)\right]$$

$$-\frac{\vec{R}\times\vec{a}_1\cdot\vec{R}\times\vec{a}_2}{\left(\left|\vec{R}\right|\vec{R}\cdot\vec{a}_1\times\vec{a}_2\right)^2+(\vec{R}\times\vec{a}_1\cdot\vec{R}\times\vec{a}_2)^2}\left[\frac{-\vec{R}}{\left|\vec{R}\right|}\vec{R}\cdot\vec{a}_1\times\vec{a}_2+\left|\vec{R}\right|\begin{pmatrix}a_{1z}a_{2y}-a_{1y}a_{2z}\\a_{1x}a_{2z}-a_{1z}a_{2x}\\a_{1y}a_{2x}-a_{1x}a_{2y}\end{pmatrix}\right]$$

$$= \frac{\left|\vec{R}\right|\vec{R}\cdot\vec{a}_1\times\vec{a}_2}{\left(\left|\vec{R}\right|\vec{R}\cdot\vec{a}_1\times\vec{a}_2\right)^2+(\vec{R}\times\vec{a}_1\cdot\vec{R}\times\vec{a}_2)^2}$$

$$\begin{bmatrix}a_{1z}(R_za_{2x}-R_xa_{2z})-a_{1y}(R_xa_{2y}-R_ya_{2z})-a_{2z}(R_za_{1x}-R_xa_{1z})-a_{2y}(R_xa_{1y}-R_ya_{1x})\\a_{1z}(R_za_{2y}-R_ya_{2z})+a_{1x}(R_xa_{2y}-R_ya_{2x})+a_{2z}(R_za_{1y}-R_ya_{1z})+a_{2x}(R_xa_{1y}-R_ya_{1x})\\a_{1y}(R_ya_{2z}-R_za_{2y})-a_{1x}(R_za_{2x}-R_xa_{2z})+a_{2y}(R_ya_{1z}-R_za_{1y})-a_{2x}(R_za_{1x}-R_xa_{1z})\end{bmatrix}$$

$$-\frac{\vec{R}\times\vec{a}_1\cdot\vec{R}\times\vec{a}_2}{\left(\left|\vec{R}\right|\vec{R}\cdot\vec{a}_1\times\vec{a}_2\right)^2+(\vec{R}\times\vec{a}_1\cdot\vec{R}\times\vec{a}_2)^2}\left[\frac{-\vec{R}}{\left|\vec{R}\right|}\vec{R}\cdot\vec{a}_1\times\vec{a}_2+\left|\vec{R}\right|(-\vec{a}_1\times\vec{a}_2)\right]$$

$$= \frac{\left|\vec{R}\right|\vec{R}\cdot\vec{a}_1\times\vec{a}_2}{\left(\left|\vec{R}\right|\vec{R}\cdot\vec{a}_1\times\vec{a}_2\right)^2+(\vec{R}\times\vec{a}_1\cdot\vec{R}\times\vec{a}_2)^2}$$

$$*\begin{bmatrix}-2R_x(a_{1y}a_{2y}+a_{1z}a_{2z})+R_y(a_{1x}a_{2y}+a_{2x}a_{1y})+R_z(a_{1x}a_{2z}+a_{1z}a_{2x})\\R_x(a_{1x}a_{2y}+a_{2x}a_{1y})-2R_y(a_{1x}a_{2x}+a_{1z}a_{2z})+R_z(a_{1z}a_{2y}+a_{2z}a_{1y})\\R_x(a_{1x}a_{2z}+a_{2x}a_{1z})+R_y(a_{1y}a_{2z}+a_{2y}a_{1z})-2R_z(a_{1x}a_{2x}+a_{1y}a_{2y})\end{bmatrix}$$

$$+\frac{\vec{R}\times\vec{a}_1\cdot\vec{R}\times\vec{a}_2}{\left(\left|\vec{R}\right|\vec{R}\cdot\vec{a}_1\times\vec{a}_2\right)^2+(\vec{R}\times\vec{a}_1\cdot\vec{R}\times\vec{a}_2)^2}\left[\frac{\vec{R}\cdot\vec{a}_1\times\vec{a}_2}{\left|\vec{R}\right|}\vec{R}+\left|\vec{R}\right|(\vec{a}_1\times\vec{a}_2)\right]$$

(A-5)

The formula for source induced velocity calculation has 3 terms.

Term 1:

$$\nabla(f_1) \equiv \begin{pmatrix} \partial f_1/\partial x \\ \partial f_1/\partial y \\ \partial f_1/\partial z \end{pmatrix} = \nabla\left(\vec{R}\times\vec{a}_1\cdot\vec{n}\frac{1}{|\vec{a}_1|}\right)\sinh^{-1}\left(\frac{\vec{R}\cdot\vec{a}_1}{|\vec{R}\times\vec{a}_1|}\right)+\left(\vec{R}\times\vec{a}_1\cdot\vec{n}\frac{1}{|\vec{a}_1|}\right)\nabla\left[\sinh^{-1}\left(\frac{\vec{R}\cdot\vec{a}_1}{|\vec{R}\times\vec{a}_1|}\right)\right]$$

$$=\frac{1}{|\vec{a}_1|}[\nabla(\vec{R}\times\vec{a}_1)\cdot\vec{n}]\sinh^{-1}\left(\frac{\vec{R}\cdot\vec{a}_1}{|\vec{R}\times\vec{a}_1|}\right)+\frac{\vec{R}\times\vec{a}_1\cdot\vec{n}}{|\vec{a}_1|}\frac{1}{\sqrt{1+(\frac{\vec{R}\cdot\vec{a}_1}{|\vec{R}\times\vec{a}_1|})^2}}\nabla\left(\frac{\vec{R}\cdot\vec{a}_1}{|\vec{R}\times\vec{a}_1|}\right)$$

$$=\frac{\sinh^{-1}\left(\frac{\vec{R}\cdot\vec{a}_1}{|\vec{R}\times\vec{a}_1|}\right)}{|\vec{a}_1|}\left[\begin{pmatrix}(0,a_{1z},-a_{1y})\\(-a_{1z},0,a_{1x})\\(a_{1y},-a_{1x},0)\end{pmatrix}\cdot\vec{n}\right]+\frac{(\vec{R}\times\vec{a}_1\cdot\vec{n})|\vec{R}\times\vec{a}_1|}{|\vec{a}_1|\sqrt{|\vec{R}\times\vec{a}_1|^2+(\vec{R}\cdot\vec{a}_1)^2}}\left(\frac{\nabla(\vec{R}\cdot\vec{a}_1)|\vec{R}\times\vec{a}_1|-(\vec{R}\cdot\vec{a}_1)\nabla|\vec{R}\times\vec{a}_1|}{|\vec{R}\times\vec{a}_1|^2}\right)$$

$$=\frac{\sinh^{-1}\left(\frac{\vec{R}\cdot\vec{a}_1}{|\vec{R}\times\vec{a}_1|}\right)}{|\vec{a}_1|}\begin{bmatrix}(a_{1z}n_y-a_{1y}n_z)\\(a_{1x}n_z-a_{1z}n_x)\\(a_{1y}n_x-a_{1x}n_y)\end{bmatrix}+\frac{(\vec{R}\times\vec{a}_1\cdot\vec{n})}{|\vec{a}_1|\sqrt{|\vec{R}\times\vec{a}_1|^2+(\vec{R}\cdot\vec{a}_1)^2}}\left(\frac{\nabla(\vec{R}\cdot\vec{a}_1)|\vec{R}\times\vec{a}_1|-(\vec{R}\cdot\vec{a}_1)\nabla|\vec{R}\times\vec{a}_1|}{|\vec{R}\times\vec{a}_1|}\right)$$

$$=\frac{\sinh^{-1}\left(\frac{\vec{R}\cdot\vec{a}_1}{|\vec{R}\times\vec{a}_1|}\right)}{|\vec{a}_1|}\begin{bmatrix}(a_{1z}n_y-a_{1y}n_z)\\(a_{1x}n_z-a_{1z}n_x)\\(a_{1y}n_x-a_{1x}n_y)\end{bmatrix}$$

$$+\frac{(\vec{R}\times\vec{a}_1\cdot\vec{n})}{|\vec{a}_1|\sqrt{|\vec{R}\times\vec{a}_1|^2+(\vec{R}\cdot\vec{a}_1)^2}}\left\{\nabla(\vec{R}\cdot\vec{a}_1)-\frac{(\vec{R}\cdot\vec{a}_1)}{|\vec{R}\times\vec{a}_1|^2}\begin{bmatrix}a_{1z}(R_za_{1x}-R_xa_{1z})-a_{1y}(R_xa_{1y}-R_ya_{1x})\\-a_{1z}(R_ya_{1z}-R_za_{1y})+a_{1x}(R_xa_{1y}-R_ya_{1x})\\a_{1y}(R_ya_{1z}-R_za_{1y})-a_{1x}(R_za_{1x}-R_xa_{1z})\end{bmatrix}\right\}$$

$$=\frac{\sinh^{-1}\left(\frac{\vec{R}\cdot\vec{a}_1}{|\vec{R}\times\vec{a}_1|}\right)}{|\vec{a}_1|}\begin{bmatrix}(a_{1z}n_y-a_{1y}n_z)\\(a_{1x}n_z-a_{1z}n_x)\\(a_{1y}n_x-a_{1x}n_y)\end{bmatrix}$$

$$-\frac{(\vec{R}\times\vec{a}_1\cdot\vec{n})}{|\vec{a}_1|\sqrt{|\vec{R}\times\vec{a}_1|^2+(\vec{R}\cdot\vec{a}_1)^2}}\left\{\begin{pmatrix}a_{1x}\\a_{1y}\\a_{1z}\end{pmatrix}+\frac{(\vec{R}\cdot\vec{a}_1)}{|\vec{R}\times\vec{a}_1|^2}\begin{bmatrix}(-R_x(a_{1y}a_{1y}+a_{1z}a_{1z})+R_ya_{1x}a_{1y}+R_za_{1x}a_{1z})\\(R_xa_{1y}a_{1x}-R_y(a_{1x}a_{1x}+a_{1z}a_{1z})+R_za_{1y}a_{1z})\\(R_xa_{1z}a_{1x}+R_ya_{1z}a_{1y}-R_z(a_{1x}a_{1x}+a_{1y}a_{1y})\end{bmatrix}\right\}$$

(A-6)

Term 2:

$$\nabla(f_2) \equiv \begin{pmatrix} \partial f_2/\partial x \\ \partial f_2/\partial y \\ \partial f_2/\partial z \end{pmatrix} = \nabla\left(\vec{R}\times\vec{a}_2\cdot\vec{n}\frac{1}{\left|\vec{a}_2\right|}\right)\sinh^{-1}\left(\frac{\vec{R}\cdot\vec{a}_2}{\left|\vec{R}\times\vec{a}_2\right|}\right)+\left(\vec{R}\times\vec{a}_2\cdot\vec{n}\frac{1}{\left|\vec{a}_2\right|}\right)\nabla\left[\sinh^{-1}\left(\frac{\vec{R}\cdot\vec{a}_2}{\left|\vec{R}\times\vec{a}_2\right|}\right)\right]$$

$$=\frac{1}{\left|\vec{a}_2\right|}[\nabla(\vec{R}\times\vec{a}_2)\cdot\vec{n}]\sinh^{-1}\left(\frac{\vec{R}\cdot\vec{a}_2}{\left|\vec{R}\times\vec{a}_2\right|}\right)+\frac{\vec{R}\times\vec{a}_2\cdot\vec{n}}{\left|\vec{a}_2\right|}\frac{1}{\sqrt{1+\left(\frac{\vec{R}\cdot\vec{a}_2}{\left|\vec{R}\times\vec{a}_2\right|}\right)^2}}\nabla\left(\frac{\vec{R}\cdot\vec{a}_2}{\left|\vec{R}\times\vec{a}_2\right|}\right)$$

$$=\frac{\sinh^{-1}\left(\frac{\vec{R}\cdot\vec{a}_2}{\left|\vec{R}\times\vec{a}_2\right|}\right)}{\left|\vec{a}_2\right|}\left[\begin{pmatrix}(0,a_{2z},-a_{2y})\\(-a_{2z},0,a_{2x})\\(a_{2y},-a_{2x},0)\end{pmatrix}\cdot\vec{n}\right]+\frac{(\vec{R}\times\vec{a}_2\cdot\vec{n})\left|\vec{R}\times\vec{a}_2\right|}{\left|\vec{a}_2\right|\sqrt{\left|\vec{R}\times\vec{a}_2\right|^2+(\vec{R}\cdot\vec{a}_2)^2}}\left(\frac{\nabla(\vec{R}\cdot\vec{a}_2)\left|\vec{R}\times\vec{a}_2\right|-(\vec{R}\cdot\vec{a}_2)\nabla\left|\vec{R}\times\vec{a}_2\right|}{\left|\vec{R}\times\vec{a}_2\right|^2}\right)$$

$$=\frac{\sinh^{-1}\left(\frac{\vec{R}\cdot\vec{a}_2}{\left|\vec{R}\times\vec{a}_2\right|}\right)}{\left|\vec{a}_2\right|}\begin{bmatrix}(a_{2z}n_y-a_{2y}n_z)\\(a_{2x}n_z-a_{2z}n_x)\\(a_{2y}n_x-a_{2x}n_y)\end{bmatrix}+\frac{(\vec{R}\times\vec{a}_2\cdot\vec{n})}{\left|\vec{a}_2\right|\sqrt{\left|\vec{R}\times\vec{a}_2\right|^2+(\vec{R}\cdot\vec{a}_2)^2}}\left(\frac{\nabla(\vec{R}\cdot\vec{a}_2)\left|\vec{R}\times\vec{a}_2\right|-(\vec{R}\cdot\vec{a}_2)\nabla\left|\vec{R}\times\vec{a}_2\right|}{\left|\vec{R}\times\vec{a}_2\right|}\right)$$

$$=\frac{\sinh^{-1}\left(\frac{\vec{R}\cdot\vec{a}_2}{\left|\vec{R}\times\vec{a}_2\right|}\right)}{\left|\vec{a}_2\right|}\begin{bmatrix}(a_{2z}n_y-a_{2y}n_z)\\(a_{2x}n_z-a_{2z}n_x)\\(a_{2y}n_x-a_{2x}n_y)\end{bmatrix}$$

$$+\frac{(\vec{R}\times\vec{a}_2\cdot\vec{n})}{\left|\vec{a}_2\right|\sqrt{\left|\vec{R}\times\vec{a}_2\right|^2+(\vec{R}\cdot\vec{a}_2)^2}}\left\{\nabla(\vec{R}\cdot\vec{a}_2)-\frac{(\vec{R}\cdot\vec{a}_2)}{\left|\vec{R}\times\vec{a}_2\right|^2}\begin{bmatrix}a_{2z}(R_za_{2x}-R_xa_{2z})-a_{2y}(R_xa_{2y}-R_ya_{2x})\\-a_{2z}(R_ya_{2z}-R_za_{2y})+a_{2x}(R_xa_{2y}-R_ya_{2x})\\a_{2y}(R_ya_{2z}-R_za_{2y})-a_{2x}(R_za_{2x}-R_xa_{2z})\end{bmatrix}\right\}$$

$$=\frac{\sinh^{-1}\left(\frac{\vec{R}\cdot\vec{a}_2}{\left|\vec{R}\times\vec{a}_2\right|}\right)}{\left|\vec{a}_2\right|}\begin{bmatrix}(a_{2z}n_y-a_{2y}n_z)\\(a_{2x}n_z-a_{2z}n_x)\\(a_{2y}n_x-a_{2x}n_y)\end{bmatrix}$$

$$-\frac{(\vec{R}\times\vec{a}_2\cdot\vec{n})}{\left|\vec{a}_2\right|\sqrt{\left|\vec{R}\times\vec{a}_2\right|^2+(\vec{R}\cdot\vec{a}_2)^2}}\left\{\begin{pmatrix}a_{2x}\\a_{2y}\\a_{2z}\end{pmatrix}+\frac{(\vec{R}\cdot\vec{a}_2)}{\left|\vec{R}\times\vec{a}_2\right|^2}\begin{bmatrix}(-R_x(a_{2y}a_{2y}+a_{2z}a_{2z})+R_ya_{2x}a_{2y}+R_za_{2x}a_{2z})\\(R_xa_{2y}a_{2x}-R_y(a_{2x}a_{2x}+a_{2z}a_{2z})+R_za_{2y}a_{2z})\\(R_xa_{2z}a_{2x}+R_ya_{2z}a_{2y}-R_z(a_{2x}a_{2x}+a_{2y}a_{2y})\end{bmatrix}\right\}$$

(A-7)

Term 3:

$$\nabla[(\vec{R}\cdot\vec{n})g(x,y,z)] = \nabla(\vec{R}\cdot\vec{n})g + (\vec{R}\cdot\vec{n})\nabla(g)$$
$$-n_x$$
$$= (-n_y)g + (\vec{R}\cdot\vec{n})\nabla(g)$$
$$-n_z$$

(A-8)

Appendix B Phase Averaged Pressure Coefficients

No of Figure	J	X/C	Z/R_p
B-1	0.548	0.381, 0.303, 0.207, 0.0, -0.164, -0.267, -0.354	1.141
B-2	0.548	0.381, 0.303, 0.207, 0.0, -0.164, -0.267, -0.354	1.067
B-3	0.548	0.381, 0.303, 0.207, 0.0, -0.164, -0.267, -0.354	0.993
B-3	0.548	0.381, 0.303, 0.207, 0.0, -0.164, -0.267, -0.354	0.919
B-5	0.548	0.381, 0.303, 0.207, 0.0, -0.164, -0.267, -0.354	0.844
B-6	0.548	0.381, 0.303, 0.207, 0.0, -0.164, -0.267, -0.354	0.770
B-7	0.548	0.381, 0.303, 0.207, 0.0, -0.164, -0.267, -0.354	0.696
B-8	0.548	0.381, 0.303, 0.207, 0.0, -0.164, -0.267, -0.354	0.622
B-9	0.676	0.381, 0.303, 0.207, 0.0, -0.164, -0.267, -0.354	1.141
B-10	0. 676	0.381, 0.303, 0.207, 0.0, -0.164, -0.267, -0.354	1.067
B-11	0. 676	0.381, 0.303, 0.207, 0.0, -0.164, -0.267, -0.354	0.993
B-12	0. 676	0.381, 0.303, 0.207, 0.0, -0.164, -0.267, -0.354	0.919
B-13	0. 676	0.381, 0.303, 0.207, 0.0, -0.164, -0.267, -0.354	0.844
B-14	0. 676	0.381, 0.303, 0.207, 0.0, -0.164, -0.267, -0.354	0.770
B-15	0. 676	0.381, 0.303, 0.207, 0.0, -0.164, -0.267, -0.354	0.696
B-16	0. 676	0.381, 0.303, 0.207, 0.0, -0.164, -0.267, -0.354	0.622
B-17	0.741	0.381, 0.303, 0.207, 0.0, -0.164, -0.267, -0.354	1.141
B-18	0. 741	0.381, 0.303, 0.207, 0.0, -0.164, -0.267, -0.354	1.067
B-19	0. 741	0.381, 0.303, 0.207, 0.0, -0.164, -0.267, -0.354	0.993
B-20	0. 741	0.381, 0.303, 0.207, 0.0, -0.164, -0.267, -0.354	0.919
B-21	0. 741	0.381, 0.303, 0.207, 0.0, -0.164, -0.267, -0.354	0.844
B-22	0. 741	0.381, 0.303, 0.207, 0.0, -0.164, -0.267, -0.354	0.770
B-23	0. 741	0.381, 0.303, 0.207, 0.0, -0.164, -0.267, -0.354	0.696
B-24	0. 741	0.381, 0.303, 0.207, 0.0, -0.164, -0.267, -0.354	0.622
B-25	0.805	0.381, 0.303, 0.207, 0.0, -0.164, -0.267, -0.354	1.141
B-26	0. 805	0.381, 0.303, 0.207, 0.0, -0.164, -0.267, -0.354	1.067
B-27	0. 805	0.381, 0.303, 0.207, 0.0, -0.164, -0.267, -0.354	0.993
B-28	0. 805	0.381, 0.303, 0.207, 0.0, -0.164, -0.267, -0.354	0.919
B-29	0. 805	0.381, 0.303, 0.207, 0.0, -0.164, -0.267, -0.354	0.844
B-30	0. 805	0.381, 0.303, 0.207, 0.0, -0.164, -0.267, -0.354	0.770
B-31	0. 805	0.381, 0.303, 0.207, 0.0, -0.164, -0.267, -0.354	0.696
B-32	0. 805	0.381, 0.303, 0.207, 0.0, -0.164, -0.267, -0.354	0.622
B-33	0.870	0.381, 0.303, 0.207, 0.0, -0.164, -0.267, -0.354	1.141
B-34	0. 870	0.381, 0.303, 0.207, 0.0, -0.164, -0.267, -0.354	1.067
B-35	0. 870	0.381, 0.303, 0.207, 0.0, -0.164, -0.267, -0.354	0.993
B-36	0. 870	0.381, 0.303, 0.207, 0.0, -0.164, -0.267, -0.354	0.919
B-37	0. 870	0.381, 0.303, 0.207, 0.0, -0.164, -0.267, -0.354	0.844
B-38	0. 870	0.381, 0.303, 0.207, 0.0, -0.164, -0.267, -0.354	0.770
B-39	0. 870	0.381, 0.303, 0.207, 0.0, -0.164, -0.267, -0.354	0.696
B-40	0. 870	0.381, 0.303, 0.207, 0.0, -0.164, -0.267, -0.354	0.622

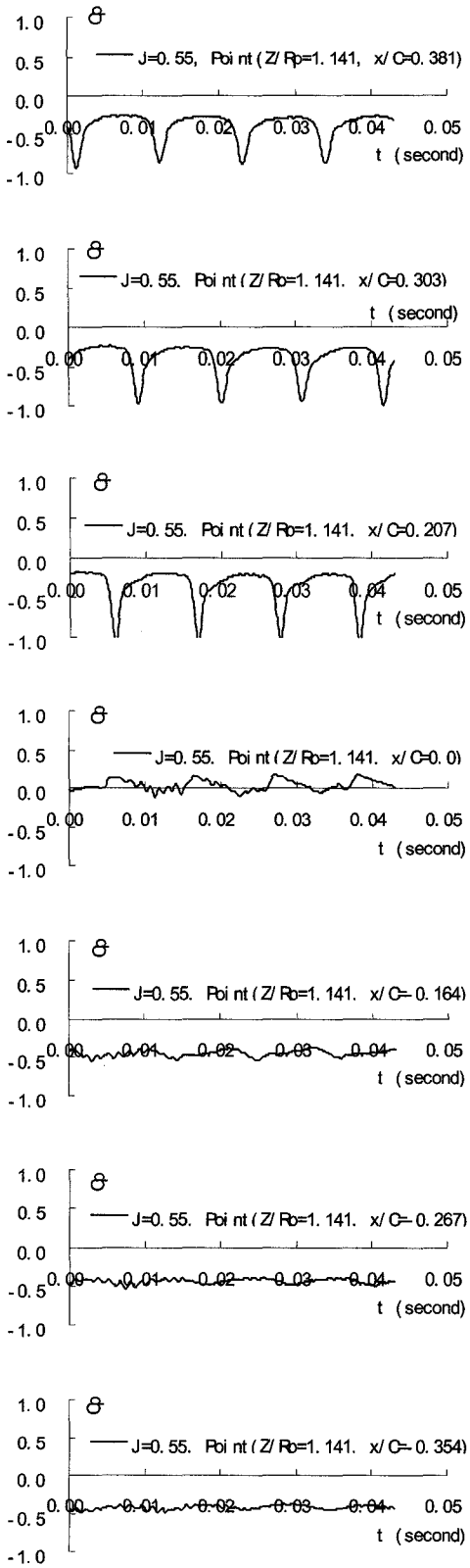

Figure B-1 $J = 0.548$, $Z / R_p = 1.141$

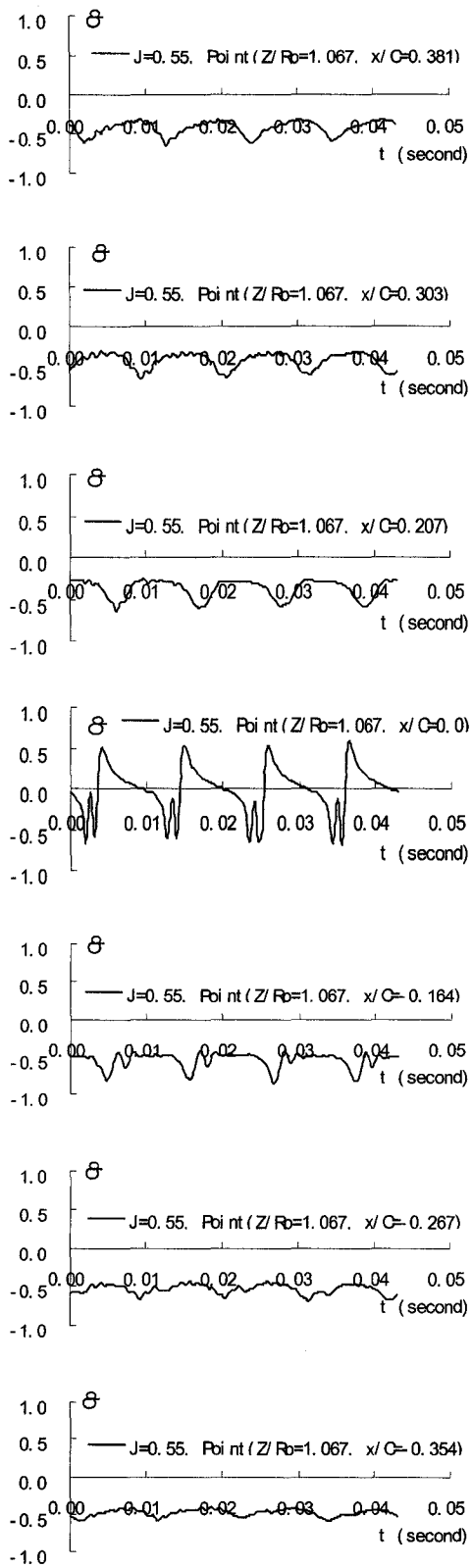

Figure B-2 $J = 0.548$, $Z / R_p = 1.067$

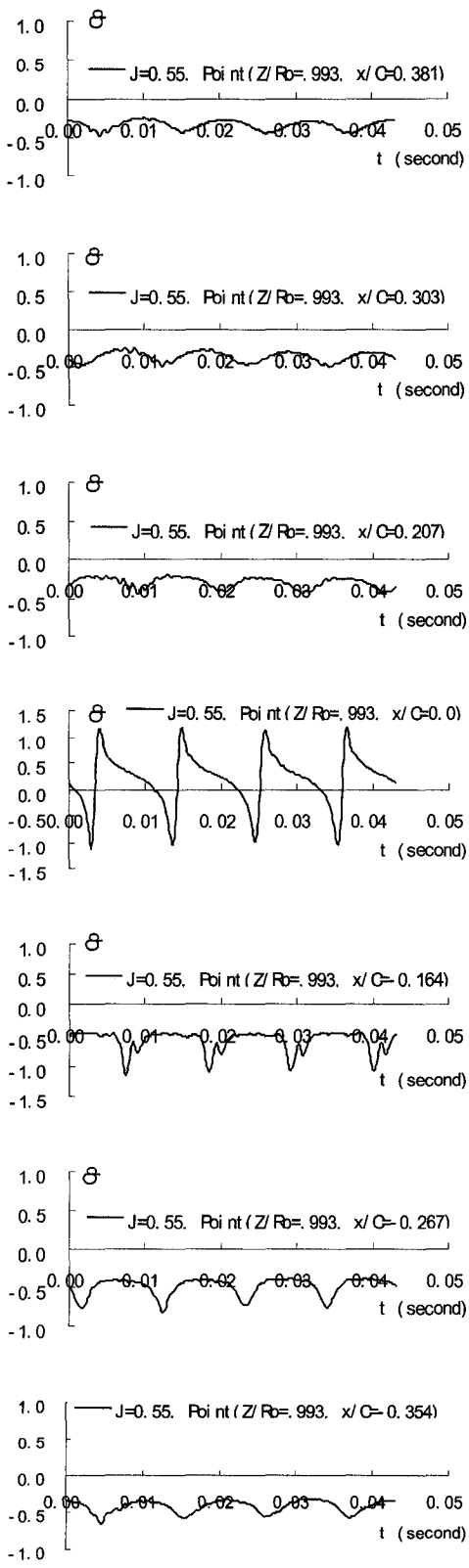

Figure B-3 $J = 0.548$, $Z / R_p = 0.993$

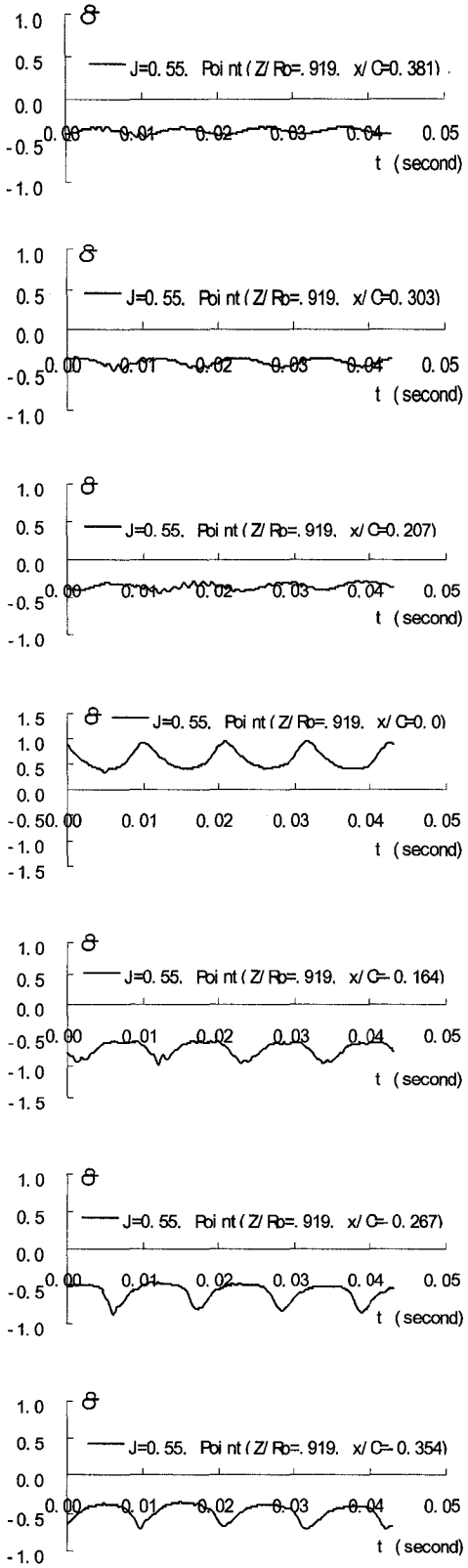

Figure B-4 $J = 0.548$, $Z / R_p = 0.919$

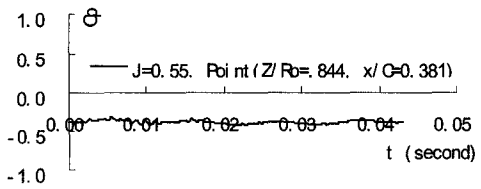

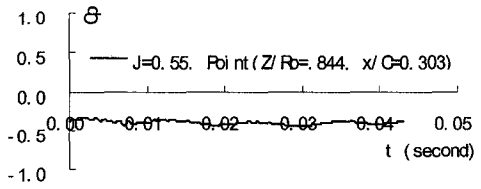

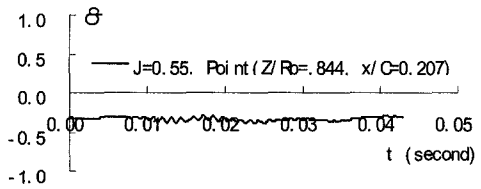

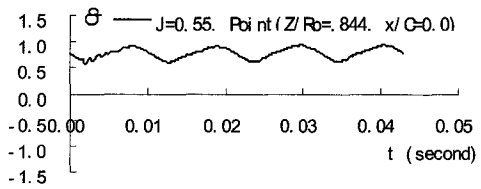

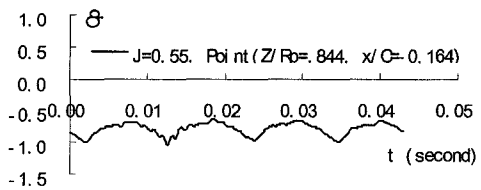

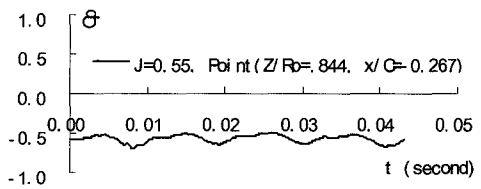

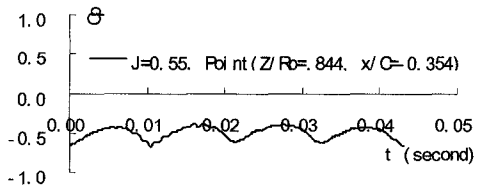

Figure B-5 $J = 0.548$, $Z / R_p = 0.844$

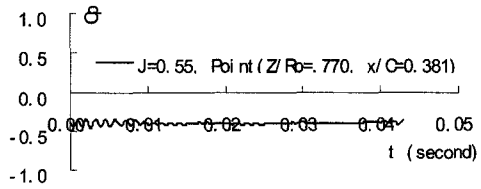

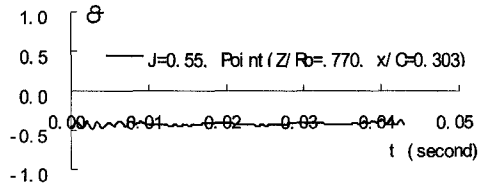

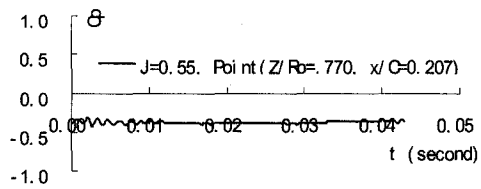

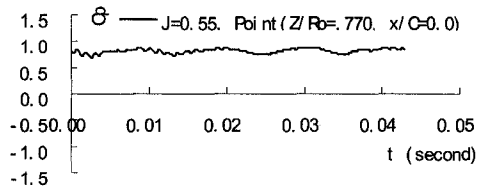

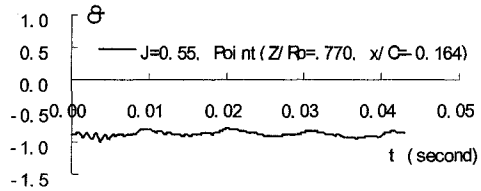

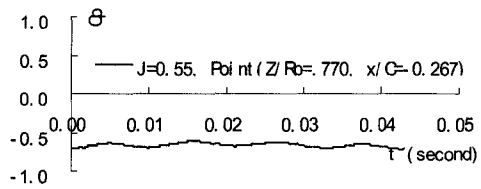

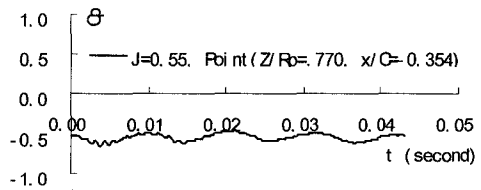

Figure B-6 $J = 0.548$, $Z / R_p = 0.770$

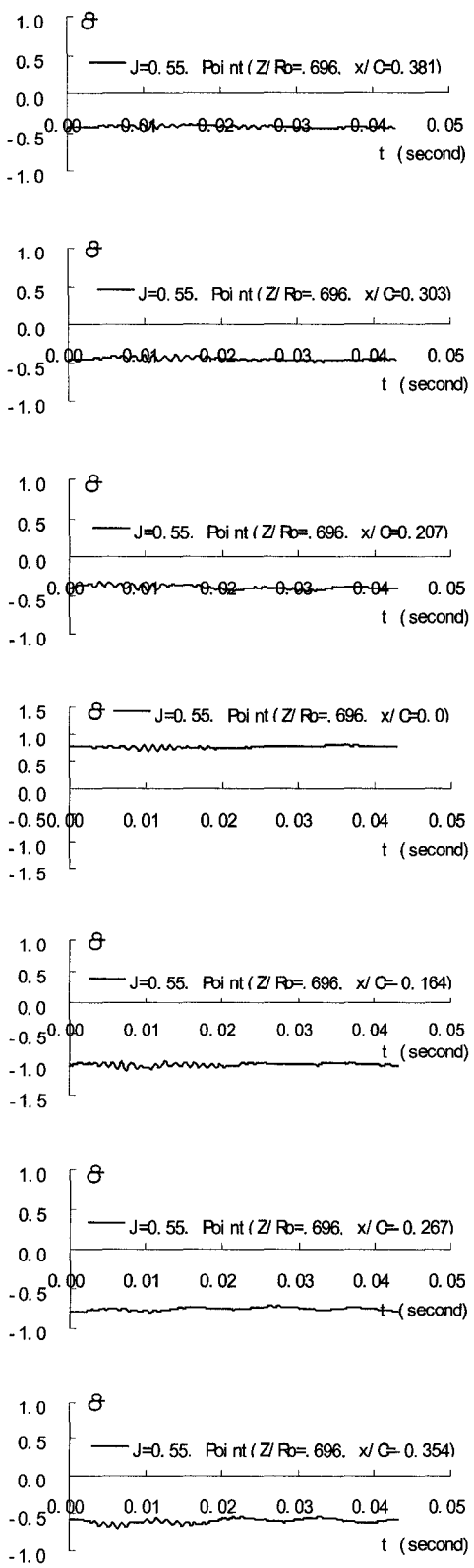

Figure B-7 $J = 0.548$, $Z / R_p = 0.696$

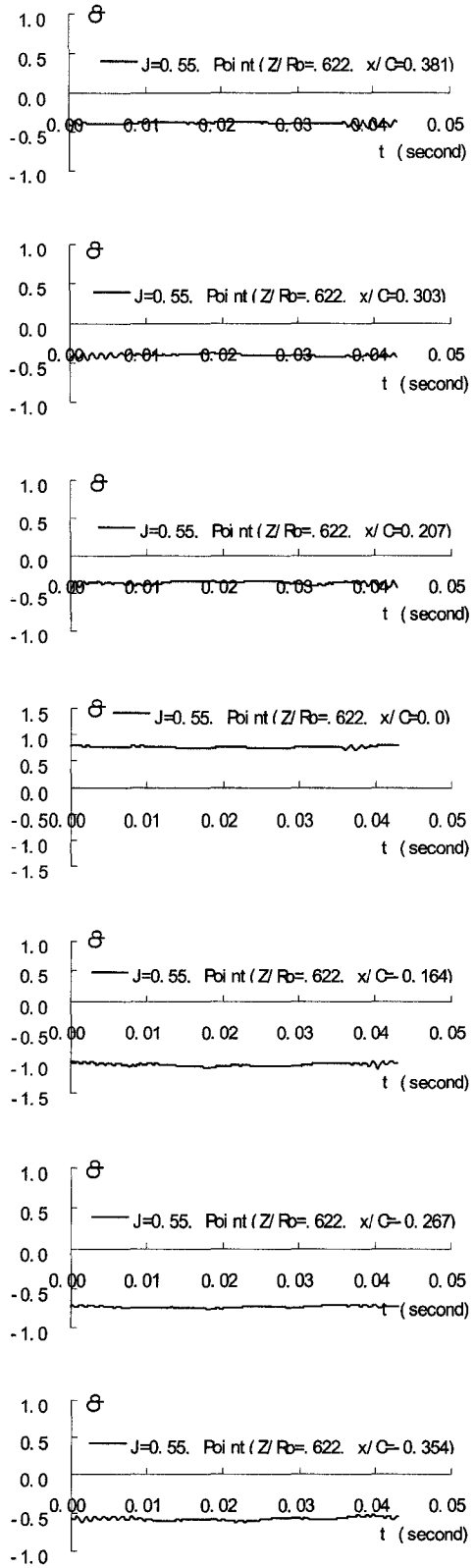

Figure B-8 $J = 0.548$, $Z / R_p = 0.622$

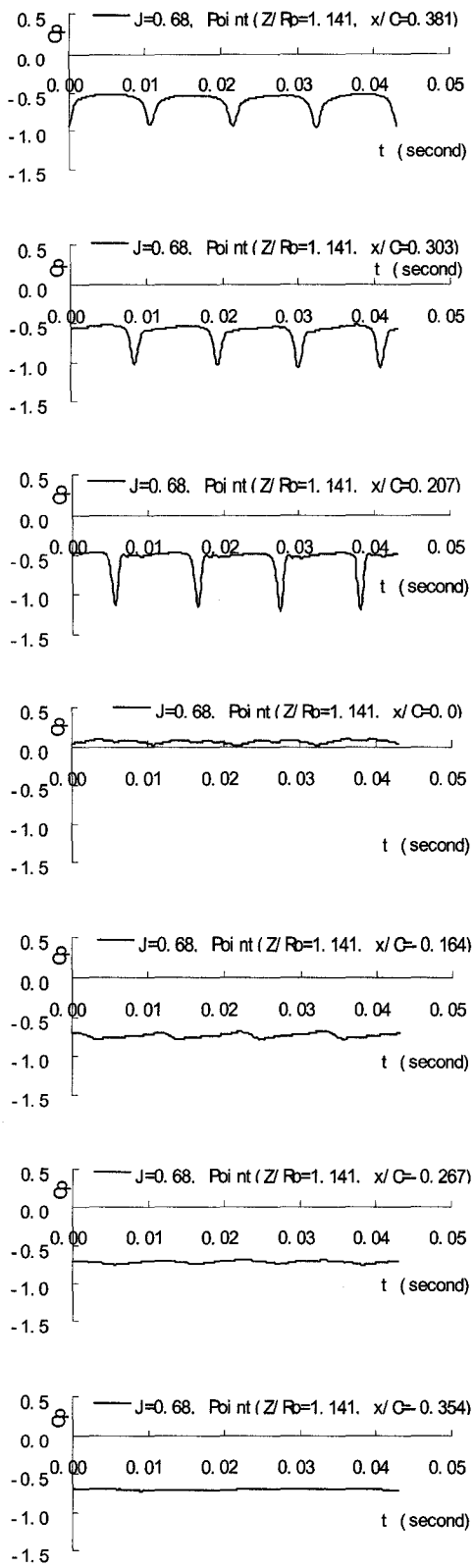

Figure B-9 $J = 0.676$, $Z / R_p = 1.141$

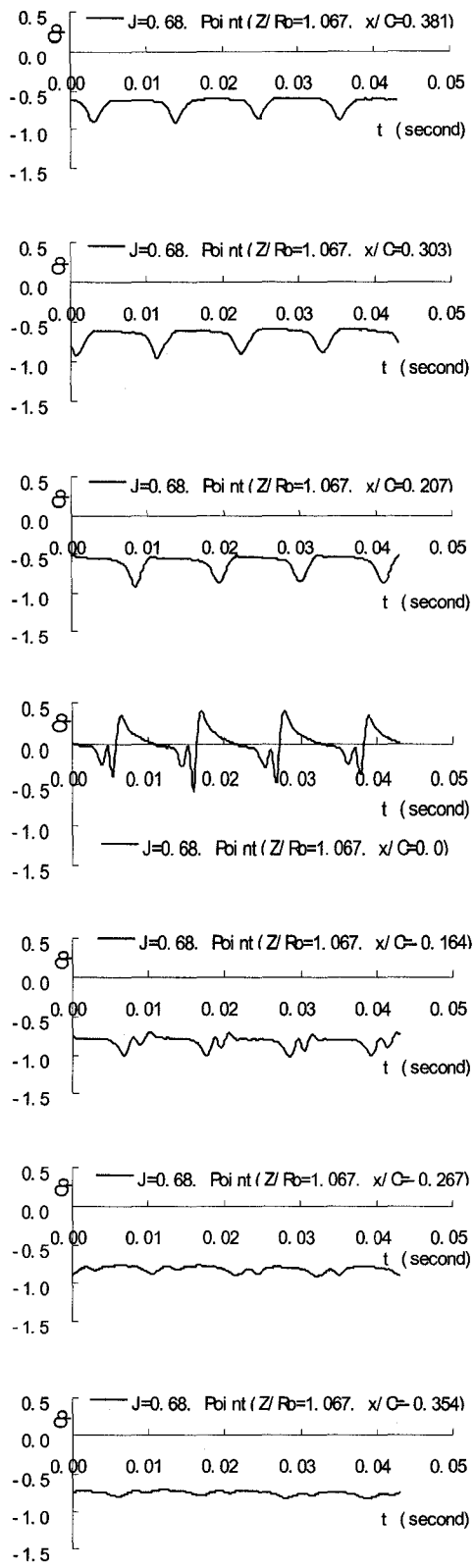

Figure B-10 $J = 0.676$, $Z / R_p = 1.067$

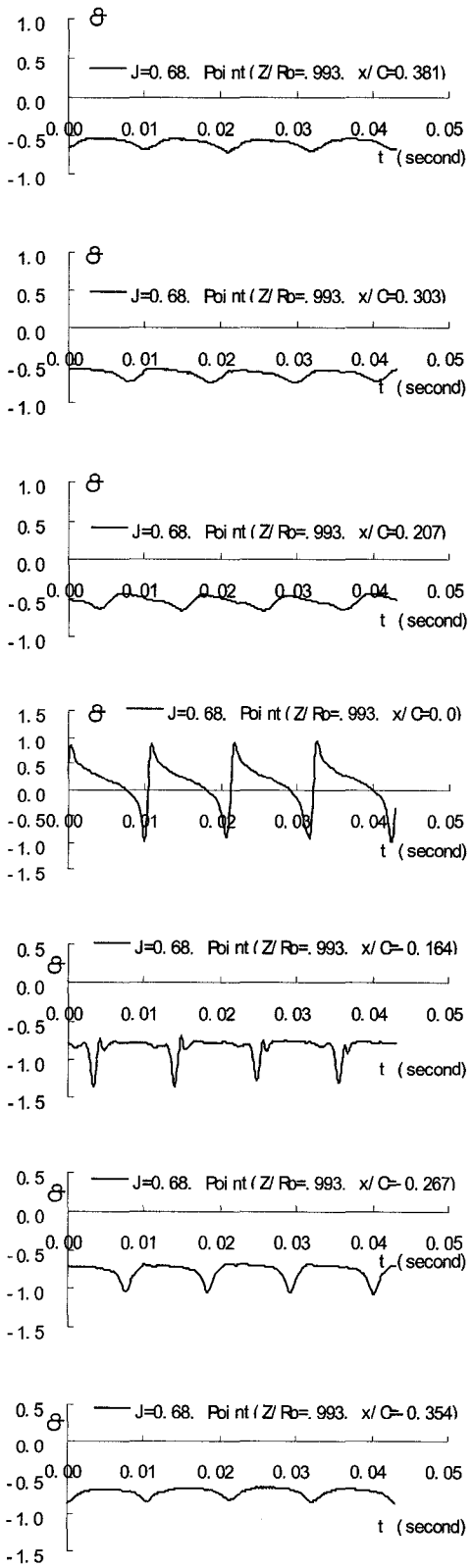

Figure B-11 $J = 0.676$, $Z/R_p = 0.993$

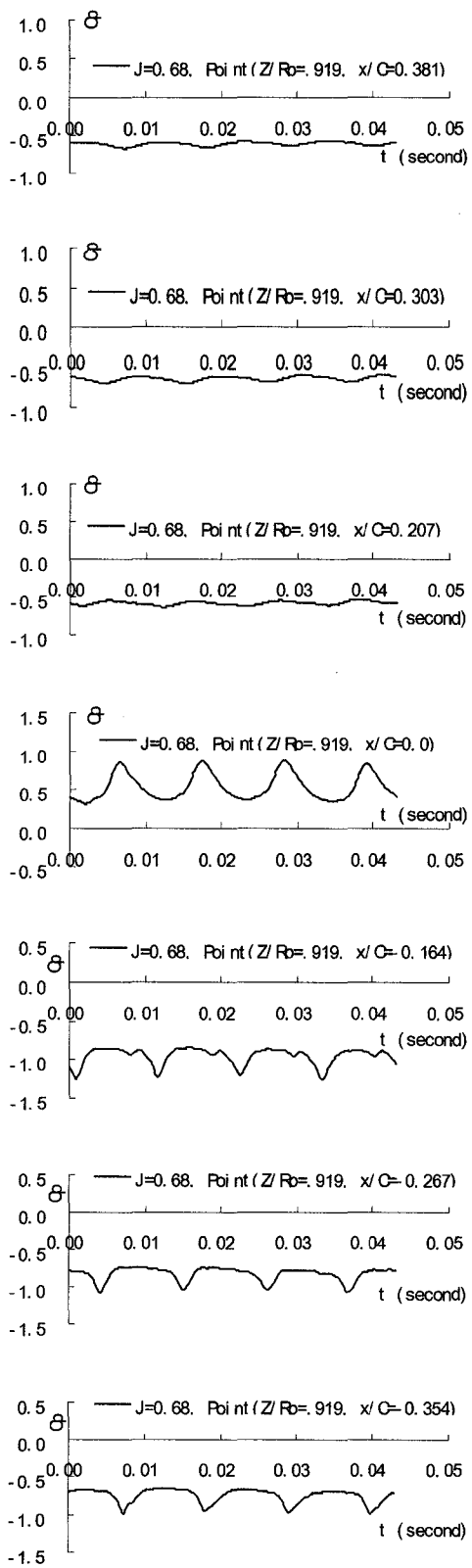

Figure B-12 $J = 0.676$, $Z/R_p = 0.919$

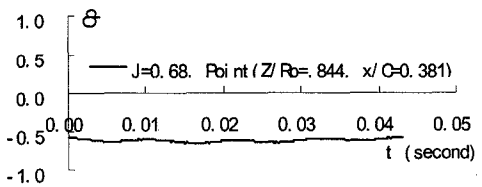

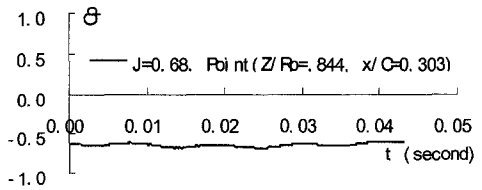

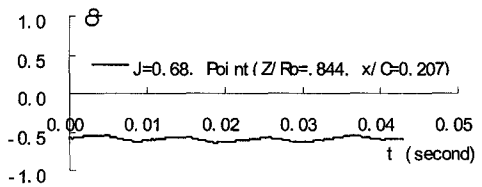

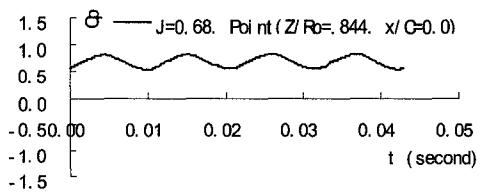

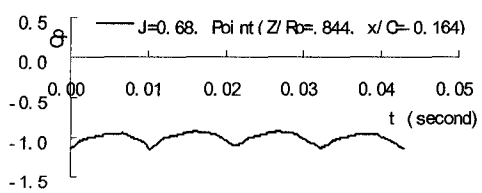

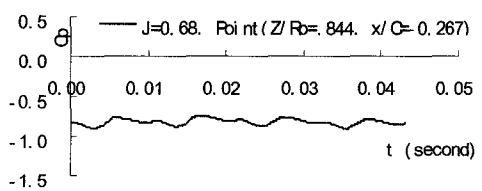

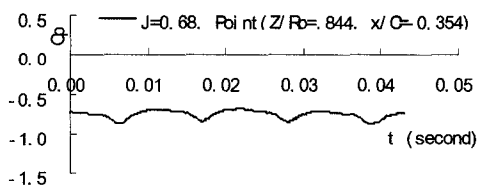

Figure B-13 $J = 0.676$, $Z / R_p = 0.844$

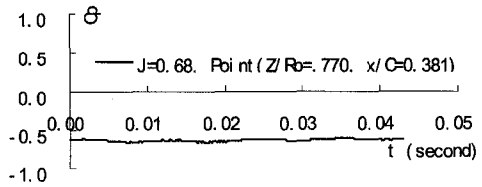

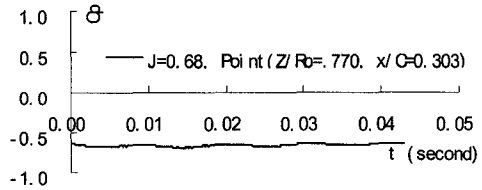

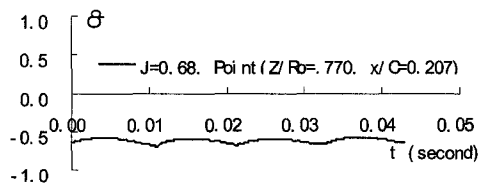

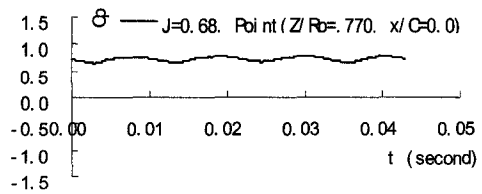

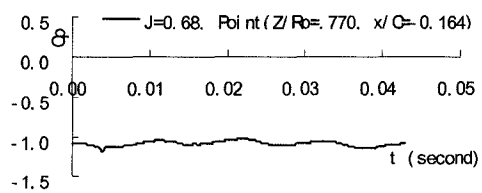

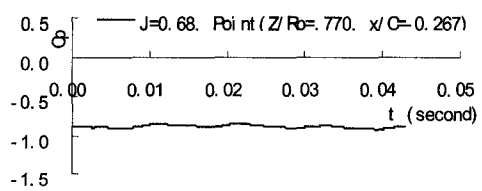

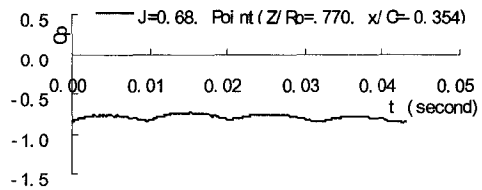

Figure B-14 $J = 0.676$, $Z / R_p = 0.770$

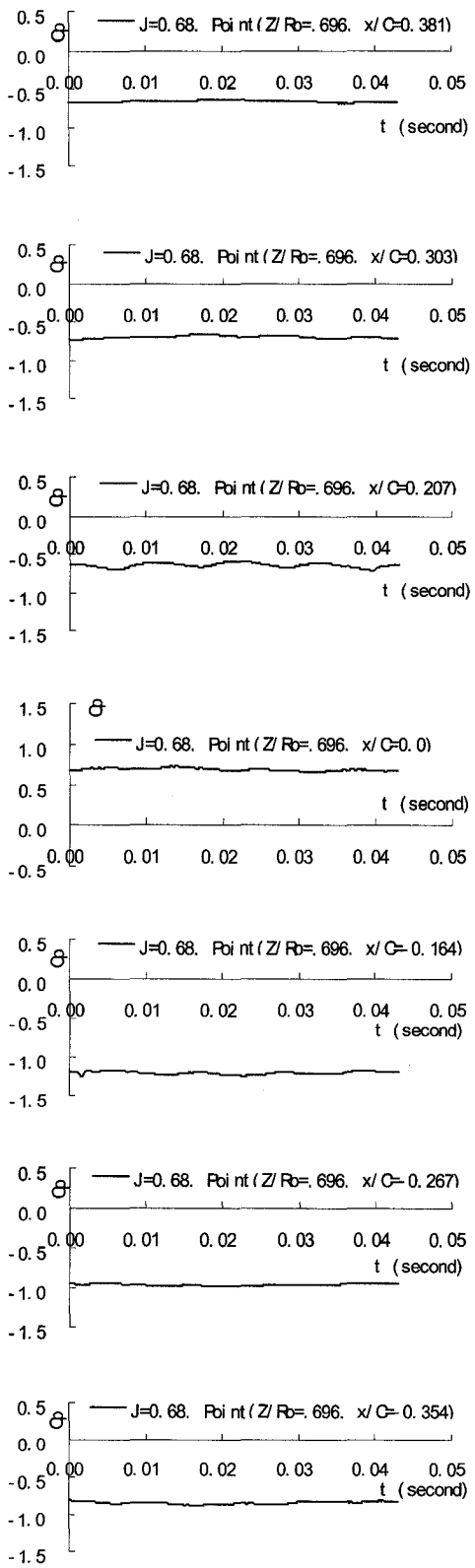

Figure B-15 $J = 0.676$, $Z / R_p = 0.696$

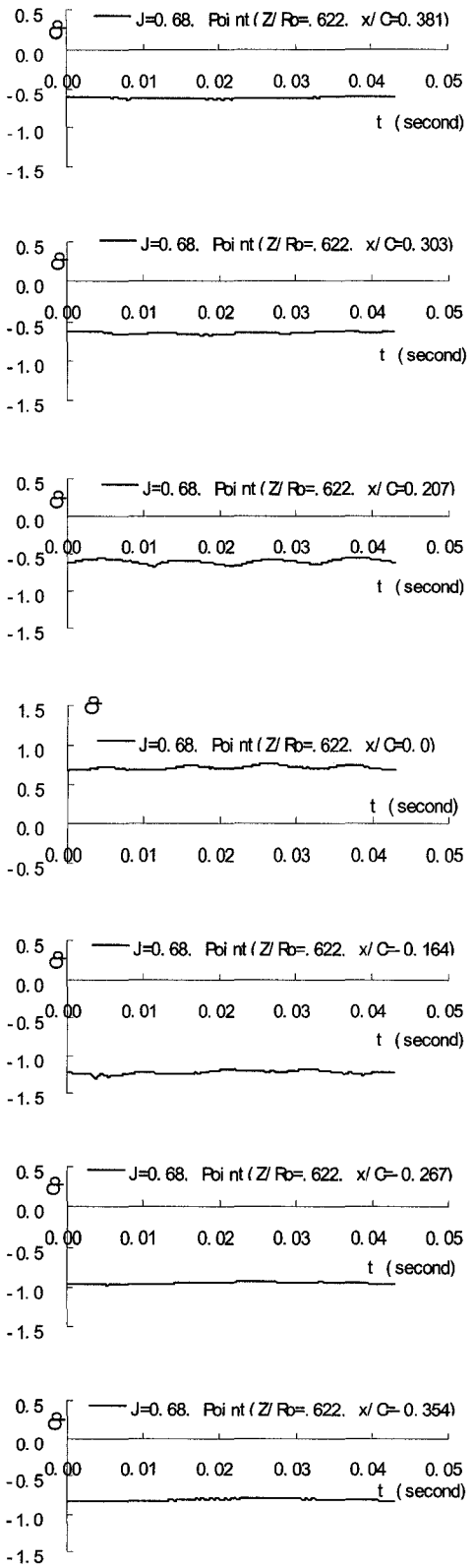

Figure B-16 $J = 0.676$, $Z / R_p = 0.622$

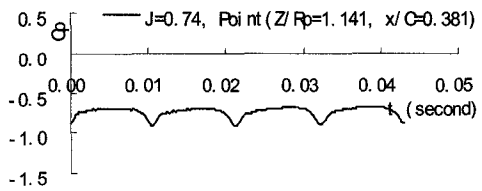

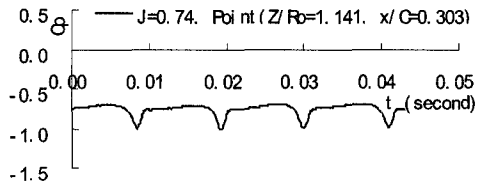

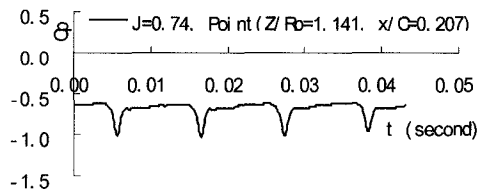

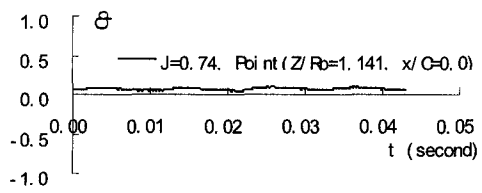

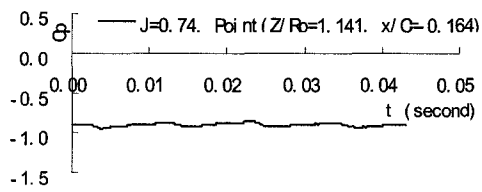

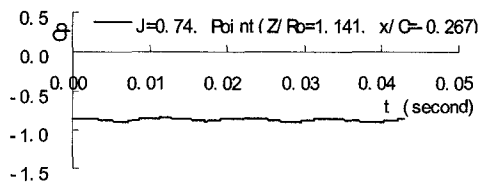

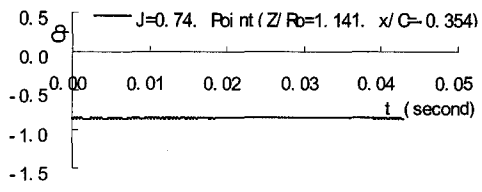

Figure B-17 $J = 0.741$, $Z / R_p = 1.141$

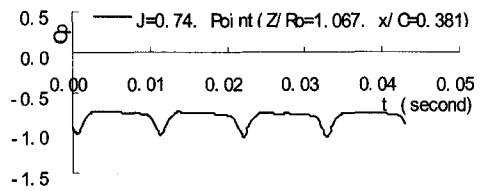

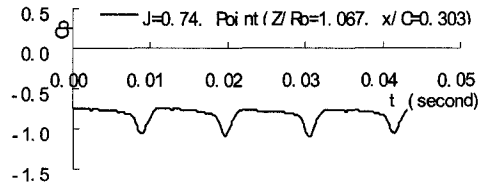

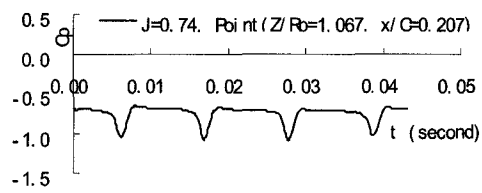

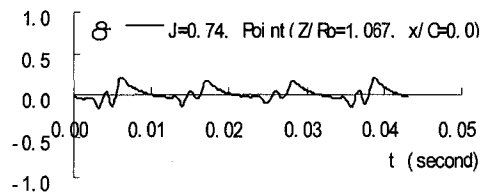

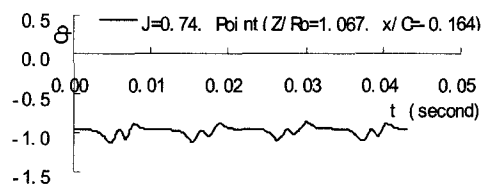

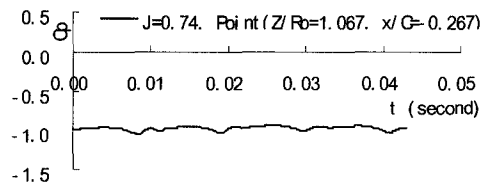

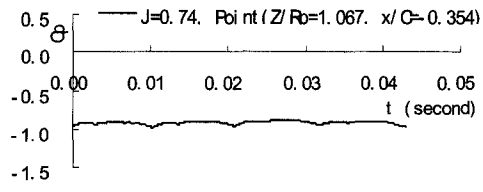

Figure B-18 $J = 0.741$, $Z / R_p = 1.067$

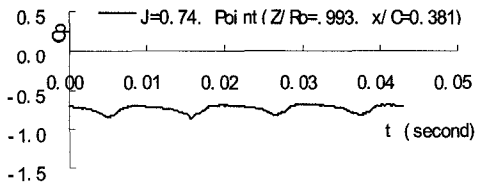

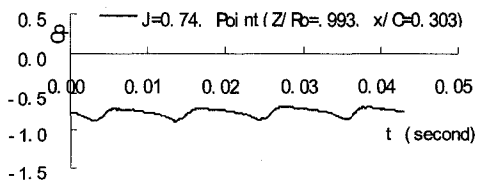

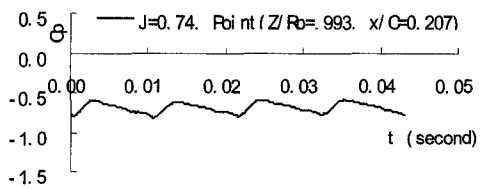

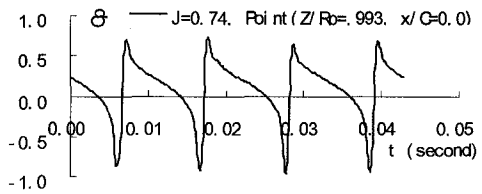

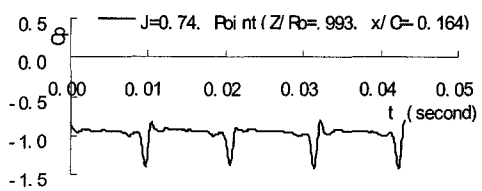

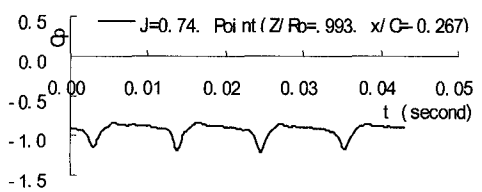

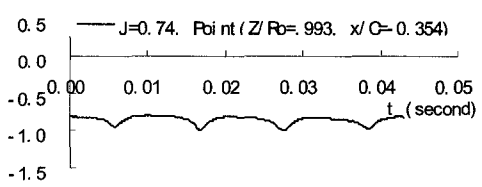

Figure B-19 $J = 0.741$, $Z / R_p = 0.993$

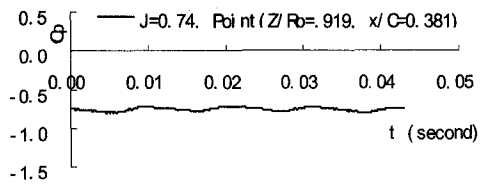

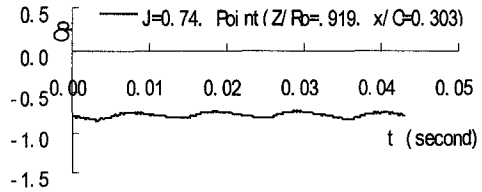

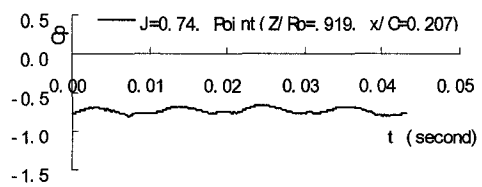

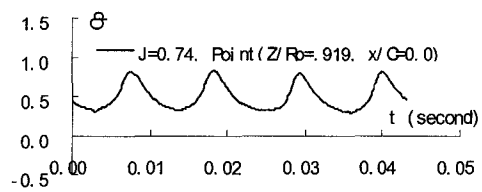

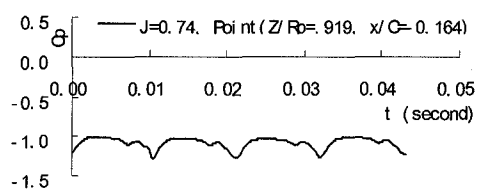

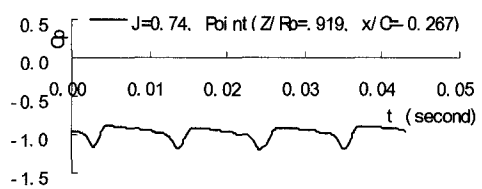

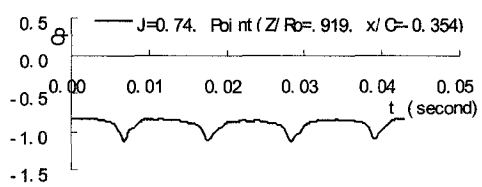

Figure B-20 $J = 0.741$, $Z / R_p = 0.919$

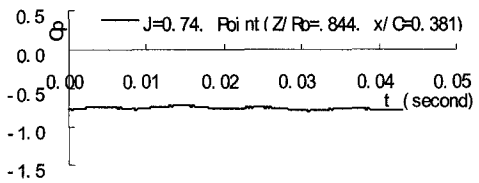

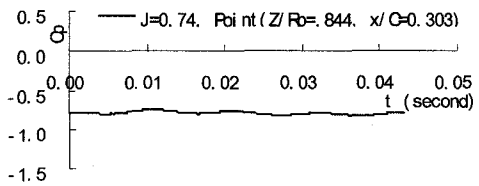

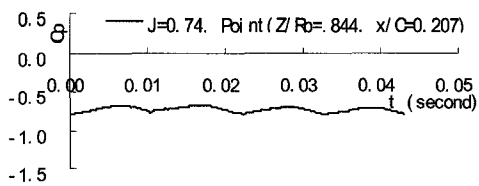

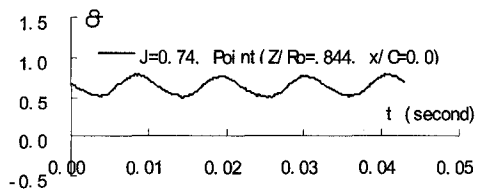

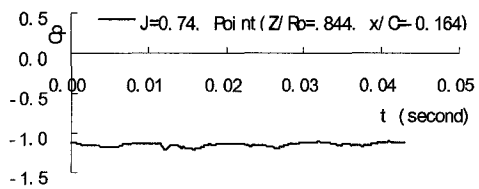

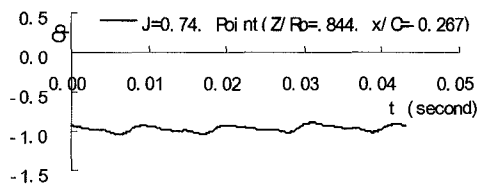

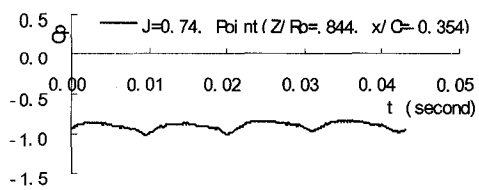

Figure B-21 $J = 0.741$, $Z / R_p = 0.844$

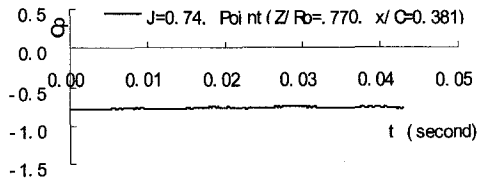

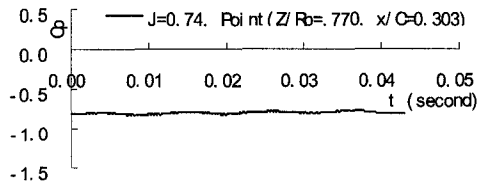

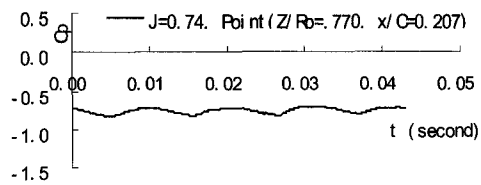

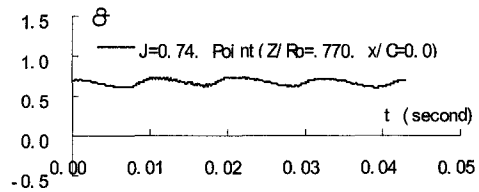

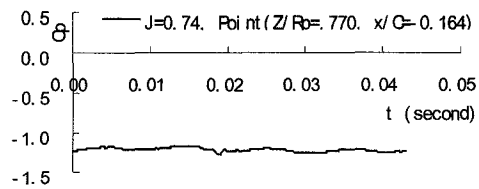

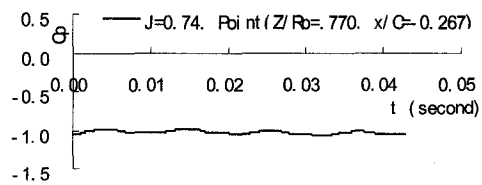

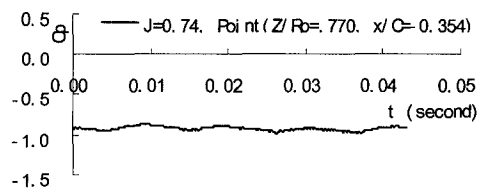

Figure B-22 $J = 0.741$, $Z / R_p = 0.770$

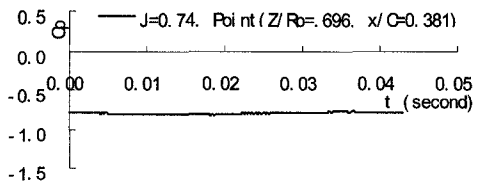

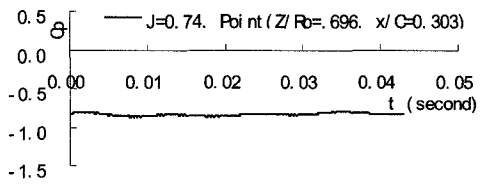

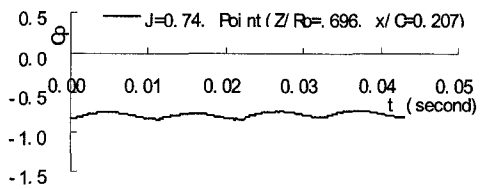

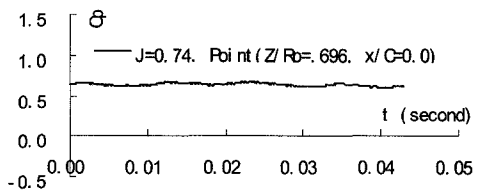

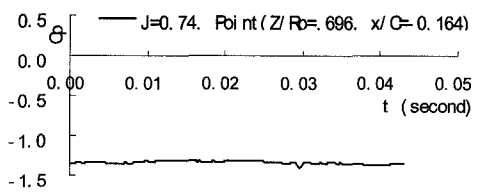

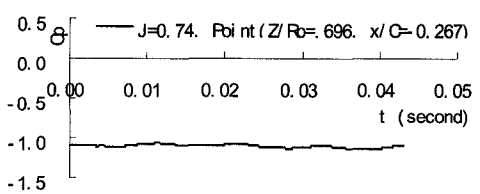

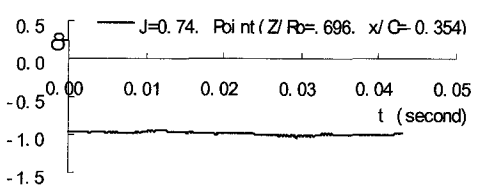

Figure B-23 $J = 0.741$, $Z / R_p = 0.696$

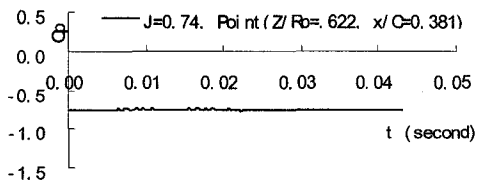

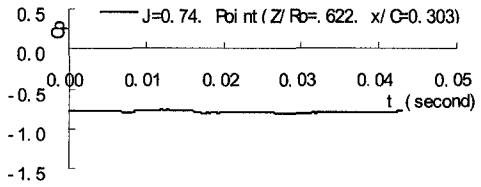

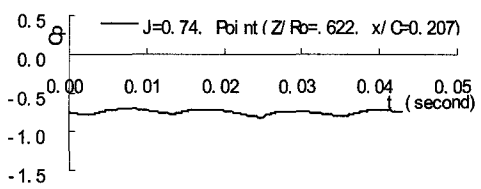

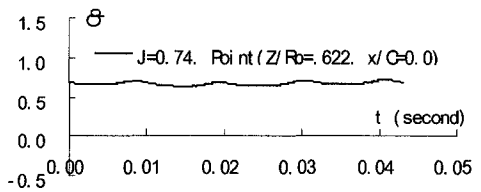

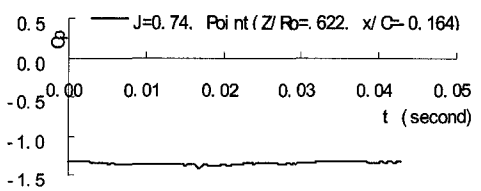

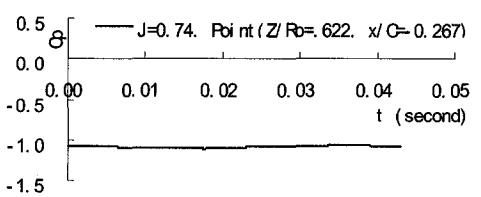

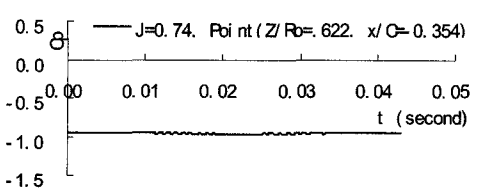

Figure B-24 $J = 0.741$, $Z / R_p = 0.622$

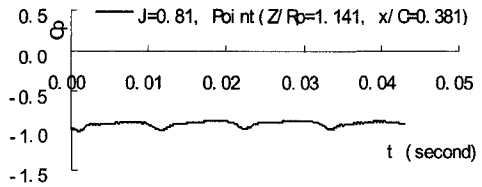

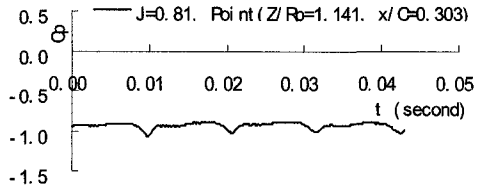

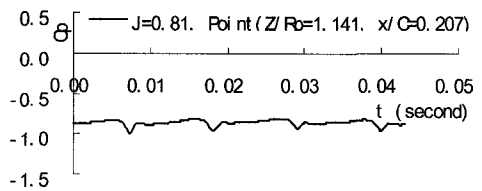

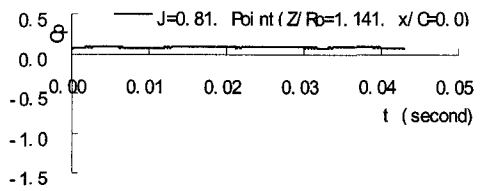

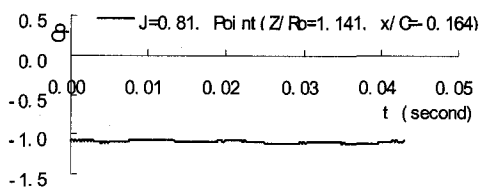

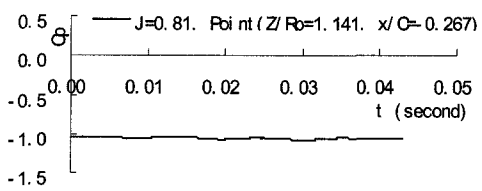

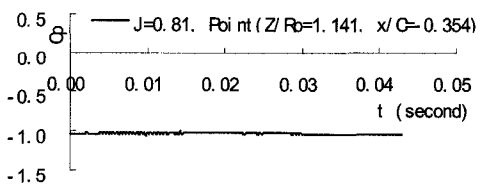

Figure B-25 $J = 0.805$, $Z / R_p = 1.141$

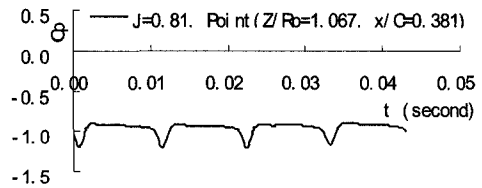

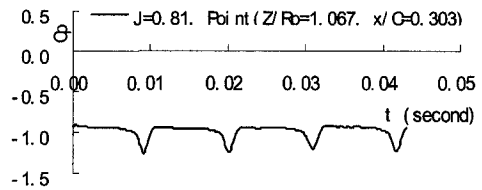

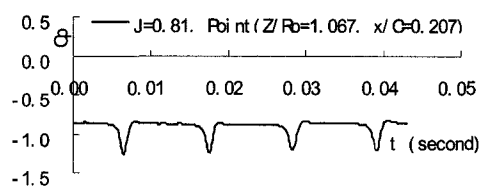

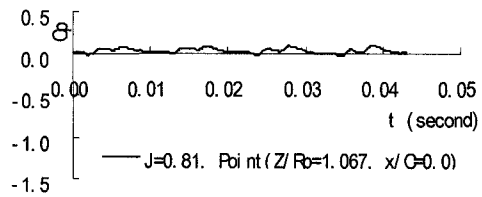

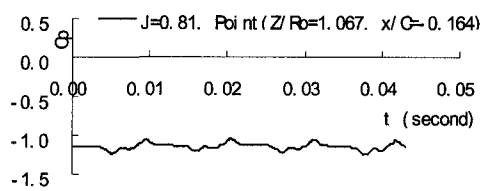

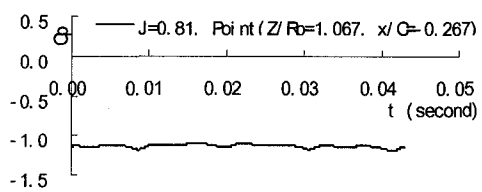

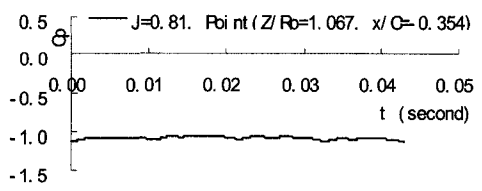

Figure B-26 $J = 0.805$, $Z / R_p = 1.067$

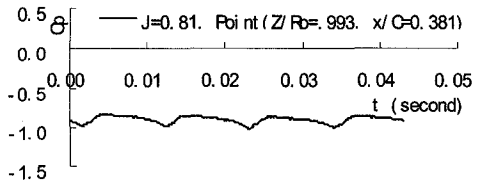

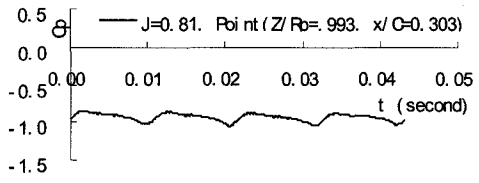

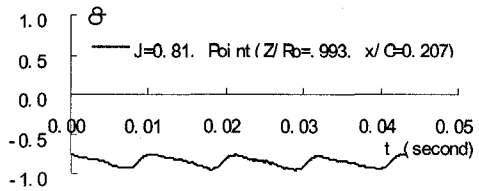

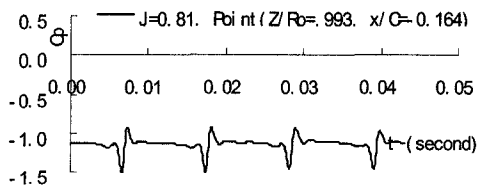

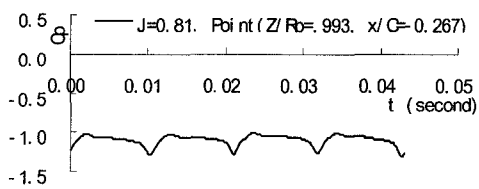

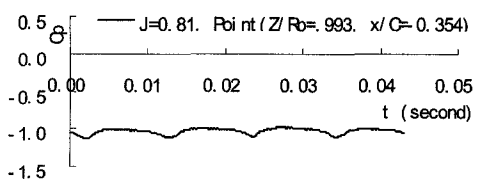

Figure B-27 $J = 0.805$, $Z / R_p = 0.993$

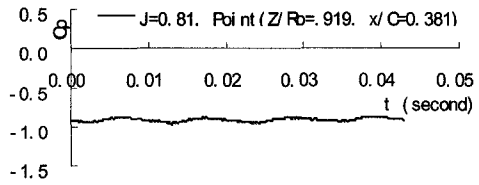

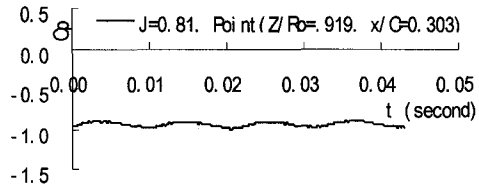

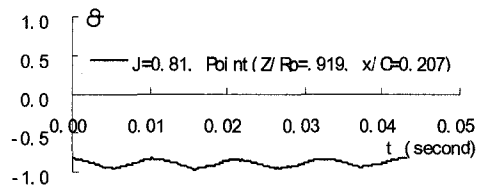

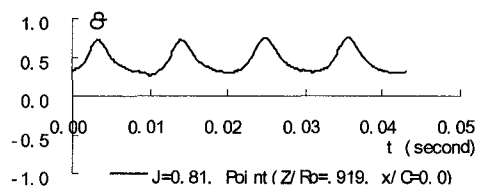

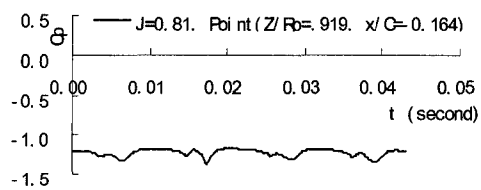

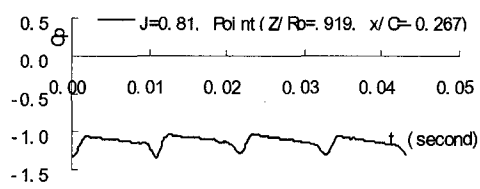

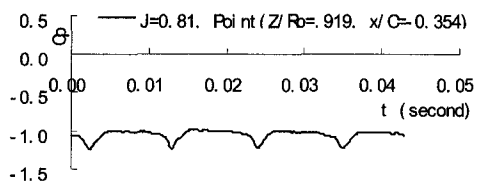

Figure B-28 $J = 0.805$, $Z / R_p = 0.919$

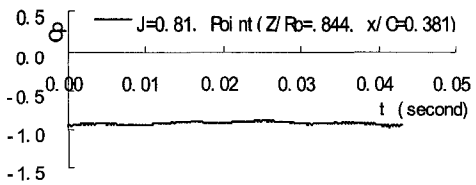

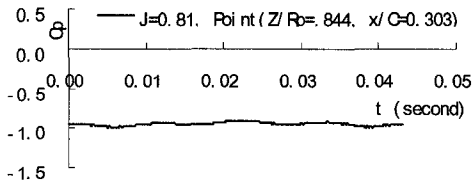

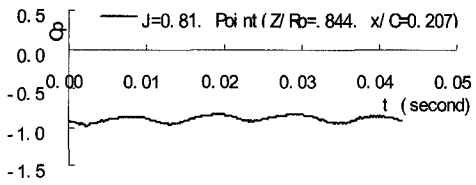

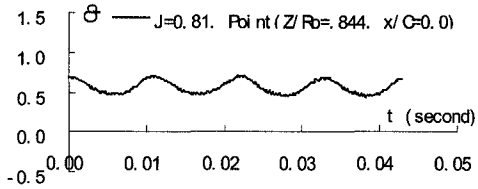

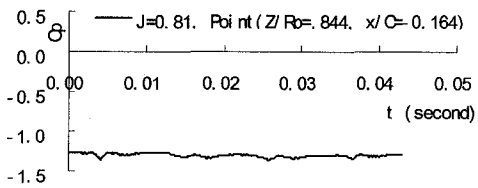

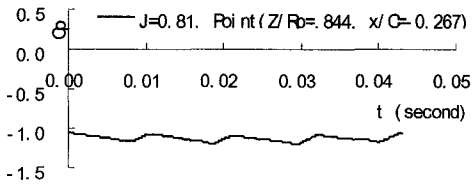

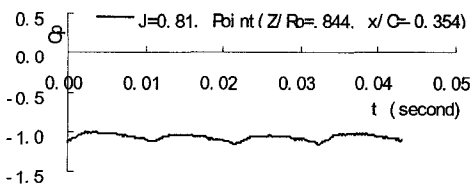

Figure B-29 $J = 0.805$, $Z/R_p = 0.844$

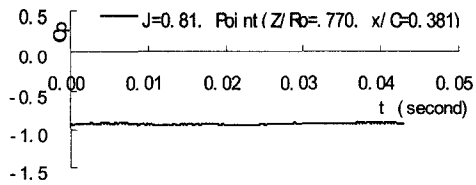

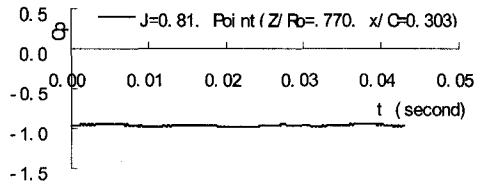

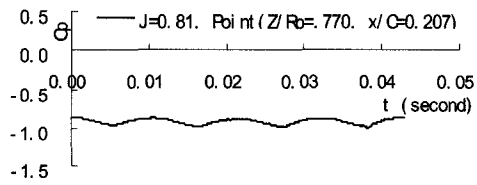

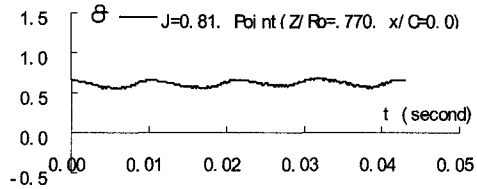

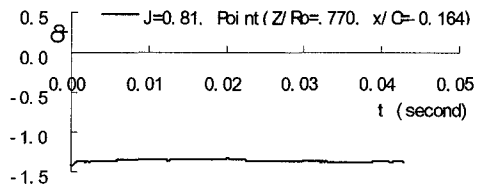

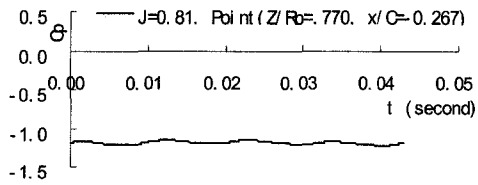

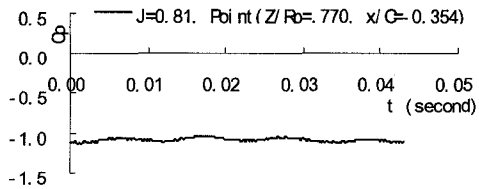

Figure B-30 $J = 0.805$, $Z/R_p = 0.770$

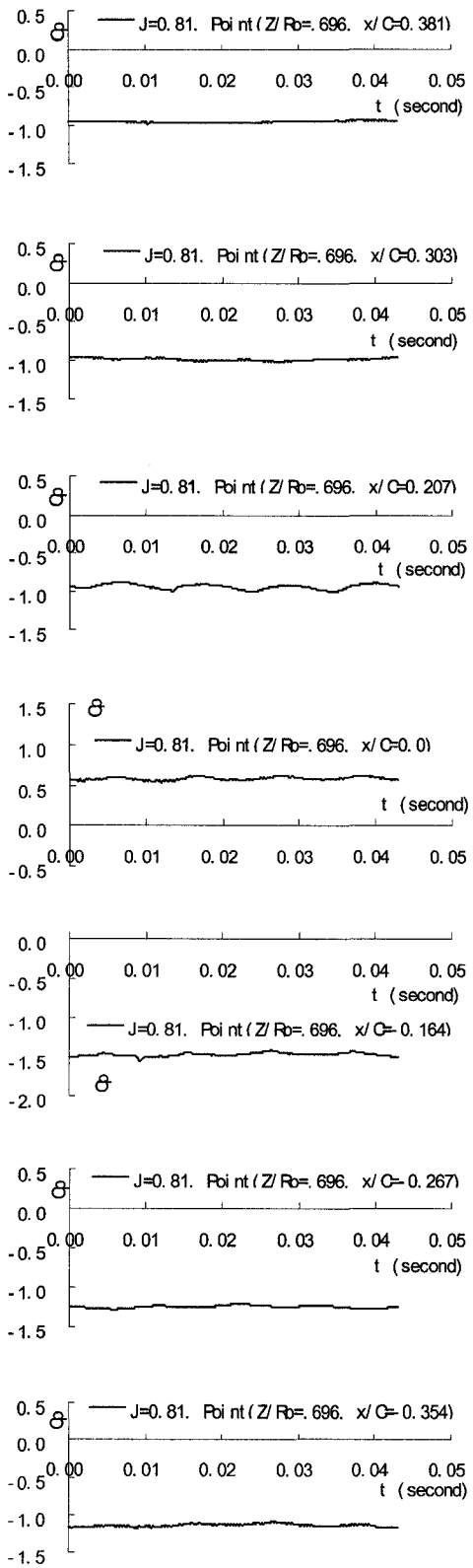

Figure B-31 $J = 0.805$, $Z / R_p = 0.696$

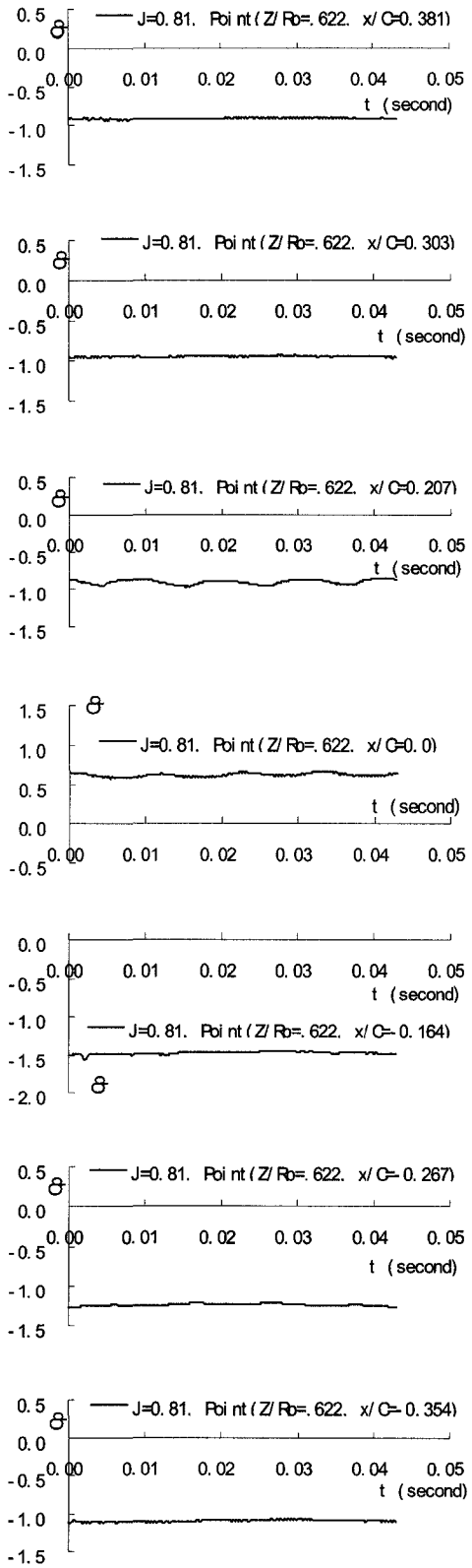

Figure B-32 $J = 0.805$, $Z / R_p = 0.622$

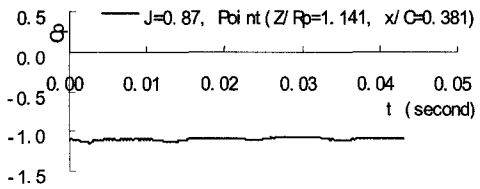

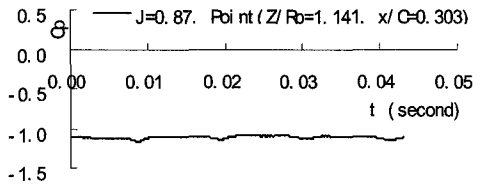

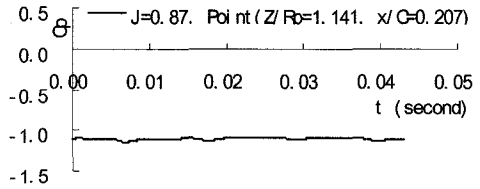

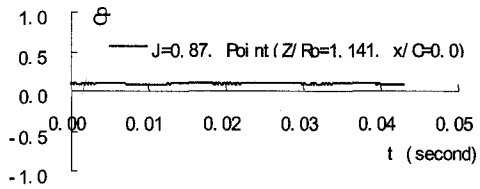

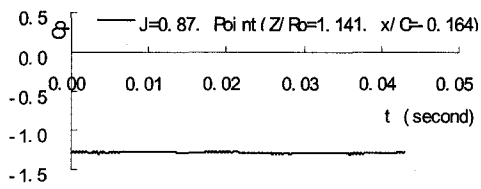

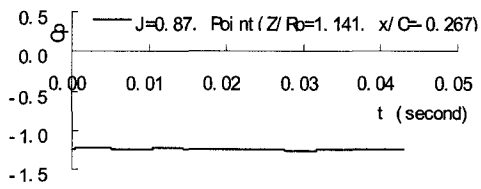

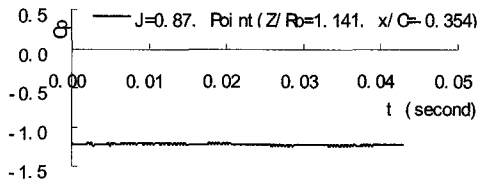

Figure B-33 $J = 0.870$, $Z / R_p = 1.141$

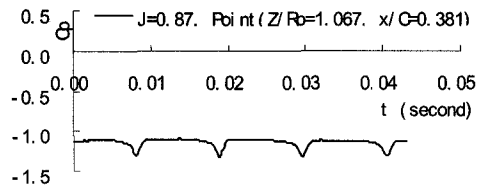

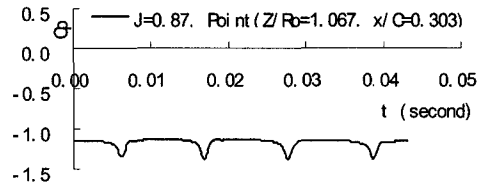

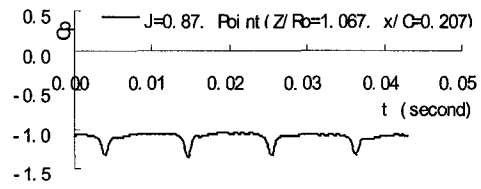

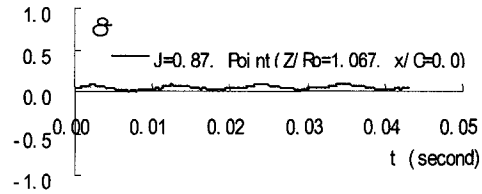

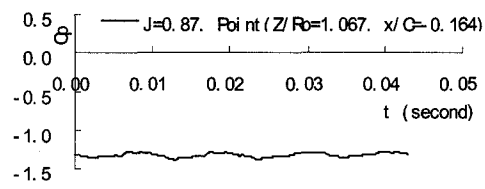

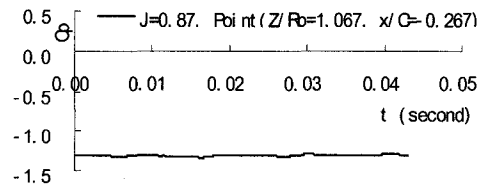

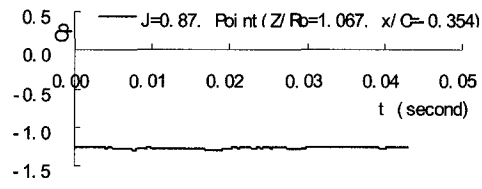

Figure B-34 $J = 0.870$, $Z / R_p = 1.067$

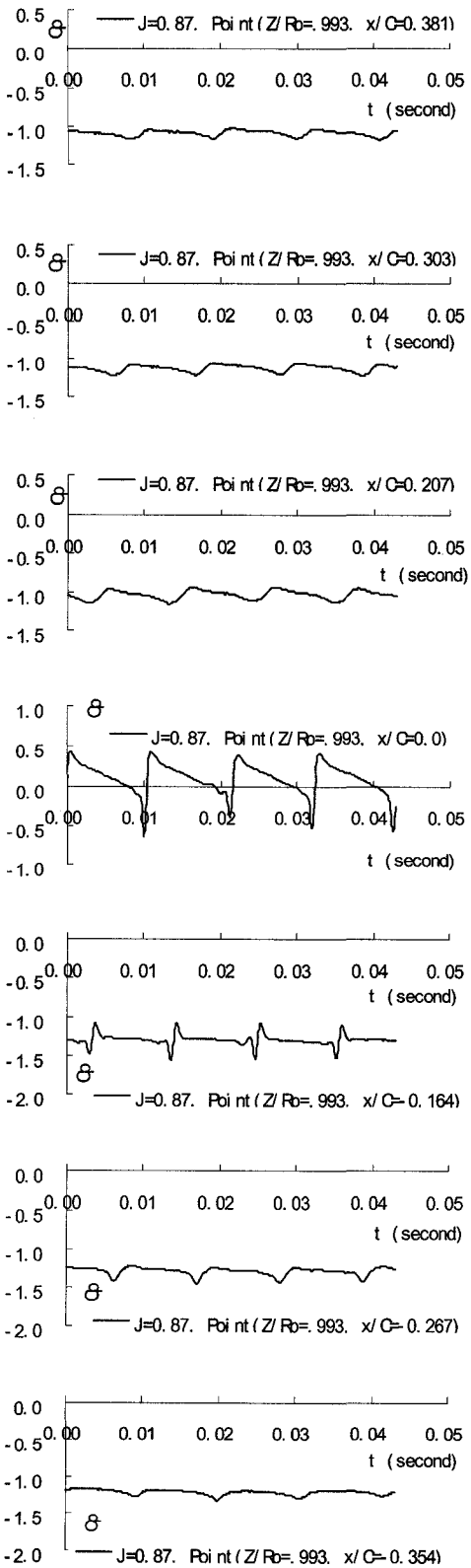

Figure B-35 $J = 0.870$, $Z / R_p = 0.993$

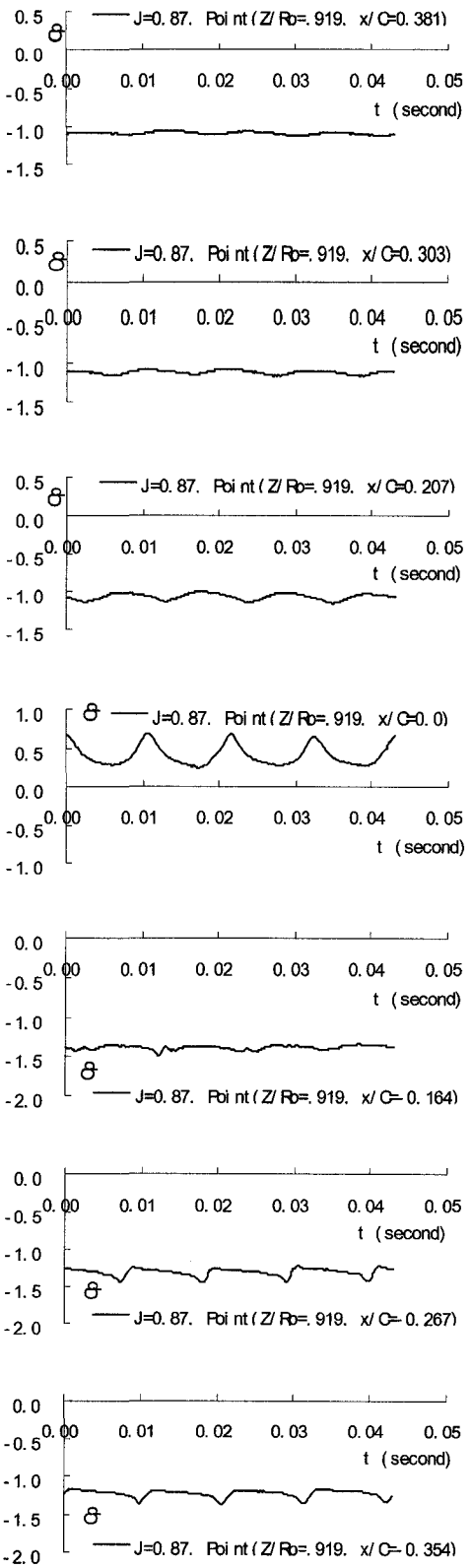

Figure B-36 $J = 0.870$, $Z / R_p = 0.919$

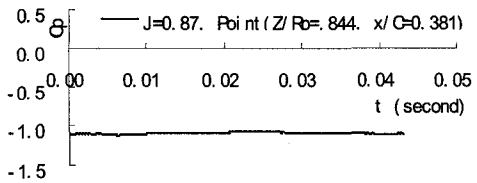

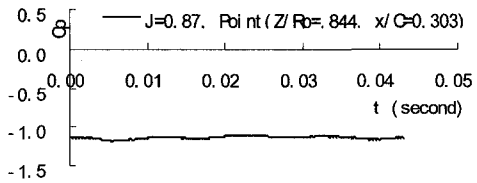

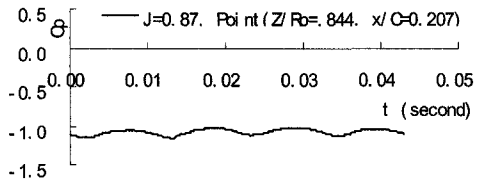

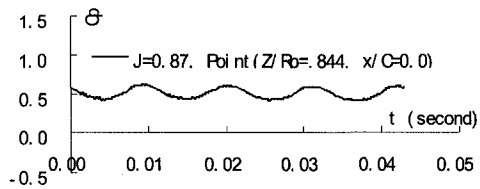

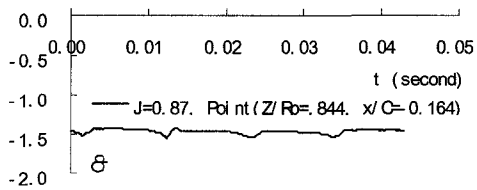

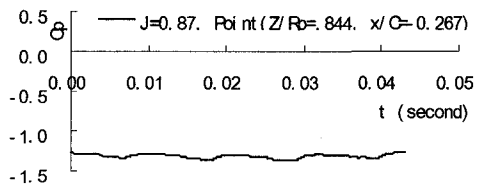

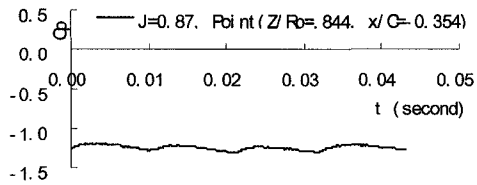

Figure B-37 $J = 0.870$, $Z/R_p = 0.844$

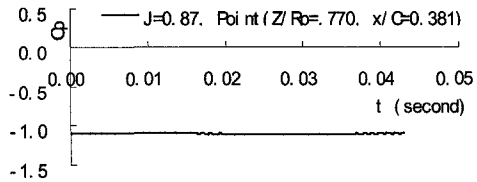

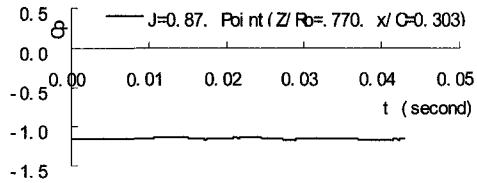

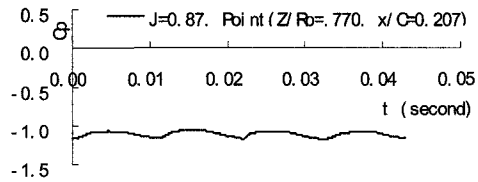

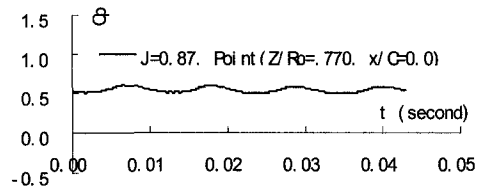

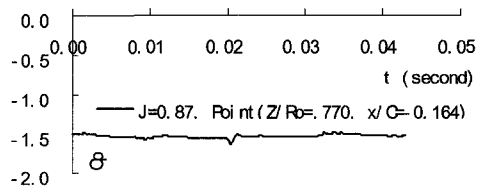

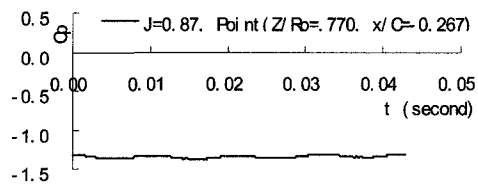

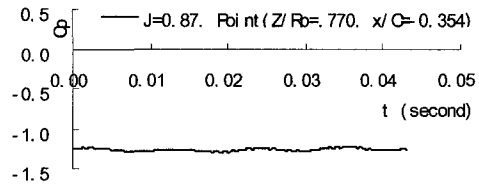

Figure B-38 $J = 0.870$, $Z/R_p = 0.770$

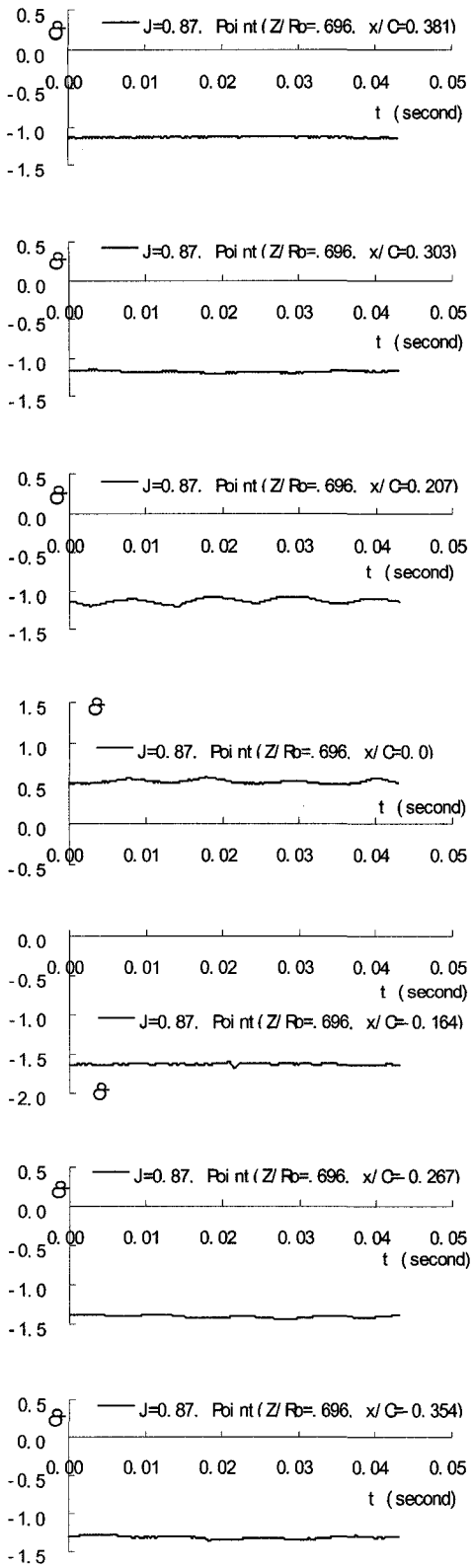

Figure B-39 $J = 0.870$, $Z / R_p = 0.696$

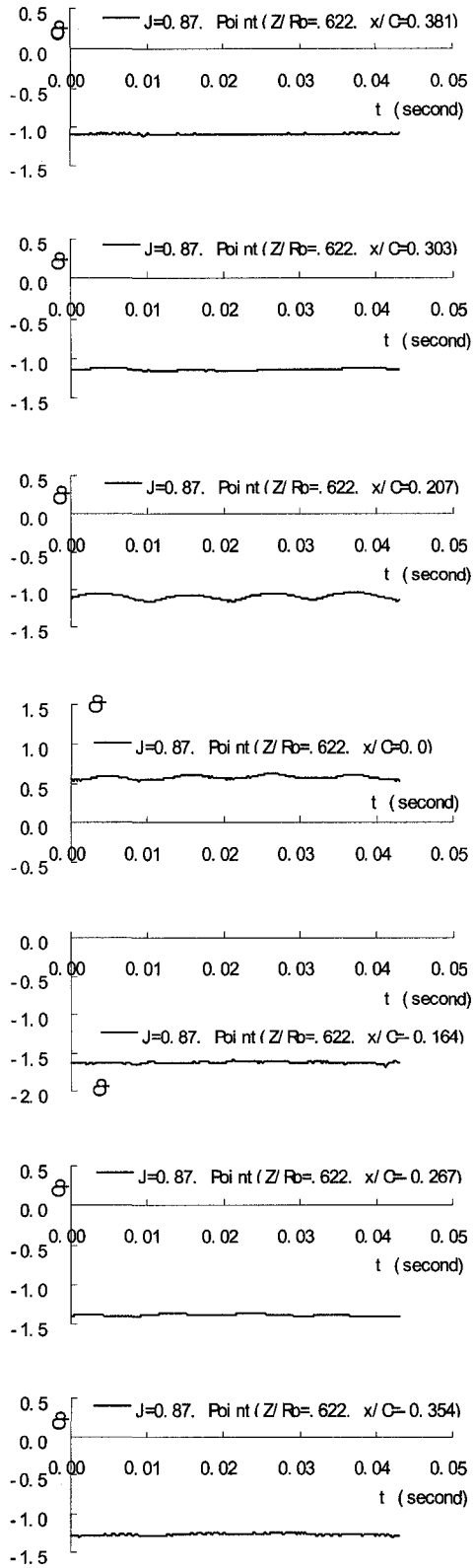

Figure B-40 $J = 0.870$, $Z / R_p = 0.622$